

Gradient topographies and functional gradient materials

Dissertation

zur Erlangung des akademischen Grades
eines Doktors der Naturwissenschaften (Dr. rer. nat.)
im Promotionsprogramm „Polymer Science“
der Bayreuther Graduiertenschule für Mathematik und Naturwissenschaften

vorgelegt von

Andreas Erich Schedl

geboren in Tirschenreuth, Deutschland

Bayreuth, 2019

Die vorliegende Arbeit wurde in der Zeit von November 2013 bis Oktober 2019 am Lehrstuhl Makromolekulare Chemie I der Universität Bayreuth unter Betreuung von Herrn Prof. Dr. Hans-Werner Schmidt angefertigt.

Vollständiger Abdruck der von der Bayreuther Graduiertenschule für Mathematik und Naturwissenschaften (BayNAT) der Universität Bayreuth genehmigten Dissertation zur Erlangung des akademischen Grades eines Doktors der Naturwissenschaften (Dr. rer. nat.).

Dissertation eingereicht am: 02. Oktober 2019

Zulassung durch das Leitungsgremium: 08. Oktober 2019

Wissenschaftliches Kolloquium: 08. Mai 2020

Amtierender Direktor: Prof. Dr. Markus Lippitz

Prüfungsausschuss:

Prof. Dr. Hans-Werner Schmidt (Gutachter)

Prof. Dr. Georg Papastavrou (Gutachter)

Prof. Dr. Thomas Scheibel (Vorsitz)

Prof. Dr. Lothar Kador

(Weiterer Gutachter: Prof. Dr. Alexander Böker)

“The ignorance of the world often makes people believe that life should be black and white – that you must choose sides – and so the world of colourful gradients goes unadmired.”

A.J. Darkholme, Rise of the Morningstar

Table of contents

Abbreviations	I
Symbols	III
Short summary	V
Kurzzusammenfassung	IX
List of publications	XIII
1. Introduction	1
1.1. Invented by nature: Functional materials with advanced surface topography and mechanics	1
1.2. Inspired by nature: Synthetic gradient materials	6
1.3. Surface modification in technology	9
1.4. Controlled wrinkling	10
1.5. Surface relief gratings	16
1.6. Photonic crystals	21
1.7. References	24
2. Objective of this thesis	45
3. Synopsis	47
3.1. Overview of the thesis	47
3.2. Hierarchical line-defect patterns in wrinkled surfaces	50
3.3. Controlled wrinkling of thin metal films	52
3.4. Confinement templates for hierarchical nanoparticle alignment prepared by azobenzene-based surface relief gratings	54
3.5. Refractive-index determination of solids from first- and second-order critical diffraction angles of periodic surface patterns	56
3.6. Inspired by the chameleon skin: Gradient photonic materials based on one-dimensional photonic crystals	59
3.7. References	61
4. Publications	63
4.1. Individual contributions to joint publications	63
4.2. Hierarchical line-defect patterns in wrinkled surfaces	67
4.3. Controlled wrinkling of gradient metal films	101
4.4. Confinement templates for hierarchical nanoparticle alignment prepared by azobenzene-based surface relief gratings	117
4.5. Refractive-index determination of solids from first- and second-order critical diffraction angles of periodic surface patterns	145
4.6. Gradient photonic materials based on one-dimensional polymer photonic crystals	159
5. Extended summary	183
6. Danksagung	187

Abbreviations

1D	One-dimensional
1DPC	One-dimensional photonic crystal
2D	Two-dimensional
3D	Three-dimensional
AFM	Atomic Force Microscopy
CAS	Chemical Abstracts Service
CIE	International Commission on Illumination (Commission Internationale de l'Éclairage)
DOI	Digital Object Identifier
DVD	Digital Versatile Disc
ESI	Electronic Supplementary Information
FCC	Face-centered cubic
FWHM	Full width at half-maximum
HMEM	2-[<i>p</i> -(2-Hydroxy-2-methylpropiophenone)]-ethylene glycol-methacrylate
hs	Hard-soft gradient
hshsh	Hard-soft-hard-soft-hard gradient
ITO	Indium tin oxide
PC	Polycarbonate
PDMS	Polydimethylsiloxane
PGM	Polymer gradient material
PP	Polypropylene
preCOL-D	Precollagen (distal portion)
preCOL-NG	Precollagen (non-gradient portion)
preCOL-P	Precollagen (proximal portion)
PS	Polystyrene
PVOH	Polyvinylalcohol

QNM	Quantitative nanomechanical mapping
RT	Room temperature
SEM	Scanning Electron Microscopy
SI	Supplementary Information
SiO _x	Silicium oxide
SRG	Surface relief grating
TEM	Transmission Electron Microscopy
THF	Tetrahydrofuran
UV	Ultraviolet light
UVO	Ultraviolet light/Ozone treatment
UV-Vis	Ultraviolet and visible light

Symbols

A	Amplitude
c	Parameter for control of anisotropy
d	Lattice constant
E	Young's modulus
E_{eff}	Effective Young's modulus
E_f	Young's modulus of hard film
\bar{E}_f	Plain strain modulus of hard film
E_s	Young's modulus of elastic substrate
\bar{E}_s	Plain strain modulus of elastic substrate
e	Euler number
ε	Buckling strain
ε_c	Critical buckling strain
F	Force
$\varphi_{l,\text{in}}$	Angle of incident light wave (order l)
$\varphi_{l,\text{out}}$	Angle of diffracted light wave (order l)
h	Film thickness (in sections about controlled wrinkling)
h	Grating height (in sections about surface relief gratings)
h	Planck constant
k_b	Boltzmann constant
L_y	Gradient length
l	Length of substrate (in sections about controlled wrinkling)
l	Diffraction order (in sections about surface relief gratings)
Λ	Grating period
λ	Wavelength
m	Modulus ratio (in sections about controlled wrinkling)
m	Diffraction order (in sections about photonic crystals)

n	Thickness ratio (in sections about controlled wrinkling)
n_{eff}	Effective refractive index
n_i	Repetitive unit for gradient
n_m	Repetitive unit for matrix
n_{mat}	Refractive index
ν	Frequency (in sections about surface relief gratings)
ν	Poisson ratio (in sections about controlled wrinkling)
ν_f	Poisson ratio of hard film
ν_s	Poisson ratio of elastic substrate
p	Pressure
q	Wavenumber
σ_d	Defect density ratio
σ_r	Radial stress
σ_z	Axial stress
T	Temperature
T_m	Melting temperature
θ	Bragg angle
u	Local height of surface
W	Parameter for control of anisotropy
ξ	Term for buckling strain

Short summary

This thesis focuses on the preparation, characterization and application of *gradient topographies and gradient functional materials*. For that, polydimethylsiloxane elastomers are surface-modified in different manners by three methods *controlled wrinkling*, formation of *surface relief gratings*, and preparation of *responsive photonic crystals*.

The motivation for the work arises from nature. Nature utilizes well-defined hierarchical structures and gradients to create functional materials with advanced surface topography and tailored mechanical properties. Examples for tailored surface topographies are colorful butterfly wings and shark skin with improved hydrodynamics. Examples for responsive functional surfaces are the impressive skin color variations of chameleons and the brilliant appearance of tropical fishes, both based on photonic crystals. Improved mechanical properties can be found for example in the sea mussel. The byssus reveals a stiffness gradient which allows an improved connection of the soft interior of the mussel to a hard surface of a rock. The natural concepts of these functional materials and surfaces can be transferred to technical systems.

In this context, the introduction gives a brief overview about tailored materials and surfaces in nature and their corresponding functionalities. Furthermore, methods to artificially prepare surface topographies and functionalities are presented with respect to the state of the art. The first method is controlled wrinkling which is a comparatively simple technique to form surface patterns. The principle is based on a hard surface film which is attached to a soft elastomer substrate. Compression of such a composite material leads to the formation of wrinkled patterns. Hereby, the wavelength can be tuned *via* the Young's moduli and Poisson ratios of film and substrate, respectively, as well as the thickness of the hard film. The second method is the inscription of surface relief gratings in azobenzene films utilizing a holographic technique. This technique allows the inscription of gratings with a sinusoidal wave pattern. The third approach utilizes photonic crystals. These materials reveal a photonic band gap and decouple a certain wavelength upon illumination with visible light.

This cumulative thesis consists of five topics which result in five publications. An overview of the thesis as well as a summary of the major achievements is presented in a synopsis.

The *first* and the *second topic* focus on the formation of gradient surfaces *via* controlled wrinkling. In the *first topic*, the formation of such gradient surfaces is based on a continuous gradient in the Young's modulus of the polydimethylsiloxane elastomer substrate. Embedding of such a stiffness gradient material in a matrix allows the systematic formation and investigation of hierarchical line-defects at the interface. The investigations on these line-defects and the developed prevention strategy contribute essentially to the fundamental understanding of controlled wrinkling.

The *second topic* covers the formation of gradient surfaces *via* controlled wrinkling by variation of the thickness of the hard film. For that, thin metal films with a gradient in film thickness were deposited on polydimethylsiloxane substrates using a combinatorial vapor deposition technique. Gold, chromium, and indium were investigated with respect to wrinkling behavior and surface morphology. The developed technique is a powerful approach to efficiently screen metal wrinkles with respect to their wavelengths on one substrate.

The *third* and the *fourth topic* cover the preparation of functional materials with sinusoidal surfaces *via* surface relief gratings. These gratings were inscribed optically in azobenzene films with a holographic technique. The *third topic* demonstrates the non-destructive grating transfer to polydimethylsiloxane and two thermoplastic polymers. Replicas with surface relief gratings with varying grating height were used as confinement templates for the alignment of nanoparticles. This represents a very elegant and efficient technique to screen the assembly of colloidal nanoobjects.

The *fourth topic* presents a novel technique to determine the refractive-index from transparent solids based on surface relief gratings. The principle is based on the angle-dependent investigation of the first and second order diffraction of monochromatic light on these gratings. The presented technique is a powerful alternative to refractive-index determination *via* an Abbe refractometer or spectral ellipsometry.

The *fifth topic* focuses on the preparation of gradient photonic materials inspired by the chameleon skin. These materials consist of a one-dimensional photonic crystal which is attached on top of a polydimethylsiloxane elastomer substrate with a gradient in stiffness. Unstrained samples reveal a uniform reflectance over the entire surface of the photonic

crystal. Upon strain, a blueshift with a gradient in reflectance occurs. The reflectance pattern can be controlled by tailoring the architecture of the polydimethylsiloxane substrate. This is demonstrated for rainbow-like and stripe-like reflectance patterns. The presented gradient photonic materials are models for the development of nature-inspired mechanochromic sensors.

Kurzzusammenfassung

Diese Arbeit befasst sich mit der Herstellung, Charakterisierung und Anwendung von Gradiententopografien und funktionellen Gradientenmaterialien. Dazu werden Polydimethylsiloxan-Elastomere auf unterschiedliche Weise durch die drei Methoden kontrollierte Faltenbildung, Präparation von Oberflächenreliefgittern und Herstellung ansprechender photonischer Kristalle oberflächenmodifiziert.

Die Motivation für diese Arbeit kommt aus der Natur. Die Natur nutzt wohldefinierte hierarchische Strukturen und Gradienten, um funktionale Materialien mit hochentwickelter Oberflächentopographie und maßgeschneiderten mechanischen Eigenschaften zu erzeugen. Beispiele für maßgeschneiderte Oberflächentopografien sind brillant schimmernde Schmetterlingsflügel sowie Haifischhaut, die eine verbesserte Hydrodynamik aufweist. Beispiele für responsive funktionelle Oberflächen sind die eindrucksvolle Farbvariation der Haut von Chamäleons und das brillante Erscheinungsbild tropischer Fische, die beide auf photonischen Kristallen basieren. Ein Beispiel für eine gezielte Optimierung der mechanischen Eigenschaften sind marine Muscheln. Der Byssus weist einen Steifigkeitsgradienten auf, der eine optimierte Anbindung des weichen Inneren der Muschel an die harte Oberfläche eines Felsens ermöglicht. Die natürlichen Konzepte dieser Funktionsmaterialien und Oberflächenstrukturen können auf technische Systeme übertragen werden.

In diesem Zusammenhang gibt die Einführung einen kurzen Überblick über maßgeschneiderte Materialien und Oberflächen in der Natur und deren entsprechende Funktionalitäten. Darüber hinaus werden Methoden zur künstlichen Erstellung von Oberflächentopografien und -funktionalitäten zum Stand der Technik vorgestellt. Die erste Methode ist die kontrollierte Faltenbildung – eine vergleichsweise einfache Technik zur Strukturierung von Oberflächen. Das Prinzip basiert auf einem harten Film, der auf die Oberfläche eines weichen Elastomersubstrats aufgebracht wird. Durch Kompression eines solchen Verbundmaterials werden Faltenmuster gebildet. Die Wellenlänge kann über die Elastizitätsmoduln und Poisson-Verhältnisse von Film bzw. Substrat sowie die Dicke des harten Films eingestellt werden. Die zweite Methode ist das Einschreiben von Oberflächenreliefgittern in Azobenzolfilme unter Verwendung einer holographischen Technik. Diese Technik ermöglicht das Einschreiben von Gittern mit sinusartigem Wellenmuster. Der dritte Ansatz verwendet photonische Kristalle.

Diese Materialien weisen eine photonische Bandlücke auf und reflektieren Licht einer bestimmten Wellenlänge.

Diese kumulative Dissertation beinhaltet fünf Themen, die als Resultat fünf Publikationen hervorbrachten. Ein Überblick über die Arbeit sowie eine Zusammenfassung der wichtigsten Leistungen ist in einer Synopse dargestellt.

Das *erste* und *zweite Thema* befasst sich mit der Bildung von Gradientenoberflächen mittels kontrollierter Faltenbildung. Im *ersten Thema* basiert die Bildung solcher Gradientenoberflächen auf einem kontinuierlichen Gradienten im Elastizitätsmodul des elastischen Substrats. Das Einbetten eines solchen Steifigkeitsgradientenmaterials in eine Matrix ermöglicht die systematische Bildung und Untersuchung von hierarchischen Liniendefekten an der Grenzfläche. Die Untersuchungen zu diesen Linienfehlern und die entwickelte Strategie zur Vermeidung dieser Defekte tragen wesentlich zum grundlegenden Verständnis der kontrollierten Faltenbildung bei.

Das *zweite Thema* befasst sich mit der kontrollierten Faltenbildung von Gradientenoberflächen durch Variation der Dicke des harten Films. Zu diesem Zweck wurden dünne Metallfilme mit einem Gradienten in der Filmdicke mittels einer kombinatorischen Aufdampftechnik auf elastischen Substraten aufgebracht. Gold, Chrom und Indium wurden im Hinblick auf die Faltenbildung und die Oberflächenmorphologie untersucht. Die entwickelte Technik ist ein leistungsstarker Ansatz, um Metallfalten in Bezug auf die ausgebildeten Wellenlängen auf einem Substrat effizient zu screenen.

Das *dritte* und *vierte Thema* befasst sich mit der Herstellung funktioneller Materialien mit sinusförmigen Oberflächenstrukturen auf Basis von Oberflächenreliefgittern. Diese Gitter wurden mit einer holographischen Technik in Azobenzolfilme optisch eingeschrieben. Das *dritte Thema* behandelt die zerstörungsfreie Übertragung von Gittern auf Polydimethylsiloxan und zwei thermoplastische Polymere. Repliken von Oberflächenreliefgittern mit einer Variation in der Gitterhöhe wurden zudem als Template für die Anordnung von Nanopartikeln verwendet. Dies ist eine sehr elegante und effiziente Technik zum Screening der Anordnung kolloidaler Nanoobjekte.

Das *vierte Thema* repräsentiert eine neuartige Technik zur Bestimmung des Brechungsindex von transparenten Festkörpern mit Hilfe von Oberflächenreliefgittern. Das Prinzip basiert auf der winkelabhängigen Untersuchung der Beugung monochromatischen Lichts erster und zweiter Ordnung an diesen Gittern. Die vorgestellte Technik ist eine leistungsstarke Alternative zur Brechungsindexbestimmung *via* Abbe-Refraktometer oder Spektral-ellipsometer.

Das *fünfte Thema* befasst sich mit der Herstellung von photonischen Gradientenmaterialien, die von der Chamäleonhaut inspiriert sind. Diese Materialien bestehen aus einem eindimensionalen photonischen Kristall, der auf einem Polydimethylsiloxan-Elastomer mit einem Steifigkeitsgradienten aufgebracht ist. Ungedehnte Proben zeigen eine gleichmäßige Reflektivität über die gesamte Oberfläche des photonischen Kristalls. Bei Verformung erfolgt eine Blauverschiebung mit einem Gradienten in der Reflektivität. Das Reflexionsmuster kann durch Anpassen der Architektur des Polydimethylsiloxansubstrats gesteuert werden. Dies wird für regenbogenartige und streifenartige Reflexionsmuster demonstriert. Die vorgestellten photonischen Gradientenmaterialien sind Modelle für die Entwicklung von bioinspirierten mechanochromen Sensoren.

List of publications

The following publications are presented within this thesis:

- [1] B. A. Glatz, M. Tebbe, B. Kaoui, R. Aichele, C. Kuttner, A. E. Schedl, H.-W. Schmidt, W. Zimmermann, A. Fery, *Hierarchical line-defect patterns in wrinkled surfaces*, *Soft Matter* **2015**, *11*, 3332-3339.
- [2] A. E. Schedl, C. Neuber, A. Fery, H.-W. Schmidt, *Controlled wrinkling of gradient metal films*, *Langmuir* **2018**, *34*, 14249-14253.
- [3] A. E. Schedl, P. T. Probst, C. Meichner, C. Neuber, L. Kador, A. Fery, H.-W. Schmidt, *Confinement templates for hierarchical nanoparticle alignment prepared by azobenzene-based surface relief gratings*, *Soft Matter* **2019**, *15*, 3872-3878.
- [4] C. Meichner, A. E. Schedl, C. Neuber, K. Kreger, H.-W. Schmidt, L. Kador, *Refractive-index determination of solids from first- and second-order critical diffraction angles of periodic surface patterns*, *AIP Advances* **2015**, *5*, 087135.
- [5] A. E. Schedl, I. R. Howell, J. J. Watkins, H.-W. Schmidt, *Gradient Photonic Materials based on One-dimensional Polymer Photonic Crystals*, *Macromolecular Rapid Communications* **2020**, *41*, 2000069.

The following publications arose from collaborations within the time frame of the thesis. They are related to topics beyond the scope of this thesis and hence are not considered further in this work.

- [6] C. Neuber, H.-W. Schmidt, P. Strohrriegl, A. Ringk, T. Kolb, A. E. Schedl, V. Fokkema, M. G. A. van Veghel, M. Cooke, C. Rawlings, U. Dürig, A. Knoll, J.-F. de Marneffe, Z. el Otell, M. Kaestner, Y. Krivoschapina, M. Budden, I. W. Rangelow, *Tailored molecular glass resists for scanning probe lithography*, *Proc. SPIE* **2015**, *9425*, 94250E.

- [7] C. Neuber, H.-W. Schmidt, P. Strohriegl, D. Wagner, F. Krohn, A. E. Schedl, S. Bonanni, F. Holzner, C. Rawlings, U. Dürig, A. W. Knoll, *PVD prepared molecular glass resists for scanning probe lithography*, Proc. SPIE **2016**, 9779, 97791C.
- [8] C. Hopmann, M. Adamy, P. Schäfer, H.-W. Schmidt, T. Kolb, A. E. Schedl, *Chemisches Recycling von Polystyrol im Doppelschneckenextruder*, IKV Fachtagung „Innovative Compoundieraufgaben – Herausforderungen, Perspektiven, Lösungen **2019**.
- [9] P. Schäfer, C. Hopmann, M. Facklam, L. Hollerbach, T. Kolb, A. E. Schedl, H.-W. Schmidt, F. Nosić, B. Wilhelmus, *Continuous chemical recycling of polystyrene with a twin-screw extruder*, Advances in Polymer Processing **2020**, Springer Vieweg, 37-49.

1. Introduction

1.1. Invented by nature: Functional materials with advanced surface topography and mechanics

Through evolution, nature developed materials, objects and processes to solve most diverse natural issues.¹ The principle behind these solutions is often based on specific structure-property relationships. The exploration, adaption, and use of these natural structure-property relationships play a key role in the development of new biomimetic materials and methods.² In the following, examples of natural materials with tailored surface topography, responsive functionalities and advanced mechanics are presented. The underlying structure concepts of these materials are used in this thesis for the development of new materials with gradient surfaces and advanced functionalities.

1.1.1. Natural materials with tailored surface topography

Natural surfaces often reveal a surface topography with specific periodic patterns. Utilizing such periodic structures, living organisms usually obtain specific functionalities and hence advantages within their environment. Sharks as the *Carcharhinus galapagensis* have riblet structures with periodicities in the micrometer range aligned in the direction of flow ([Figure 1.1.1a](#) and [Figure 1.1.1b](#)).^{3,4} These scales diminish the hydrodynamic resistance in water and hence provide a faster forward motion in water. Butterflies like *Ancyluris meliboeus* often have brilliant reflectance patterns on their wings ([Figure 1.1.1c](#)). These are based on light diffraction and interference caused by periodic structures in the nanometer range ([Figure 1.1.1d](#)).⁵

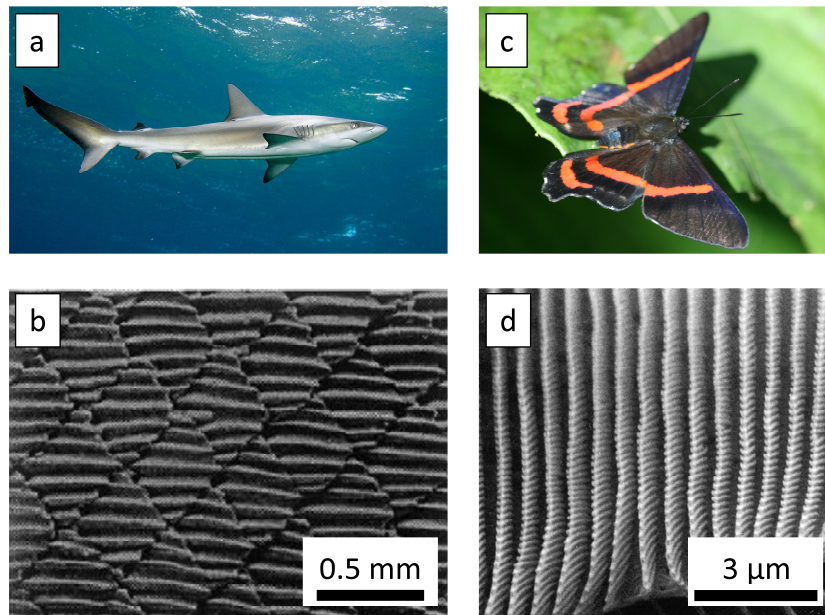


Figure 1.1.1: Natural examples for periodic surface patterns. a) Shark *Carcharhinus galapagensis* (image by Andrew J. Green,⁶ provided under CC BY 4.0 license⁷). b) The shark skin consists of small micrometer-scaled riblets (image adapted and reproduced with permission from reference 8, © 2010 The Royal Society). c) Butterfly *Ancyluris meliboeus* (image by Dr. Alexey Yakovlev,⁹ provided under CC BY-SA 2.0 license¹⁰). d) *Ancyluris meliboeus* obtains its structural color from multilayered nanostructured arrangements (adapted and reproduced with permission from reference 11, © 2001 The Royal Society).

1.1.2. Natural materials with responsive functionality

Besides periodically aligned surfaces, nature uses further periodic structures to provide specific tunable functionalities to certain species. One class are responsive photonic crystals which allow animals to reversibly tune their color and hence their appearance. Such color changes can be triggered by different motivations such as communication, exhibition, camouflage, and warning.¹²

Natural responsive photonic crystals can be found in tropical fish such as *Neon tetra*,¹³ cephalopods such as octopus and squids,¹⁴ beetles such as *Charidotella egregia*,¹⁵ and chameleons.¹⁶ Male panther chameleons (*Furcifer pardalis*) show a very impressive color change upon excitation (Figure 1.1.2a).¹⁷ The skin color is thereby varied in a broad range from blue to red in the visible electromagnetic spectrum (Figure 1.1.2b). The mechanism is based on guanine nanocrystals which are embedded in two thick cell layers denoted as S- and D-

iridophores (Figure 1.1.2c). TEM investigations revealed that these nanocrystals differ in size, shape and arrangement in the S-iridophores (Figure 1.1.2d) and D-iridophores (Figure 1.1.2e). The close-packed arrangement of nanocrystals as it is present in the S-iridophores builds up a three-dimensional photonic crystal. This photonic crystal is responsible for the structural color of chameleons. Excitation of the skin alters the lattice distance within this crystal. This causes the well-known color change. Details about the function of photonic crystals are described in chapter 1.6.

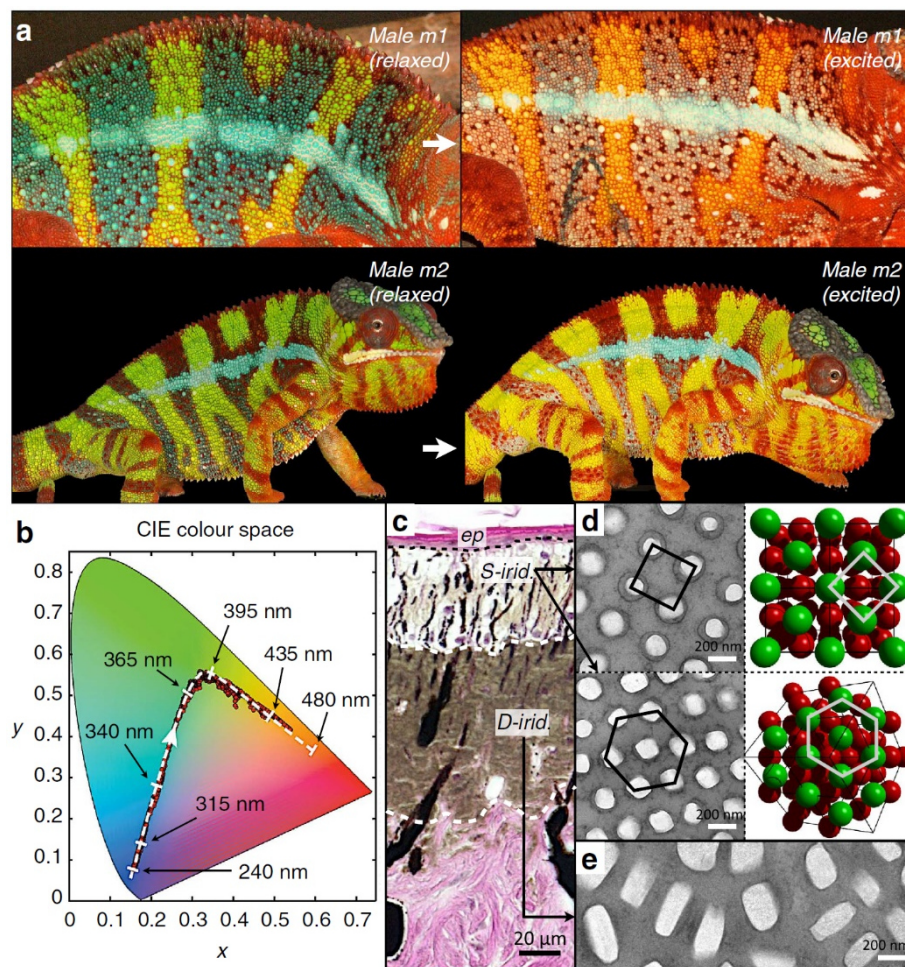


Figure 1.1.2: Color change in chameleons. a) Male panther chameleons change their skin color upon excitation. b) Tunable color range of chameleon skin in the CIE color space. c) Cross section of chameleon skin with indicated iridophores. d) TEM images of guanine nanocrystals in S-iridophores (excited state) and corresponding FCC crystal lattice. e) TEM image of guanine nanocrystals in D-iridophores. Adapted and reproduced with permission from reference 17 (© 2015 Springer Nature).

1.1.3. Natural materials with tailored mechanics

Beside the topographical aspect of the surface structure, also the composition of the material plays a key role for the functionality of natural materials. An example is the byssus of marine mussels like *Mytilus edulis* (Figure 1.1.3a) and *Mytilus galloprovincialis*.¹⁸ This byssus typically consists of 50 – 100 threads (length: 3 – 4 cm, diameter: 50 μm) which connect the mussel to stones in the sea (Figure 1.1.3b).^{19,20} The requirements on these byssus threads are demanding. On the one hand, they must mediate a huge stiffness mismatch between the very soft living mussel tissue ($E = 0.2 \text{ MPa}$) and the very hard stone ($E = 25 \text{ GPa}$).²⁰ On the other hand, they must provide excellent adhesion within the rough environment of the sea. Nature solved this issue by utilizing a gradient material. Each byssus thread consists of a gradient material with a Young's modulus of 50 MPa at the proximal end and a Young's modulus of 500 MPa at the distal end.²¹ This allows a remarkable mediation by a factor of 10. Further adaptations to compensate the huge stiffness mismatch between mussel interior and stone are made in the stem and in the plaque.^{22,23}

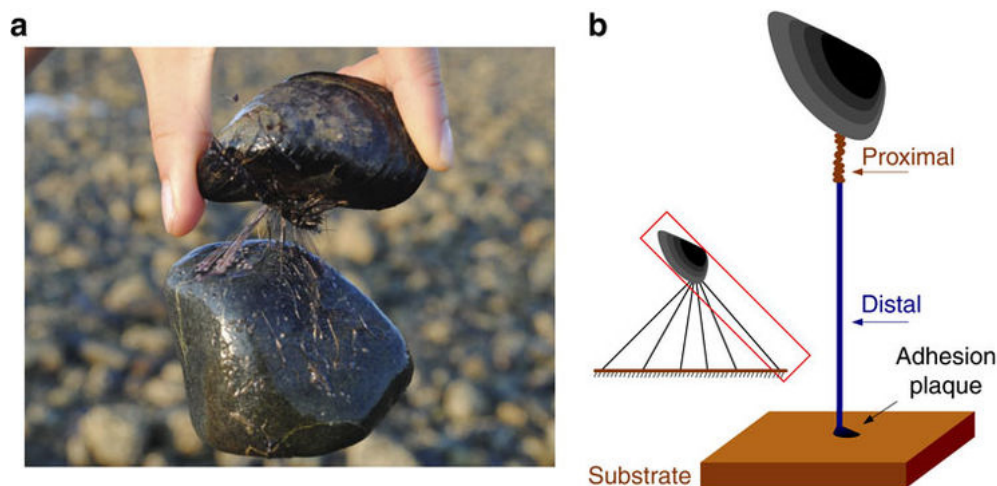


Figure 1.1.3: a) Mussel *Mytilus edulis* attached to a stone. b) The soft mussel interior is connected to the surface of a hard stone *via* mussel byssus threads. Adapted and reproduced with permission from reference 18 (© 2013 Springer Nature).

The microfibrils of the byssus thread are built up from different precursor building blocks known as preCOL-P, preCOL-D and preCOL-NG (with the postscripts -P, -D and -NG standing for proximal, distal, and non-graded, respectively).²⁴ Each of these blocks consist of a collagen core, two flanking units and two terminal histidine-rich domains. The structure and functionality of the collagen core and the histidine-rich domains are comparable in all three

precursor building blocks. The flanking units, however, differ strongly with respect to their structure and resemble silk fibroin in preCOL-D, poly-Glycin in preCOL-NG and elastin in preCOL-P. This structural variation in the flanking units causes a huge variation in stiffness of the corresponding fully hydrated biopolymers, ranging from 2 MPa in preCOL-P and 150 MPa in preCOL-NG up to 10.000 MPa in preCOL-D.

Nature uses this toolbox to create a longitudinal gradient in composition along the byssus thread (Figure 1.1.4). The stiff PreCOL-D is mainly present at the distal end and decreases gradually towards the proximal end. By contrast, the content of the soft preCOL-P increases gradually from the distal towards the proximal end. PreCOL-NG is evenly distributed and not varied along the entire thread. The compositional gradient prepared with these preCOLs causes the above-mentioned stiffness gradient from 50 MPa to 500 MPa. This gradient material has an enhanced strain energy and therefore provides excellent shock absorption within the rough environment of the sea.²⁴

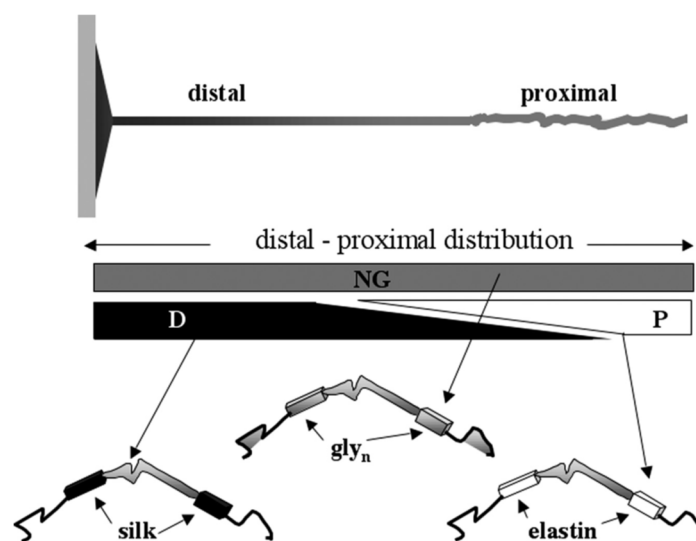


Figure 1.1.4: Composition of the mussel byssus thread. The thread is built up by three building blocks (preCOL-D, preCOL-P and preCOL-NG) which differ in their flanking units. PreCOL-D and preCOL-P form a compositional gradient along the thread. Adapted and reproduced with permission from reference 19 (© 2005 Taylor & Francis).

1.2. Inspired by nature: Synthetic gradient materials

Biomimicking gradient materials like the mussel byssus is a very promising approach for the development of new polymer gradient materials (PGMs) with outstanding mechanical characteristics like stiffness and enhanced failure resistance.²⁵ These PGMs have to be differentiated from gradient copolymers. PGMs reveal a macroscopic gradient along one axis. Gradient copolymers, however, possess a gradient along the polymer chain, but do not form a macroscopic gradient.²⁶

PGMs can be classified according to their geometry. If the aspect ratio of the material is larger than one, compositional gradients in x -, y - and z -direction are denoted as *longitudinal*, *lateral* and *cross-sectional*, respectively (Figure 1.2.1). Materials with a changing geometry in z -direction but discrete composition are denoted as *thickness* gradient.

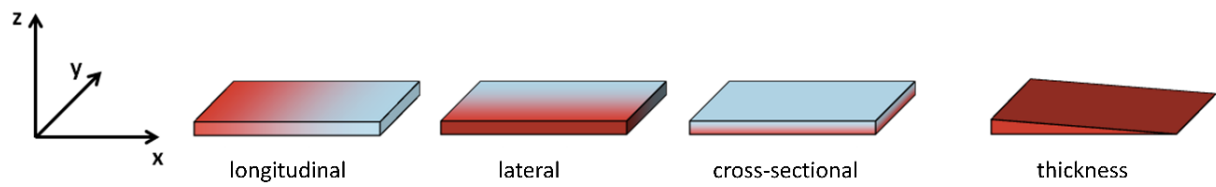


Figure 1.2.1: Possible geometries of one-dimensional polymer gradient materials.

Claussen *et al.* demonstrated the artificial preparation of longitudinal polymer gradient materials by utilizing a high-precision syringe pump setup for various systems, including polyurethane,²⁷ polyacrylate,²⁷ fibroin/gelatin,²⁸ and polydimethylsiloxane.^{29,30} All these gradient materials revealed gradients in stiffness. This was proven by compressive modulus testing as depicted in Figure 1.2.2 for a polydimethylsiloxane gradient material. Polydimethylsiloxane gradient materials were also used within this thesis for tailoring the surface topography and functionalization.

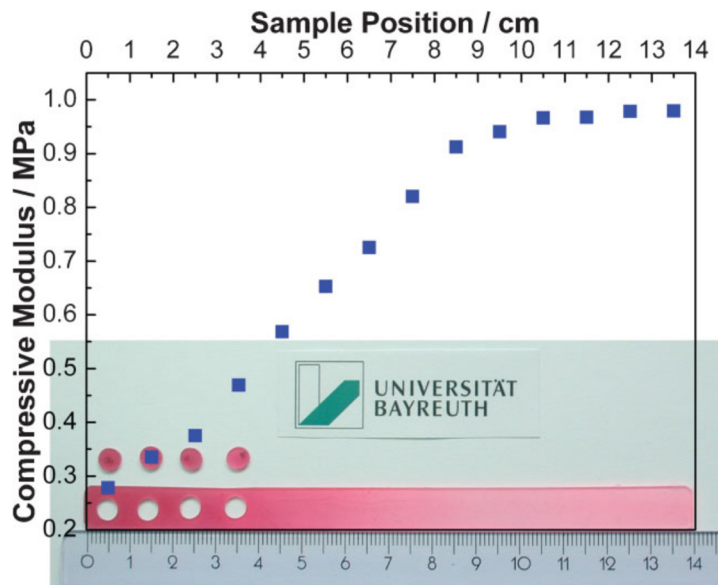


Figure 1.2.2: Compressive modulus testing of a longitudinal PDMS polymer gradient. Reproduced with permission from reference 25 (© 2012 WILEY-VCH Verlag GmbH & Co. KGaA, Weinheim).

The enhanced failure resistance of gradient materials can be explained with the concept of mismatch.²⁰ This concept considers two materials *A* and *B* which are bonded at a contact zone (Figure 1.2.3). Tension leads to an overall present axial stress σ_z . If the stiffness of *A* and *B* is different, also the deformation behavior of those materials is different. This rises interfacial stresses such as the radial stress σ_r in the contact zone. σ_r acts normal to the applied stress and causes failure of the joint upon exceeding a critical value. Assuming a constant Poisson ratio and a nominal axial stress $\sigma_z = 1$, the radial stress is correlated to the mismatch between the Young's moduli of material *A* and *B*. A decreasing mismatch between material *A* and *B* leads to a decreasing radial stress and hence to a decreased probability for failure. Gradient materials do not have a sharp transition between two materials with different stiffnesses. Instead, the gradual and very smooth transition allows an efficient suppression of the critical radial stress and hence decreases the probability for failure.

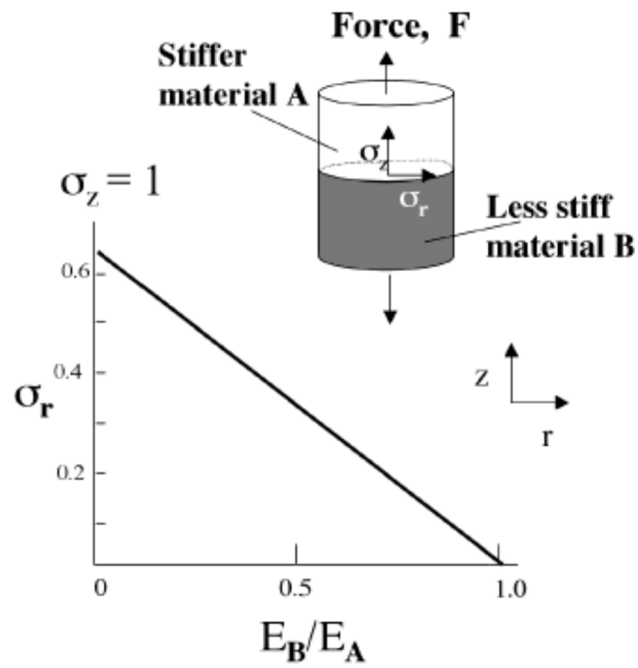


Figure 1.2.3: Connection of two materials A and B with different stiffnesses. Upon load, a radial stress σ_r occurs at the interface. For a constant Poisson ratio and axial stress σ_z , this radial stress decreases with decreasing mismatch of the Young's moduli E_A and E_B at the interface. Adapted and reproduced with permission from reference 20 (© 2004 American Chemical Society).

1.3. Surface modification in technology

Tailoring the *surface topography* on the micro- and nanoscale is a key technology in various fields of research and in the development of diverse applications. Especially surfaces with a periodicity in their patterns play a crucial role. Unique optical, acoustic and electronic properties can be obtained utilizing interference phenomena on such periodically patterned surfaces. Furthermore, such periodic surface patterns can be used to tune hydrodynamic and wetting properties. As demonstrated by the natural example of shark skin, the hydrodynamic friction can be diminished by such surfaces.³ Superhydrophobic surfaces can be generated by utilizing the Lotus effect.³¹ Furthermore, such surface patterns can be used as templates to guide the build-up of even more complex structures.^{32,33}

Various methods to prepare periodic surface patterns are established.³⁴ Typical examples are etching,³⁵ conventional lithography,³⁶ UV-nanoimprint lithography,³⁷ scanning probe lithography,^{38,39} replica molding processes,⁴⁰ and micro-contact printing.⁴¹ Periodic surface patterns with a sinusoidal profile can also be formed *via* controlled wrinkling^{42,43} and the inscription of surface relief gratings in azobenzene films.^{44,45} These two methods are in the focus of this thesis and described briefly in the following chapters 1.4 and 1.5.

Beside surface patterning, the targeted *surface functionalization* plays a further key role in technology. Motivations for that are manifold and include tailoring of properties such as adhesion,⁴⁶ biocompatibility,⁴⁷ conductivity,⁴⁸ wetting,⁴⁹ and optical appearance⁵⁰ such as reflectance. One way to achieve this for the latter is the preparation of a photonic crystal on the surface. This is also in the focus of this thesis and described briefly in chapter 1.6.

1.4. Controlled wrinkling

1.4.1. Fundamentals of controlled wrinkling

Controlled wrinkling is a comparatively simple technique for surface patterning.⁵¹ It requires a thin hard film which is connected to a soft macroscopic elastic substrate.⁵² Common techniques to prepare this hard film on the substrate are oxidation of the surface *via* UV/ozone,⁵³ oxygen plasma⁵⁴ or acids,⁵⁵ evaporation⁵⁶ or sputtering⁵⁷ of a metal, and the deposition of a polymer film⁵⁸ on top of the substrate. An in-plane compression of this system results in a so-called buckling instability.⁵⁹ These instabilities can be formed by planar forces such as mechanical compression,^{60–62} thermal expansion,^{56,63,64} swelling,^{65–67} and capillarity.^{68,69} To relieve the stress built up from this instability, the planarity of the film is destroyed. This results in a spontaneous formation of wrinkles which are oriented perpendicularly to the compressive stress direction (Figure 1.4.1).⁷⁰

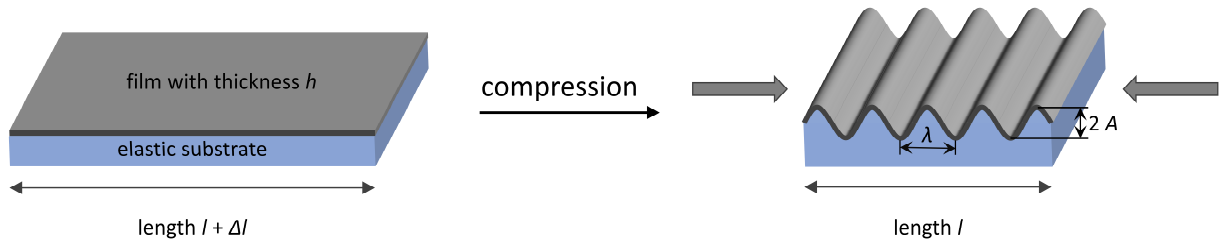


Figure 1.4.1: Wrinkling of a thin hard film (with thickness h) connected to a soft substrate. Upon application of a planar compression force, a wrinkled pattern with a wavelength λ and an amplitude A is formed.

Characteristic parameters to describe the patterned surface are the wavelength λ and the amplitude A of the formed wrinkles, the thickness h of the film, the Young's moduli of film E_f and substrate E_s , as well as the Poisson ratios of film ν_f and substrate ν_s . The initial length of the sample is $l + \Delta l$, the final length is l .

The wrinkle wavelength can be predicted by Equation 1.4.1:⁷⁰

$$\lambda = 2\pi h \sqrt[3]{\frac{E_f(1 - \nu_s^2)}{3E_s(1 - \nu_f^2)}} \quad (1.4.1)$$

The amplitude depends on the film thickness h , the buckling strain $\varepsilon = \Delta l/l$ and the critical buckling strain ε_c which is necessary to induce wrinkling. For $\varepsilon > \varepsilon_c$, the amplitude follows [Equation 1.4.2](#):^{71,72}

$$A = h \sqrt{\frac{\varepsilon}{\varepsilon_c} - 1} \quad (1.4.2)$$

The critical buckling strain hereby is ([Equation 1.4.3](#)):

$$\varepsilon_c = \frac{1}{4} \sqrt[3]{9 \frac{E_s^2 (1 - \nu_f^2)^2}{E_f^2 (1 - \nu_s^2)^2}} \quad (1.4.3)$$

The above-mentioned theory is valid for comparatively small buckling strain values ε . In applications, typically larger buckling strains and hence larger deformations are used. Considering the buckling strain ε in a prefactor, the wrinkle wavelength can then be described according to [Equation 1.4.4](#):⁷²

$$\lambda = \frac{2\pi h}{(1 + \varepsilon) \sqrt[3]{1 + \xi}} \sqrt[3]{\frac{E_f (1 - \nu_s^2)}{3E_s (1 - \nu_f^2)}} \quad (1.4.4)$$

Thereby, ξ is a term for the buckling strain and denoted in [Equation 1.4.5](#):

$$\xi = \frac{5}{32} \varepsilon (1 + \varepsilon) \quad (1.4.5)$$

The theory up to now considered only one layer on the elastic substrate. However, bilayers are sometimes used in applications. To describe this case, Stafford *et al.* developed an equation for the effective modulus of this bilayer from composite beam theory ([Equation 1.4.6](#)):⁷³

$$E_{\text{eff}} = \frac{1 + m^2 n^4 + 2mn(2n^2 + 3n + 2)}{(1 + n)^3 (1 + mn)} E_1 \quad (1.4.6)$$

Hereby, m is the modulus ratio E_2/E_1 and n is the thickness ratio h_2/h_1 of the two layers. Index 1 indicates the layer attached to the substrate and index 2 the top layer.

Within this thesis, these theoretical concepts were utilized for the preparation of gradient wrinkled surfaces with a gradient in wavelength.

1.4.2. Gradient wrinkled surfaces

Gradient wrinkled surfaces with a variation in wavelength can be prepared by tuning the film thickness or the Young's modulus of the elastomer substrate in [Equation 1.4.1](#). Theoretical studies about the buckling mechanism of such a thickness gradient film were done by Yin *et al.*⁷⁴ They developed numerical and analytical methods to predict the wrinkling behavior.

Hiltl *et al.* varied the film thickness of the oxide layer in a system based on plasma treatment of polydimethylsiloxane (PDMS) by utilizing a shielding technique.⁷⁵ A silicon wafer was rested on one side of the stretched substrate and lifted with a spacer at the opposite side. Treatment with air plasma yields a gradient wrinkled surface with a wavelength range from 250 nm to 900 nm. Such gradient surfaces exhibit a gradient wetting behavior. Water droplets placed on such gradient surfaces exhibited a guided motion towards smaller wrinkles.⁷⁶

Li *et al.* also prepared gradient wrinkled surfaces from oxide layers on PDMS.⁷⁷ They used UV/ozone instead of oxygen plasma and inclined the PDMS substrate towards the UV lamp. The continuous change of the irradiation dose with UV light caused a gradient in oxide layer thickness along the sample. This led to a gradient in wavelength.

A gradient wrinkled surface based on sputtering of nickel films was presented by Yu *et al.*⁷⁸ They used a shielding technique to prepare a thickness-gradient film on the edge of unstrained PDMS substrates ([Figure 1.4.2](#)). Thermal contraction of the sample revealed a gradient wrinkled surface over a length of about 400 μm .

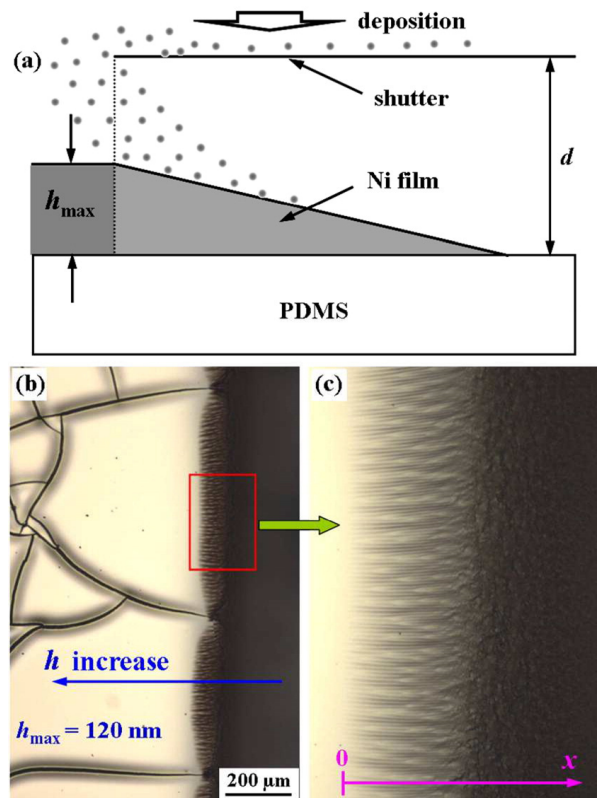


Figure 1.4.2: Formation of a gradient wrinkled surface *via* sputtering of nickel on unstrained PDMS. a) Formation of a thickness gradient by using a shutter during the sputtering process. b) Optical micrograph of the edge of the sputtered sample. c) Gradient wrinkles formed at the edge due to thermal contraction. Reprinted with permission from reference 78 (© 2015 American Chemical Society).

Beside the approach to tune the film thickness, gradient wrinkles can also be prepared by tuning the Young's modulus of the substrate. This was demonstrated by Claussen *et al.* by utilizing a longitudinal gradient material made from PDMS.³⁰ This material was embedded in a PDMS matrix with discrete Young's modulus, strained to 25% and treated with O₂ plasma. After relaxation of the sample, a gradient surface with a wavelength variation from 700 nm to 1200 nm was obtained (Figure 1.4.3).

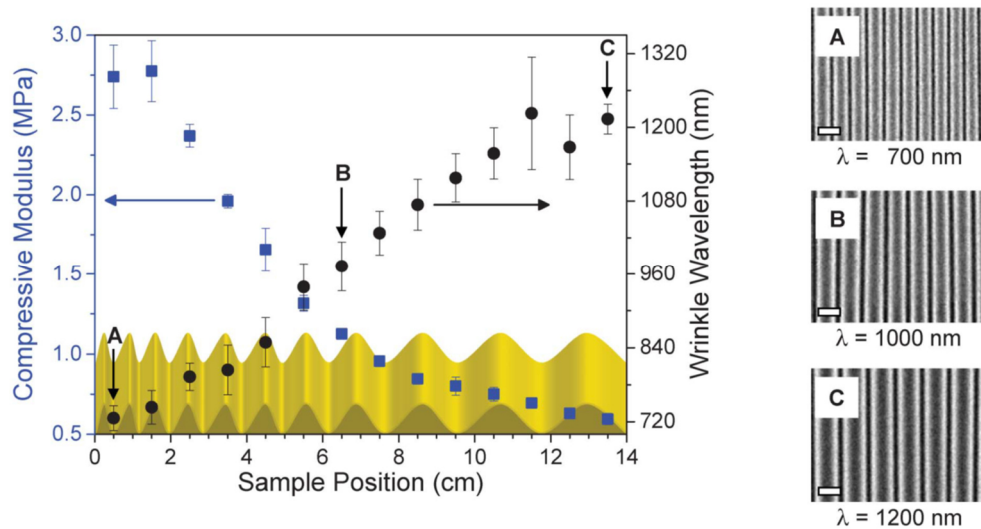


Figure 1.4.3: Gradient wrinkled surface formed by tuning the stiffness of the substrate. Reproduced with permission from reference 30 (© 2012 The Royal Society).

1.4.3. Defect formation in wrinkling

Drawbacks of the controlled wrinkling approach is the typical formation of cracks⁷⁹ and line defects.⁸⁰ Crack formation is attributed to the different Poisson ratios of film and substrate. This causes a different lateral expansion behavior of film and substrate during strain relaxation. As a consequence, the film forms cracks to overcome lateral stress.

Efimenko *et al.* studied the formation of these cracks and defects with respect to the strain release rate (Figure 1.4.4).⁸⁰ They found that line defect formation decreases with decreasing strain release rate. However, slower strain release rates also provoked a stronger crack formation.

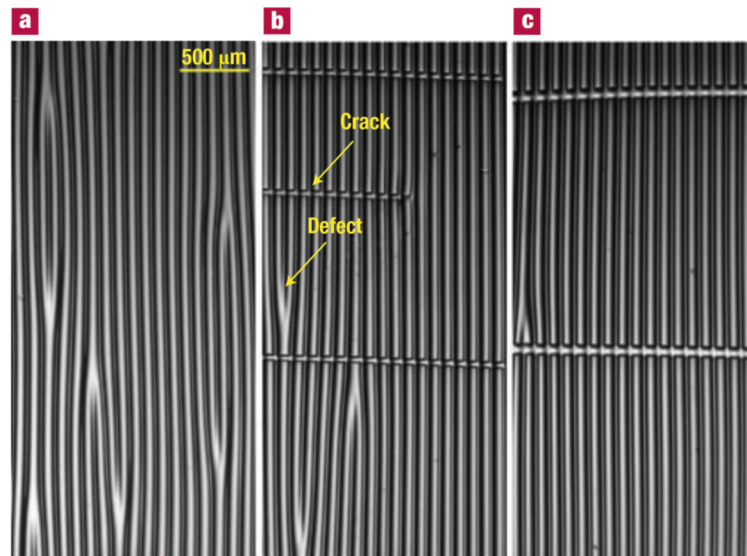


Figure 1.4.4: Formation of cracks and line defects at different strain release rates. a) Instantaneous relaxation. b) Relaxation with a strain release rate of $\approx 900 \mu\text{m min}^{-1}$. c) Relaxation with a strain release rate of $\approx 58 \mu\text{m min}^{-1}$. Reproduced with permission from reference 80 (© 2005 Springer Nature).

Different strategies have been developed to prevent the crack formation. Xuan *et al.* used UV-curable resists for the formation of a hard film on top of a pre-strained PDMS substrate.⁸¹ UV-exposure leads to a gradient interpenetrating network between PDMS and the UV-curable film. This gradient is beneficial to suppress crack formation. Rhee *et al.* formed a comparably soft fluoropolymer film on top of PDMS.⁸² The diminished mismatch between the Young's modulus of film and substrate also suppressed crack formation.

Line defects have not been investigated in detail so far. Thereby, the targeted formation and prevention of these defects is one topic of this thesis.

1.5. Surface relief gratings

1.5.1. Fundamentals of surface relief grating inscription

The preparation of surface relief gratings (SRGs) is an alternative method to obtain periodic sinusoidal surface patterns.⁸³ These gratings are inscribed in photochromic materials using a holographic setup.⁸⁴ The most important class of photochromic materials are azobenzene-containing components which were synthesized in a large variety of small molecules and polymers.⁸⁵

The principle of the inscription process is based on the *trans-cis-trans* photo-isomerization of the azobenzene moieties.⁸⁶ Upon light absorption, the moieties can reorient in the solid state by reversible *trans-cis-trans* transitions (Figure 1.5.1). Absorption of UV light induces a *trans*-to-*cis* conversion of the azobenzene. In reverse, absorption of visible blue light leads to a *cis*-to-*trans* conversion until an equilibrium between both isomers is achieved. The *cis* isomer is thermodynamically less stable and can also return to the *trans* state thermally.

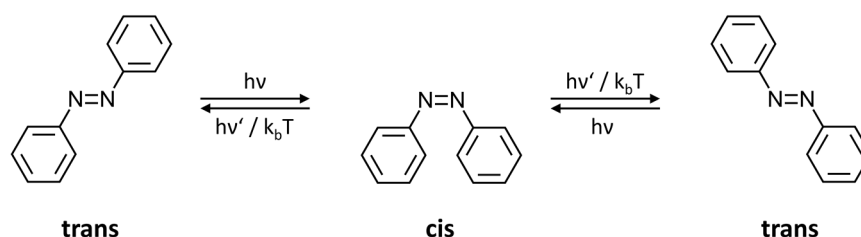


Figure 1.5.1: Reversible *trans-cis-trans* photoisomerization of azobenzene.

Continued illumination with linearly polarized light leads to an orientation of the chromophores perpendicular to the polarization direction of the incident light in the solid state (Figure 1.5.2).⁸⁷ This changes the molecular order from an isotropic to a highly anisotropic state and leads to a macroscopically birefringent behavior of the exposed area.⁸⁸ SRGs can be inscribed into azobenzene-containing films by utilizing a light intensity pattern formed by the interference of two coherent laser beams.⁸⁹ The formation process of SRGs can be attributed to a light-induced macroscopic mass transport at temperatures far below the glass transition temperature.⁹⁰ This was first discovered in 1995 by Natansohn *et al.* and Kumar *et al.*^{91,92} Depending on the material, chromophores migrate from or to illuminated areas of the pattern.⁸⁵ Numerous theories and models have been proposed to describe the photo-induced mass transport, including mean-field theory⁹³, microscopic theory,^{94,95} fluid mechanics,⁹⁶ stochastics,^{97,98} thermodynamics,⁹⁹ molecular dynamics,¹⁰⁰ surface-enhanced

diffusion,¹⁰¹ diffusion *via* random-walk motion,^{102,103} phase-separation,¹⁰⁴ liquid-crystal interactions,¹⁰⁵ dipole interaction with electric field gradients,¹⁰⁶ light-induced pressure gradients,¹⁰⁷ photoisomerization forces,¹⁰⁸ and statistical orientation of polymer side chains¹⁰⁹ or polymer backbones.¹¹⁰ However, the exact mechanism is still not understood in full detail.

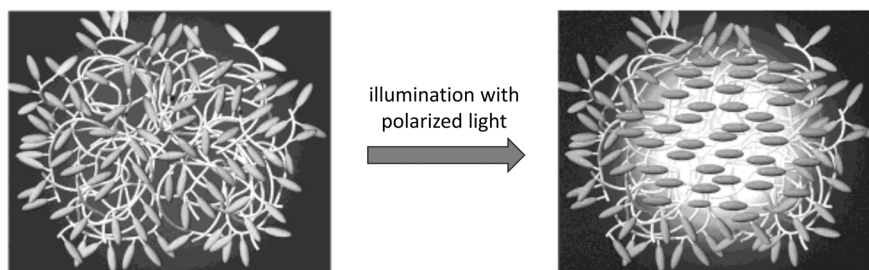


Figure 1.5.2: Reorientation of azobenzene chromophores upon illumination with linear polarized light. The molecular order changes from an isotropic to a highly anisotropic state. Adapted and reproduced with permission from reference 111 (© 2001 WILEY-VCH Verlag GmbH & Co. KGaA, Weinheim).

1.5.2. Azobenzene materials

Azobenzene materials used for the inscription of SRGs must be suitable to form an adequate thick and highly homogeneous amorphous film which remains stable below the glass transition temperature. Furthermore, a close neighborhood of azobenzene chromophores within the film is preferable to use the cooperative effect for enhanced writing speeds.¹¹²

A huge variety of photochromic azobenzene-containing compounds has been synthesized so far. In general, these compounds can be classified into polymer-based systems and molecular glasses. Polymer-based azobenzene systems were built up from homopolymers,^{87,113} block copolymers,^{114–116} statistical copolymers,^{117,118} and polymer blends.¹¹⁹ In contrast, azobenzene-containing molecular glasses consist of small molecules.^{120–124} These have the advantage of a well-defined molecular structure and a defined molar mass. Further benefits are the absence of undefined end groups and structural defects. Finally, the absence of entanglements results in a more efficient mass transport.¹²⁵ The amorphous character of molecular glasses is achieved by a suppression of the crystallization tendency. This is done by designing a space-filling and non-planar molecular structure.⁸³

Within this thesis, a molecular glass consisting of a spirobischroman-based 6,6',7,7'-tetraester with four azobenzene moieties per molecule was used. This molecule can be synthesized *via* ester coupling of 6,6',7,7'-Tetrahydroxy-4,4,4',4'-tetramethyl-2,2-spirobischroman with 4-(phenylazo)benzoyl chloride (Figure 1.5.3).¹²⁶

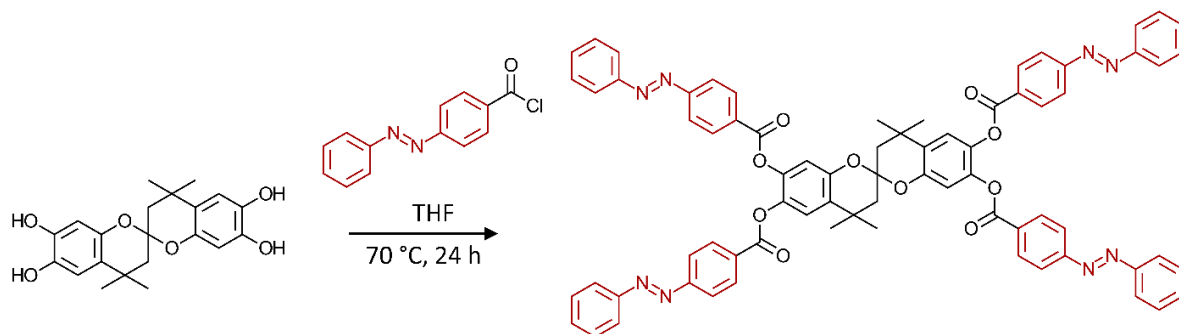


Figure 1.5.3: Synthetic route to prepare the spiro-based photoresponsive azobenzene material with four azobenzene moieties which is used within this thesis.

1.5.3. Preparation of surface relief gratings

Azobenzene chromophores reveal a significant different absorption behavior for the *cis*-rich and the *trans*-rich state (Figure 1.5.4).¹²⁷ SRGs are inscribed with a holographic technique at a wavelength where both species absorb light. Typically, the blue-green line (488 nm) or the green line (514 nm) of an Ar⁺ ion laser is used for writing.⁸³ Reading is performed at a wavelength which is outside of the absorption range of the chromophore. This allows a continuous control without an influence on the grating.

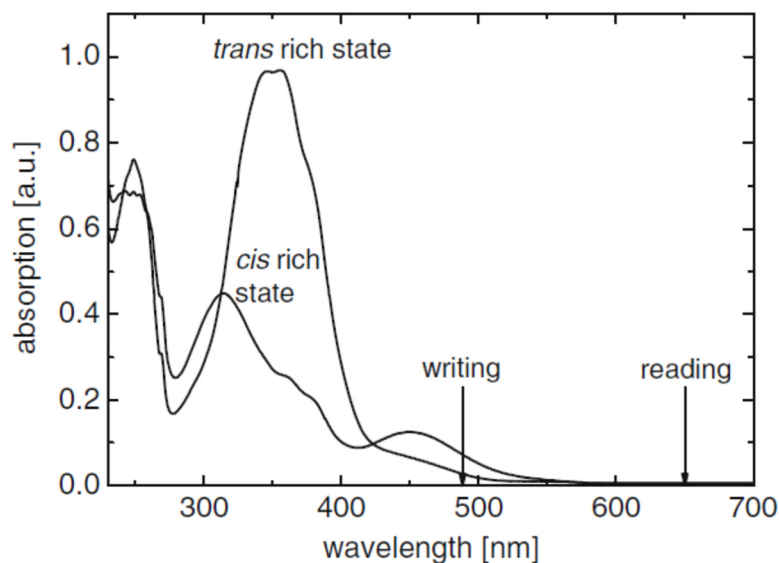


Figure 1.5.4: Typical absorption spectra for the *cis*-rich and the *trans*-rich state of an azobenzene chromophore. Exemplary wavelengths for SRG inscription are indicated at 488 nm for writing and 685 nm for reading. Reproduced with permissions from reference 83 and 127 (© 2004 WILEY-VCH Verlag GmbH & Co. KGaA, Weinheim / © 2009 Springer).

A typical holographic setup as it is used for the inscription of surface relief gratings within this thesis consists of a writing and a reading laser (Figure 1.5.5).⁸⁴ The writing laser is divided into two coherent beams by a beam splitter. The polarization state of each beam is adjusted *via* $\lambda/2$ or $\lambda/4$ plates and polarizers. Both beams are interfered at the azobenzene film surface to inscribe surface relief gratings. The grating formation can be monitored by the reading laser. The power of the diffracted and the transmitted beam is measured with two photodiodes.

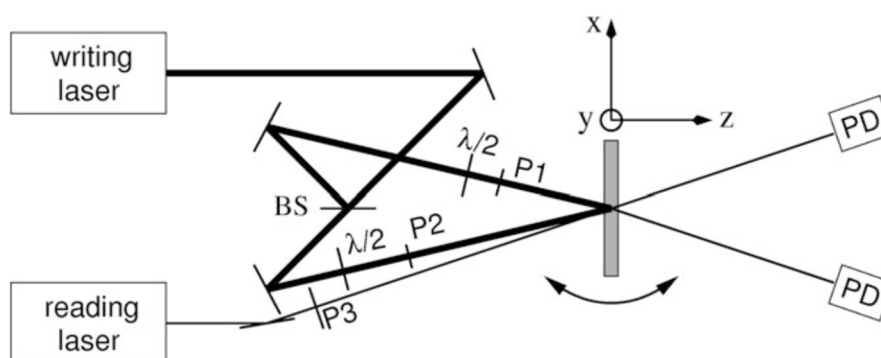


Figure 1.5.5: Schematic representation of the holographic setup used for the inscription process. The polarization state of the writing beam is adjusted by $\lambda/2$ and $\lambda/4$ plates. Reprinted with permissions from references 83 and 84. (© 2009 American Chemical Society / © 2009 Springer).

SRGs are characterized by their grating period Λ and their grating height h (Figure 1.5.6). The grating period can be tuned *via* the angle of the two incident beams in the holographic setup. The grating height can be tuned *via* irradiation time.

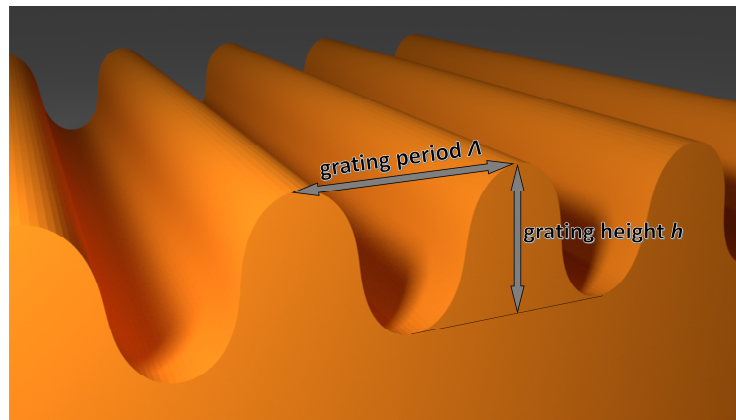


Figure 1.5.6: Schematic illustration of an SRG with grating period Λ and grating height h .

The optical inscription process makes SRGs highly defect-free. This results in a grating period which is constant over the entire exposed area. The grating height, however, is a *gradient* function of the irradiation intensity of the writing laser. Lasers typically follow a Gaussian intensity profile.¹²⁸ This intensity profile causes a Gaussian profile of the grating height (Figure 1.5.7).

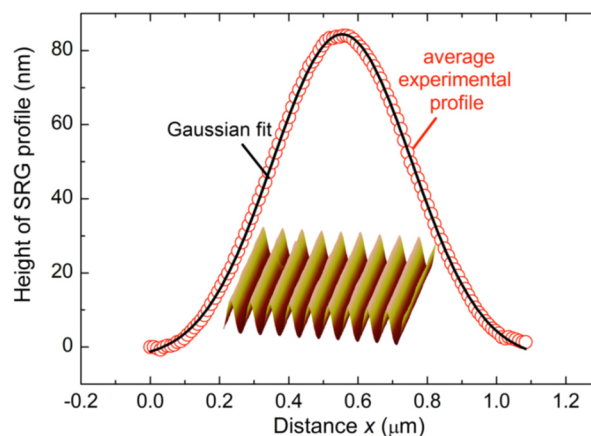


Figure 1.5.7: Typical Gaussian distribution of grating heights within an SRG inscribed in an azopolymer film. The depicted profile was obtained from AFM line scans and averaged over 9 periods. Reprinted with permission from reference 129 (© 2018 Authors).

Potential application fields of SRGs are holographic optical elements,¹³⁰ channel waveguides,¹³¹ optical security devices,¹³² antireflective coatings,¹³³ and lithographic masks.^{134,135}

Within this thesis, surface relief gratings are replicated to various polymers. This gives access to promising application fields such as particle alignment and metrology.

1.6. Photonic crystals

A further class of materials exhibiting structural color are photonic crystals.¹³⁶ The underlying concept was developed by John and Yablanovitch in the late 1980s.^{137,138} In general, a photonic crystal consists of a periodic arrangement of regularly shaped materials with different dielectric constants which exhibits a photonic band gap.¹³⁹ Photons with energies lying in this band gap are not allowed to propagate through the medium.¹⁴⁰ Due to their feature of manipulating light, photonic crystals find applications in the field of sensors,^{141–144} optical fibers,^{145–147} light emitting diodes,^{148–150} color display technology,^{151,152} photovoltaics,^{153–155} reflectors,¹⁵⁶ lasers,¹⁵⁷ and catalysis.¹⁵⁸

1.6.1. Types of photonic crystals

The periodicity of a photonic crystal can vary from three dimensions (3D) down to one (1D) dimension (Figure 1.6.1). Three-dimensional photonic crystals reveal a periodicity in three spatial directions and can be built up either in a top-down^{159–162} or in a bottom-up approach *via* self-assembly.^{163–166} Two-dimensional photonic crystals have a periodicity in two spatial directions and are typically prepared in a top-down approach *via* etching processes.^{167,168} One-dimensional photonic crystals – often also called Bragg mirrors or Bragg reflectors – are the simplest form of such a structure and reveal a periodicity in only one spatial direction. They consist of layers of alternating high and low refractive index materials and reflect only one specific wavelength due to Bragg diffraction and constructive interference.¹⁶⁹ Typical preparation techniques for one-dimensional photonic crystals are spin-coating of multiple layers,^{170–172} layer-by-layer deposition,^{173–175} and photolithography.¹⁷⁶

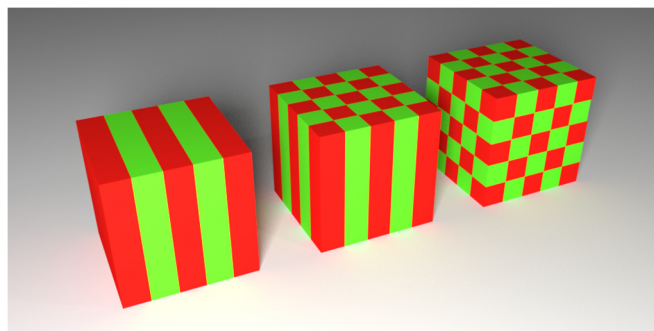


Figure 1.6.1: Schematic illustration of 1D (left), 2D (middle), and 3D photonic crystals (right). The different colors represent the different dielectric constants of the materials utilized.

1.6.2. Reflection in photonic crystals

The principle of the formed band gap of a photonic crystal can be explained with Bragg's law of diffraction (Figure 1.6.2). This law is well-known from X-ray diffraction on a lattice of regularly arranged atoms.¹⁷⁷ In the case of a photonic crystal, the lattice is built up of macroscopic dielectric media instead of atoms.¹⁴⁰ Bragg scattering occurs if the mismatch of the dielectric constants of the different media is big enough. Incident light waves with a wavelength λ are scattered at an angle θ on lattice planes. Each of these parallel planes has a distance d to the adjacent plane. Incident waves reveal a path difference if scattered on different lattice planes. At specific angles, this path difference is appropriate for constructive interference of the diffracted waves.¹⁷⁸ This results in an intense reflection.

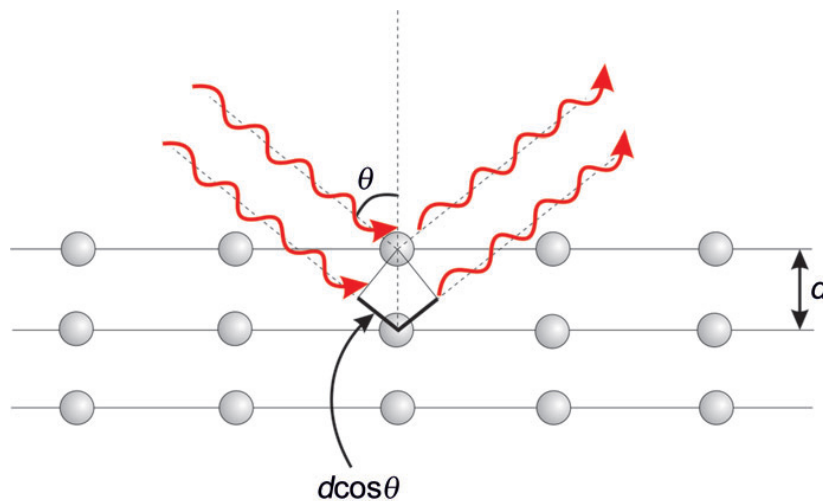


Figure 1.6.2: Bragg diffraction in periodic arrangements. Reproduced with permission from reference 139 (© 2014 Wiley-VCH Verlag GmbH & Co. KGaA, Weinheim).

This case can be described with the Bragg equation (Equation 1.6.1):¹⁷⁹

$$m\lambda = 2d \cos \theta \quad (1.6.1)$$

Hereby, m is the diffraction order. Finally, considering Snell's law of refraction¹⁸⁰ leads to Equation 1.6.2 which contains the effective refractive index n_{eff} :

$$m\lambda = 2d\sqrt{n_{\text{eff}}^2 - \sin^2 \theta} \quad (1.6.2)$$

1.6.3. Responsive photonic crystals

Responsive photonic crystals combine an ordered nanostructure with a responsive polymer.¹⁸¹ The lattice constant in such a responsive photonic crystal can be tuned by external stimuli. This allows a tunable color change of the material.¹⁸² A very promising application field for such responsive photonic crystals with a tunable structural color lies in the field of sensors which was demonstrated for different types of stimuli. Pressure sensors respond on mechanical deformations of elastomers and hydrogels.^{183–187} Organic solvent sensors based on an inverse-opal hydrogel can detect the presence of alcohols¹⁸⁸ and other volatile organic components.¹⁸⁹ Responsive photonic crystals embedded in hydrogels can act as temperature sensors.^{190,191} The ion strength and the pH value can be sensed with responsive photonic crystals based on hydrogels with ion-responsive groups.^{143,192,193} Magnetic field sensors respond on a change of the lattice constant of photonic crystals built up from superparamagnetic colloidal nanoparticles.^{194–196} Electrically responsive photonic crystals are based on redox-active polymers such as poly(ferrocenylsilane).^{151,197} Optically responsive photonic crystals contain photoactive groups like azobenzene which change their molecular structure and hence their structural color upon illumination with UV-light.¹⁹⁸ Finally, responsive photonic crystals with tailored hydrogels can act as sensors for specific substances. Examples are the specific detection of sugars like glucose and galactose,^{199,200} amino acids like glycine,²⁰¹ proteins like avidin,²⁰² and DNA.²⁰³

Within this thesis, responsive photonic crystals are used for the preparation of gradient photonic materials with regard to mechanochromic sensing.

1.7. References

- [1] B. Bhushan,
Philos. Trans. R. Soc., A **2009**, *367*, 1445–1486,
“Biomimetics: lessons from nature — an overview”.
- [2] M. Antonietti and P. Fratzl,
Macromol. Chem. Phys. **2010**, *211*, 166–170,
“Biomimetic Principles in Polymer and Material Science”.
- [3] D. Bechert and W. Reif,
23rd Aerospace Sciences Meeting, American Institute of Aeronautics and Astronautics,
Reston, Virginia **1985**, 747,
“On the drag reduction of the shark skin”.
- [4] D. W. Bechert, M. Bruse and W. Hage,
Exp. Fluids **2000**, *28*, 403–412,
“Experiments with three-dimensional riblets as an idealized model of shark skin”.
- [5] R. A. Potyrailo, H. Ghiradella, A. Vertiatchikh, K. Dovidenko, J. R. Cournoyer and E. Olson,
Nat. Photonics **2007**, *1*, 123–128,
“Morpho butterfly wing scales demonstrate highly selective vapour response”.
- [6] available at:
commons.wikimedia.org/wiki/File:Carcharhinus_galapagensis_erscotts_hole2.jpg,
accessed 1 September 2017.
- [7] available at: creativecommons.org/licenses/by/4.0/deed.en, accessed 1 September 2017.
- [8] B. Dean and B. Bhushan,
Philos. Trans. R. Soc., A **2010**, *368*, 4775–4806,
“Shark-skin surfaces for fluid-drag reduction in turbulent flow: a review”.
- [9] available at: www.flickr.com/photos/botalex/2871460321/in/photostream/,
accessed 1 September 2017.
- [10] available at: creativecommons.org/licenses/by-sa/2.0/, accessed 1 September 2017.
- [11] P. Vukusic, J. R. Sambles, C. R. Lawrence and R. J. Wootton,
Proc. R. Soc. Lond. B **2002**, *269*, 7–14,
*“Limited-view iridescence in the butterfly *Ancyluris meliboeus*”*.

-
- [12] H. Fudouzi,
Sci. Technol. Adv. Mater. **2011**, *12*, 64704,
"Tunable structural color in organisms and photonic materials for design of bioinspired materials".
- [13] D. Gur, B. A. Palmer, B. Leshem, D. Oron, P. Fratzl, S. Weiner and L. Addadi,
Angew. Chem., Int. Ed. Engl. **2015**, *54*, 12426–12430,
"The mechanism of color change in the neon tetra fish: a light-induced tunable photonic crystal array".
- [14] L. M. Mähger, E. J. Denton, N. J. Marshall and R. T. Hanlon,
J. R. Soc., Interface **2009**, *6 Suppl 2*, S149-63,
"Mechanisms and behavioural functions of structural coloration in cephalopods".
- [15] J. P. Vigneron, J. M. Pasteels, D. M. Windsor, Z. Vértesy, M. Rassart, T. Seldrum, J. Dumont, O. Deparis, V. Lousse, L. P. Biró, D. Ertz and V. Welch,
Phys. Rev. E: Stat., Nonlinear, Soft Matter Phys. **2007**, *76*, 31907,
"Switchable reflector in the Panamanian tortoise beetle *Charidotella egregia* (Chrysomelidae: Cassidinae)".
- [16] D. P. Badger and J. Netherton,
Voyageur Press, St. Paul, MN **2006**,
"Lizards. A natural history of some uncommon creatures—extraordinary chameleons, iguanas, geckos, and more".
- [17] J. Teyssier, S. V. Saenko, D. van der Marel and M. C. Milinkovitch,
Nat. Commun. **2015**, *6*, 6368,
"Photonic crystals cause active colour change in chameleons".
- [18] Z. Qin and M. J. Buehler,
Nat. Commun. **2013**, *4*, 2187,
"Impact tolerance in mussel thread networks by heterogeneous material distribution".
- [19] J. H. Waite, N. H. Andersen, S. Jewhurst and C. Sun,
J. Adhes. **2005**, *81*, 297–317,
"Mussel Adhesion: Finding the Tricks Worth Mimicking".
- [20] J. H. Waite, H. C. Lichtenegger, G. D. Stucky and P. Hansma,
Biochemistry **2004**, *43*, 7653–7662,
"Exploring molecular and mechanical gradients in structural bioscaffolds".
- [21] J. H. Waite, E. Vaccaro, C. Sun and J. M. Lucas,
Philos. Trans. R. Soc. London, Ser. B **2002**, *357*, 143–153,
"Elastomeric gradients: a hedge against stress concentration in marine holdfasts?".

- [22] K. J. Coyne and J. H. Waite,
J. Exp. Biol. **2000**, *203*, 1425–1431,
"In search of molecular dovetails in mussel byssus: from the threads to the stem".
- [23] J. H. Waite,
Int. J. Adhes. Adhes. **1987**, *7*, 9–14,
"Nature's underwater adhesive specialist".
- [24] J.H. Waite, X.-X. Qin and K. J. Coyne,
Matrix Biology **1998**, *17*, 93–106,
"The peculiar collagens of mussel byssus".
- [25] K. U. Claussen, T. Scheibel, H.-W. Schmidt and R. Giesa,
Macromol. Mater. Eng. **2012**, *297*, 938–957,
"Polymer Gradient Materials".
- [26] M. M. Alam, K. S. Jack, D. J.T. Hill, A. K. Whittaker and H. Peng,
Eur. Polym. J. **2019**, *116*, 394–414,
"Gradient copolymers – Preparation, properties and practice".
- [27] K. U. Claussen, R. Giesa and H.-W. Schmidt,
Polymer **2014**, *55*, 29–38,
"Longitudinal polymer gradient materials based on crosslinked polymers".
- [28] K. U. Claussen, E. S. Lintz, R. Giesa, H.-W. Schmidt and T. Scheibel,
Macromol. Biosci. **2013**, *13*, 1396–1403,
"Protein gradient films of fibroin and gelatine".
- [29] K. U. Claussen, R. Giesa, T. Scheibel and H.-W. Schmidt,
Macromol. Rapid Commun. **2012**, *33*, 206–211,
"Learning from nature: synthesis and characterization of longitudinal polymer gradient materials inspired by mussel byssus threads".
- [30] K. U. Claussen, M. Tebbe, R. Giesa, A. Schweikart, A. Fery and H.-W. Schmidt,
RSC Adv. **2012**, *2*, 10185,
"Towards tailored topography".
- [31] S. S. Latthe, C. Terashima, K. Nakata and A. Fujishima,
Molecules **2014**, *19*, 4256–4283,
"Superhydrophobic surfaces developed by mimicking hierarchical surface morphology of lotus leaf".
- [32] A. Schweikart, N. Pazos-Pérez, R. A. Alvarez-Puebla and A. Fery,
Soft Matter **2011**, *7*, 4093,
"Controlling inter-nanoparticle coupling by wrinkle-assisted assembly".

- [33] M. Mayer, M. Tebbe, C. Kuttner, M. J. Schnepf, T. A. F. König and A. Fery, *Faraday Discuss.* **2016**, *191*, 159–176, “Template-assisted colloidal self-assembly of macroscopic magnetic metasurfaces”.
- [34] A. del Campo and E. Arzt, *Chem. Rev.* **2008**, *108*, 911–945, “Fabrication approaches for generating complex micro- and nanopatterns on polymeric surfaces”.
- [35] D.-G. Choi, H. K. Yu, S. G. Jang and S.-M. Yang, *J. Am. Chem. Soc.* **2004**, *126*, 7019–7025, “Colloidal lithographic nanopatterning via reactive ion etching”.
- [36] N. R. Tas, J. W. Berenschot, P. Mela, H. V. Jansen, M. Elwenspoek and A. van den Berg, *Nano Lett.* **2002**, *2*, 1031–1032, “2D-Confined Nanochannels Fabricated by Conventional Micromachining”.
- [37] J.-h. Jeong, Y.-s. Sim, H. Sohn and E.-s. Lee, *Microelectron. Eng.* **2004**, *75*, 165–171, “UV-nanoimprint lithography using an elementwise patterned stamp”.
- [38] C. Neuber, H.-W. Schmidt, P. Strohrriegl, D. Wagner, F. Krohn, A. Schedl, S. Bonanni, F. Holzner, C. Rawlings, U. Dürig and A. W. Knoll, *Advances in Patterning Materials and Processes XXXIII*, ed. C. K. Hohle and T. R. Younkin, SPIE **2016**, 97791C, “PVD prepared molecular glass resists for scanning probe lithography”.
- [39] C. Neuber, H.-W. Schmidt, P. Strohrriegl, A. Ringk, T. Kolb, A. Schedl, V. Fokkema, M. G. A. van Veghel, M. Cooke, C. Rawlings, U. Dürig, A. Knoll, J.-F. de Marneffe, Z. el Otell, M. Kaestner, Y. Krivoschapkina, M. Budden and I. W. Rangelow, *SPIE Advanced Lithography*, ed. T. I. Wallow and C. K. Hohle, SPIE **2015**, 94250E, “Tailored molecular glass resists for Scanning Probe Lithography”.
- [40] I. D. Block, L. L. Chan and B. T. Cunningham, *Microelectron. Eng.* **2007**, *84*, 603–608, “Large-area submicron replica molding of porous low-k dielectric films and application to photonic crystal biosensor fabrication”.
- [41] C. D. James, R. C. Davis, L. Kam, H. G. Craighead, M. Isaacson, J. N. Turner and W. Shain, *Langmuir* **1998**, *14*, 741–744, “Patterned Protein Layers on Solid Substrates by Thin Stamp Microcontact Printing”.
- [42] A. E. Schedl, C. Neuber, A. Fery and H.-W. Schmidt, *Langmuir* **2018**, *34*, 14249–14253, “Controlled Wrinkling of Gradient Metal Films”.

- [43] B. A. Glatz, M. Tebbe, B. Kaoui, R. Aichele, C. Kuttner, A. E. Schedl, H.-W. Schmidt, W. Zimmermann and A. Fery,
Soft Matter **2015**, *11*, 3332–3339,
"Hierarchical line-defect patterns in wrinkled surfaces".
- [44] A. E. Schedl, P. T. Probst, C. Meichner, C. Neuber, L. Kador, A. Fery and H.-W. Schmidt,
Soft Matter **2019**, *15*, 3872–3878,
"Confinement templates for hierarchical nanoparticle alignment prepared by azobenzene-based surface relief gratings".
- [45] C. Meichner, A. E. Schedl, C. Neuber, K. Kreger, H.-W. Schmidt and L. Kador,
AIP Adv. **2015**, *5*, 87135,
"Refractive-index determination of solids from first- and second-order critical diffraction angles of periodic surface patterns".
- [46] S. M. Kang, N. S. Hwang, J. Yeom, S. Y. Park, P. B. Messersmith, I. S. Choi, R. Langer, D. G. Anderson and H. Lee,
Adv. Funct. Mater. **2012**, *22*, 2949–2955,
"One-Step Multipurpose Surface Functionalization by Adhesive Catecholamine".
- [47] S. C. M. Fernandes, P. Sadocco, A. Alonso-Varona, T. Palomares, A. Eceiza, A. J. D. Silvestre, I. Mondragon and C. S. R. Freire,
ACS Appl. Mater. Interfaces **2013**, *5*, 3290–3297,
"Bioinspired antimicrobial and biocompatible bacterial cellulose membranes obtained by surface functionalization with aminoalkyl groups".
- [48] B. D. Gates,
Science **2009**, *323*, 1566–1567,
"Materials science. Flexible electronics".
- [49] D. Bodas and C. Khan-Malek,
Microelectron. Eng. **2006**, *83*, 1277–1279,
"Formation of more stable hydrophilic surfaces of PDMS by plasma and chemical treatments".
- [50] A. N. Shipway, E. Katz and I. Willner,
ChemPhysChem **2000**, *1*, 18–52,
"Nanoparticle Arrays on Surfaces for Electronic, Optical, and Sensor Applications".
- [51] J. Genzer and J. Groenewold,
Soft Matter **2006**, *2*, 310,
"Soft matter with hard skin".
- [52] C.-M. Chen and S. Yang,
Polym. Int. **2012**, *61*, 1041–1047,
"Wrinkling instabilities in polymer films and their applications".

-
- [53] J. Rodríguez-Hernández and A. del Campo, *J. Appl. Polym. Sci.* **2015**, *132*, 1771, "Fabrication of hierarchical wrinkled morphologies through sequential UVO treatments".
- [54] N. Bowden, W. T. S. Huck, K. E. Paul and G. M. Whitesides, *Appl. Phys. Lett.* **1999**, *75*, 2557–2559, "The controlled formation of ordered, sinusoidal structures by plasma oxidation of an elastomeric polymer".
- [55] M. Watanabe and K. Mizukami, *Macromolecules* **2012**, *45*, 7128–7134, "Well-Ordered Wrinkling Patterns on Chemically Oxidized Poly(dimethylsiloxane) Surfaces".
- [56] N. Bowden, S. Brittain, A. G. Evans, J. W. Hutchinson and G. M. Whitesides, *Nature* **1998**, *393*, 146–149, "Spontaneous formation of ordered structures in thin films of metals supported on an elastomeric polymer".
- [57] M. Watanabe, *Polym. Adv. Technol.* **2005**, *16*, 744–748, "Wrinkles formed on a thin gold film deposited onto stretched elastic substrates".
- [58] C. M. Stafford, C. Harrison, K. L. Beers, A. Karim, E. J. Amis, M. R. VanLandingham, H.-C. Kim, W. Volksen, R. D. Miller and E. E. Simonyi, *Nat. Mater.* **2004**, *3*, 545–550, "A buckling-based metrology for measuring the elastic moduli of polymeric thin films".
- [59] G. Gille and B. Rau, *Thin Solid Films* **1984**, *120*, 109–121, "Buckling instability and adhesion of carbon layers".
- [60] E. Cerda and L. Mahadevan, *Phys. Rev. Lett.* **2003**, *90*, 74302, "Geometry and physics of wrinkling".
- [61] C. Harrison, C. M. Stafford, W. Zhang and A. Karim, *Nature* **2004**, *85*, 4016–4018, "Sinusoidal phase grating created by a tunably buckled surface".
- [62] A. J. Nolte, R. E. Cohen and M. F. Rubner, *Macromolecules* **2006**, *39*, 4841–4847, "A Two-Plate Buckling Technique for Thin Film Modulus Measurements: Applications to Polyelectrolyte Multilayers".

- [63] H. Mei, R. Huang, J. Y. Chung, C. M. Stafford and H.-H. Yu, *Appl. Phys. Lett.* **2007**, *90*, 151902, "Buckling modes of elastic thin films on elastic substrates".
- [64] P. J. Yoo, K. Y. Suh, H. Kang and H. H. Lee, *Phys. Rev. Lett.* **2004**, *93*, 34301, "Polymer elasticity-driven wrinkling and coarsening in high temperature buckling of metal-capped polymer thin films".
- [65] M. Guvendiren, S. Yang and J. A. Burdick, *Adv. Funct. Mater.* **2009**, *19*, 3038–3045, "Swelling-Induced Surface Patterns in Hydrogels with Gradient Crosslinking Density".
- [66] E. P. Chan and A. J. Crosby, *Soft Matter* **2006**, *2*, 324, "Spontaneous formation of stable aligned wrinkling patterns".
- [67] J. Y. Chung, A. J. Nolte and C. M. Stafford, *Adv. Mater.* **2009**, *21*, 1358–1362, "Diffusion-Controlled, Self-Organized Growth of Symmetric Wrinkling Patterns".
- [68] J. Huang, M. Juskiewicz, W. H. de Jeu, E. Cerda, T. Emrick, N. Menon and T. P. Russell, *Science* **2007**, *317*, 650–653, "Capillary wrinkling of floating thin polymer films".
- [69] D. Vella, M. Adda-Bedia and E. Cerda, *Soft Matter* **2010**, *6*, 5778, "Capillary wrinkling of elastic membranes".
- [70] A. Schweikart and A. Fery, *Microchim. Acta* **2009**, *165*, 249–263, "Controlled wrinkling as a novel method for the fabrication of patterned surfaces".
- [71] R. Huang, *J. Mech. Phys. Solids* **2005**, *53*, 63–89, "Kinetic wrinkling of an elastic film on a viscoelastic substrate".
- [72] H. Jiang, D.-Y. Khang, J. Song, Y. Sun, Y. Huang and J. A. Rogers, *Proc. Natl. Acad. Sci. U. S. A.* **2007**, *104*, 15607–15612, "Finite deformation mechanics in buckled thin films on compliant supports".
- [73] C. M. Stafford, S. Guo, C. Harrison and M. Y. M. Chiang, *Rev. Sci. Instrum.* **2005**, *76*, 62207, "Combinatorial and high-throughput measurements of the modulus of thin polymer films".

- [74] J. Yin and X. Chen,
Philos. Mag. Lett. **2010**, *90*, 423–433,
"Elastic buckling of gradient thin films on compliant substrates".
- [75] S. Hiltl, J. Oltmanns and A. Böker,
Nanoscale **2012**, *4*, 7338–7345,
"A one-step screening process for optimal alignment of (soft) colloidal particles".
- [76] S. Hiltl and A. Böker,
Langmuir **2016**, *32*, 8882–8888,
"Wetting Phenomena on (Gradient) Wrinkle Substrates".
- [77] H. Li, B. Sheng, H. Wu, Y. Huang, D. Zhang and S. Zhuang,
Materials **2018**, *11*,
"Ring Wrinkle Patterns with Continuously Changing Wavelength Produced Using a Controlled-Gradient Light Field".
- [78] S. Yu, Y. Ni, L. He and Q.-L. Ye,
ACS Appl. Mater. Interfaces **2015**, *7*, 5160–5167,
"Tunable formation of ordered wrinkles in metal films with controlled thickness gradients deposited on soft elastic substrates".
- [79] G. Lin, Q. Zhang, C. Lv, Y. Tang and J. Yin,
Soft Matter **2018**, *14*, 1517–1529,
"Small degree of anisotropic wetting on self-similar hierarchical wrinkled surfaces".
- [80] K. Efimenko, M. Rackaitis, E. Manias, A. Vaziri, L. Mahadevan and J. Genzer,
Nat. Mater. **2005**, *4*, 293–297,
"Nested self-similar wrinkling patterns in skins".
- [81] Y. Xuan, X. Guo, Y. Cui, C. Yuan, H. Ge, B. Cui and Y. Chen,
Soft Matter **2012**, *8*, 9603,
"Crack-free controlled wrinkling of a bilayer film with a gradient interface".
- [82] D. Rhee, W.-K. Lee and T. W. Odom,
Angew. Chem., Int. Ed. Engl. **2017**, *56*, 6523–6527,
"Crack-Free, Soft Wrinkles Enable Switchable Anisotropic Wetting".
- [83] H. Audorff, K. Kreger, R. Walker, D. Haarer, L. Kador and H.-W. Schmidt,
ed. A. H. E. Müller and H.-W. Schmidt, Springer Berlin Heidelberg, Berlin, Heidelberg
2010, pp. 59–121,
"Complex Macromolecular Systems II".
- [84] H. Audorff, R. Walker, L. Kador and H.-W. Schmidt,
J. Phys. Chem. B **2009**, *113*, 3379–3384,
"Polarization dependence of the formation of surface relief gratings in azobenzene-containing molecular glasses".

- [85] Y. Zhao and T. Ikeda, John Wiley & Sons, Inc, Hoboken, NJ, USA **2009**, *"Smart Light-Responsive Materials"*.
- [86] C. J. Barrett, J.-i. Mamiya, K. G. Yager and T. Ikeda, *Soft Matter* **2007**, *3*, 1249, *"Photo-mechanical effects in azobenzene-containing soft materials"*.
- [87] M. Eich, J. H. Wendorff, B. Reck and H. Ringsdorf, *Makromol. Chem., Rapid Commun.* **1987**, *8*, 59–63, *"Reversible digital and holographic optical storage in polymeric liquid crystals"*.
- [88] A. Priimagi and A. Shevchenko, *J. Polym. Sci. Part B: Polym. Phys.* **2014**, *52*, 163–182, *"Azopolymer-based micro- and nanopatterning for photonic applications"*.
- [89] M. Hendrikx, A. Schenning, M. Debije and D. Broer, *Crystals* **2017**, *7*, 231, *"Light-Triggered Formation of Surface Topographies in Azo Polymers"*.
- [90] P. Weis, W. Tian and S. Wu, *Chemistry* **2018**, *24*, 6494–6505, *"Photoinduced Liquefaction of Azobenzene-Containing Polymers"*.
- [91] D. Y. Kim, S. K. Tripathy, L. Li and J. Kumar, *Appl. Phys. Lett.* **1995**, *66*, 1166–1168, *"Laser-induced holographic surface relief gratings on nonlinear optical polymer films"*.
- [92] P. Rochon, E. Batalla and A. Natansohn, *Appl. Phys. Lett.* **1995**, *66*, 136–138, *"Optically induced surface gratings on azoaromatic polymer films"*.
- [93] T. G. Pedersen, P. M. Johansen, N. C. R. Holme, P. S. Ramanujam and S. Hvilsted, *Phys. Rev. Lett.* **1998**, *80*, 89–92, *"Mean-Field Theory of Photoinduced Formation of Surface Reliefs in Side-Chain Azobenzene Polymers"*.
- [94] V. Toshchevikov, M. Saphiannikova and G. Heinrich, *J. Phys. Chem. B* **2009**, *113*, 5032–5045, *"Microscopic theory of light-induced deformation in amorphous side-chain azobenzene polymers"*.
- [95] V. Toshchevikov, M. Saphiannikova and G. Heinrich, *J. Phys. Chem. B* **2012**, *116*, 913–924, *"Light-induced deformation of azobenzene elastomers: a regular cubic network model"*.

-
- [96] K. Sumaru, T. Yamanaka, T. Fukuda and H. Matsuda, *Appl. Phys. Lett.* **1999**, *75*, 1878–1880, "Photoinduced surface relief gratings on azopolymer films: Analysis by a fluid mechanics model".
- [97] M. L. Juan, J. Plain, R. Bachelot, P. Royer, S. K. Gray and G. P. Wiederrecht, *Appl. Phys. Lett.* **2008**, *93*, 153304, "Stochastic model for photoinduced surface relief grating formation through molecular transport in polymer films".
- [98] M. L. Juan, J. Plain, R. Bachelot, P. Royer, S. K. Gray and G. P. Wiederrecht, *ACS Nano* **2009**, *3*, 1573–1579, "Multiscale model for photoinduced molecular motion in azo polymers".
- [99] M. Saphiannikova and D. Neher, *J. Phys. Chem. B* **2005**, *109*, 19428–19436, "Thermodynamic theory of light-induced material transport in amorphous azobenzene polymer films".
- [100] J. M. Ilnytskyi, D. Neher and M. Saphiannikova, *J. Chem. Phys.* **2011**, *135*, 44901, "Opposite photo-induced deformations in azobenzene-containing polymers with different molecular architecture: molecular dynamics study".
- [101] A. Ambrosio, P. Maddalena and L. Marrucci, *Phys. Rev. Lett.* **2013**, *110*, 146102, "Molecular model for light-driven spiral mass transport in azopolymer films".
- [102] P. Lefin, C. Fiorini and J.-M. Nunzi, *Opt. Lett.* **1998**, *7*, 71–82, "Anisotropy of the photo-induced translation diffusion of azobenzene dyes in polymer matrices".
- [103] B. Bellini, J. Ackermann, H. Klein, C. Grave, P. Dumas and V. Safarov, *Appl. Phys. B: Lasers Opt.* **2006**, *18*, S1817-S1835, "Light-induced molecular motion of azobenzene-containing molecules: a random-walk model".
- [104] H. Galinski, A. Ambrosio, P. Maddalena, I. Schenker, R. Spolenak and F. Capasso, *Proc. Natl. Acad. Sci. U. S. A.* **2014**, *111*, 17017–17022, "Instability-induced pattern formation of photoactivated functional polymers".
- [105] V. Toshchevnikov and M. Saphiannikova, *J. Phys. Chem. B* **2014**, *118*, 12297–12309, "Theory of light-induced deformation of azobenzene elastomers: effects of the liquid-crystalline interactions and biaxiality".

- [106] J. Kumar, L. Li, X. L. Jiang, D.-Y. Kim, T. S. Lee and S. Tripathy, *Appl. Phys. Lett.* **1998**, *72*, 2096–2098, "Gradient force".
- [107] C. J. Barrett, P. L. Rochon and A. L. Natansohn, *J. Chem. Phys.* **1998**, *109*, 1505–1516, "Model of laser-driven mass transport in thin films of dye-functionalized polymers".
- [108] Z. Sekkat, *Appl. Opt.* **2016**, *55*, 259–268, "Optical tweezing by photomigration".
- [109] D. Bublitz, B. Fleck and L. Wenke, *Appl. Phys. B: Lasers Opt.* **2001**, *72*, 931–936, "A model for surface-relief formation in azobenzene polymers".
- [110] N. S. Yadavalli, S. Loebner, T. Papke, E. Sava, N. Hurduc and S. Santer, *Soft Matter* **2016**, *12*, 2593–2603, "A comparative study of photoinduced deformation in azobenzene containing polymer films".
- [111] R. Hagen and T. Bieringer, *Adv. Mater.* **2001**, *13*, 1805–1810, "Photoaddressable Polymers for Optical Data Storage".
- [112] C. Probst, C. Meichner, H. Audorff, R. Walker, K. Kreger, L. Kador and H.-W. Schmidt, *J. Polym. Sci. Part B: Polym. Phys.* **2016**, *54*, 2110–2117, "Improving holographic writing performance of photo-orientable azobenzene polymers by molecular glasses".
- [113] H. Ringsdorf and H.-W. Schmidt, *Makromol. Chem.* **1984**, *185*, 1327–1334, "Electro-optical effects of azo dye containing liquid crystalline copolymers".
- [114] L. Ding, H. Mao, J. Xu, J. He, X. Ding, T. P. Russell, D. R. Robello and M. Mis, *Macromolecules* **2008**, *41*, 1897–1900, "Morphological Study on an Azobenzene-Containing Liquid Crystalline Diblock Copolymer".
- [115] S. Gimeno, P. Forcén, L. Oriol, M. Piñol, C. Sánchez, F. J. Rodríguez, R. Alcalá, K. Jankova and S. Hvilsted, *Eur. Polym. J.* **2009**, *45*, 262–271, "Photoinduced optical anisotropy in azobenzene methacrylate block copolymers: Influence of molecular weight and irradiation conditions".

- [116] X. He, W. Sun, D. Yan, M. Xie and Y. Zhang, *J. Polym. Sci. A Polym. Chem.* **2008**, *46*, 4442–4450, "Synthesis and characterization of side-chain liquid crystalline ABC triblock copolymers with *p*-methoxyazobenzene moieties by atom transfer radical polymerization".
- [117] S. J. Zilker, M. R. Huber, T. Bieringer and D. Haarer, *Appl. Phys. B: Lasers Opt.* **1999**, *68*, 893–897, "Holographic recording in amorphous side-chain polymers: a comparison of two different design philosophies".
- [118] S. J. Zilker, T. Bieringer, D. Haarer, R. S. Stein, J. W. van Egmond and S. G. Kostromine, *Adv. Mater.* **1998**, *10*, 855–859, "Holographic Data Storage in Amorphous Polymers".
- [119] J. Minabe, T. Maruyama, S. Yasuda, K. Kawano, K. Hayashi and Y. Ogasawara, *Jpn. J. Appl. Phys.* **2004**, *43*, 4964–4967, "Design of Dye Concentrations in Azobenzene-Containing Polymer films for Volume Holographic Storage".
- [120] C. Chun, M.-J. Kim, D. Vak and D. Y. Kim, *J. Mater. Chem.* **2003**, *13*, 2904, "A novel azobenzene-based amorphous molecular material with a spiro linked bifluorene".
- [121] E. Ishow, B. Lebon, Y. He, X. Wang, L. Bouteiller, L. Galmiche and K. Nakatani, *Chem. Mater.* **2006**, *18*, 1261–1267, "Structural and Photoisomerization Cross Studies of Polar Photochromic Monomeric Glasses Forming Surface Relief Gratings".
- [122] Y. Shirota, *J. Mater. Chem.* **2005**, *15*, 75–93, "Photo- and electroactive amorphous molecular materials—molecular design, syntheses, reactions, properties, and applications".
- [123] E. Zarins, K. Balodis, A. Ruduss, V. Kokars, A. Ozols, P. Augustovs and D. Saharovs, *Opt. Mater.* **2018**, *79*, 45–52, "Molecular glasses of azobenzene for holographic data storage applications".
- [124] K. Kreger, P. Wolfer, H. Audorff, L. Kador, N. Stingelin-Stutzmann, P. Smith and H.-W. Schmidt, *J. Am. Chem. Soc.* **2010**, *132*, 509–516, "Stable holographic gratings with small-molecular trisazobenzene derivatives".
- [125] M.-J. Kim, E.-M. Seo, D. Vak and D.-Y. Kim, *Chem. Mater.* **2003**, *15*, 4021–4027, "Photodynamic Properties of Azobenzene Molecular Films with Triphenylamines".

- [126] H. Audorff, R. Walker, L. Kador and H.-W. Schmidt, *Chemistry* **2011**, *17*, 12722–12728, "Holographic investigations of azobenzene-containing low-molecular-weight compounds in pure materials and binary blends with polystyrene".
- [127] C. Frenz, A. Fuchs, H.-W. Schmidt, U. Theissen and D. Haarer, *Macromol. Chem. Phys.* **2004**, *205*, 1246–1258, "Diblock Copolymers with Azobenzene Side-Groups and Polystyrene Matrix: Synthesis, Characterization and Photoaddressing".
- [128] L. C. Andrews and R. L. Phillips, SPIE, St. Bellingham WA, 2nd edn. **2005**, PM152, "Laser beam propagation through random media".
- [129] S. Moujdi, A. Rahmouni, T. Mahfoud, D. V. Nesterenko, M. Halim and Z. Sekkat, *J. Appl. Phys.* **2018**, *124*, 213103, "Surface relief gratings in azo-polymers revisited".
- [130] H. Akbari, I. Naydenova and S. Martin, *Appl. Opt.* **2014**, *53*, 1343–1353, "Using acrylamide-based photopolymers for fabrication of holographic optical elements in solar energy applications".
- [131] G. Quaranta, G. Basset, O. J. F. Martin and B. Gallinet, *Laser Photonics Rev.* **2018**, *12*, 1800017, "Recent Advances in Resonant Waveguide Gratings".
- [132] T. Sabel and M. C. Lensen, ed. I. Naydenova, D. Nazarova and T. Babeva, *InTech* **2017**, "Holographic Materials and Optical Systems".
- [133] A. Gombert, K. Rose, A. Heinzl, W. Horbelt, C. Zanke, B. Bläsi and V. Wittwer, *Sol. Energy Mater. Sol. Cells* **1998**, *54*, 333–342, "Antireflective submicrometer surface-relief gratings for solar applications".
- [134] A. Kravchenko, A. Shevchenko, V. Ovchinnikov, A. Priimagi and M. Kaivola, *Adv. Mater.* **2011**, *23*, 4174–4177, "Optical interference lithography using azobenzene-functionalized polymers for micro- and nanopatterning of silicon".
- [135] C. Probst, C. Meichner, K. Kreger, L. Kador, C. Neuber and H.-W. Schmidt, *Adv. Mater.* **2016**, *28*, 2624–2628, "Athermal Azobenzene-Based Nanoimprint Lithography".
- [136] J. Sun, B. Bhushan and J. Tong, *RSC Adv.* **2013**, *3*, 14862, "Structural coloration in nature".

-
- [137] E. Yablonovitch,
Phys. Rev. Lett. **1987**, *58*, 2059–2062,
"Inhibited spontaneous emission in solid-state physics and electronics".
- [138] S. John,
Phys. Rev. Lett. **1987**, *58*, 2486–2489,
"Strong localization of photons in certain disordered dielectric superlattices".
- [139] C. Fenzl, T. Hirsch and O. S. Wolfbeis,
Angew. Chem., Int. Ed. Engl. **2014**, *53*, 3318–3335,
"Photonic crystals for chemical sensing and biosensing".
- [140] J. D. Joannopoulos, P. R. Villeneuve and S. Fan,
Nature **1997**, *386*, 143–149,
"Photonic crystals: putting a new twist on light".
- [141] S. A. Asher, V. L. Alexeev, A. V. Goponenko, A. C. Sharma, I. K. Lednev, C. S. Wilcox
and D. N. Finegold,
J. Am. Chem. Soc. **2003**, *125*, 3322–3329,
"Photonic crystal carbohydrate sensors: low ionic strength sugar sensing".
- [142] D. K. C. Wu, B. T. Kuhlmeier and B. J. Eggleton,
Opt. Lett. **2009**, *34*, 322–324,
"Ultrasensitive photonic crystal fiber refractive index sensor".
- [143] K. Lee and S. A. Asher,
J. Am. Chem. Soc. **2000**, *122*, 9534–9537,
"Photonic Crystal Chemical Sensors: pH and Ionic Strength".
- [144] E. Chow, A. Grot, L. W. Mirkarimi, M. Sigalas and G. Girolami,
Opt. Lett. **2004**, *29*, 1093,
*"Ultracompact biochemical sensor built with two-dimensional photonic crystal
microcavity"*.
- [145] J. C. Knight,
Nature **2003**, *424*, 847–851,
"Photonic crystal fibres".
- [146] A. Ortigosa-Blanch, J. C. Knight, W. J. Wadsworth, J. Arriaga, B. J. Mangan, T. A. Birks
and P. S. Russell,
Opt. Lett. **2000**, *25*, 1325–1327,
"Highly birefringent photonic crystal fibers".
- [147] P. Russell,
Science **2003**, *299*, 358–362,
"Photonic crystal fibers".

- [148] K. McGroddy, A. David, E. Matioli, M. Iza, S. Nakamura, S. DenBaars, J. S. Speck, C. Weisbuch and E. L. Hu,
Appl. Phys. Lett. **2008**, *93*, 103502,
"Directional emission control and increased light extraction in GaN photonic crystal light emitting diodes".
- [149] T. N. Oder, K. H. Kim, J. Y. Lin and H. X. Jiang,
Appl. Phys. Lett. **2004**, *84*, 466–468,
"III-nitride blue and ultraviolet photonic crystal light emitting diodes".
- [150] J. J. Wierer, A. David and M. M. Megens,
Nat. Photonics **2009**, *3*, 163–169,
"III-nitride photonic-crystal light-emitting diodes with high extraction efficiency".
- [151] A. C. Arsenault, D. P. Puzzo, I. Manners and G. A. Ozin,
Nat. Photonics **2007**, *1*, 468–472,
"Photonic-crystal full-colour displays".
- [152] Y. Lu, H. Xia, G. Zhang and C. Wu,
J. Mater. Chem. **2009**, *19*, 5952,
"Electrically tunable block copolymer photonic crystals with a full color display".
- [153] P. G. O'Brien, A. Chutinan, K. Leong, N. P. Kherani, G. A. Ozin and S. Zukotynski,
Opt. Express **2010**, *18*, 4478–4490,
"Photonic crystal intermediate reflectors for micromorph solar cells: a comparative study".
- [154] A. Soman and A. Antony,
2014 IEEE 2nd International Conference on Emerging Electronics (ICEE) **2014**, 1-4,
"One-dimensional photonic crystal reflector using silicon-rich silicon nitride and silicon oxynitride multilayers for solar cells".
- [155] A. Chutinan, N. P. Kherani and S. Zukotynski,
Opt. Express **2009**, *17*, 8871,
"High-efficiency photonic crystal solar cell architecture".
- [156] S.-P. Yu, H. Jung, T. C. Briles, K. Srinivasan and S. B. Papp,
ACS Photonics **2019**, *6*, 2083–2089,
"Photonic-Crystal-Reflector Nanoresonators for Kerr-Frequency Combs".
- [157] H.-G. Park, S.-H. Kim, S.-H. Kwon, Y.-G. Ju, J.-K. Yang, J.-H. Baek, S.-B. Kim and Y.-H. Lee,
Science **2004**, *305*, 1444–1447,
"Electrically driven single-cell photonic crystal laser".

-
- [158] J. I. L. Chen, G. von Freymann, S. Y. Choi, V. Kitaev and G. A. Ozin, *Adv. Mater.* **2006**, *18*, 1915–1919, “*Amplified Photochemistry with Slow Photons*”.
- [159] J. G. Fleming and S. Y. Lin, *Opt. Lett.* **1999**, *24*, 49–51, “*Three-dimensional photonic crystal with a stop band from 1.35 to 1.95 microm*”.
- [160] S. Y. Lin, J. G. Fleming, D. L. Hetherington, B. K. Smith, R. Biswas, K. M. Ho, M. M. Sigalas, W. Zubrzycki, S. R. Kurtz and J. Bur, *Nature* **1998**, *394*, 251–253, “*A three-dimensional photonic crystal operating at infrared wavelengths*”.
- [161] S. Takahashi, M. Okano, M. Imada and S. Noda, *Appl. Phys. Lett.* **2006**, *89*, 123106, “*Three-dimensional photonic crystals based on double-angled etching and wafer-fusion techniques*”.
- [162] S. Takahashi, K. Suzuki, M. Okano, M. Imada, T. Nakamori, Y. Ota, K. Ishizaki and S. Noda, *Nat. Mater.* **2009**, *8*, 721–725, “*Direct creation of three-dimensional photonic crystals by a top-down approach*”.
- [163] H. Cong, B. Yu, J. Tang, Z. Li and X. Liu, *Chem. Soc. Rev.* **2013**, *42*, 7774–7800, “*Current status and future developments in preparation and application of colloidal crystals*”.
- [164] G. von Freymann, V. Kitaev, B. V. Lotsch and G. A. Ozin, *Chem. Soc. Rev.* **2013**, *42*, 2528–2554, “*Bottom-up assembly of photonic crystals*”.
- [165] F. Li, D. P. Josephson and A. Stein, *Angew. Chem., Int. Ed. Engl.* **2011**, *50*, 360–388, “*Colloidal assembly: the road from particles to colloidal molecules and crystals*”.
- [166] J. Hou, M. Li and Y. Song, *Angew. Chem., Int. Ed. Engl.* **2018**, *57*, 2544–2553, “*Patterned Colloidal Photonic Crystals*”.
- [167] S.-P. Yu, J. A. Muniz, C.-L. Hung and H. J. Kimble, *Proc. Natl. Acad. Sci. U. S. A.* **2019**, *116*, 12743–12751, “*Two-dimensional photonic crystals for engineering atom-light interactions*”.

- [168] T. F. Krauss, R. M. D. La Rue and S. Brand,
Nature **1996**, *383*, 699–702,
“Two-dimensional photonic-bandgap structures operating at near-infrared wavelengths”.
- [169] I. R. Howell, C. Li, N. S. Colella, K. Ito and J. J. Watkins,
ACS Appl. Mater. Interfaces **2015**, *7*, 3641–3646,
“Strain-tunable one dimensional photonic crystals based on zirconium dioxide/sliding elastomer nanocomposites for mechanochromic sensing”.
- [170] S. Y. Choi, M. Mamak, G. von Freymann, N. Chopra and G. A. Ozin,
Nano Lett. **2006**, *6*, 2456–2461,
“Mesoporous bragg stack color tunable sensors”.
- [171] B. V. Lotsch and G. A. Ozin,
Adv. Mater. **2008**, *20*, 4079–4084,
“Clay Bragg Stack Optical Sensors”.
- [172] B. V. Lotsch and G. A. Ozin,
ACS Nano **2008**, *2*, 2065–2074,
“Photonic clays: a new family of functional 1D photonic crystals”.
- [173] E. Redel, C. Huai, M. Renner, G. von Freymann and G. A. Ozin,
Small **2011**, *7*, 3465–3471,
“Hierarchical nanoparticle bragg mirrors: tandem and gradient architectures”.
- [174] D. Lee, M. F. Rubner and R. E. Cohen,
Nano Lett. **2006**, *6*, 2305–2312,
“All-nanoparticle thin-film coatings”.
- [175] Z. Wu, D. Lee, M. F. Rubner and R. E. Cohen,
Small **2007**, *3*, 1445–1451,
“Structural color in porous, superhydrophilic, and self-cleaning SiO₂/TiO₂ Bragg stacks”.
- [176] Z. Wang, J. Zhang, J. Xie, Y. Yin, Z. Wang, H. Shen, Y. Li, J. Li, S. Liang, L. Cui, L. Zhang, H. Zhang and B. Yang,
ACS Appl. Mater. Interfaces **2012**, *4*, 1397–1403,
“Patterning organic/inorganic hybrid Bragg stacks by integrating one-dimensional photonic crystals and macrocavities through photolithography: toward tunable colorful patterns as highly selective sensors”.
- [177] W. C. Marra, P. Eisenberger and A. Y. Cho,
J. Appl. Phys. **1979**, *50*, 6927–6933,
“X-ray total-external-reflection–Bragg diffraction: A structural study of the GaAs–Al interface”.

- [178] H. Krischner,
Vieweg, Braunschweig, 2nd edn. **1980**,
“Einführung in die Röntgenfeinstrukturanalyse“.
- [179] P. W. Atkins and J. de Paula,
Oxford Univ. Press, Oxford, 8th edn. **2006**,
“Atkins’ physical chemistry”.
- [180] D. Halliday, R. Resnick, J. Walker and S. W. Koch, eds.,
Wiley-VCH, Weinheim, 1st edn. **2005**,
“Physik”.
- [181] Z. Lin, Y. Yang and A. Zhang,
Springer International Publishing, Cham **2017**,
“Polymer-Engineered Nanostructures for Advanced Energy Applications”.
- [182] J. Ge and Y. Yin,
Angew. Chem., Int. Ed. Engl. **2011**, *50*, 1492–1522,
“Responsive photonic crystals”.
- [183] G. H. Lee, T. M. Choi, B. Kim, S. H. Han, J. M. Lee and S.-H. Kim,
ACS Nano **2017**, *11*, 11350–11357,
“Chameleon-Inspired Mechanochromic Photonic Films Composed of Non-Close-Packed Colloidal Arrays”.
- [184] X.-Q. Wang, C.-F. Wang, Z.-F. Zhou and S. Chen,
Adv. Opt. Mater. **2014**, *2*, 652–662,
“Robust Mechanochromic Elastic One-Dimensional Photonic Hydrogels for Touch Sensing and Flexible Displays”.
- [185] H. Fudouzi and T. Sawada,
Langmuir **2006**, *22*, 1365–1368,
“Photonic rubber sheets with tunable color by elastic deformation”.
- [186] X. Jia, J. Wang, K. Wang and J. Zhu,
Langmuir **2015**, *31*, 8732–8737,
“Highly Sensitive Mechanochromic Photonic Hydrogels with Fast Reversibility and Mechanical Stability”.
- [187] Y. Yue, T. Kurokawa, M. A. Haque, T. Nakajima, T. Nonoyama, X. Li, I. Kajiwara and J. P. Gong,
Nat. Commun. **2014**, *5*, 4659,
“Mechano-actuated ultrafast full-colour switching in layered photonic hydrogels”.
- [188] Z. Pan, J. Ma, J. Yan, M. Zhou and J. Gao,
J. Mater. Chem. **2012**, *22*, 2018–2025,
“Response of inverse-opal hydrogels to alcohols”.

- [189] M. Qin, M. Sun, R. Bai, Y. Mao, X. Qian, D. Sikka, Y. Zhao, H. J. Qi, Z. Suo and X. He, *Adv. Mater.* **2018**, *30*, e1800468, "Bioinspired Hydrogel Interferometer for Adaptive Coloration and Chemical Sensing".
- [190] K. Ueno, K. Matsubara, M. Watanabe and Y. Takeoka, *Adv. Mater.* **2007**, *19*, 2807–2812, "An Electro- and Thermochromic Hydrogel as a Full-Color Indicator".
- [191] K. Matsubara, M. Watanabe and Y. Takeoka, *Angew. Chem., Int. Ed. Engl.* **2007**, *46*, 1688–1692, "A thermally adjustable multicolor photochromic hydrogel".
- [192] D. Vigneswaran, N. Ayyanar, M. Sharma, M. Sumathi, M. R. M.S. and K. Porsezian, *Sensors and Actuators A: Physical* **2018**, *269*, 22–28, "Salinity sensor using photonic crystal fiber".
- [193] J. H. Holtz and S. A. Asher, *Nature* **1997**, *389*, 829–832, "Polymerized colloidal crystal hydrogel films as intelligent chemical sensing materials".
- [194] H. Hu, Q.-W. Chen, J. Tang, X.-Y. Hu and X.-H. Zhou, *J. Mater. Chem.* **2012**, *22*, 11048, "Photonic anti-counterfeiting using structural colors derived from magnetic-responsive photonic crystals with double photonic bandgap heterostructures".
- [195] H. Kim, J. Ge, J. Kim, S.-e. Choi, H. Lee, H. Lee, W. Park, Y. Yin and S. Kwon, *Nat. Photonics* **2009**, *3*, 534–540, "Structural colour printing using a magnetically tunable and lithographically fixable photonic crystal".
- [196] X. Xu, G. Friedman, K. D. Humfeld, S. A. Majetich and S. A. Asher, *Adv. Mater.* **2001**, *13*, 1681–1684, "Superparamagnetic Photonic Crystals".
- [197] D. P. Puzzo, A. C. Arsenault, I. Manners and G. A. Ozin, *Angew. Chem., Int. Ed. Engl.* **2009**, *48*, 943–947, "Electroactive inverse opal: a single material for all colors".
- [198] M. Kamenjicki, I. K. Lednev, A. Mikhonin, R. Kesavamoorthy and S. A. Asher, *Adv. Funct. Mater.* **2003**, *13*, 774–780, "Photochemically Controlled Photonic Crystals".
- [199] J. H. Holtz, J. S. W. Holtz, C. H. Munro and S. A. Asher, *Anal. Chem.* **1998**, *70*, 780–791, "Intelligent Polymerized Crystalline Colloidal Arrays: Novel Chemical Sensor Materials".

- [200] X. Hong, Y. Peng, J. Bai, B. Ning, Y. Liu, Z. Zhou and Z. Gao,
Small **2014**, *10*, 1308–1313,
"A Novel Opal Closest-Packing Photonic Crystal for Naked-Eye Glucose Detection".
- [201] M. Liu and L.-P. Yu,
The Analyst **2013**, *138*, 3376–3379,
"A novel platform for sensing an amino acid by integrating hydrogel photonic crystals with ternary complexes".
- [202] J.-T. Zhang, X. Chao, X. Liu and S. A. Asher,
Chem. Commun. (Cambridge, U. K.) **2013**, *49*, 6337–6339,
"Two-dimensional array Debye ring diffraction protein recognition sensing".
- [203] Y. Zhao, X. Zhao, B. Tang, W. Xu, J. Li, J. Hu and Z. Gu,
Adv. Funct. Mater. **2010**, *20*, 976–982,
"Quantum-Dot-Tagged Bioresponsive Hydrogel Suspension Array for Multiplex Label-Free DNA Detection".

2. Objective of this thesis

The main objective of this thesis is the preparation, characterization and application of *gradient topographies and functional gradient materials*. For that, materials based on polydimethylsiloxane (PDMS) are surface-modified in different manners to obtain gradient surface topographies and gradient functionalities. Here, the objectives and motivations of the following topics of this thesis based on gradient topographies *via* controlled wrinkling, surface relief gratings, and gradient photonic materials are briefly presented.

Gradient topographies *via* controlled wrinkling

Controlled wrinkling is an established method in literature to prepare sinusoidal wave patterns. The process is comparably simple in terms of fabrication. In general, the wavelength of the wrinkles formed depends on the Young's moduli of film and substrate, the corresponding Poisson ratios and the thickness of the deposited film. Drawbacks are the formation of defects like cracks and line defects, like Y-branches. However, the prevention of those cracks and the formation of gradient wrinkled surfaces has not been studied extensively in literature.

Therefore, the *first topic* of this thesis is focused on the formation process and potential preventions of line defects in wrinkles. For that, an understanding of the line defect formation is necessary. A very promising approach for that is the use of gradient wrinkled surfaces which are connected to a non-gradient wrinkled surface *via* a sharp transition zone. Such gradient wrinkled surfaces can be prepared utilizing PDMS elastomer substrates with a longitudinal gradient in Young's modulus. At the interface to the non-gradient wrinkles, the formation of very defined line defects is expected. Beyond that, the experimental findings shall be compared to theoretical line defect simulations.

Besides the gradient in the Young's modulus of the substrate, a gradient in film thickness can also be used to form a controlled gradient wrinkled surface. The *second topic* addresses on the controlled wrinkling of such gradient thin films. For this study, several metals shall be selected and evaporated with a gradient in film thickness on top of strained PDMS substrates. After relaxation, the influence of the type of metal and the metal film thickness on the morphology of the formed wrinkles shall be evaluated.

Surface relief gratings

A defect-free generation of sinusoidal wave patterns can be achieved using surface relief gratings. These gratings can be inscribed optically in azobenzene films *via* a holographic technique. Compared to a controlled wrinkling approach, the grating height can be independently tuned from the grating distance by applied exposure time.

In the *third topic*, such surface relief gratings shall be used to align nanoparticles. Here, the focus is set on the replication of surface relief gratings with a grating distance of 1.0 μm to PDMS substrates as well as other thermoplastic polymers. Replicas with surface relief gratings of varying height shall be used as efficient screening templates for the confinement of nanoparticles. Beyond that, the line character of the particle arrays obtained shall be studied with respect to their packing behavior.

In addition to the confinement of nanoparticles, PDMS replicas of surface relief gratings have high potential for applications in metrology. Therefore, the *fourth topic* focuses on the determination of the refractive index of such replicas. Two approaches of determining the refractive index from grating diffraction shall be investigated in collaboration with partners from experimental physics. The determined indices from those methods shall be compared to values from an Abbe refractometer.

Gradient photonic materials

Tuning the refractive index in metrological applications opens up further potential of polymer gradient materials in the field of mechanochromic sensors. Instead of a grating, a strain-tunable photonic crystal can be used for light diffraction alternatively. Upon strain, such photonic crystals can change their reflectance.

The *fifth topic* addresses on the formation of gradient photonic materials. For that, strain-tunable photonic crystals shall be fixed on top of PDMS elastomers with a gradient in stiffness. Upon application of a mechanical strain, those materials are expected to undergo a gradient in local strain and hence form a gradient in reflectance. By using this principle, we intend to biomimick the chameleon skin.

3. Synopsis

3.1. Overview of the thesis

The focus of this thesis is on *gradient topographies and functional gradient materials*, consisting of five topics all involving surface modifications of polydimethylsiloxane elastomers. A general overview over the topics is depicted in [Figure 3.1.1](#).

Topic 1 is concerned with the investigation of line-defects which occur typically during controlled wrinkling experiments but have not been studied in literature in detail up to now. In this work, gradient wrinkled surfaces are used for a targeted formation and prevention of these line-defects. These gradient wrinkled surfaces are prepared from elastomers with a gradient in Young's modulus which are embedded in an appropriate matrix. Findings of this topic are published as a full paper article.

As an alternative to the tuning of the Young's modulus of the substrate, gradient wrinkled surfaces are also accessible by a precise control of the thickness of the hard film. This is demonstrated in *Topic 2* for the controlled wrinkling of gradient thin metal films on elastomers. Hereby, the wrinkle wavelength is varied by a gradient in the thickness of the deposited metal film. The results are published as a full paper article.

Highly defect-free sinusoidal surfaces are desired in many applications such as particle alignment. Such defect-free surfaces are accessible *via* surface relief gratings inscribed in azobenzene films. *Topic 3* covers the grating replication and preparation of confinement templates with varying grating height. Utilizing these templates allows a guided self-assembly of nanoparticles. The findings are published as a full paper article.

Topic 4 covers a novel approach to determine the refractive index of transparent solids. This is achieved by investigation of the angle-dependent diffraction of light on replicated surface relief gratings. Two techniques for the refractive-index determination are presented which depend on the knowledge of different parameters. Refractive indices are determined for varying laser wavelengths and compared to established methods. The results are published as full paper article.

Topic 5 deals with biomimicking the chameleon skin with regard to the development of mechanochromic sensors. This is achieved by the preparation of gradient photonic materials. Hereby, a strain-tunable one-dimensional photonic crystal is deposited on top of the elastic substrate. The gradient reflectance pattern obtained upon deformation is tuned by a variation of the Young's modulus of the substrate and demonstrated for different substrate architectures. Results of this topic are published as a communication article.

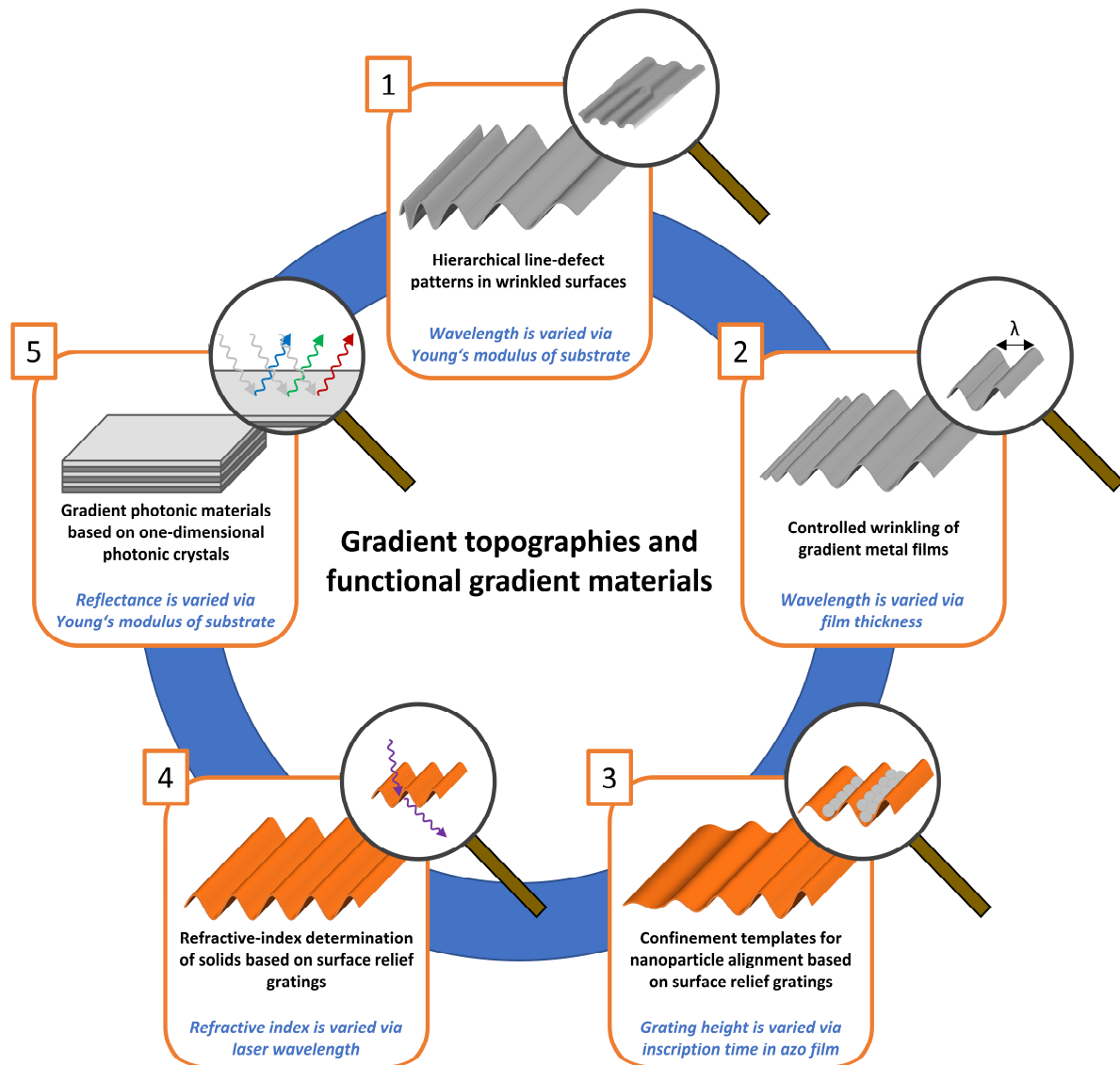


Figure 3.1.1: Overview of the five topics of this cumulative thesis. Gradient topographies and functional gradient materials are relevant in all topics: 1) Controlled wrinkled surfaces with a gradient in wavelength are prepared by variation of the Young's modulus of the elastic substrate. Hierarchical line-defect patterns are formed and investigated. 2) Controlled wrinkled surfaces with a gradient in wavelength *via* variation of the thickness of the metal film deposited. 3) Utilizing replicated surface relief gratings as confinement templates is an elegant and efficient approach to screen the guided self-assembly of colloidal nanoparticles. For that, the grating height is varied by the inscription time in the azobenzene films. 4) Utilizing surface relief gratings for the refractive-index determination of solids. Refractive-index is determined for varying laser wavelengths. 5) Gradient photonic materials by deposition of a strain-tunable one-dimensional photonic crystal to an elastomer with a gradient in Young's modulus. Deformation causes a gradient in reflectance.

3.2. Hierarchical line-defect patterns in wrinkled surfaces

Controlled wrinkling is a very simple method for the patterning of surfaces. The mechanism is based on the compression of a hard film on a soft substrate. The resulting sinusoidal wrinkle patterns can be tuned *via* the film thickness as well as the Young's moduli of film and substrate. Wrinkles reported in literature typically reveal only a certain wavelength over the entire surface area. However, a targeted variation in wavelength over the entire surface area of one substrate is desirable for an effective and efficient screening. The present chapter describes the formation of gradient wrinkled surfaces based on a variation in the Young's modulus of the substrate (Equation 3.2.1).

$$\lambda = 2\pi h \sqrt[3]{\frac{E_f(1 - \nu_s^2)}{3E_s(1 - \nu_f^2)}} \quad (3.2.1)$$

In controlled wrinkling, it is well-known that typically many defects occur in such patterns. One type of defects are surface cracks which occur perpendicularly to the wrinkle grooves. They can be attributed to mismatches in the Poisson ratio of film and substrate which lead to stresses perpendicular to the compression force in the thin hard film during compression. A second type of defects are line-defects which may be attributed to local stiffness differences and inhomogeneous stress fields along the surface. Although there are many publications about controlled wrinkling, a focused investigation of the defect formation and possible prevention strategies was not done in detail before. A detailed investigation of line-defect patterns with respect to local stiffness differences was done in this publication.

For that, we produced PDMS elastomers with a compositional gradient and hence a gradient in the Young's modulus. To obtain a more uniform stress field, we embedded the elastomer stripes additionally in a hard PDMS matrix. The gradient composite materials were then strained and oxidized *via* UV/ozone. Subsequent relaxation induces the formation of gradient wrinkles in the embedded PDMS stripe due to the gradient variation of the Young's modulus of the substrate. Simultaneously, wrinkles with a uniform wavelength are formed in the surrounding matrix. At the interface between embedded specimen and matrix, defined mismatches in stiffness occur which lead to the formation of very defined line defects (Figure 3.2.1). Their density increases with increasing mismatch in stiffness at the interface

between embedded specimen and matrix. Our experimental findings agree very well with theoretical simulations based on a generalized Swift-Hohenberg equation.

Our findings contribute to the fundamental understanding and control of defect formation within the wrinkling process. We envision applications of a targeted line defect formation within microfluidics, particle alignment, and nanophotonics.

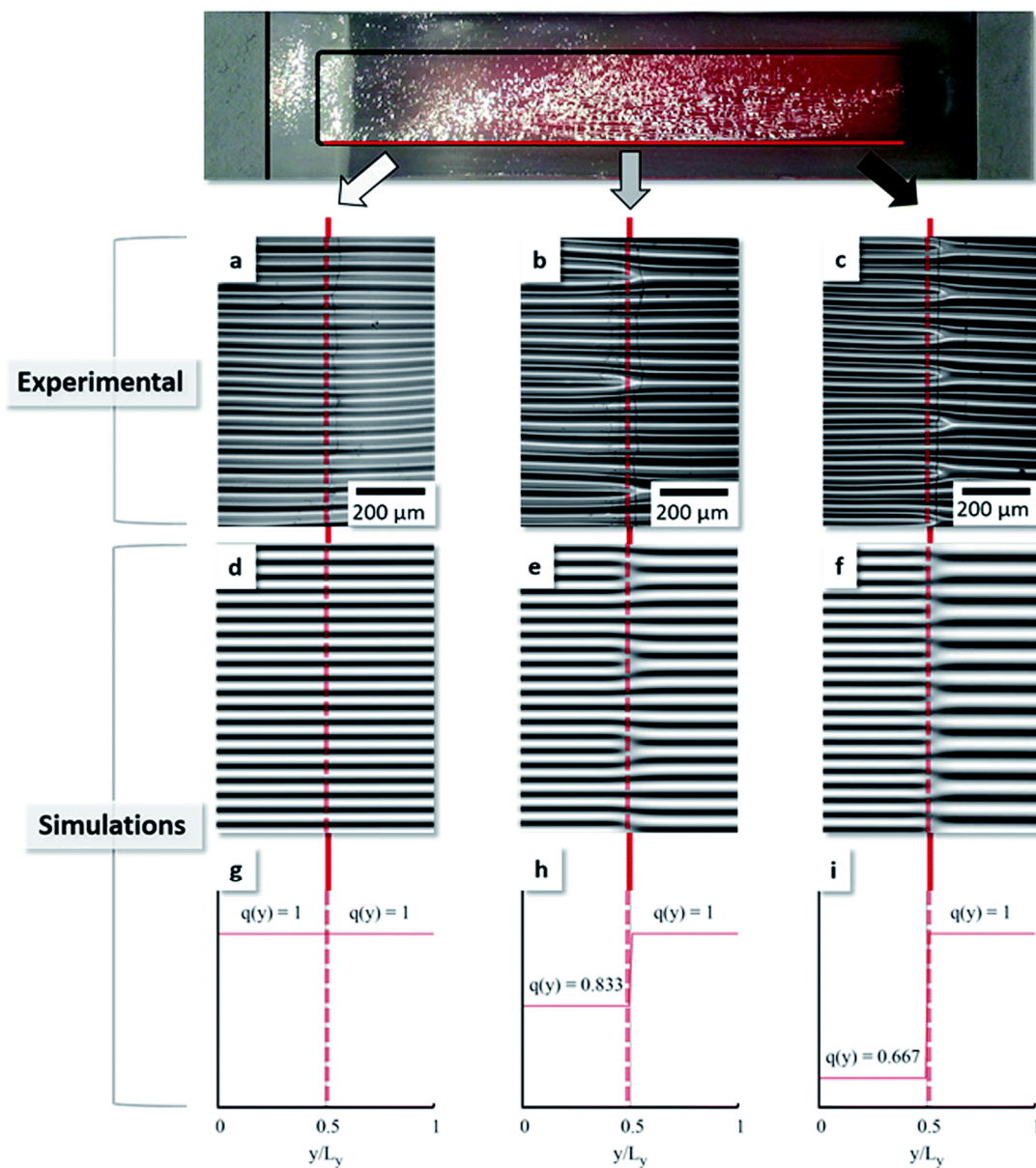


Figure 3.2.1: Line defects at the interface between stiffness gradient PDMS and PDMS matrix. a – c) Line defects obtained experimentally at different positions along the interface between matrix and the longitudinal stiffness gradient. d – f) Corresponding simulations based on step functions (g – i). Reproduced with permission of reference 1 (© 2005 The Royal Society of Chemistry).

3.3. Controlled wrinkling of thin metal films

In the work presented before, we obtained gradient wrinkled surfaces *via* variation of the Young's modulus of the PDMS substrate. As stated in the wrinkling theory, another approach to build up gradient wrinkled surfaces is the tuning of the thickness of the hard film while keeping the Young's modulus of the substrate constant (Equation 3.3.1). This allows also a more effective and efficient screening than the non-gradient wrinkles with a uniform wavelength over the entire surface area which are typically reported in literature.

$$\lambda = 2\pi h \sqrt[3]{\frac{E_f(1 - \nu_s^2)}{3E_s(1 - \nu_f^2)}} \quad (3.3.1)$$

Keeping all the other parameters constant, the film thickness can be varied by a selective deposition of a film with a gradient in thickness. In the work presented here, we did this for metals *via* physical vapor deposition on strained and pretreated PDMS elastomers (Figure 3.3.1). The thickness gradient was achieved by using a combinatorial shutter technique. Subsequent relaxation of the sample induces the formation of gradient wrinkles.

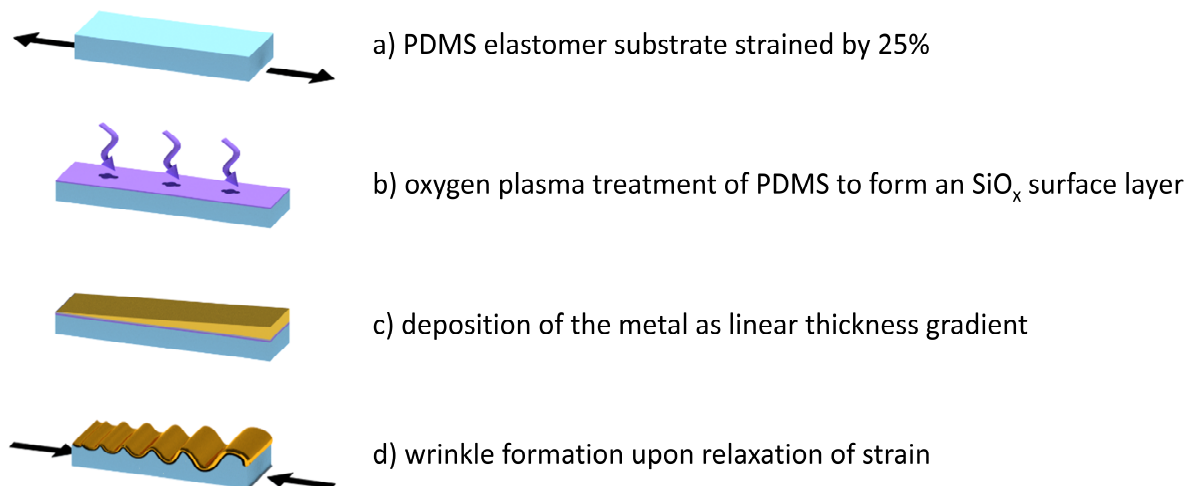


Figure 3.3.1: Preparation of gradient wrinkle patterns based on wrinkled gradient metal films. A PDMS elastomer strip was strained by 25% (a) and treated with oxygen plasma to produce a thin SiO_x layer on the surface (b). A linear thickness gradient metal film was evaporated by physical vapor deposition (c). Relaxation of the sample resulted in the wrinkled gradient metal film (d). Adapted and reproduced with permission of reference 2 (© 2018 American Chemical Society).

We selected three metals for the study: gold, chromium, and indium. Gold was selected due to its important role in electronic applications. Chromium has a very strong adhesion to PDMS and a comparably high Young's modulus, resulting in larger wavelengths. Indium can be deposited at already mild conditions. In contrast to the smooth gold and indium films, indium reveals a grainy surface structure. Our experimental findings agree well with predictions from the wrinkling theory including a bilayer model from Stafford *et al.* (Figure 3.3.2).

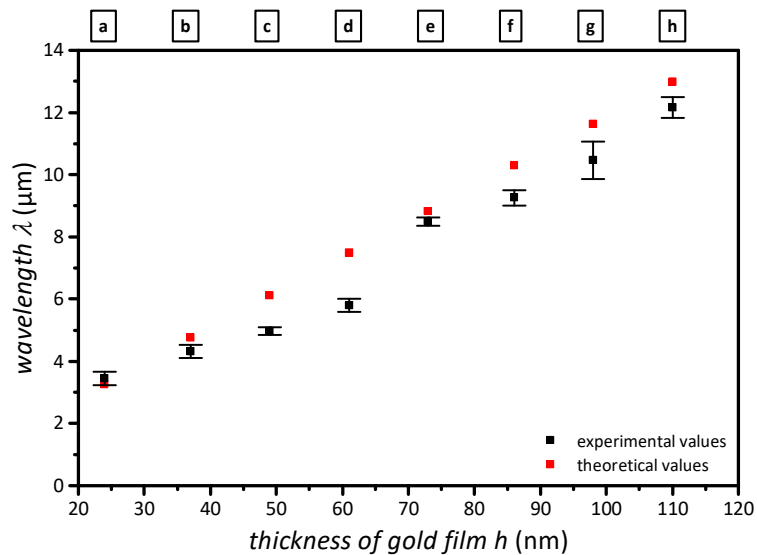


Figure 3.3.2: Wrinkle wavelength in dependency of the gold film thickness. Theoretical values from calculations from the wrinkling theory agree well with the experimental determined values. Reproduced with permission of reference 2 (© 2018 American Chemical Society).

The preparation of gradient wrinkled metal films offers a big potential for efficient screening applications. We envision applications of these gradient metal wrinkle patterns in the field of flexible electronics, tunable optical gratings, and mechanochromic sensors.

3.4. Confinement templates for hierarchical nanoparticle alignment prepared by azobenzene-based surface relief gratings

Sinusoidal surface patterns obtained by controlled wrinkling are easy to prepare but typically reveal also a lot of defects. The *third* and *fourth topic* of this thesis focus on defect-free sinusoidal surface patterns which are accessible *via* the preparation of surface relief gratings. We inscribed such gratings in azobenzene films utilizing a well-known holographic technique and transferred them to PDMS and thermoplastic polymers. Remarkably, this was achieved without significant losses in grating height and distance. We studied the influence of the inscription time in the azobenzene film on the grating height of PDMS replicas. That allowed us a precise tuning of the grating height independently from the grating period (Figure 3.4.1).

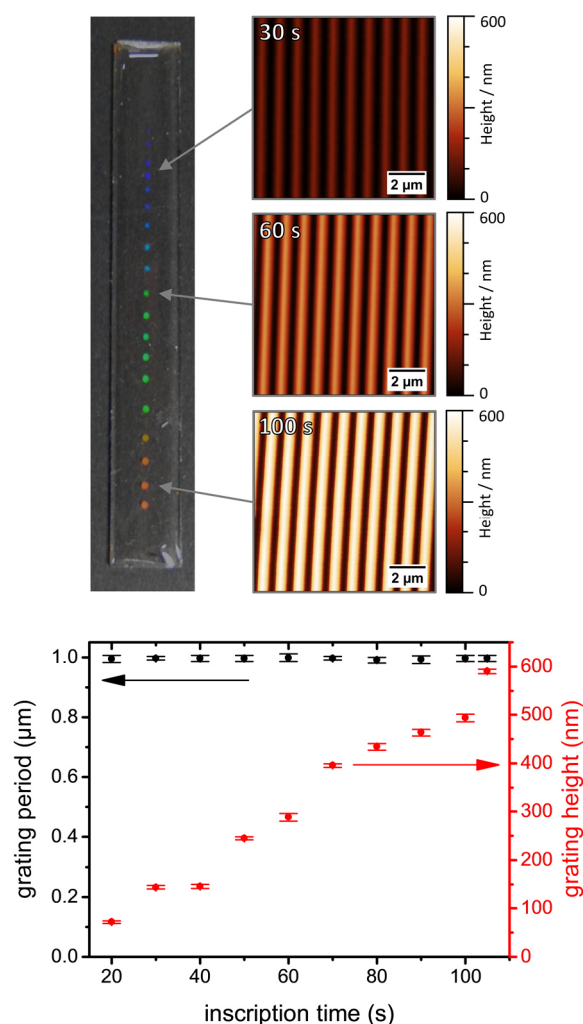


Figure 3.4.1: Dependency of grating height and grating period of surface relief gratings in PDMS on the inscription time in the original azobenzene film. The grating height can be tuned independently from the grating period. Reproduced with permission of reference 3 (© 2019 The Royal Society of Chemistry).

We utilized these highly regular periodic sinusoidal patterns for the guided self-assembly of polystyrene nanoparticles. For that, disk-like confinement templates were prepared *via* replication of surface relief gratings to PDMS. We varied the height of these gratings systematically while keeping the grating period constant. Screening of the confinement was done by spin-coating a PS nanoparticle solution on top of the templates. The grating height has a direct influence on the formed line character of the particle assemblies (Figure 3.4.2). If no grating or gratings with only a small grating height are present, no confinement was observed. Instead, a hexagonal monolayer is formed. With increasing grating height, defined particle arrays from single and double lines up to more complex cubic structures are formed.

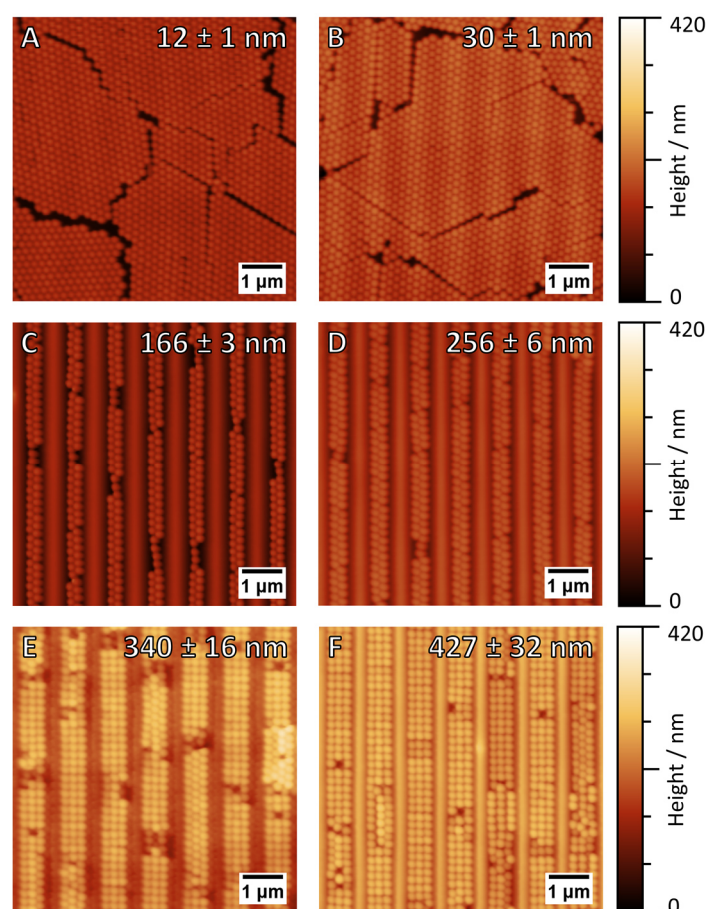


Figure 3.4.2: Screening of particle confinement with surface relief gratings in PDMS. The grating height defines the line character of the formed particle assemblies. Reproduced with permission of reference 3 (© 2019 The Royal Society of Chemistry).

The presented approach offers an elegant and efficient screening of the formed particle assemblies upon confinement. Besides the possibility to screen different particle systems within the geometrical confinement, we also see potential applications in the field of strain sensing, tunable gratings and metamaterials.

3.5. Refractive-index determination of solids from first- and second-order critical diffraction angles of periodic surface patterns

Besides the possibility to align particles, periodic surface patterns in PDMS also allow the determination of the refractive index from diffraction on these gratings. This is the *fourth topic* of this thesis and is demonstrated in chapter 4.5.

The precise knowledge of the refractive index is essential for many applications. Standard methods like the determination *via* Abbe refractometer are simple for liquids. For solids, however, often aggressive index-matching fluids are necessary which may damage the sample to be investigated or even the prism of the refractometer. Furthermore, a very precise knowledge about these auxiliary fluids as well as the dispersion of the prism is necessary. Lastly, complex calculations are necessary to calibrate the refractometer scale for different wavelengths. Spectral ellipsometry is an alternative technique for the refractive index determination of thin solid films. While this technique can circumvent most of the drawbacks of the Abbe refractometer, the accuracy of the results is highly dependent on the precise knowledge about the thickness and homogeneity of the films as well as the model used.

In this work, we present two alternative approaches for the refractive index determination of transparent solids. They are based on the first and second order of diffraction on periodic surface patterns (Figure 3.5.1). We demonstrate the principle with PDMS replicas of SRGs using collimated monochromatic light and a rotation stage.

The first approach for the refractive index determination uses first order diffraction according to Equation 3.5.1. This equation is valid, if the sample is oriented in such a way that the first order plane light wave is diffracted at an angle of $\pi/2$.

$$n_{\text{mat}} = \sin \varphi_{1,\text{in}}^{90^\circ} + \frac{\lambda}{\Lambda} \quad (3.5.1)$$

The second approach includes the second order diffraction. The refractive index follows then Equation 3.5.2:

$$n_{\text{mat}} = 2 \sin \varphi_{1,\text{in}}^{90^\circ} - \sin \varphi_{2,\text{in}}^{90^\circ} \quad (3.5.2)$$

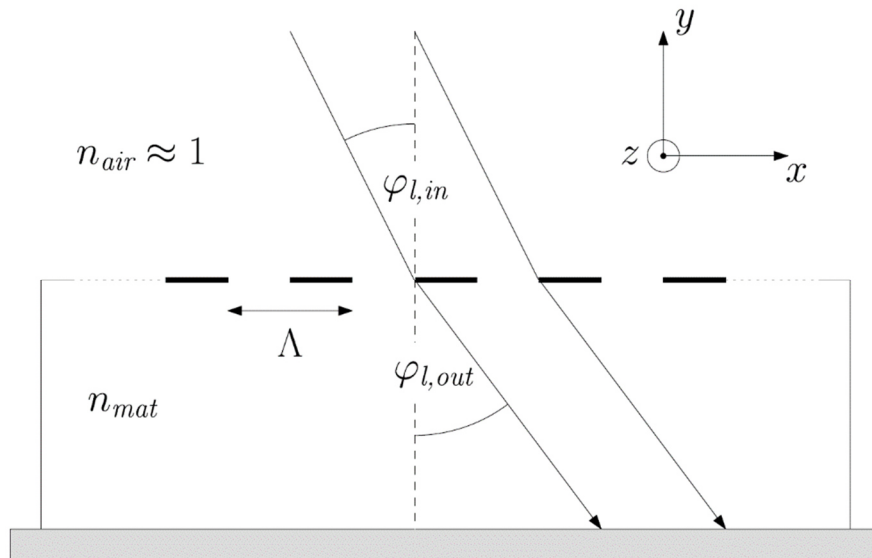


Figure 3.5.1: Diffraction of an incident light beam with diffraction order l on a periodic surface pattern. Reproduced from reference 4. Published by the *American Institute of Physics* under a Creative Commons Attribution 3.0 Unported License (© 2019 Authors).

The accuracy of the determined refractive index plays an important role in many applications. The choice of the appropriate approach for the determination of the refractive index depends on which parameters in Equation 3.5.1 and Equation 3.5.2, respectively, can be determined more precisely. To investigate the degree of precision, we compare the experimental determined values from both approaches with values obtained from an Abbe-refractometer (Figure 3.5.2). This was done for several laser wavelengths.

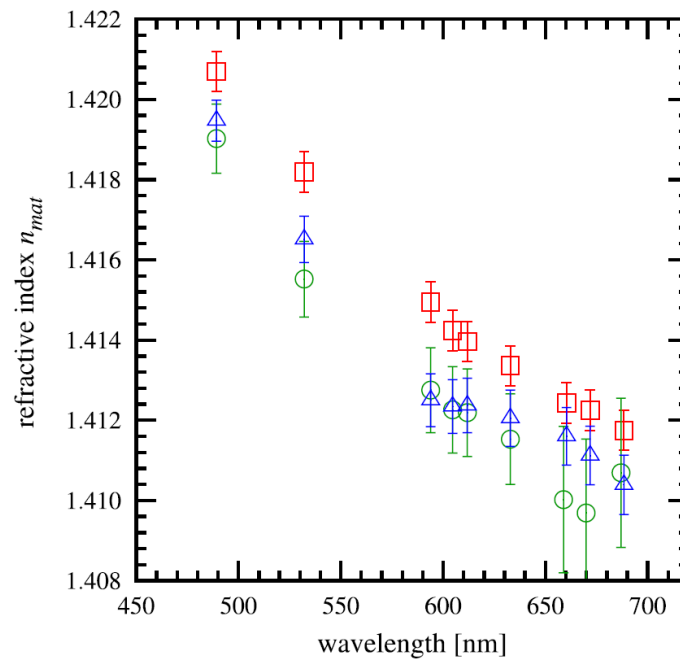


Figure 3.5.2: Wavelength-dependent refractive index of the PDMS elastomer, determined via Abbe refractometer (red squares), Equation 3.5.1 (green circles), and Equation 3.5.2 (blue triangles), respectively. Reproduced from reference 4. Published by the *American Institute of Physics* under a Creative Commons Attribution 3.0 Unported License (© 2019 Authors).

In conclusion, the two approaches presented are a very powerful alternative to precisely determine the refractive index of transparent solids. Advantages compared to existing methods like Abbe refractometry and spectral ellipsometry are the independency of aggressive auxiliary liquids and an easier access to mandatory parameters for the precise calculation of the refractive index.

3.6. Gradient photonic materials based on one-dimensional polymer photonic crystals

The last topic presents gradient photonic materials inspired by nature. Chameleon skin has the remarkable property to change the color rapidly upon stretching. The phenomenon is based on photonic crystals – in that case small guanine nanocrystals which are periodically aligned and embedded in dermal cell layers. Upon stretching, the lattice distance is changed. This results in a change in the photonic band gap and hence influences the reflectance.

We developed gradient photonic materials with the intention to biomimick this natural phenomenon. Our materials consist of a polymer-based strain-tunable one-dimensional photonic crystal (1DPC) which is attached to the surface of a PDMS substrate with a gradient in stiffness. We built up the 1DPC from alternating layers of high and low refractive index layers. The layer thicknesses and the refractive indices determine a photonic gap. Light of a specific wavelength is forbidden to propagate within the material. As a result, the light is outcoupled from the material and appears as reflectance. The PDMS substrate with a longitudinal gradient in stiffness influences the reflectance behavior upon strain. Materials were designed to reveal a uniform red reflectance over the entire surface area in an unstrained state. Upon load, the PDMS elastomer reveals a gradient in local strain due to the stiffness gradient. This gradient in local strain is transferred to the attached 1DPC and induces a gradient in refractive index layer thickness. This leads to a gradient blue-shift in the reflected wavelength.

For PDMS substrates with a hard-soft gradient, we obtained a rainbow-like spectrum with a gradient in reflectance from red to blue upon strain ([Figure 3.6.1](#)). In addition, even more complex reflectance patterns are accessible by tailoring the substrate architecture. Stripe-like reflectance patterns as they occur in chameleons were obtained by utilizing a complex hard-soft-hard-soft-hard profile for the stiffness gradient in the PDMS substrate.

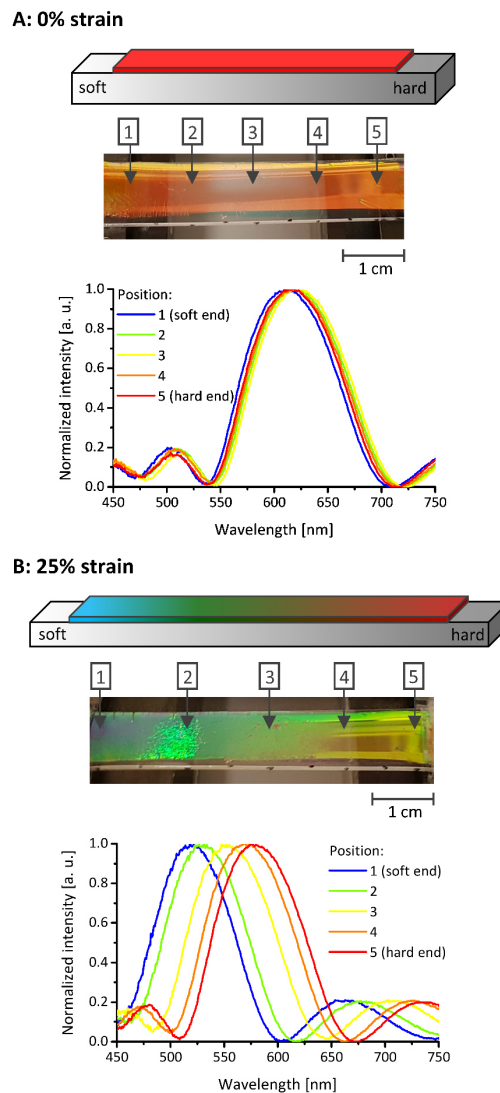


Figure 3.6.1: Reflectance of the prepared gradient photonic material based on a PDMS substrate with a hard-soft stiffness gradient. In an unstrained state, the reflectance is uniform over the entire surface. Upon 25% strain, the sample reveals a gradient in reflectance from red to blue. Reproduced from reference 5. Published by WILEY-VCH Verlag GmbH & Co. KGaA under a Creative Commons Attribution 4.0 International License (© 2020 Authors).

In conclusion, the presented gradient photonic material is inspired by the remarkable color change behavior of chameleons. Like the natural model, these materials yield strain-tunable reflectance patterns. The reflectance is directly correlated to the local strain. Due to this fact, we envision applications within the field of mechanochromic sensors, telemedicine, smart materials, and metamaterials.

3.7. References

- [1] B. A. Glatz, M. Tebbe, B. Kaoui, R. Aichele, C. Kuttner, A. E. Schedl, H.-W. Schmidt, W. Zimmermann and A. Fery
Soft Matter **2015**, *11*, 3332-3339,
“Hierarchical line-defect patterns in wrinkled surfaces”.

- [2] A. E. Schedl, C. Neuber, A. Fery and H.-W. Schmidt
Langmuir **2018**, *34*, 14249-14253
“Controlled wrinkling of gradient metal films”.

- [3] A. E. Schedl, P. T. Probst, C. Meichner, C. Neuber, L. Kador, A. Fery and H.-W. Schmidt
Soft Matter **2019**, *15*, 3872-3878,
“Confinement templates for hierarchical nanoparticle alignment prepared by azobenzene-based surface relief gratings”.

- [4] C. Meichner, A. E. Schedl, C. Neuber, K. Kreger, H.-W. Schmidt and L. Kador
AIP Advances **2015**, *5*, 087135,
“Refractive-index determination of solids from first- and second-order critical diffraction angles of periodic surface patterns”.

- [5] A. E. Schedl, I. R. Howell, J. J. Watkins and H.-W. Schmidt
Macromol. Rapid Commun. **2020**, *41*, 2000069,
“Gradient photonic materials based on one-dimensional polymer photonic crystals”.

4. Publications

4.1. Individual contributions to joint publications

The publications presented in this thesis arose from joint collaborations with several departments. In the following, the individual contributions of each author are outlined. Work done by myself was carried out at the chair of Macromolecular Chemistry I at the University of Bayreuth under the supervision of Prof. Dr. Hans-Werner Schmidt.

Publication 1: Hierarchical line-defect patterns in wrinkled surfaces

Soft Matter **2015**, 11, 3332-3339.

B. A. Glatz, M. Tebbe, B. Kaoui, R. Aichele, C. Kuttner, A. E. Schedl, H.-W. Schmidt, W. Zimmermann and A. Fery.

The first publication is a full paper article on the control of line-defect patterns in wrinkled surfaces of gradient elastomer substrates. I further improved the combinatorial preparation of gradient materials particular in view of the publication and conducted the synthesis and corresponding material characterization of all gradient materials. I was involved during the entire time in scientific discussions as well as finalizing the manuscript. B. A. Glatz (Physical Chemistry II, University of Bayreuth) performed the characterization experiments of the wrinkles as well as the FEM simulations and wrote the first draft of the manuscript. R. Aichele, B. Kaoui and W. Zimmermann (Theoretical Physics I, University of Bayreuth) did the wrinkling simulations and wrote the corresponding part of the manuscript. M. Tebbe (Physical Chemistry II, University of Bayreuth) contributed with scientific discussions about the topic and helped with writing the first draft of the manuscript. H.-W. Schmidt (Macromolecular Chemistry I, University of Bayreuth) and A. Fery (Physical Chemistry II, University of Bayreuth) supervised the project, were involved in scientific discussions and finalizing the manuscript.

Publication 2: Controlled wrinkling of gradient metal films*Langmuir* **2018**, 34, 14249-14253

A. E. Schedl, C. Neuber, A. Fery and H.-W. Schmidt.

This publication on controlled wrinkling of gradient metal films was published as a full paper article. The first draft of the manuscript was written by me. I also performed all the experiments and did all the analyses. C. Neuber (Macromolecular Chemistry I, University of Bayreuth) introduced me to the physical vapor deposition process and contributed with helpful discussions about combinatorial vapor deposition of thin films. A. Fery (Leibniz Institute of Polymer Research Dresden) was involved in scientific discussions of the experiments and suggested the bilayer model for the description of wrinkles prepared from gold films. H.-W. Schmidt (Macromolecular Chemistry I, University of Bayreuth) conceived the topic, supervised the project and contributed with helpful discussions about optimization of metal film adhesion. All authors were involved in finalizing the manuscript.

Publication 3: Confinement templates for hierarchical nanoparticle alignment prepared by azobenzene-based surface relief gratings*Soft Matter* **2019**, 15, 3872-3878

A. E. Schedl, P. T. Probst, C. Meichner, C. Neuber, L. Kador, A. Fery and H.-W. Schmidt.

The nanoparticle confinement *via* surface relief gratings is the content of this publication which was published as a full paper article. I conceived the topic and wrote the first draft of the manuscript. Furthermore, I performed the azobenzene film preparation for the holographic inscription process, the grating transfer to all polymers, and the preparation of the confinement templates. I did all analyses except of the AFM images correlated to the particle alignment. P. T. Probst (Leibniz Institute of Polymer Research Dresden) did the particle alignment experiments and recorded the corresponding AFM images. C. Meichner (Bayreuth Institute of Macromolecular Research, University of Bayreuth) performed the inscription of surface relief gratings to azobenzene films. C. Neuber (Macromolecular Chemistry I, University of Bayreuth) and L. Kador (Bayreuth Institute of Macromolecular Research, University of Bayreuth) were involved in scientific discussions. A. Fery (Leibniz Institute of Polymer Research Dresden) and H.-W. Schmidt (Macromolecular Chemistry I, University of Bayreuth) supervised the project and were involved in scientific discussions about particle alignment and grating transfer. All authors were involved in finalizing the manuscript.

Publication 4: Refractive-index determination of solids from first- and second-order critical diffraction angles of periodic surface patterns

AIP Advances **2015**, 5, 087135

C. Meichner, A. E. Schedl, C. Neuber, K. Kreger, H.-W. Schmidt and L. Kador.

This publication is a full paper article on the refractive-index determination by utilizing surface relief gratings. I prepared the samples for the holographic inscription process and performed the grating transfer for the refractive-index determination. I wrote the corresponding part of the manuscript. Furthermore, I was involved in scientific discussions of the results over the entire time. C. Meichner (Bayreuth Institute of Macromolecular Research, University of Bayreuth) inscribed surface relief gratings into azobenzene films and performed the refractive-index determination. He also wrote the major part of the manuscript. C. Neuber, K. Kreger, H.-W. Schmidt (Macromolecular Chemistry I, University of Bayreuth) and L. Kador (Bayreuth Institute of Macromolecular Research, University of Bayreuth) contributed with scientific discussions of the results. All authors were involved in finalizing the manuscript.

Publication 5: Gradient photonic materials based on one-dimensional polymer photonic crystals

Macromolecular Rapid Communications **2020**, 41, 2000069

A. E. Schedl, I. R. Howell, J. J. Watkins and H.-W. Schmidt.

This publication is a communication article about gradient photonic materials. I conceived the topic and wrote the first draft of the manuscript. Furthermore, I optimized the gradient synthesis particular in view of this publication and performed the synthesis of all gradient substrates. I built up the gradient photonic materials and did the mechanical and optical characterization. I. R. Howell (Polymer Science and Engineering, University of Massachusetts, Amherst, MA, USA) prepared the one-dimensional photonic crystal and assisted with reflectance measurements. J. J. Watkins (Polymer Science and Engineering, University of Massachusetts, Amherst, MA, USA) was involved in scientific discussions about Bragg mirrors and helped with material selection for the one-dimensional photonic crystal. H.-W. Schmidt (Macromolecular Chemistry I, University of Bayreuth) supervised the project, contributed with scientific discussions about gradient materials and suggested the preparation of the complex gradient photonic material. All authors were involved in finalizing the manuscript.

4.2. Hierarchical line-defect patterns in wrinkled surfaces

Bernhard A. Glatz,^a Moritz Tebbe,^a Badr Kaoui,^b Roland Aichele,^b Christian Kuttner,^a
Andreas E. Schedl,^c Hans-Werner Schmidt,^c Walter Zimmermann^b and Andreas Fery*^a

a) Department of Physical Chemistry II, University of Bayreuth, 95440 Bayreuth, Germany

b) Theoretical Physics I, University of Bayreuth, 95440 Bayreuth, Germany

c) Department of Macromolecular Chemistry I, University of Bayreuth, 95440 Bayreuth, Germany

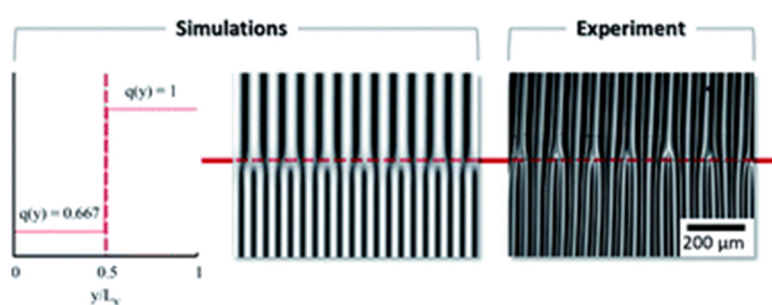
The results of this chapter have been published as a full paper article in

Soft Matter **2015**, *11*, 3332-3339.

Published by *The Royal Society of Chemistry*

under a Creative Commons Attribution 3.0 Unported License.

DOI: 10.1039/c5sm00318k



We show experimentally and theoretically that step-wise changes in the Young's Modulus can trigger hierarchical wrinkle pattern formation.

4.2.1. Abstract

We demonstrate a novel approach for controlling the formation of line-defects in wrinkling patterns by introducing step-like changes in the Young's modulus of elastomeric substrates supporting thin, stiff layers. Wrinkles are formed upon treating the poly(dimethylsiloxane) (PDMS) substrates by UV/Ozone (UVO) exposure in a uniaxially stretched state and subsequent relaxation. Line defects such as minutiae known from fingerprints are a typical feature in wrinkling patterns. The position where these defects occur is random for homogenous substrate elasticity and film thickness. However, we show that they can be predetermined by using PDMS substrates consisting of areas with different cross-linking densities. While changing the cross-linking density is well known to influence the wrinkling wavelength, we use this parameter in this study to force defect formation. The defect formation is monitored in situ using light microscopy and the mechanical parameters/film thicknesses are determined using imaging AFM indentation measurements. Thus, the observed wrinkle-wavelengths can be compared to theoretical predictions. We study the density and morphology of defects for different changes in elasticity and compare our findings with theoretical considerations based on a generalized Swift–Hohenberg-equation to simply emulate the observed pattern-formation process, finding good agreement. The fact that for suitable changes in elasticity, well-ordered defect patterns are observed is discussed with respect to formation of hierarchical structures for applications in optics and nanotechnology.

4.2.2. Introduction

Wrinkling is a mechanical instability phenomenon of thin films. Wrinkles form, if a laminar system consisting of a stiff, thin layer in strong adhesive contact with a soft, macroscopic elastomer is subject to in-plane compression. Under these conditions, the well-known buckling instability results in periodic surface corrugations. Due to its generic nature, wrinkling can be found in biological,^{1,2} geomorphological^{3,4} as well as artificial structures.^{5,6} In the framework of surface patterning and structuring, controlled formation of wrinkles has been investigated and characterized intensively in the last two decades.^{7–12} Importantly, permanent wrinkle patterns can be formed, if the thin layer is created while an elastomeric substrate is under strain and subsequently relaxed. Possible preparation methods are in situ oxidation of poly(dimethylsiloxane) (PDMS) substrates by treatment with plasma,^{13,14} UVO,^{15–17} wet chemicals¹⁸ or coating of these substrates with metals¹⁹ and polymers,²⁰ respectively. Besides, other methods are employed, e.g. the utilization of distortion effects of elastomers at a water–substrate-interface that lead to sinusoidal bending²¹ or the coating of an elastomer with a UV-curable material instead of attaching two layers to each other.²²

Wrinkle patterns display always deviations from an ideal structure, even in the simplest case of uni-axial strain, yielding parallel oriented wrinkles. These defects can be classified into two categories, cracks and line defects, respectively. Most work has been done on the investigation of cracks, which are mechanically induced film fractures.^{23–25} Recently, some publications report on specific applications of thin-film-cracking where the evolving channels are filled with metals and consequently utilized as conducting 2D-networks.^{26,27} In contrast our work focuses on the second defect type – the line defects that are known as minutiae in fingerprints. Their evolution in random fingerprint-like structures with defects has been simulated lately.²⁸ Line defects are characterized by two adjacent ridges merging into one single ridge or by a termination of a ridge, as illustrated in [Figure 4.2.1](#) for fingerprints, where the term minutiae is used for the line defects, and for wrinkle patterns formed using the method presented in this study.

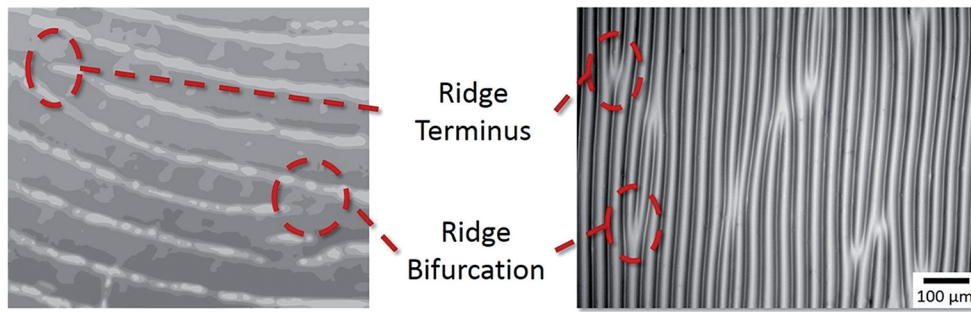


Figure 4.2.1: Comparison of a human fingerprint (left) and a wrinkled PDMS sample (right). Line defects as ridge termini and bifurcations are found in both cases. However, the size differs from the millimeter-range on human hands down to the micrometer and nanometer-range for artificially wrinkled samples.

For ideal homogenous, infinite systems line defect nucleation is a homogenous nucleation process. However, in real systems line defects are frequently found to nucleate at heterogeneities in elastic constants or film thicknesses or at boundaries. In many applications, these line defects are considered a nuisance since they appear stochastically and thus limit the structural perfection and long-range order of wrinkling patterns. However, they as well present an interesting example of symmetry breaking and harnessing the position at which line defects occur might pave the road to control symmetry breaking and formation of complex hierarchical structures.

Following this rationale, we present a method to generate patterned defects in a controlled fashion. We introduce a novel method for the preparation of PDMS with steep local changes in the Young's modulus and study permanent wrinkle formation in these systems. We investigate the mechanical properties of the system using nanomechanical AFM techniques. Furthermore, we employ light microscopy for *in situ* investigation of wrinkle and line-defect formation. These studies are the basis to elucidate the underlying structure formation mechanism. We investigate the spatial distribution of line defects and long-range ordering effects. Finally, we discuss potential applications in optics, particle alignment or microfluidics.^{29,30}

4.2.3. Results and discussion

Wrinkled samples were prepared from commercially available PDMS system Sylgard 184 (Dow Corning Ltd., Midland, USA). PDMS samples were treated with UVO in uni-axially stretched state to induce wrinkle formation upon relaxation. A buckling instability caused by mechanical mismatch between the applied thin oxide layer and the elastic substrate leads to wrinkle formation perpendicular to the strain direction (see [Figure 4.2.2](#)). The resulting wavelengths of the buckling instability can be calculated for small strains according to the well-known [Equations 4.2.1 – 4.2.3](#)^{31,32}

$$\varepsilon_c = \frac{\sigma_c}{\bar{E}_f} = \frac{1}{4} \left(\frac{3\bar{E}_s}{\bar{E}_f} \right)^{2/3} \quad (4.2.1)$$

$$\lambda = 2\pi h \left(\frac{\bar{E}_f}{3\bar{E}_s} \right)^{1/3} \quad (4.2.2)$$

with

$$\bar{E} = \frac{E}{1 - \nu^2} \quad (4.2.3)$$

Herein, ε_c represents the critical uniaxial strain necessary to induce wrinkling, while λ describes the wavelength of the buckling instability, h is denoted as layer thickness and \bar{E}_f and \bar{E}_s are the plane-strain-moduli of the layer and substrate respectively that can be calculated with the according Poisson's ratio ν . Modifying the ratio of the pre-polymer to curing-agent results in a stiffness variation of the resulting silicone from 0.24 MPa to 1.82 MPa. To create a sample that features two different wrinkling wavelengths and a small, defined crossover area in between, we combined these materials displaying large differences in stiffness.

Sample preparation

The samples were prepared sequentially in three steps: (1) a matrix containing the highest cross-linker content was prepared, (2) fluid soft PDMS being discrete or gradient-like was cast into the matrix presenting one side and (3) the matrix was cross-linked thermally, ensuring a covalent linkage between both phases. The process is depicted in the Supplementary Information (SI 4.2.7) schematically in Figure 4.2.7. Thus, PDMS of adjustable Young's modulus was embedded in a matrix of hard PDMS. Consequently, the interface between both materials displayed a sharp mechanical transition between the different phases of PDMS. According to Equation 4.2.2 a change of substrate elasticity is directly correlated with a change in wavelength for constant film elasticity and thickness. To investigate wrinkling of substrates with different Young's moduli focusing on the defect formation process two different sample types were prepared (Figure 4.2.2). One sample type was prepared casting soft PDMS into a mold consisting of only hard PDMS (Figure 4.2.2a) giving a composite consisting of two pure materials. The other sample type was prepared by casting a soft-to-hard-gradient into a mold of hard PDMS using a modified method of Claussen *et al.*³³ (Figure 4.2.2b). The line-defects are expected to preferentially nucleate at the interface of hard-to-soft material. This is due to a difference in substrate stiffness, which forces a local change of preferred wavelength that goes along with formation of line branches. Additionally, the speed of relaxation has an impact on their number and shape,³⁴ that is why the samples were allowed to relax with highest possible rate after oxidation to create as many line defects as possible. Furthermore, according to Equation 4.2.1 the wrinkle evolution is not simultaneous in both phases but will occur when the critical strain ε_c is reached, depending on the respective Young's moduli. In order to analyze this predicted behavior, we used a custom-built *in situ* setup (see also Figure 4.2.8) based on optical microscopy to study wrinkle and defect formation along the stiffness modification lines.

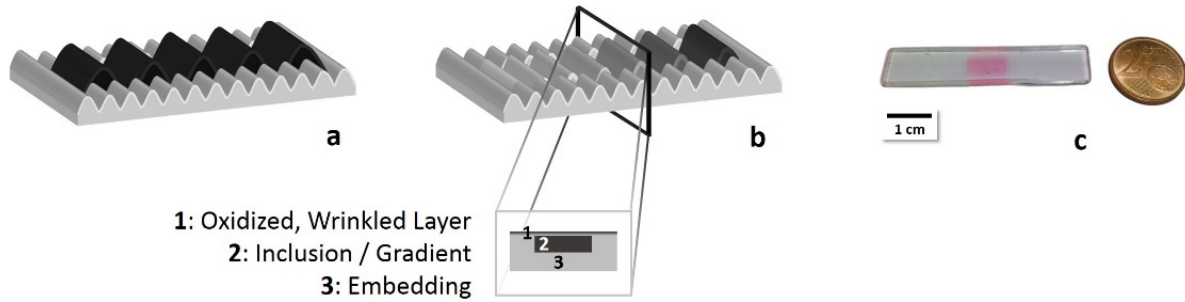


Figure 4.2.2: Schematic illustration of the two sample types: a soft, discrete (a) and a soft-to-hard gradient, both embedded in a hard matrix (b) with a cross profile of the sample. In (c) a typical sample of type (a) is shown scaled with a 2 €-cent coin. It consists of the hard, transparent matrix that includes the soft, red dyed inner part.

Qualitative analysis

The stretched and oxidized samples were released with a defined speed. The wrinkle evolution was tracked *in situ via* reflected light microscopy focused at the oxidized surface layer in order to capture changes in the surface morphology. Figure 4.2.3 shows representative results for a homogeneous sample with a discrete step in substrate elasticity: After focusing the interface between hard and soft polymer the wrinkle evolution was induced by slowly decreasing the strain from an elongation of $\varepsilon = 50\%$ (15 mm initial sample length and 22.5 mm strained state) with 6.1 mm min^{-1} . For a ε of 41% the first wrinkles can be observed in the soft phase (Figure 4.2.3b). They were entirely shaped at a ε of 39% (Figure 4.2.3c), meaning the amount of waves and line-defects remains constant. For a ε of 35% buckling is induced within the hard phase (Figure 4.2.3d). The wrinkle evolution is completed at a ε of 30% resulting in a fully wrinkle-covered surface (Figure 4.2.3e). The corrugations on the soft phase slightly protrude into the unwrinkled hard phase (Figure 4.2.3c). It is caused by different boundary conditions of the two phases which results in a singularity within the interphase that consequently induces line-defect formation close to the interface. Here the critical strain as well as the final wavelength changes dramatically. Thus, line defects caused by singularity are pinned to the interface transition or nucleate in close proximity. Further strain release afterwards only leads to a compression of the waves, which results in increasing amplitudes and reduced wavelengths. The underlying wrinkle formation process can be divided into two different steps. First the waves emerge within domains with sizes of a few buckling periods, followed by a rapid growth with decreasing strain resulting in wrinkle joining. The latter is accompanied

by the appearance of line-defects.³⁵ Furthermore, the buckling period depends on the stiffness (Young's modulus) of the underlying substrate following a third root law, in consistence with Equation 4.2.2. The results observed for low strains are shown in Figure 4.2.3e. As expected, a large wavelength is obtained on substrates with low stiffness values.

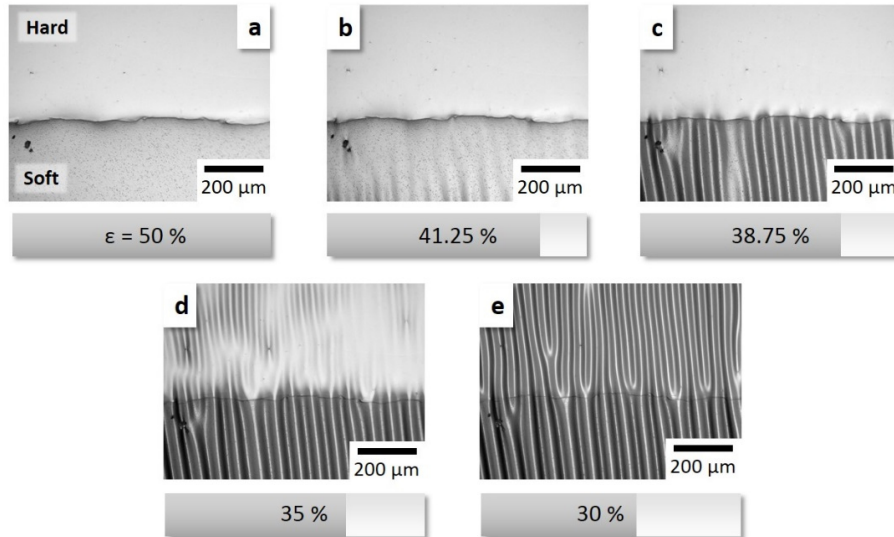


Figure 4.2.3: Same-spot in situ observation of the release process, focused on the crossover line from hard to soft PDMS. The soft discrete inclusion is present at the bottom each, the hard at the top. In the beginning the substrate is pre-strained to 50% of its initial length (a), the oxidized layer on top is unstrained. Upon strain release wrinkles do form first within the soft inclusion (b and c) followed by the hard matrix (d and e). For a video capture of this process, see Electronic Supplementary Information.

Quantitative parameter analysis

To compare our experimental results with theory we quantitatively determined all relevant parameters. According to Equation 4.2.2, the required parameters are the Young's moduli \bar{E}_s and \bar{E}_f respectively, and the layer height h_f of homogenous (non-embedded) hard and soft PDMS. The data for the substrate moduli of hard and soft phase were taken from Claussen *et al.*³³ They determined 1.82 ± 0.04 MPa for hard and 0.24 ± 0.01 MPa for soft PDMS. Additionally, we performed indentation measurements to check for the mechanical uniformity of the individual phases. Therefore, the samples were analyzed prior to oxidation with a sapphire sphere (400 μm radius) along the line of previous publications.^{15,36} For statistical reasons every sample was measured five times on different spots. For hard PDMS the averaged Young's modulus was determined to be 2.9 ± 0.31 MPa and for soft 0.65 ± 0.14 MPa. These results are higher compared to the data taken from Claussen *et al.*

obtained for bulk measurements.³³ Other groups showed that this effect is due to general differences between the mechanical testing setups.^{37–39} Consequently we relied on the data of bulk tensile tests for further calculations. However, based on the performed indentation measurements we could not identify any stiffness gradient at the interface between soft and hard phase, as the modulus abruptly changes.

Next peak force tapping atomic force microscopy (AFM) allows for quantitative nanomechanical mapping (QNM) at nanometer lateral resolutions.^{40–42} Consequently, this technique was applied to determine the Young's modulus and thickness of the oxide layer present on PDMS after UVO treatment. UVO-oxidized surfaces are assumed to show a vertical gradient in stiffness from the hard film to the soft substrate. Consequently, there is no distinct borderline but a declining interphase between layer and substrate.⁴³ This method enabled us to map areas of $20\ \mu\text{m} \times 20\ \mu\text{m}$ at the interphase of bulk and oxidized PDMS. For this we took an oxidized and wrinkled sample and cut a cross profile at the layer edge from the sample middle with a scalpel. Afterwards a cryo-microtome was used to smoothen the surface (subsequent roughness: $\sim 5\ \text{nm}$) followed by peakforce QNM measurements (for detailed sample preparation see Supplementary Information). The local maxima of Young's moduli for both hard and soft oxidized PDMS are found to be in the range of 90 - 100 MPa (Figure 4.2.4). The effective layer thickness of the oxide-films was determined as the intersection of a linear fit of the gradient slope (green lines in Figure 4.2.4) and the baseline of the profile (red lines). The resulting film thickness was determined to be $4.9\ \mu\text{m}$ for hard and $5.7\ \mu\text{m}$ for soft PDMS, respectively. Averaging the elastic constants allowed for estimation of the wrinkling wavelengths of the UVO oxidized samples. The averaging was performed by calculating the arithmetic mean of all Young's moduli from the layer top to its bottom. Doing so the average Young's modulus was determined to be 54.0 MPa for the oxidized layer on hard PDMS and 55.3 MPa on soft PDMS, respectively, which is compatible with the range found in literature.⁴⁴ The linear-like slope of hard PDMS is slightly steeper for soft PDMS. Most likely the less dense polymer network facilitates the ozone to penetrate deeper into the substrate. In general, UVO results in a low degree of oxidation compared to plasma treated PDMS ($0.4\ \text{GPa} < E < 7.1\ \text{GPa}$)⁴⁴ or to glass ($E \sim 73\ \text{GPa}$).⁴⁵

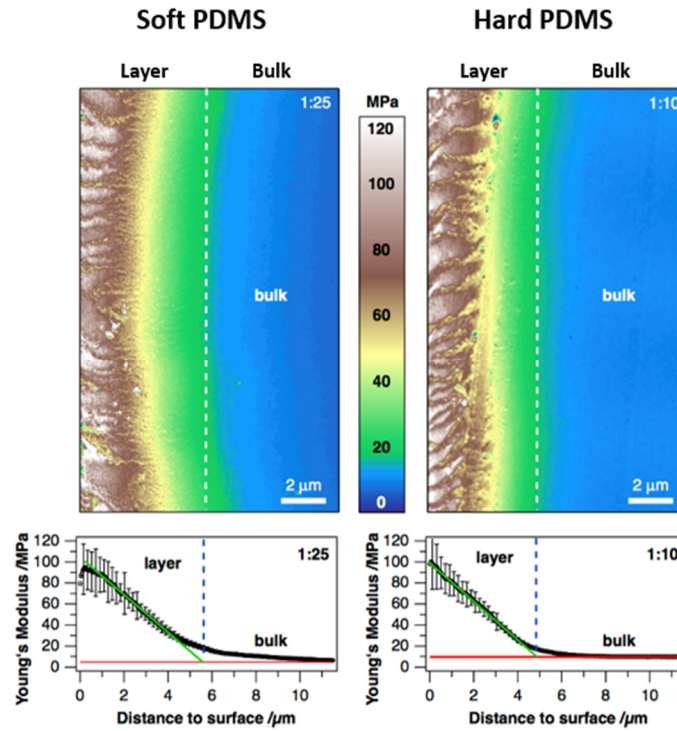


Figure 4.2.4: Peak Force QNM analysis: the terrain images are nanomechanical mappings of the Young's modulus at the bulk/oxide layer interphase of soft (left) and hard PDMS (right). Below are the according cross section profiles that were averaged over the whole image size consisting of 469 lines.

Wrinkled surfaces were analyzed using a profilometer in order to determine the wavelengths of $\lambda_{hard} = 46 \mu\text{m}$ and $\lambda_{soft} = 72 \mu\text{m}$. From the above discussed values, the theoretical wavelength for the homogeneous samples were calculated according to Equation 4.2.2 (in first order approximation) and compared to the experimentally determined wavelengths. Besides all known variables the Poisson's ratios used in Equation 4.2.3 were set to 0.5 for PDMS and 0.17 for the oxidized, glassy film. Here, theory predicts wavelengths that are 30% above our experimental results. Furthermore, we performed calculations based on a higher order approximation introduced by Jiang *et al.*⁴⁶ (Table 4.2.1). This approach also considers the effect of the applied strain on the wrinkle wavelength and amplitude as described in Equation 4.2.4. Wrinkles always evolve at the same compression, if the stiffness values of layer and substrate are not modified. Nevertheless, further compression reduces the wavelength and increases the amplitude.

$$\lambda_2 = \frac{\lambda}{(1 + \varepsilon) \left(1 + \frac{5\varepsilon(1 + \varepsilon)}{32} \right)^{1/3}} \quad (4.2.4)$$

Table 4.2.1: Comparison of experimental findings and theoretical predictions for hard and soft PDMS samples.

Sample	Young's modulus/ MPa	λ experimental/ μm	λ_1 (Eq. 4.2.2)/ μm	Deviation/ %	λ_2 (Eq. 4.2.4)/ μm	Deviation/ %
Hard PDMS	1.82 ± 0.04	46.00 ± 1.28	60.63	+31.80	38.96	-15.30
Soft PDMS	0.24 ± 0.01	72.89 ± 6.05	139.67	+91.62	89.74	-23.12

Calculations based on [Equation 4.2.4](#) yield wavelengths of 39 μm for hard and 90 μm for soft PDMS ([Table 4.2.2](#)). In comparison to the simple approximation ([Equation 4.2.2](#)), which significantly overestimates the wavelength, [Equation 4.2.4](#) yields wavelengths that are slightly reduced compared to the values determined experimentally. Thus, the measured data are in better agreement with higher order approximation. We assume that the applied strain is well-above the critical value resulting in creeping at least for the hard PDMS, causing better agreement with the Jiang's equation ([Equation 4.2.4](#)).

After this complete analysis of homogenous PDMS systems, we applied the results to the more complex embedded situation as sketched in [Figure 4.2.2a](#). [Table 4.2.2](#) compares the calculations according to Jiang and the values of elastic constants and layer thicknesses determined for the homogenous samples and experimental results performed for the composite sample. Both, hard matrix and discrete inclusion show smaller wavelengths (35 μm and 45 μm , respectively) than the equally stiff homogenous materials. However, the deviation in the hard matrix is not as pronounced as for the soft discrete inclusion. This difference is mainly caused by the complex stress/strain situation in the embedded sample: for the homogenous sample, the strain can be considered to be homogenous and directly related to the elongation of the sample in stretching direction. As defined by Hook's law stress is directly related to strain. The composite nature of the embedded sample however causes heterogeneity of the stress and strain. Neither can the local strain be inferred from the elongation of the sample, nor can stress be considered to be homogenous.

Table 4.2.2: Comparison of hard and soft PDMS calculations with the heterogeneous sample from Figure 4.2.2.

	$\lambda_{2 \text{ theoretical, homogeneous}}/\mu\text{m}$	$\lambda_{\text{heterogeneous}}/\mu\text{m}$	Deviation/%
Matrix (hard PDMS)	38.96	35.26 ± 0.96	-9.50
Discrete inclusion (soft PDMS)	89.74	45.60 ± 2.63	-49.19

To gain a more quantitative picture of the stress/strain situation, mechanical finite element modelling was performed to understand the underlying mechanisms and distortions of the composite sample compared to homogenous PDMS. In a block of homogenous hard or soft PDMS the stress upon compression is distributed homogeneously within the sample, as depicted in Figure 4.2.5a. In contrast the stress is not uniformly distributed for soft PDMS embedded in hard PDMS. The stress within the soft discrete inclusion is much lower than for the surrounding hard PDMS (Figure 4.2.5a and Figure 4.2.5c). Furthermore, the stress within the hard matrix is focused at the sides of the inclusion leading to an increase from ~ 1.6 MPa (Figure 4.2.5b) to ~ 2.4 MPa (Figure 4.2.5c). Stress and strain correlate over the Young's modulus according to $\varepsilon = \frac{\sigma}{E}$, as a consequence an increase of the applied stress leads to smaller wrinkle wavelengths when considering Equation 4.2.4. This finding fits to our experimentally found data.

Nevertheless, it does not explain the shrinkage in wavelength for the soft PDMS. We identified two other potential reasons for this observation: (1) an inhomogeneous stress distribution within the asymmetric matrix of soft PDMS (from all sides but one) causes a vertical distortion of the compressed sample, (2) changes in sample composition have however larger effects. Indentation measurements on unwrinkled composite substrates revealed differences in the Young's modulus compared to the neat samples. The soft phase is hardened from 0.65 to 0.8 MPa while at the same time the hard phase is slightly weakened from 2.9 to 2.5 MPa. These changes are most likely caused by diffusion of the Pt-catalyst from the hard into the soft phase either while gelation at room temperature and during thermal curing, respectively. In combination with the increase of stress within the matrix that is indicated by simulations the drastic changes in wavelength for both matrix and inner part can be explained.

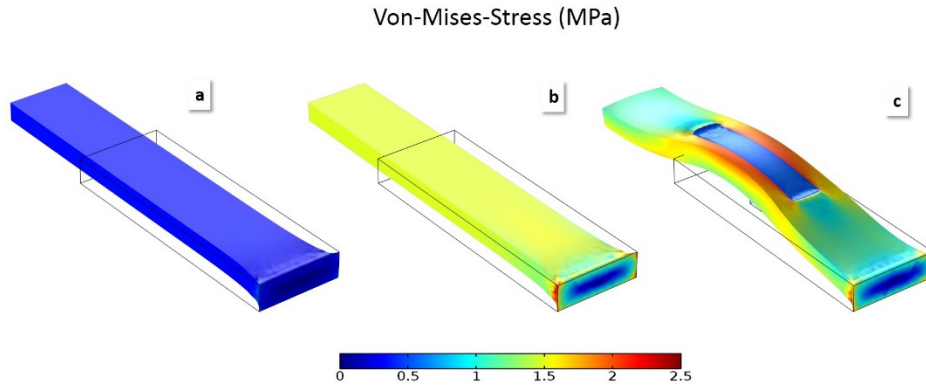


Figure 4.2.5: Mechanical simulations of neat, soft (a) respectively hard PDMS block (b) and a composite of soft block in a hard matrix (b). In all cases the initial dimensions of the outer block were set to $30 \times 10 \times 3 \text{ mm}^3$ indicated by the black box, in (c) the inner block is sized $10 \times 5 \times 1.5 \text{ mm}^3$, positioned lateral in the middle of the outer block, vertical on the upper side of it. The applied strain ε is set for all simulations to 50%. Von-Mises-stress distribution was modeled using COMSOL multiphysics with the same parameters as before except ν_s , which was set to 0.499.

Defect formation in gradient structures

The observed effects at the border between discrete inclusion and surrounding revealed that defects preferentially nucleate in close proximity to the mechanical transition. In order to study the underlying processes in more detail we substituted the discrete soft inclusion with a lateral, defined gradient in Young's modulus³³ and embedded it as before in a matrix of hard PDMS. Thus, the crossover from inclusion to matrix within this composite material is no longer at a fixed ratio between two stiffness values but changes gradually along the substrate. The initial Young's modulus ratio is 1:5 and it decreases to a ratio of 1:1 at the hard end.

At the interface bearing a Young's modulus ratio of 1:1 a similar wrinkle wavelength developed in both areas and no line-defects were observed (see Figure 4.2.6a). For the other cases, we defined a defect density by counting the number of waves in both areas from one to the next defect (Equation 4.2.5). Dividing the counted number derived from the gradient by this of the matrix gives a defect density ratio σ_d defined by the number of waves in one repetitive unit n_i for the gradient and n_m for the matrix.

$$\sigma_d = \frac{n_i}{n_m} \quad (4.2.5)$$

So at the center of the composite material the defect density from microscopy images is 0.83 (5 gradient waves divided by 6 matrix waves), with a measured modulus ratio of 1:2 (Figure 4.2.6b). The measured difference in wavelength by profilometry at the sample middle is as high as $43 \pm 3 \mu\text{m}$ to $56 \pm 2 \mu\text{m}$, giving an average ratio of 0.77, so slightly lower. For the soft end however the defect density was determined to be 0.66 (Figure 4.2.6c) compared to 0.67 for profilometry, so in perfect agreement. These values are directly correlated with the change in wavelength and consequently the branching period. Furthermore, a drastic but uniform change of wavelength again indicates that no stiffness gradient perpendicular to the interface is present. Using numerical simulations for samples with a step-like transition function recover the same features and pinning of the line defects to the interface as observed experimentally. Figure 4.2.6d–f show patterns obtained by solving a generalized version of the Swift-Hohenberg equation⁴⁷ that includes both anisotropy⁴⁸ and a spatially periodic inhomogeneity (Equation 4.2.6)⁴⁹ using the pseudo-spectral method and considering a flat surface with small noise as initial condition.

$$\begin{aligned} \partial_t u = & [\varepsilon - (q^2(y) + \Delta)^2]u - W\partial_x^2\partial_y^2u - c\partial_y^4u - u^3 - 2(\partial_y u)\partial_y[q^2(y)] \\ & - u\partial_y^2[q^2(y)] \end{aligned} \quad (4.2.6)$$

u mimics the local height of the surface, ε is the dimensionless strain and the parameters W and c control the anisotropy of the system. We chose $W = 1$ and $c = 0.5$. The spatially varying “natural” wavelength was set to be $2\pi/q(y)$. Perfectly aligned straight wrinkles (Figure 4.2.6d) are obtained for constant natural wavenumber q (Figure 4.2.6g). For a steep transition in wavenumber (Figure 4.2.6h) branching defects emerge (Figure 4.2.6e). The periodicity of these line-defects is further decreased resulting in higher branching density (Figure 4.2.6f) for increased values of the wavenumber jump (Figure 4.2.6i). Here, all the branching-defects are stationary and emerge spontaneously along the contact line between the two domains with different preferred wavenumbers. Those correspond well to the ratios determined experimentally at the middle and the soft end of the gradient, respectively.

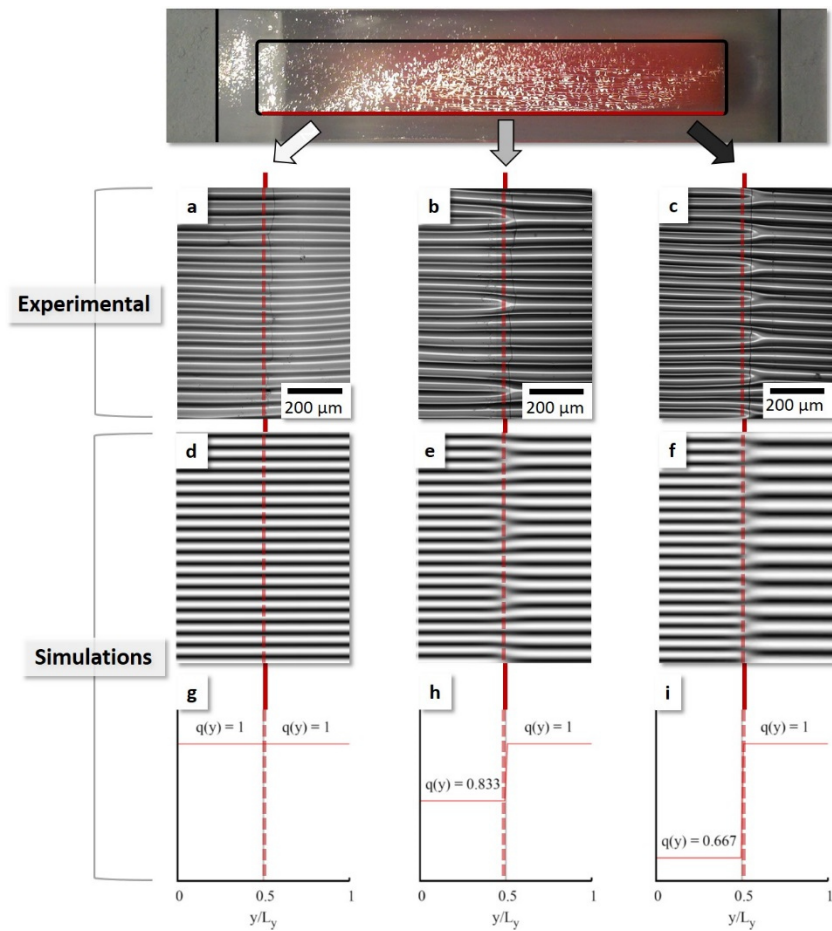


Figure 4.2.6: Branching points ordered along the gradient borderline with a jump in elasticity and wavenumber, respectively; (a - c) show experimental results, (d - f) the according simulations that are based on predetermined step-functions (g - i).

The presented method has high potential for the systematic production of gradients and so not only for the aimed generation and understanding of ordered line branching structures. Beyond this the presented results might find application within the field of particle alignment. Controlled induction of line-defects can be used to break the symmetry within particle assemblies by generating Y-shaped particle lines. Furthermore, microfluidics might benefit from well-defined size- and angle-tunable channel junctions.

4.2.4. Conclusion

The objective of this work was the investigation of line defects observed in wrinkled substrates. Composite PDMS samples consisting of two covalently attached PDMS phases with different mechanical properties were prepared, wrinkled and analyzed. The predetermined change of substrate stiffness along the phase border resulted in different wavelengths caused by the buckling instability and so reinforced the wrinkles to branch more frequently here. Consequently, the branches had a main orientation at the border, pointing from the soft side with large waves to the hard side, where shorter waves were found. The gradient sample showed an interesting behavior of oriented, patterned defects. We concluded that the stiffness difference of both substrate phases did match a value here that induced a whole-number ratio of the buckling instability. This was not observed in the sample with discrete, soft PDMS in the inclusion. In order to confront empirical wrinkling theories with our results, we had to measure h_f and E_f of the UVO-oxidized layer. *Via* Peak Force QNM we gained values of $h_f = 4.9 - 5.7 \mu\text{m}$ and $E_f = 54.0 \text{ MPa}$ and 55.3 MPa , respectively. Wavelengths and amplitudes of the wrinkles were determined *via* profilometry resulting in $46 \mu\text{m}$ and $73 \mu\text{m}$ for the homogeneous samples, $35 \mu\text{m}$ and $45 \mu\text{m}$ in the heterogeneous system with just hard and soft PDMS respectively $51 \mu\text{m}$ and $63 \mu\text{m}$ in the gradient system. A mechanical stress simulation revealed an increase in the surface stress distribution around the embedded discrete inclusion that induces a wave shortage. In the wider dimensioned gradient sample this problem was less pronounced. Summarized the system presented in this paper has a high potential for ordering defects in a patterned way and beyond to keep the adjacent wrinkled areas defect-free. Our findings increase the understanding of the formation of defects in controlled wrinkling systems. One application that may use line defects of adjustable number and direction is the generation of size- and angle-tunable channel junctions for microfluidic devices. Two waves terminating into one act as the micro-channel junction that may be sealed on top with another layer of PDMS or glass. Another application might be the organization of nanoparticles onto well-defined, equidistant Y-shaped templates. Stamping these assemblies onto a flat substrate creates lines of particles that split on predefined positions. This might be useful for light management in nanophotonics.

4.2.5. Acknowledgements

We thank M. Lehmann for Peak Force QNM measurements as well as M. P. Neubauer for indentation measurements. Also, we thank the European Research Council for financing this work within the Starting Grant Project ERC-2012-StG 306686 METAMECH. M. Tebbe was supported by the Elite Network Bavaria in the frame of the Elite Study Program “Macromolecular Science” and funded *via* a grant for PhD candidates according to Bavarian elite promotion law (BayEFG).

4.2.6. References

- [1] P. Yamato, B. J. P. Kaus, F. Mouthereau and S. Castelltort, *Geology* **2011**, *39*, 815–818, “Dynamic constraints on the crustal-scale rheology of the Zagros fold belt, Iran”.
- [2] B. Prüm, H. Florian Bohn, R. Seidel, S. Rubach and T. Speck, *Acta Biomater.* **2013**, *9*, 6360–6368, “Plant surfaces with cuticular folds and their replicas: Influence of microstructuring and surface chemistry on the attachment of a leaf beetle”.
- [3] C.-D. Reuther, Springer Publishing, Berlin, Heidelberg, **2012**, „Grundlagen der Tektonik“.
- [4] A. Mohamed, Ludwig-Maximilians-Universität München, München, **2003**, „Die Krusten der Ränder der Fayoum-Depression“.
- [5] M. Berneburg, H. Plettenberg and J. Krutmann, *Photodermatol., Photoimmunol. Photomed.* **2000**, *16*, 239–244. “Photoaging of human skin”.
- [6] H. Vandeparre, M. Piñeirua, F. Brau, B. Roman, J. Bico, C. Gay, W. Bao, C. N. Lau, P. M. Reis and P. Damman, *Phys. Rev. Lett.* **2011**, *106*, 224301, “Wrinkling Hierarchy in Constrained Thin Sheets from Suspended Graphene to Curtains”.
- [7] J. Genzer and J. Groenewold, *Soft Matter* **2006**, *2*, 310–323, “Soft matter with hard skin: From skin wrinkles to templating and material characterization”.
- [8] C. Jiang, S. Singamaneni, E. Merrick and V. V. Tsukruk, *Nano Lett.* **2006**, *6*, 2254–2259, “Complex Buckling Instability Patterns of Nanomembranes with Encapsulated Gold Nanoparticle Arrays”.

-
- [9] D.-Y. Khang, J. A. Rogers and H. H. Lee,
Adv. Funct. Mater. **2009**, *19*, 1526–1536,
“Mechanical Buckling: Mechanics, Metrology, and Stretchable Electronics”.
- [10] A. Schweikart and A. Fery,
Microchim. Acta **2009**, *165*, 249–263,
“Controlled wrinkling as a novel method for the fabrication of patterned surfaces”.
- [11] S. Singamaneni and V. V. Tsukruk,
Soft Matter **2010**, *6*, 5681–5692,
“Buckling instabilities in periodic composite polymeric materials”.
- [12] J. Y. Chung, A. J. Nolte and C. M. Stafford,
Adv. Mater. **2011**, *23*, 349–368,
“Surface Wrinkling: A Versatile Platform for Measuring Thin-Film Properties”.
- [13] M. Pretzl, A. Schweikart, C. Hanske, A. Chiche, U. Zettl, A. Horn, A. Böker and A. Fery,
Langmuir **2008**, *24*, 12748–12753,
“A Lithography-Free Pathway for Chemical Microstructuring of Macromolecules from Aqueous Solution Based on Wrinkling”.
- [14] F. A. Bayley, J. L. Liao, P. N. Stavrinou, A. Chiche and J. T. Cabral,
Soft Matter **2014**, *10*, 1155–1166,
“Wavefront kinetics of plasma oxidation of polydimethylsiloxane: limits for sub- μm wrinkling”.
- [15] K. Efimenko, M. Rackaitis, E. Manias, A. Vaziri, L. Mahadevan and J. Genzer,
Nat. Mater. **2005**, *4*, 293–297,
“Nested self-similar wrinkling patterns in skins”.
- [16] C. J. Rand, R. Sweeney, M. Morrissey, L. Hazel and A. J. Crosby,
Soft Matter **2008**, *4*, 1805–1807,
“Fracture-induced alignment of surface wrinkles”.
- [17] J. Rodríguez-Hernández and A. Del Campo,
J. Appl. Polym. Sci. **2015**, *132*, 41863,
“Fabrication of hierarchical wrinkled morphologies through sequential UVO treatments”.

- [18] M. Watanabe and K. Mizukami, *Macromolecules* **2012**, *45*, 7128–7134, “Well-Ordered Wrinkling Patterns on Chemically Oxidized Poly(dimethylsiloxane) Surfaces”.
- [19] H. Vandeparre, J. Léopoldès, C. Poulard, S. Desprez, G. Derue, C. Gay and P. Damman, *Phys. Rev. Lett.* **2007**, *99*, 188302, “Slippery or Sticky Boundary Conditions: Control of Wrinkling in Metal-Capped Thin Polymer Films by Selective Adhesion to Substrates”.
- [20] D. U. Ahn, Z. Wang, R. Yang and Y. Ding, *Soft Matter* **2010**, *6*, 4900–4907, “Hierarchical polymer patterns driven by capillary instabilities at mobile and corrugated polymer–polymer interfaces”.
- [21] G. Miquelard-Garnier, A. B. Croll, C. S. Davis and A. J. Crosby, *Soft Matter* **2010**, *6*, 5789–5794, “Contact-line mechanics for pattern control”.
- [22] Y. Xuan, X. Guo, Y. Cui, C. Yuan, H. Ge, B. Cui and Y. Chen, *Soft Matter* **2012**, *8*, 9603–9609, “Crack-free controlled wrinkling of a bilayer film with a gradient interface”.
- [23] W. P. Lee and A. F. Routh, *Langmuir* **2004**, *20*, 9885–9888, “Why Do Drying Films Crack?”.
- [24] S. Frank, U. A. Handge, S. Olliges and R. Spolenak, *Acta Mater.* **2009**, *57*, 1442–1453, “The relationship between thin film fragmentation and buckle formation: Synchrotron-based in situ studies and two-dimensional stress analysis”.
- [25] J. Y. Chung, J.-H. Lee, K. L. Beers and C. M. Stafford, *Nano Lett.* **2011**, *11*, 3361–3365, “Stiffness, Strength, and Ductility of Nanoscale Thin Films and Membranes: A Combined Wrinkling–Cracking Methodology”.

-
- [26] J. Gao, K. Pei, T. Sun, Y. Wang, L. Zhang, W. Peng, Q. Lin, M. Giersig, K. Kempa, Z. Ren and Y. Wang,
Small **2013**, *9*, 732,
“Metallic Nanowire Networks: Transparent Nanowire Network Electrode for Textured Semiconductors”.
- [27] B. Han, K. Pei, Y. Huang, X. Zhang, Q. Rong, Q. Lin, Y. Guo, T. Sun, C. Guo, D. Carnahan, M. Giersig, Y. Wang, J. Gao, Z. Ren and K. Kempa,
Adv. Mater. **2014**, *26*, 873–877,
“Uniform Self-Forming Metallic Network as a High-Performance Transparent Conductive Electrode”.
- [28] N. Stoop, R. Lagrange, D. Terwagne, P. M. Reis and J. Dunkel,
Nat. Mater. **2015**, *14*, 337–342,
“Curvature-induced symmetry breaking determines elastic surface patterns”.
- [29] A. Ahmadvand and S. Golmohammadi,
Opt. Commun. **2014**, *310*, 1–11,
“Comprehensive investigation of noble metal nanoparticles shape, size and material on the optical response of optimal plasmonic Y-splitter waveguides”.
- [30] C. P. Ody, C. N. Baroud and E. de Langre,
J. Colloid Interface Sci. **2007**, *308*, 231–238,
“Transport of wetting liquid plugs in bifurcating microfluidic channels”.
- [31] N. Bowden, W. T. S. Huck, K. E. Paul and G. M. Whitesides,
Appl. Phys. Lett. **1999**, *75*, 2557–2559,
“The controlled formation of ordered, sinusoidal structures by plasma oxidation of an elastomeric polymer”.
- [32] R. Huang,
J. Mech. Phys. Solids **2005**, *53*, 63–89,
“Kinetic wrinkling of an elastic film on a viscoelastic substrate”.
- [33] K. U. Claussen, M. Tebbe, R. Giesa, A. Schweikart, A. Fery and H.-W. Schmidt,
RSC Adv. **2012**, *2*, 10185–10188,
“Towards tailored topography: facile preparation of surface-wrinkled gradient poly(dimethyl siloxane) with continuously changing wavelength”.

- [34] P. Ball,
Oxford University Press, Oxford, **2009**,
“Branches”.
- [35] Z. Li, S. Zhang, P. Zhang, D. Yang, G. Jin and H. Ma,
Polym. Adv. Technol. **2012**, *23*, 1240–1245,
“Surface initiated polymerization from integrated poly(dimethylsiloxane) enables crack-free large area wrinkle formation”.
- [36] C. M. Stafford, C. Harrison, K. L. Beers, A. Karim, E. J. Amis, M. R. VanLandingham, H.-C. Kim, W. Volksen, R. D. Miller and E. E. Simonyi,
Nat. Mater. **2004**, *3*, 545–550,
“A buckling-based metrology for measuring the elastic moduli of polymeric thin films”.
- [37] A. Mata, A. Fleischman and S. Roy,
Biomed. Microdevices **2005**, *7*, 281–293,
“Characterization of Polydimethylsiloxane (PDMS) Properties for Biomedical Micro/Nanosystems”.
- [38] C. C. White, M. R. VanLandingham, P. L. Drzal, N. K. Chang and S. H. Chang,
J. Polym. Sci., Part B: Polym. Phys. **2005**, *43*, 1812–1824,
“Viscoelastic characterization of polymers using instrumented indentation. II. Dynamic testing”.
- [39] J.-H. Seo, K. Sakai and N. Yui,
Acta Biomater. **2013**, *9*, 5493–5501,
“Adsorption state of fibronectin on poly(dimethylsiloxane) surfaces with varied stiffness can dominate adhesion density of fibroblasts”.
- [40] B. Foster,
Am. Lab. **2012**, *42*, 215–221,
“New Atomic Force Microscopy (AFM) Approaches Life Sciences Gently, Quantitatively, and Correlatively”.
- [41] P. Trtik, J. Kaufmann and U. Volz,
Cem. Concr. Res. **2012**, *42*, 215–221,
“On the use of peak-force tapping atomic force microscopy for quantification of the local elastic modulus in hardened cement paste”.

-
- [42] C. Kuttner, M. Tebbe, H. Schlaad, I. Burgert and A. Fery, *ACS Appl. Mater. Interfaces* **2012**, *4*, 3484–3492, “Photochemical Synthesis of Polymeric Fiber Coatings and Their Embedding in Matrix Material: Morphology and Nanomechanical Properties at the Fiber-Matrix Interface”.
- [43] C. Kuttner, A. Hanisch, H. Schmalz, M. Eder, H. Schlaad, I. Burgert and A. Fery, *ACS Appl. Mater. Interfaces* **2013**, *5*, 2469–2478, “Influence of the Polymeric Interphase Design on the Interfacial Properties of (Fiber-Reinforced) Composites”.
- [44] S. p. Béfahy, P. Lipnik, T. Pardoën, C. Nascimento, B. Patris, P. Bertrand and S. Yunus, *Langmuir* **2009**, *26*, 3372–3375, “Thickness and Elastic Modulus of Plasma Treated PDMS Silica-like Surface Layer”.
- [45] S. Inaba, S. Fujino and K. Morinaga, *J. Am. Ceram. Soc.* **1999**, *82*, 3501–3507, “Young's Modulus and Compositional Parameters of Oxide Glasses”.
- [46] H. Jiang, D.-Y. Khang, J. Song, Y. Sun, Y. Huang and J. A. Rogers, *Proc. Natl. Acad. Sci. U. S. A.* **2007**, *104*, 15607–15612, “Finite deformation mechanics in buckled thin films on compliant supports”.
- [47] J. Swift and P. Hohenberg, *Phys. Rev. A* **1977**, *15*, 319–328, “Hydrodynamic fluctuations at the convective instability”.
- [48] W. Pesch and L. Kramer, *Z. Phys. B* **1986**, *63*, 121–130, “Nonlinear analysis of spatial structures in two-dimensional anisotropic pattern forming systems”.
- [49] B. Kaoui, A. Guckenberger, F. Ziebert, A. Krekhov and W. Zimmermann, *ArXiv* **2015**: 1503.04234. “Coexistence of Stable Branched Patterns in Anisotropic Inhomogeneous Systems”.

4.2.7. Supplementary Information

4.2.7.1. Experimental

PDMS solution

The substrates were prepared with commercially available Sylgard 184 PDMS by Dow Corning Ltd, Midland, USA. A well-dispersed and degassed mixture of 20 g pre-polymer and 2 g curing agent was used for 1:10 ratio as well as 25 g pre-polymer with 1 g curing agent for 1:25 ratio.

Homogeneous samples

1:10 and 1:25 PDMS were cast each in a 10 x 10 cm PS-mold, set for 24 h at RT (48 h, respectively) and subsequently cured for 4 h at 80 °C. Stripes of 4.5 cm x 1 cm x 0.16 cm (resp. 0.17 cm) were cut out, ultrasonicated in Milli-Q H₂O for 10 min and dried with N₂.

1:25 Inclusion in 1:10 matrix

A 1:10 stripe from the homogeneous sample preparation was punched out in the size of 1 cm x 0.5 cm right in the middle. The hole was filled with 1:25 PDMS solution just to level out with the surrounding matrix and allowed to set for 48 h at RT. Afterwards another 1:10 layer of 0.1 cm thickness was cast on top, set for 24 h at RT and then cured at 80 °C for 5 h. Eventually the stripe was ultrasonicated in Milli-Q H₂O for 10 min and dried with N₂.

Gradient Inclusion in 1:10 matrix

1:10 PDMS was cast into a 14 cm diameter glass petri dish to fill it up for 2 mm. It was allowed to set for 24 h. A 7 cm x 1 cm hole was punched out from the middle and filled with a slightly modified gradient of Claussen *et al.*¹ with halved casting speed to reach a doubled layer thickness. After setting at RT for 48 h another layer of 1:10 was cast on top of gradient and matrix with a height of 1 mm. It was allowed to set for 24 h at RT followed by curing at 80 °C for 4 h. Afterwards the gradient with surrounding matrix was cut out to give a sample of 11 cm overall length and 3 cm overall width, so 2 cm of protruding matrix on the long sides respectively 1 cm on the short sides. The sample was ultrasonicated in Milli-Q H₂O for 10 min and dried with N₂.

Wrinkle generation

The stripes from above described preparation were attached to a custom-made stretching device, strained by 50% and placed in a UV/Ozone (UVO)-cleaner (Novascan PSD-UV 8, Novascan Technologies, Ames, USA) for 90 min. All samples were oxidized at their contact face with the glass petri dish. This was to ensure a levelled interface of inclusion and matrix and for reproducibility. The stress then was released instantaneously, and wrinkles did form immediately. For the wrinkling process all samples were oxidized at their bottom sides.

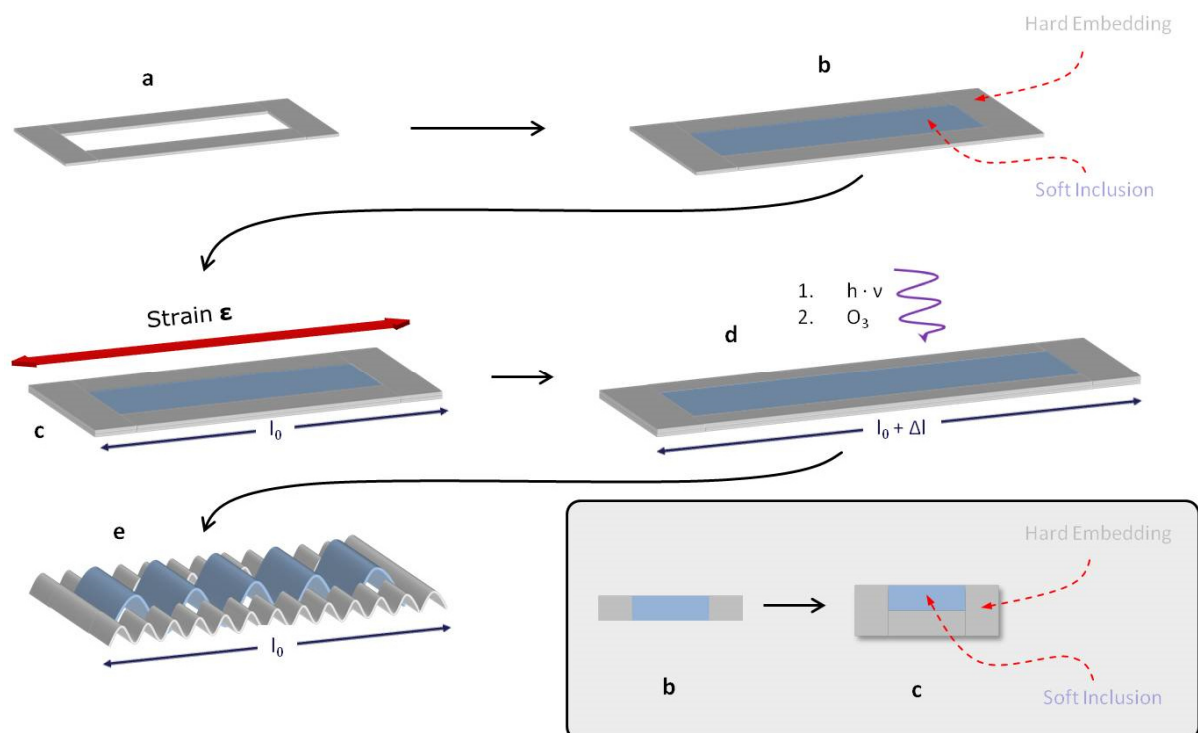


Figure 4.2.7: Heterogeneous sample preparation for a soft inclusion into a hard matrix. (a) RT-set, hard PDMS becomes punched out and filled with soft PDMS (b), followed by a cover layer over hard and soft (b \rightarrow c). The sample then is strained (c), UVO-oxidized (d) and strain-released (e) to form wrinkles.

Characterization

Three different qualitative and quantitative methods were used for characterizing the formed morphologies as well as mechanical properties, namely reflected light microscopy, profilometry and Peak Force QNM.

Optical Microscopy

Optical Microscopy was performed with Axiovert 200, Carl Zeiss GmbH (Jena, Germany), equipped with a Plan-Apochromat 10x / 0.25 lens, an Axiocam ERc 5s computer-controlled camera and AxioVision V. 4.8.2.0 (2010, Carl Zeiss MicroImaging GmbH, Jena, Germany) analysis software.

Profilometry

Measurements were done with a Dektak 150 Profilometer from Veeco (Plainview, USA) with following boundary conditions: stylus force = 1 mg for 1:10 and 0.05 mg for 1:25, a stylus radius of 2.5 μm (N-Lite sensor) and a scan length of 500 μm for each measurement.

Peak-Force QNM

Layer thickness and nanomechanical measurements were performed with a Dimension V Icon AFM (Bruker, Karlsruhe, Germany) with Peak-Force QNM Software on a 20 μm x 20 μm area with 512 samples / line, Peak-Force set point = 0.15 V, driving amplitude = 150 V and tip radius = 5 nm.

Simulations

Wrinkling and branching property simulations were performed by solving a modified Swift-Hohenberg-Equation with initial surface noise.

4.2.7.2. Microscopy setup for in-situ analysis

In-situ measurements were accomplished with a custom-made stretching setup that allows control over strain and relaxation speed of the sample, respectively. It is schematically depicted in Figure 4.2.8. In order to ensure that a fixed section of the sample's surface may be observable throughout all the relaxation process, both ends of the clamping device were designed to move uniformly. This requires thoroughly focusing on the sample middle. An exemplary recorded video is also available within the ESI.

During the relaxation process the speed is set to 6.1 mm/min at an initial clamping length of 15 mm respectively 22.5 mm for the stretched state ($\epsilon = 50\%$). The samples were not strain released back to the initial length to avoid cracking of the film or bulging of the sample. For the latter also the focus would have been lost.

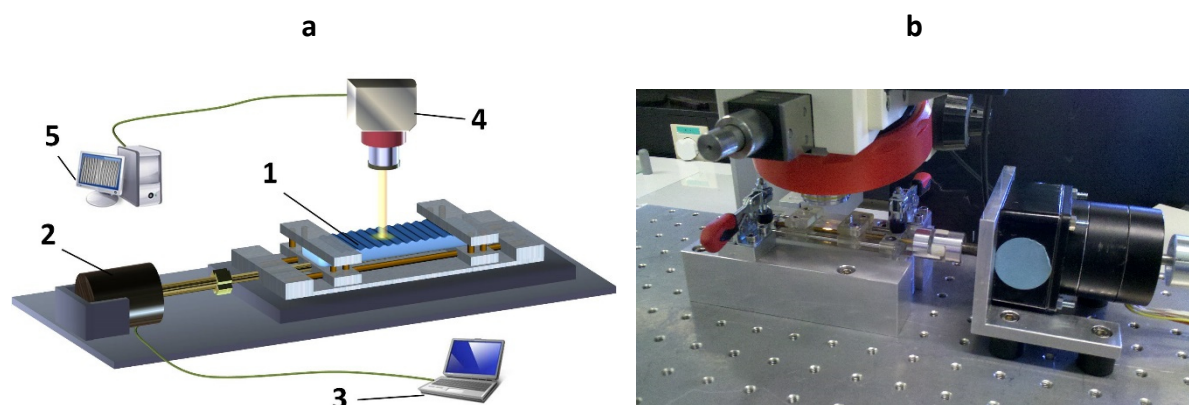


Figure 4.2.8: Reflected Light Microscopy setup for in-situ observations of the wrinkle formation schematically (a) and real (b). (1) custom-made stretching device with UVO-oxidized sample, (2) step-motor to adjust the relaxation speed, (3) computer control for step-motor, (4) reflected light microscope with attached video camera, (5) computer control for microscope and camera.

In most cases impurities on the PDMS surface were used to focus. Only in few cases it was possible without.

4.2.7.3. Peak-Force QNM

For Peak-Force the UVO-oxidized and wrinkled samples were prepared in the following way: In step 1 a cross profile at the layer edge was cut from the sample middle with a scalpel. For step 2 a cryo-mikrotome was used to smoothen surface (subsequent roughness: ~ 5 nm). In the final step 3 the surface was analyzed with Peak-Force QNM and optical microscopy.

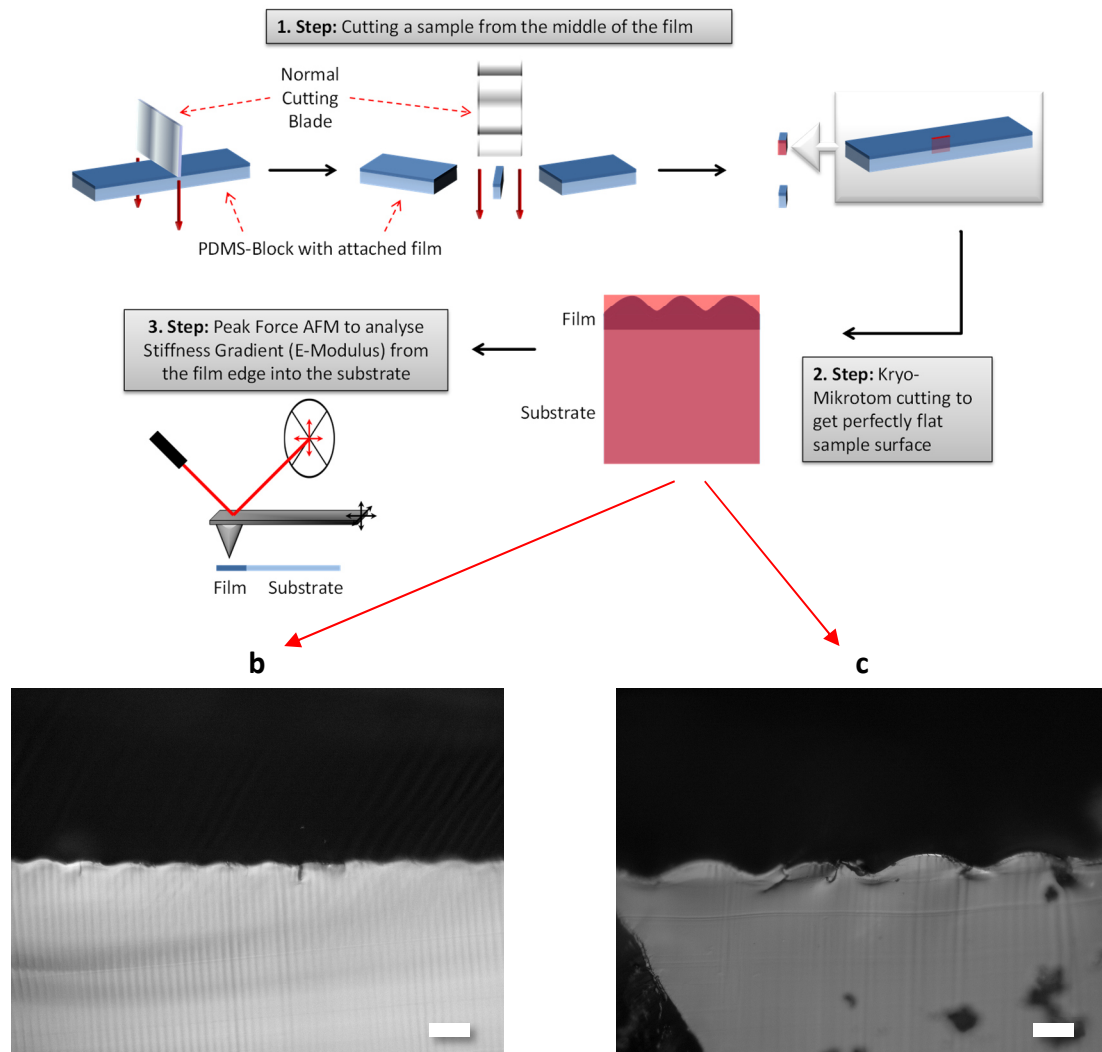


Figure 4.2.9: (a) Preparation of a UVO-oxidized and wrinkled sample for Peak-Force QNM analysis. (b) and (c): Optical microscopy images of the cross profiles from hard (b) and soft PDMS (c); scale bar length is 100 μm .

4.2.7.4. Wrinkling with a lateral gradient

As for pure PDMS and the composite sample we also performed profilometry measurements to compare given Equations 4.2.1 – 4.2.4 with experimental data. The wrinkles show an exponential increase that can be explained by the process of gradient preparation where hard and soft PDMS tend to diffuse into each other.¹ The results fit well to theoretical predictions, especially when compared to the samples with a neat soft inclusion. Figure 4.2.10 shows the results of wavelength and amplitude variation from the gradient's hard end (left, 1 cm) to its soft end (right, 6 cm). A slight increase of λ and A is recognizable that were fitted with exponential growth functions.

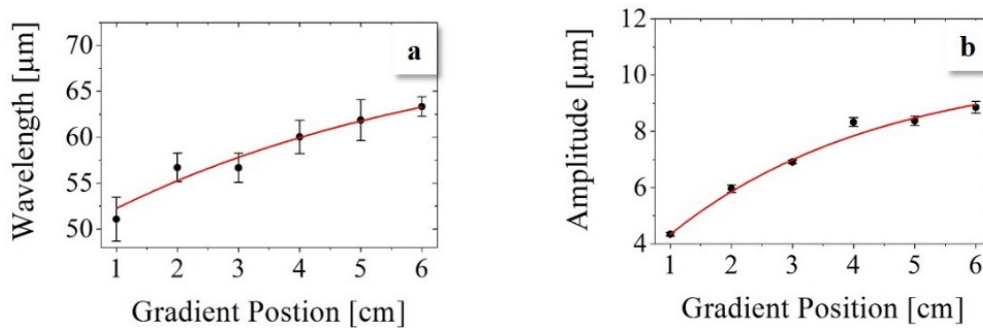


Figure 4.2.10: Modification of λ (a) and A (b) along the gradient.

Table 4.2.3: Comparison of theoretical values for λ with the gradient's hard left and soft end right, respectively; the applied strain is $\epsilon = 20\%$.

Gradient Position	Theoretical λ	λ on Gradient	Deviation
	/μm	/μm	/%
1 cm	54.73	51.07 ± 2.40	- 6.69
6 cm	103.40	63.34 ± 1.07	- 38.74

Those slighter deviations can be explained with the different sizes of the samples, as the gradient has distinctly larger dimensions of 90 mm x 40 mm x 3 mm compared to 30 mm x 10 mm x 3 mm for the two-phase-system. It is also the reason, why only 20% strain were applied: Strain and stress within the sample are connected over $= \frac{\epsilon}{A}$, where A is larger in the gradient than in the composite (12 mm² respectively 2.7 mm²). A strain of 50% would therefore have led to a rupture of the sample.

4.2.7.5. *Double gradient along the soft-to-hard-crossover*

In contrast to distinct interfaces as shown in the paper itself a few number of sample areas showed diffuse transition between both composite materials, where the transition spreads over several 100 μm . This is due to a partially tilted cut during the sample preparation. Soft and hard PDMS may flow underneath each other and create a blurred stiffness interface. It generates a second gradient, however rectangular to the first and in a much shorter length scale. It features interesting effects, as within these regions the line-defect formation between hard and soft phase took place in a quantized manner, meaning defects did not occur randomly along the short gradient but in bands lateral to the wrinkling direction ([Figure 4.2.11a](#)). We also employed numerical simulations on this behavior, where $q(y)$ was used to generate an imposed wavenumber ([Figure 4.2.11c](#)) that increases linearly along the short gradient. Simulations revealed a similar behavior in branching ([Figure 4.2.11b](#)), which allowed only few, quantized wavelengths for different gradient slopes and heights. Thus, simulations performed for distinct jumps in the wavelength are in good agreement with the experimentally determined values with slight deviations in the branch positions and step widths.

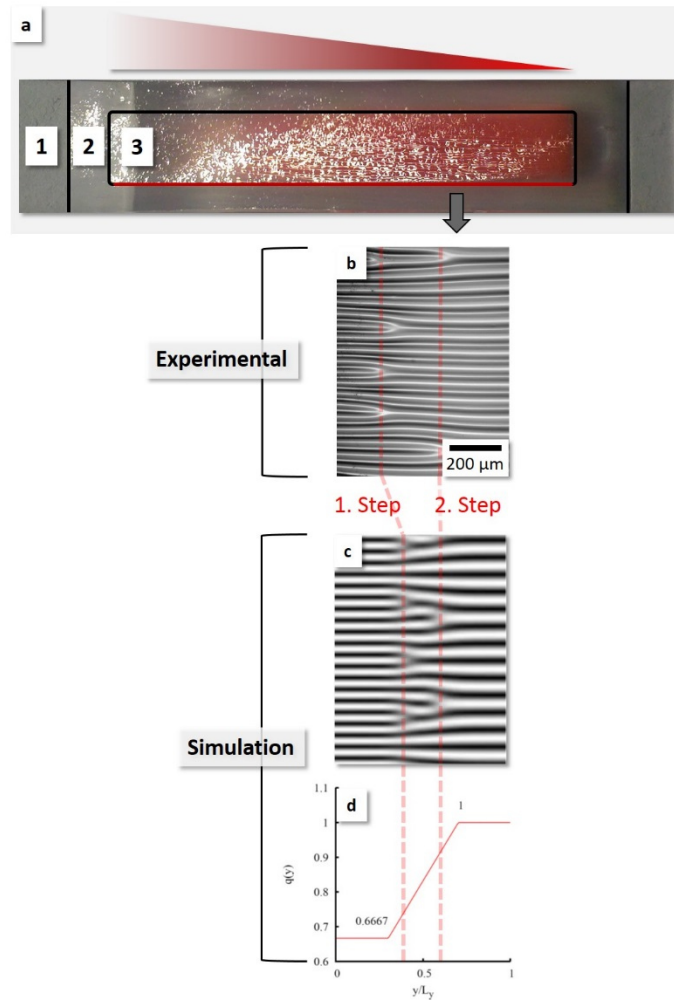


Figure 4.2.11: (a) Photo of the gradient sample; (1) shows the unwrinkled matrix, where the sample was clamped for stretching, (2) the wrinkled matrix and (3) the gradient with a stiffness decrease from left (translucent) to right (red dyed). (b) Microscopy image of disordered branching over two steps, (c) numerical simulation (d) with a predetermined linear increase of $q(y)$ over a given gradient length L_y .

4.2.7.6. Specific Wrinkling

A side aspect of heterogeneous substrates is the ability of specifically wrinkling just one of the participating PDMS phases. According to $\varepsilon_c = \frac{\sigma_c}{\bar{E}_f} = \frac{1}{4} \left(\frac{3\bar{E}_s}{\bar{E}_f} \right)^{2/3}$ the Young's Moduli of layer and substrate influence the critical strain required for wrinkling. Providing that both hard and soft PDMS get oxidized equally and so \bar{E}_f is constant, their difference in \bar{E}_s can be measured directly. In this experiment the strain was set to $\varepsilon = 10\%$, with plain strain moduli of the soft substrate being \bar{E}_{hS} : 0.3 MPa and for the hard substrate \bar{E}_{hS} : 2.5 MPa. The film's modulus \bar{E}_f

had to be determined in a subsequent measurement and was roughly estimated to 25 MPa. According to this a hard substrate starts to wrinkle not before $\varepsilon_c = 10.9\%$, while the soft one buckles already at a critical strain ε_c of 2.5%. We found the expected wrinkling behavior (Figure 4.2.12), with a well-defined crossover from the hard, unwrinkled to the soft and wrinkled PDMS. The surface corrugations at the boundary of soft and hard substrates induce a stress-field in the hard elastomer. Initial waves form close to the crossover, though they completely flatten out in a range of $\sim 50 \mu\text{m}$. The result is a chemically homogeneous surface, which is in parts mechanically modified.

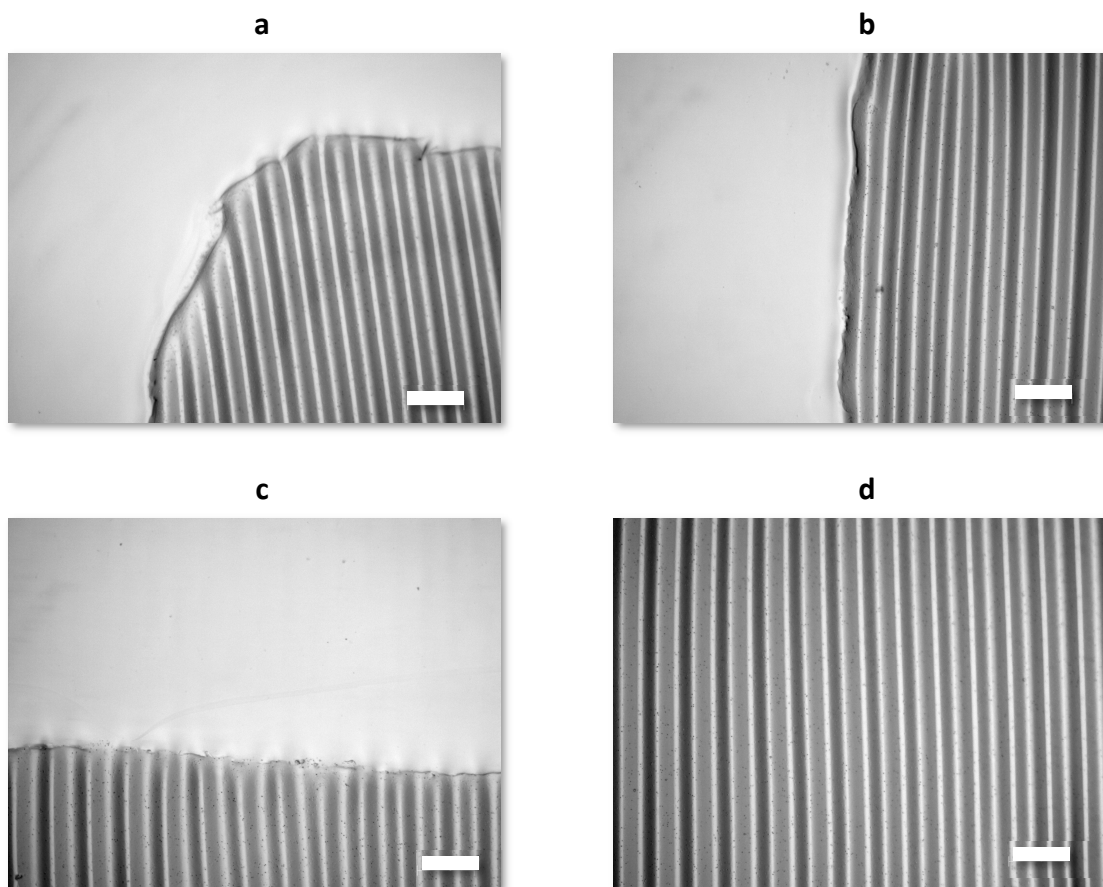


Figure 4.2.12: Wrinkled soft inclusion surrounded by an unwrinkled hard matrix; at the inclusion edge (a), the vertical and horizontal boundary lines (b and c) and inside the inclusion (d) with an average wavelength of $65 \mu\text{m}$ and an amplitude of $3 \mu\text{m}$; scale bar length is $100 \mu\text{m}$.

4.2.7.7. References

- [1] K. U. Claussen, M. Tebbe, R. Giesa, A. Schweikart, A. Fery and H.-W. Schmidt, *RSC Adv.* **2012**, 2, 10185–10188, *“Towards tailored topography: facile preparation of surface-wrinkled gradient poly(dimethyl siloxane) with continuously changing wavelength”*.

4.3. Controlled wrinkling of gradient metal films

Andreas E. Schedl,^a Christian Neuber,^a Andreas Fery^b and Hans-Werner Schmidt^{*a}

a) Macromolecular Chemistry I, Bavarian Polymer Institute (BPI) and Bayreuth Center for Colloids and Interfaces (BZKG), University of Bayreuth, 95440 Bayreuth, Germany

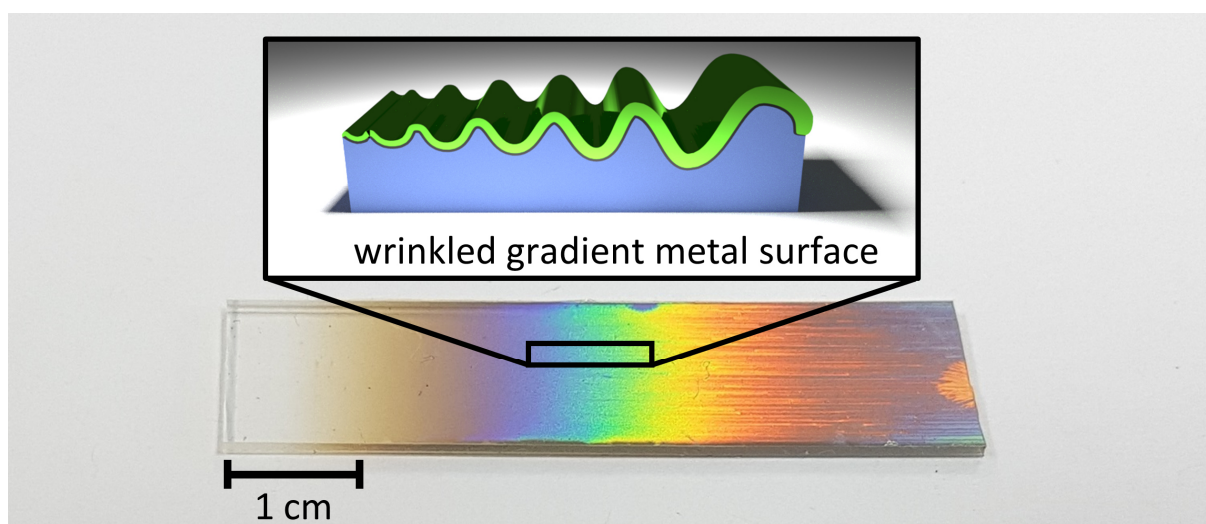
b) Institute of Physical Chemistry and Polymer Physics, Leibniz Institute of Polymer Research Dresden e.V. and Chair for Physical Chemistry of Polymeric Materials, Technical University Dresden, 01069 Dresden, Germany

The results of this chapter have been published as full paper article in

Langmuir **2018**, *34*, 14249-14253.

Reprinted with permission from *Langmuir* **2018**, *34*, 14249-14253. Copyright 2018 American Chemical Society.

DOI: 10.1021/acs.langmuir.8b03123



Scheme of a wrinkled gradient indium film on top of PDMS substrate. The linear gradient in wavelength and amplitude results from controlled wrinkling of an indium film with a linear gradient in film thickness.

4.3.1. Abstract

Controlled wrinkling is a rather simple method of fabricating surface topographies. The production process is based on the spontaneous formation of wrinkles upon compression of a hard film attached to a soft elastic substrate. Controlled wrinkling typically features large-scale wrinkled samples with a discrete wavelength and amplitude. In this report, we employ an approach utilizing linear metal layer thickness gradients for the controlled formation of gradient wrinkle patterns. The observed wavelength modulation was experimentally achieved by preparing layer thickness gradients of gold, chromium, and indium by physical vapor deposition in combination with a poly(dimethyl siloxane) elastomer substrate. In case of chromium and indium, a thin SiO_x surface layer was sufficient to ensure adhesion. However, in case of gold, an additional thin chromium adhesion layer was required. For the wrinkled gradient gold film, it was possible to tune the wavelength from 3.4 to 12.2 μm on a single substrate. The experimental data correspond well to the theoretical bilayer model from Stafford *et al.* Chromium has a significant higher Young's modulus and melting temperature than gold. However, chromium was successfully evaporated and gradient wrinkle patterns with wavelengths from 1.0 to 3.5 μm were realized. In contrast, indium has a considerably lower Young's modulus than gold and chromium, respectively. Consequently, lower wavelengths (0.6 – 1.0 μm) of the wrinkled gradient indium film were observed. These tunable wrinkled gradient metal films can be envisioned as components in sensors and optical and electro-optical devices.

4.3.2. Introduction

Controlled wrinkling is a rather simple method for the formation of periodically patterned surfaces.^{1,2} The formation process requires a thin hard film connected to an elastic substrate. Such hard films can be applied *via* oxidation of the surface³ or deposition of a harder material, such as a polymer thin film with a high glass transition temperature⁴ or a metal film.⁵ Upon application of a critical compression force, sinusoidal wrinkling of the hard film occurs because of a buckling instability of the hard film.⁶ The wavelength of the formed wrinkles is a function of the film thickness and corresponding Young's moduli of the film and substrate.⁷

A gradient in surface topography is expected if the Young's modulus of the substrate, the Young's modulus of the film, or the film thickness is varied continuously. The formation of surface-wrinkled gradient materials by varying the substrate's modulus was experimentally shown by Claussen *et al.*⁸ and Glatz *et al.*⁹. In these approaches, a poly(dimethyl siloxane) (PDMS) strip with a stiffness gradient was strained and homogeneously oxidized *via* O₂ plasma. After relaxation, a gradient wrinkle pattern was obtained. A variation in the Young's modulus of the hard film is typically difficult to realize. An alternative simpler approach to obtaining a controlled gradient wrinkle pattern is the variation of the film thickness. The theoretical buckling behavior of this approach was studied by Yin *et al.*¹⁰ If the compression force is applied along the gradient, the resulting wavelength and amplitude are nonuniform in the loading direction. Hiltl *et al.*¹¹ and Lee *et al.*¹² varied the SiO_x layer thickness because of a shielding technique during oxygen plasma treatment of PDMS elastomers to obtain surface-wrinkled gradient SiO_x films. Yu *et al.* studied the wrinkle formation close to the edge of thin magnetron-sputtered nickel films on non-prestrained PDMS substrates.¹³ A hierarchically ordered wrinkle pattern because of a thermal contraction of the PDMS substrate was obtained within small areas after film deposition.

Such layer thickness gradient films can also be prepared *via* a combinatorial vapor deposition approach utilizing movable shadow masks.^{14,15} This allows the controlled deposition of vaporizable materials on substrates in a film thickness gradient. Quartz crystal microbalances monitor the evaporation rate and by controlling the movement of the mask, the layer thickness of the metal film can be adjusted in a precise manner. We used this technique in our studies to prepare thin metal films with a controlled gradient in layer thickness on prestrained PDMS elastomers. This prestrain causes a uniform restoring force over the entire centimeter-sized sample, which induces the formation of a regular parallel wrinkled pattern of the thin metal film upon relaxation of the sample. In this manner, we prepared different wrinkled gradient metal films of gold, chromium, and indium with a local variation of the formed wavelength.

4.3.3. Experimental Section

Materials. PDMS elastomer resin Sylgard 184 was purchased from Dow Corning. All metals were purchased from Balzers with purities of 99.99% (gold), 99.999% (indium), and 99.5% (chromium). All metals were used without further purification.

Elastomer Synthesis. The elastomer substrate was prepared from PDMS elastomer resin Sylgard 184. The siloxane and the curing agent were premixed in a ratio of 10:1 using SpeedMixer DAC 150 SP (Hauschild, Germany) at a rotation speed of 2000 rpm for 2 min. Using a high-precision syringe pump system (Cetoni neMESYS, Germany), the mixed resin was cast into Teflon molds ($140 \times 10 \times 1 \text{ mm}^3$), which were attached to a linear motion slide. The samples were cured at room temperature overnight on a leveled glass plate, followed by a thermal curing step at 150 °C for 2 h.

Plasma Oxidation. PDMS elastomer strips were stretched by 25% in length with a custom-made stretching device and fixed in a custommade specimen mount. To improve the adhesion of the metal film, the strained substrates were oxidized with oxygen plasma to create a more polar surface layer. Oxidation of the surface was carried out using a plasma activate Flecto 10 USB plasma cleaner (Plasma Technology, Germany) at an oxygen pressure of 0.1 mbar and 100% power. Before treatment, the chamber was flushed with oxygen for 60 s. Typical plasma treatment time periods were 30 s for indium films and 60 s for chromium and gold films.

Metal Film Deposition. Metal films were deposited using a vapor deposition chamber PLS 500 E (Balzers, Germany). Resistance heating filaments, which possess a boat or a coil containing the metal source, were installed at the bottom of the chamber. A wolfram coil was used as the target material for chromium. For gold and indium, molybdenum and tantalum boats were used, respectively. The deposition process was done under vacuum ($p = 10^{-6}$ mbar) to suppress oxidation and to reduce the required sublimation temperature. Homogeneous deposition was achieved by means of a rotatable combinatorial setup on top of the chamber, which carried the substrates facing down. The relative film thickness was monitored by quartz microbalances which change their frequency depending on the thickness of the deposited metal film. The thickness gradient was achieved with a computer-controlled shutter mask. The closing speed was controlled by the determined thickness value of the quartz crystal microbalances.

The absolute thickness of the metal film was measured *via* mechanical profilometry (Dektak 150 Surface Profiler, Veeco, USA). For this measurement, a piece of a native silicon wafer was attached next to the PDMS elastomer during vapor deposition. By doing so, the deposited thickness of the metal film on the silicon wafer corresponds to the thickness of the thin metal gradient film on the PDMS elastomer. At least three measurements were taken per sample on the silicon wafer and averaged.

Scanning Electron Microscopy. The samples were prepared on conductive tabs which were attached on top of aluminum sample holders. To provide efficient conductivity between the metal film and sample holder, the nonconducting sides of the PDMS substrate were sputtered with a thin platinum layer (1.3 nm) in a tilted geometry (tilt angle about 45°) on 208HR (Cressington Scientific Instruments, UK). Scanning electron microscopy (SEM) images were recorded on LEO 1530 FE-SEM (Zeiss, Germany) at a cathode voltage of 2–3 kV. For wavelength determinations, at least 10 waves were measured per position and averaged.

Optical Microscopy. Optical micrographs were acquired with a Axiotech KS 100 reflected-light microscope (Zeiss, Germany) with an attached AxioCam ERc 5s camera. Overview pictures were taken at 10-fold magnification. Detailed view of the micrographs of the sample were acquired at 50-fold magnification. To determine wavelengths, at least 10 waves were measured per position and averaged.

4.3.4. Results and Discussion

Figure 4.3.1 illustrates the preparation steps of wrinkled gradient metal films. First, the PDMS elastomer substrate with the dimensions of 14 cm × 1 cm × 0.1 cm was prepared from an elastomer resin kit and cured. The Young's modulus of the resulting PDMS elastomer was determined with a value of 1.8 MPa. The elastomer was stretched by 25% in comparison with its initial length and fixed in a frame. In the next step, the surface was treated with oxygen plasma to create a very thin SiO_x layer, which promotes adhesion to the evaporated thin metal film. Subsequently, a linear thickness gradient metal film was evaporated by physical vapor deposition. Finally, the gradient wrinkle pattern based on a wrinkled gradient metal film is formed by relaxing the sample to its original length. Using this process, we prepared wrinkled gradient metal films of gold, chromium, and indium. Physical properties of these metals are

listed in Table 4.3.1. Gold and indium can be deposited under vacuum at moderate temperatures. Chromium has a comparatively high melting point and requires significantly more thermal energy for physical vapor deposition. In case of gold, the direct deposition of the thickness gradient metal film on top of the SiO_x layer did not result in sufficient adhesion over the entire sample in the applied wrinkling process. To overcome this, an additional evaporated thin uniform chromium layer of about 2 nm layer thickness improved the adhesion between SiO_x and gold.¹⁶ All prepared gradient wrinkle patterns based on wrinkled gradient metal films show a linear increase in wavelength with increasing layer thickness of the metal film.

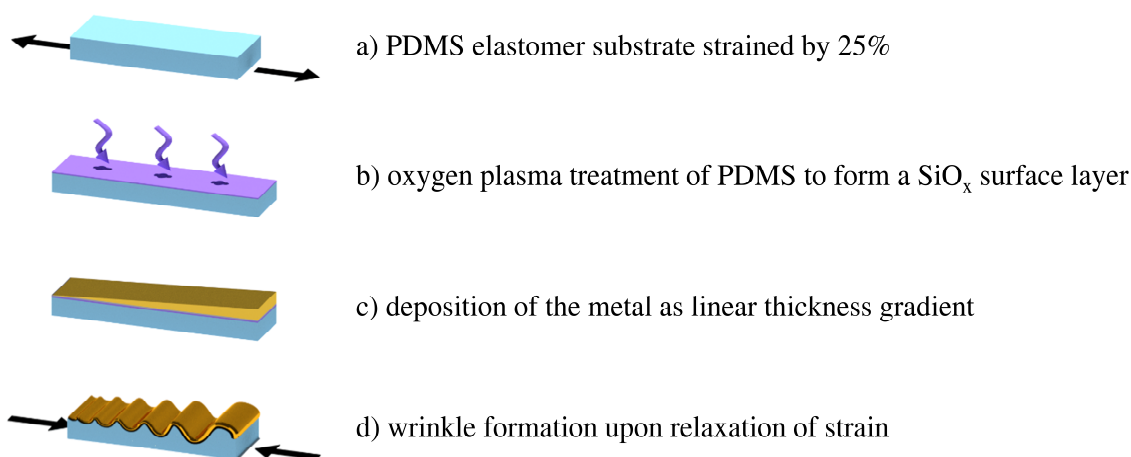


Figure 4.3.1: Preparation scheme for gradient wrinkle patterns based on wrinkled gradient metal films. A PDMS elastomer strip was strained by 25% (a) and treated with oxygen plasma to produce a thin SiO_x layer on the surface (b). A linear thickness gradient metal film was evaporated by physical vapor deposition (c). Relaxation of the sample resulted in the wrinkled gradient metal film (d).

Table 4.3.1: Physical properties of the metals used in the study.

	Young's modulus E_f (GPa)	Poisson ratio ν_f	melting temperature T_m (°C)
chromium	279 ¹⁷	0.21 ¹⁸	1907 °C ¹⁹
gold	78.5 ¹⁷	0.42 ²⁰	1064.18 °C ¹⁹
indium	10.6 ¹⁷	0.45 ²¹	156.60 °C ¹⁹

In theory, the obtained wavelength of formed wrinkles is a function of the thickness of the thin hard film and the Young's moduli of the hard film and substrate as given in Equation 4.3.1⁶

$$\lambda = 2\pi h \sqrt[3]{\frac{E_f(1 - \nu_s^2)}{3E_s(1 - \nu_f^2)}} \quad (4.3.1)$$

where λ is the wavelength of formed wrinkles, h is the thickness of the hard film, E_f is the Young's modulus, and ν_f is the Poisson's ratio of the hard film and E_s and ν_s for the substrate, respectively. In conclusion, the obtained wavelength is proportional to the film thickness.

Wrinkled Gradient Gold Film

As shown in the SEM images of Figure 4.3.2, the gradient wrinkle patterns based on the wrinkled gradient gold film show a linear increase in wavelength with increasing gold thickness. The gold films are very homogeneous independent of the film thickness of up to 85 nm (Figure 4.3.2a–f). At a film thickness of 98 and 110 nm (Figure 4.3.2g and Figure 4.3.2h), cracks are clearly visible at the ridges of the wrinkles. The formation of these cracks can be attributed to the bending stiffness of the gold film, which leads to a break at higher film thicknesses.

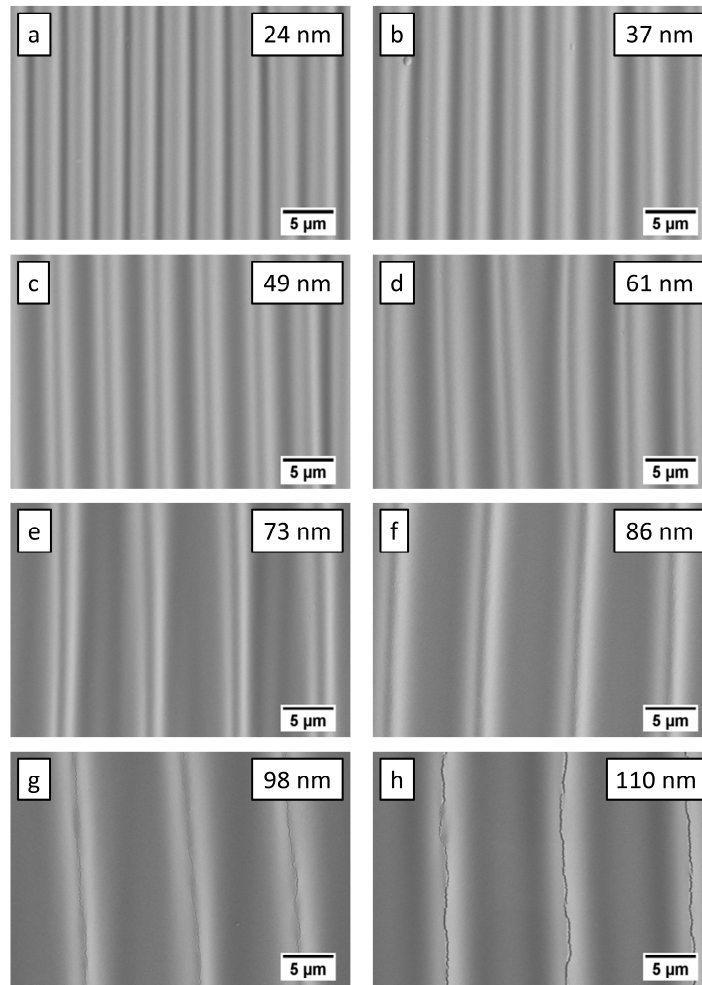


Figure 4.3.2: SEM images of a wrinkled gradient gold film on a PDMS substrate. The noted thickness values correspond to the gold film. With increasing thickness of the gold film from 24 to 110 nm (a – h), the wavelength increases continuously. At a thickness of 98 and 110 nm, cracks occur at the ridges of the wrinkles (g and h).

In order to predict the wavelengths according to [Equation 4.3.1](#), we have to consider that we used an additional chromium adhesion layer. In this case, the theoretical model from Stafford *et al.*²² has to be applied. This model is derived from the composite beam theory and is applicable for systems with two different hard layers on top of an elastomeric substrate. It calculates an effective Young's modulus of the hard bilayer film as given in [Equation 4.3.2](#)

$$E_{\text{eff}} = \frac{1 + m^2n^4 + 2mn(2n^2 + 3n + 2)}{(1 + n)^3(1 + mn)} E_1 \quad (4.3.2)$$

where m is the modulus ratio E_2/E_1 and n is the layer thickness ratio h_2/h_1 of the two layers. Index 1 corresponds to the layer which is attached to the substrate, here the chromium adhesion layer and index 2 to the top layer, here the gold layer.

Because of the high prestrain ε_{pre} of 25%, a correction factor for the theoretical prediction is needed in Equation 4.3.1 as reported by Jiang *et al.*²³ and applied in Equation 4.3.3

$$\lambda = \frac{2\pi h}{(1 + \varepsilon_{\text{pre}})^3 \sqrt{1 + \xi}} \sqrt[3]{\frac{E_f(1 - \nu_s^2)}{3E_s(1 - \nu_f^2)}} \quad (4.3.3)$$

with

$$\xi = \frac{5}{32} \varepsilon_{\text{pre}} (1 + \varepsilon_{\text{pre}}) \quad (4.3.4)$$

The comparison of the experimental and theoretical wavelengths as function of the gold film thickness including the chromium adhesion layer but neglecting the very thin SiO_x layer is shown in Figure 4.3.3. The values for the theoretical wavelengths increase linearly from about 3 to 13 μm and are in general agreement with the measured wavelength values from the SEM images of Figure 4.3.2.

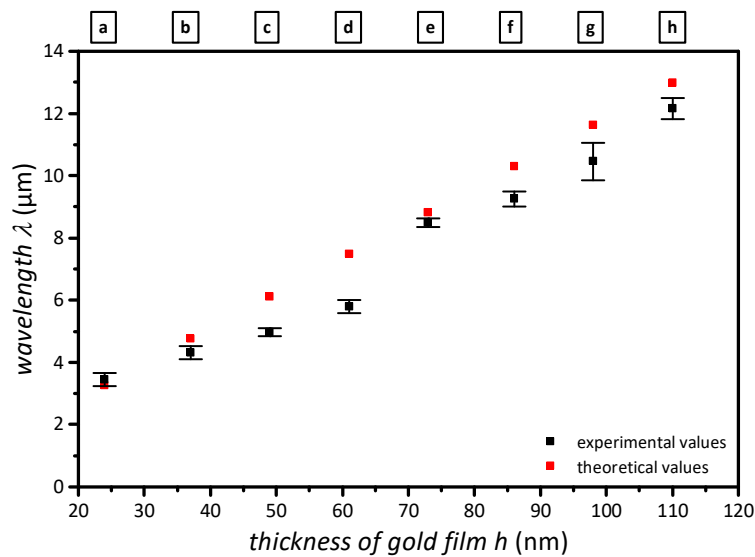


Figure 4.3.3: Comparison of the experimental and theoretical wavelengths as function of the gold film thickness of the wrinkled gradient gold film. Theoretical values were calculated according to the bilayer model taking the chromium adhesion layer into account. The characters (a – h) correspond to the SEM images of Figure 4.3.2.

Wrinkled Gradient Chromium Film

Besides the gold/chromium bilayer, we also investigated a pure wrinkled gradient chromium film. Here, the wavelength of the formed gradient wrinkle pattern also increases linearly with film thickness from 1.0 to 3.5 μm (cf. Figure 4.3.4). However, the theoretical wavelengths were about 4 times higher than experimentally determined ones. We believe that this effect could be attributed to the high deposition temperature of chromium ($T_m = 1907\text{ }^\circ\text{C}^{19}$). The PDMS elastomer absorbs a high amount of thermal energy during the evaporation process. This probably leads to a post curing of the elastomer particularly at the substrate–metal interface. It is well-known that curing conditions affect the properties of the PDMS substrate.²⁴ The modulus of the postcured substrate can be calculated from transformed Equation 4.3.3 using the measured wavelengths. The chromium film thickness correlates to the time of thermal exposure during evaporation. This results in a substrate modulus increase from 6 to 94 MPa over the entire sample and in turn smaller wrinkles are formed.

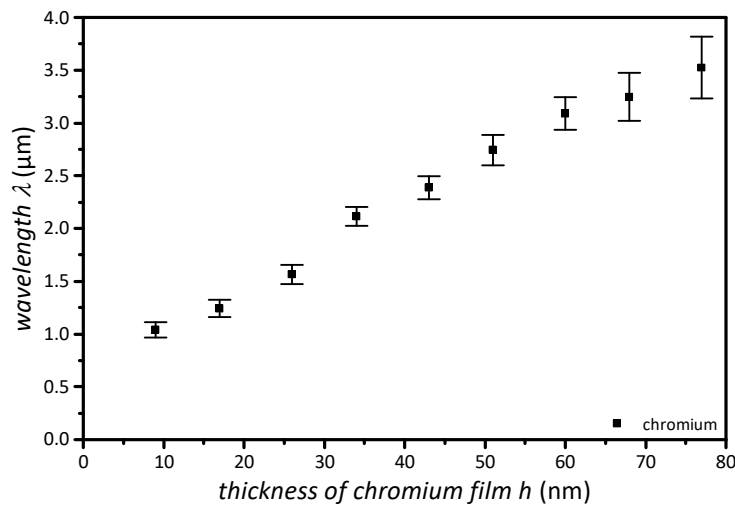


Figure 4.3.4: Plot of wavelength vs film thickness of a wrinkled gradient chromium film on the plasma-treated PDMS substrate. The wavelength increases linearly with increasing chromium film thickness. Wavelengths were determined from optical micrographs.

Wrinkled Gradient Indium Film

As a third metal, we selected indium. Indium has a very low deposition temperature and does not affect the PDMS substrate in a distinct manner during physical vapor deposition. In addition, the Young's modulus is very low ($E = 10.6\text{ GPa}^{17}$), which allows the formation of wrinkles with smaller amplitudes and shorter wavelengths. In contrast to the wrinkled gradient gold and the wrinkled gradient chromium films, the wavelength of the formed

gradient wrinkle patterns based on indium increases up to a film thickness of about 50 nm and remains constant at about 1 μm for higher film thicknesses (cf. [Figure 4.3.5](#) and [Figure 4.3.6](#)). This behavior may be explained by the obtained fine-grained indium film surface, with grain size and film thickness increasing proportionately up to a layer thickness of about 50 nm. The size distribution of obtained indium surface nanoparticles does not significantly vary above this layer thickness,²⁵ and thus the corresponding wavelength of wrinkle levels out at about 1 μm .

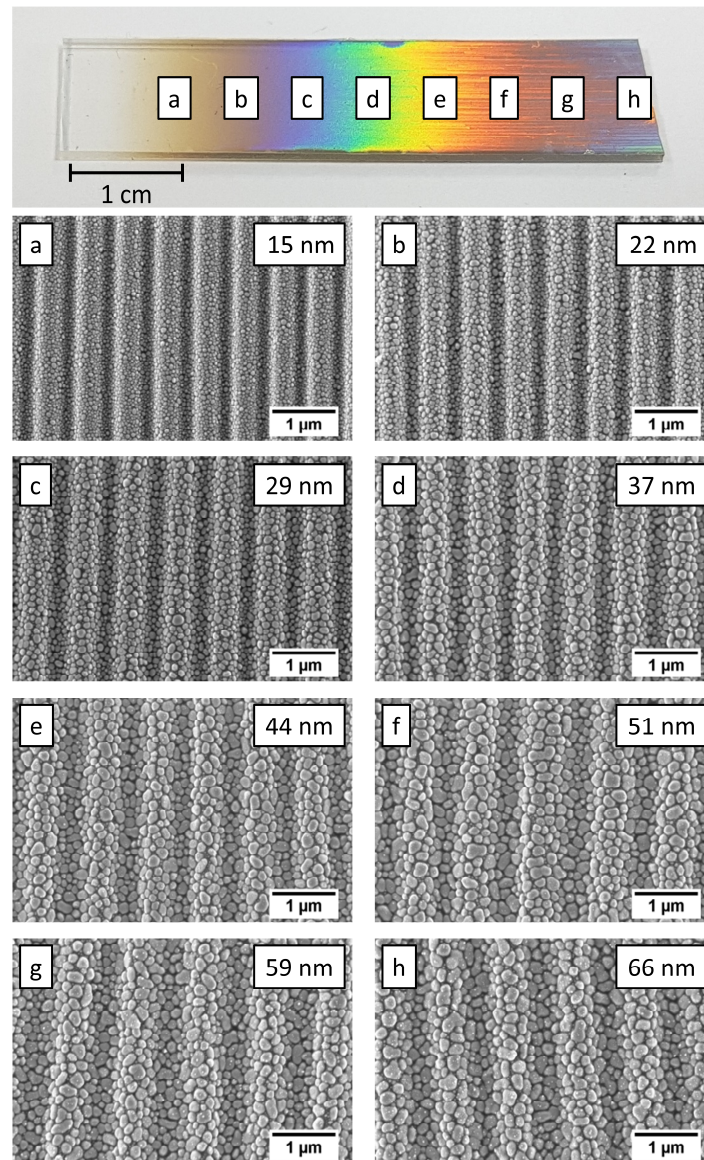


Figure 4.3.5: Photograph of the wrinkled gradient indium film on a PDMS substrate showing a gradient in reflection colors (top). SEM images of a wrinkled gradient indium film at different positions (bottom). The noted thickness values correspond to the indium film. With increasing the thickness of the indium film from 15 to 51 nm (a – h), the wavelength increases continuously and remains constant up to a thickness of 66 nm. Indium films show a distinct fine-grained structure.

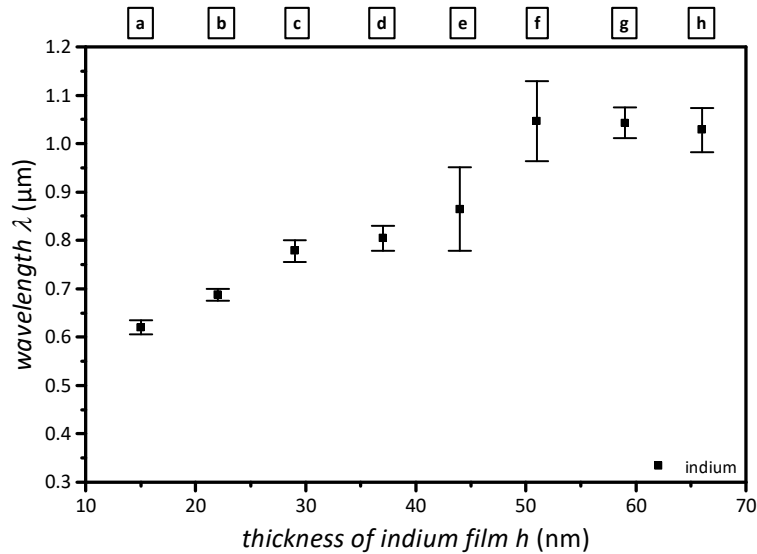


Figure 4.3.6: Plot of wavelength vs film thickness of indium on top of the plasma-treated PDMS substrate. The wavelength increases with increasing film thickness of the deposited indium film up to a film thickness of about 50 nm and stays at about 1 μm for higher film thicknesses. Wavelengths were determined from SEM images (cf. Figure 4.3.5). The characters above indicate the corresponding measurement positions.

In many electronic devices, indium tin oxide (ITO) is used as a transparent electrode material.²⁶ The fine-grained surface structure of ITO could form wrinkling, too, if prepared in a similar manner, for example by sputtering or e-beam evaporating a thin film. This would allow applications in the field of flexible electronics.

4.3.5. Conclusions

We have demonstrated a versatile and reliable process to prepare gradient wrinkled metal films on elastic substrates. Thickness gradient thin metal films were successfully vapor deposited on prestrained substrates and wrinkled upon relaxation. Gradient metal films of gold, chromium, and indium demonstrate the applicability of this approach for both smooth and grainy metal films. The principle can also be transferred to other metals, if the adhesion between the film and elastic substrate is sufficient. Our experimental wavelength values are in good agreement with theoretical considerations from the wrinkling theory. Envisioned application areas of such centimeter-sized metal wrinkle patterns are flexible electronics, tunable optical gratings, and mechanochromic sensors.

4.3.6. Author information

Corresponding Author

*E-mail: hans-werner.schmidt@uni-bayreuth.de

Phone: +49 921 55-3200

Fax: +49 921 55-3206.

ORCID

Hans-Werner Schmidt: 0000-0002-1761-1153

Author Contributions

All the authors contributed to the writing of the manuscript and have approved its final version.

Notes

The authors declare no competing financial interest.

4.3.7. Acknowledgments

Financial support by the Bavarian State Ministry of Science, Research, and the Arts for the Collaborative Research Network “Solar Technologies go Hybrid” and the Elite Network of Bavaria (ENB), Macromolecular Science, is gratefully acknowledged. A.F. acknowledges financial support from German Science Foundation (DFG) within project FE 600/20-1. We thank Dr. Moritz Tebbe and Dr. Reiner Giesa (Bavarian Polymer Institute) for their support and inspiring discussions and Martina Heider (Bavarian Polymer Institute) for SEM measurements.

4.3.8. References

- [1] J. Y. Chung, A. J. Nolte and C. M. Stafford, *Adv. Mater.* **2011**, *23*, 349–368, "Surface wrinkling: a versatile platform for measuring thin-film properties".
- [2] A. Schweikart and A. Fery, *Microchim. Acta* **2009**, *165*, 249–263, "Controlled wrinkling as a novel method for the fabrication of patterned surfaces".
- [3] N. Pazos-Pérez, W. Ni, A. Schweikart, R. A. Alvarez-Puebla, A. Fery and L. M. Liz-Marzán, *Chem. Sci.* **2010**, *1*, 174, "Highly uniform SERS substrates formed by wrinkle-confined drying of gold colloids".
- [4] C. M. Stafford, C. Harrison, K. L. Beers, A. Karim, E. J. Amis, M. R. VanLandingham, H.-C. Kim, W. Volksen, R. D. Miller and E. E. Simonyi, *Nat. Mater.* **2004**, *3*, 545–550, "A buckling-based metrology for measuring the elastic moduli of polymeric thin films".
- [5] M. Watanabe, *Polym. Adv. Technol.* **2005**, *16*, 744–748, "Wrinkles formed on a thin gold film deposited onto stretched elastic substrates".
- [6] J. Genzer and J. Groenewold, *Soft Matter* **2006**, *2*, 310, "Soft matter with hard skin".
- [7] C.-M. Chen and S. Yang, *Polym. Int.* **2012**, *61*, 1041–1047, "Wrinkling instabilities in polymer films and their applications".
- [8] K. U. Claussen, M. Tebbe, R. Giesa, A. Schweikart, A. Fery and H.-W. Schmidt, *RSC Adv.* **2012**, *2*, 10185, "Towards tailored topography".
- [9] B. A. Glatz, M. Tebbe, B. Kaoui, R. Aichele, C. Kuttner, A. E. Schedl, H.-W. Schmidt, W. Zimmermann and A. Fery, *Soft Matter* **2015**, *11*, 3332–3339, "Hierarchical line-defect patterns in wrinkled surfaces".

-
- [10] J. Yin and X. Chen,
Philos. Mag. Lett. **2010**, *90*, 423–433,
“Elastic buckling of gradient thin films on compliant substrates”.
- [11] S. Hiltl and A. Böker,
Langmuir **2016**, *32*, 8882–8888,
“Wetting Phenomena on (Gradient) Wrinkle Substrates”.
- [12] J. S. Lee, H. Hong, S. J. Park, S. J. Lee and D. S. Kim,
Microelectron. Eng. **2017**, *176*, 101–105,
“A simple fabrication process for stepwise gradient wrinkle pattern with spatially-controlled wavelength based on sequential oxygen plasma treatment”.
- [13] S. Yu, Y. Ni, L. He and Q.-L. Ye,
ACS Appl. Mater. Interfaces **2015**, *7*, 5160–5167,
“Tunable formation of ordered wrinkles in metal films with controlled thickness gradients deposited on soft elastic substrates”.
- [14] C. Neuber, M. Bäte, M. Thelakkat, H.-W. Schmidt, H. Hänsel, H. Zettl and G. Krausch,
Rev. Sci. Instrum. **2007**, *78*, 72216,
“Combinatorial preparation and characterization of thin-film multilayer electro-optical devices”.
- [15] C. Schmitz, P. Pösch, M. Thelakkat and H.-W. Schmidt,
Phys. Chem. Chem. Phys. **1999**, *1*, 1777–1781,
“Efficient screening of electron transport material in multi-layer organic light emitting diodes by combinatorial methods”.
- [16] N. Bowden, S. Brittain, A. G. Evans, J. W. Hutchinson and G. M. Whitesides,
Nature **1998**, *393*, 146–149,
“Spontaneous formation of ordered structures in thin films of metals supported on an elastomeric polymer”.
- [17] W. F. Gale and T. C. Totemeier, eds.,
Elsevier/Butterworth-Heinemann, Amsterdam, 8th edn. **2004**,
“Smithells Metals Reference Book”.
- [18] H. Gercek,
Int. J. Rock Mech. Min. Sci. **2007**, *44*, 1–13,
“Poisson’s ratio values for rocks”.

- [19] D. R. Lide, ed.,
CRC Press, Boca Raton, FL, 86th edn. **2005**,
"CRC Handbook of Chemistry and Physics".
- [20] T. H. Courtney,
Waveland Press, Long Grove, IL, 2nd edn. **2005**,
"Mechanical Behavior of Materials".
- [21] S. Kim and H. Ledbetter,
Mater. Sci. Eng., A **1998**, 252, 139–143,
"Low-temperature elastic coefficients of polycrystalline indium".
- [22] C. M. Stafford, S. Guo, C. Harrison and M. Y. M. Chiang,
Rev. Sci. Instrum. **2005**, 76, 62207,
"Combinatorial and high-throughput measurements of the modulus of thin polymer films".
- [23] H. Jiang, D.-Y. Khang, J. Song, Y. Sun, Y. Huang and J. A. Rogers,
Proc. Natl. Acad. Sci. U. S. A. **2007**, 104, 15607–15612,
"Finite deformation mechanics in buckled thin films on compliant supports".
- [24] S. Yu, Y. Sun, Y. Ni, X. Zhang and H. Zhou,
ACS Appl. Mater. Interfaces **2016**, 8, 5706–5714,
"Controlled Formation of Surface Patterns in Metal Films Deposited on Elasticity-Gradient PDMS Substrates".
- [25] P. R. Elliott, S. P. Stagon and H. Huang,
Sci. Rep. **2015**, 5, 16826,
"Control of Separation and Diameter of Ag Nanorods through Self-organized Seeds".
- [26] C. Guillén and J. Herrero,
Thin Solid Films **2011**, 520, 1–17,
"TCO/metal/TCO structures for energy and flexible electronics".

4.4. Confinement templates for hierarchical nanoparticle alignment prepared by azobenzene-based surface relief gratings

*Andreas E. Schedl,^a Patrick T. Probst,^b Christoph Meichner,^c Christian Neuber,^a Lothar Kador,^c Andreas Fery^{*b} and Hans-Werner Schmidt^{*a}*

a) Macromolecular Chemistry I, Bavarian Polymer Institute (BPI) and Bayreuth Center for Colloids and Interfaces (BZKG), University of Bayreuth, 95440 Bayreuth, Germany

b) Institute of Physical Chemistry and Polymer Physics, Leibniz Institute of Polymer Research Dresden e.V., 01069 Dresden, Germany

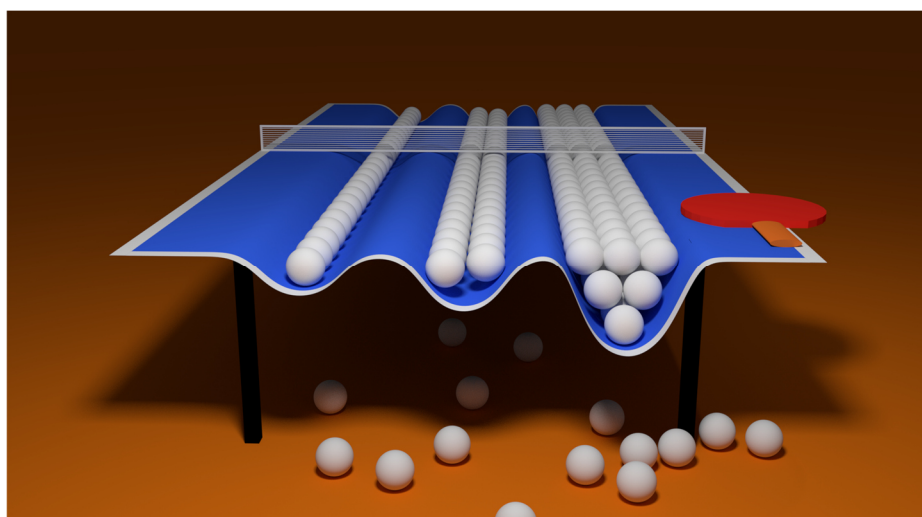
c) Bayreuth Institute for Macromolecular Research, University of Bayreuth, 95440 Bayreuth

The results of this chapter have been published as full paper article in

Soft Matter **2019**, *15*, 3872-3878.

Reproduced with permission from *The Royal Society of Chemistry*.

DOI: 10.1039/C8SM02585A



Substrate-assisted nanoparticle alignment *via* surface relief gratings. Modulation of the grating height allows control over the formed particle patterns.

4.4.1. Back cover



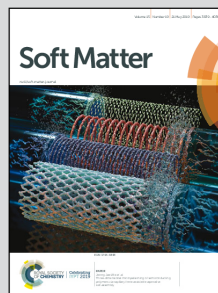
Graphic: Daniela Leitner

Highlighting research performed in the research group of Hans-Werner Schmidt from Macromolecular Chemistry and Bavarian Polymer Institute at the University of Bayreuth, in collaboration with the research groups of Andreas Fery from the Institute of Physical Chemistry and Polymer Physics at the Leibniz Institute of Polymer Research Dresden, and Lothar Kador from the Bayreuth Institute for Macromolecular Research at the University of Bayreuth.

Confinement templates for hierarchical nanoparticle alignment prepared by azobenzene-based surface relief gratings

Surface relief gratings can be utilized as confinement templates to align nanoparticles. Variation of the grating height on one substrate allows an efficient screening and control of the nanoparticle assemblies.

As featured in:



See Andreas Fery, Hans-Werner Schmidt *et al.*, *Soft Matter*, 2019, 15, 3872.

4.4.2. Abstract

Alignment of nanoparticles to hierarchical periodic structures is an emerging field in the development of patterned surfaces. Common alignment methods are based on templates that guide particle self-assembly. These can be formed using lithographic methods offering an almost free choice of the motif, while being expensive and time-consuming for large-scale production. Alternatively, template formation by controlled wrinkling offers a low-cost formation, but often suffers from the formation of defect structures like line-defects and cracks. Here, we show a preparation technique for nanoparticle alignment substrates that is based on the inscription of holographic surface relief gratings with a periodic sinusoidal wave pattern on the surface of azobenzene films. As interference patterns are employed for structure formation, very uniform and defect-free gratings with tunable grating height and grating period can be prepared. These substrates were successfully replicated to poly(dimethyl siloxane) and the replicas used for the alignment of polystyrene latex particles. Accordingly produced substrates exhibiting gratings with a variation in grating height allow for efficient screening of nanoparticle alignment in a geometrical confinement in one single experiment. We anticipate our studies as a promising tool for the development of sensors, tunable gratings and metamaterials.

4.4.3. Introduction

Surface relief gratings (SRGs) are sinusoidal wave patterns that can be inscribed on the surface of azobenzene-containing films with a holographic setup.¹ The formation of these structures was discovered by Natansohn *et al.*² and Kumar *et al.*³ Since then, surface relief gratings have been extensively studied, and the technique has been developed and established.^{4–12} Employing the photo-active *cis–trans* isomerization of the azo unit and the resulting mass transport, SRGs can be written on the surface of azobenzene chromophore films.¹³ Besides azobenzene-containing polymers,^{14,15} small molecules with azo-functionalities can be used.¹⁶ By irradiation with linearly polarized light at an appropriate wavelength, the conjugation of the azo group can be switched from *trans* to *cis* and *vice versa*.¹⁷ In a holographic setup, a laser beam is split into two beams that are weakly focused onto the surface of the film.¹⁸ Interference phenomena lead to bright and dark areas on the azobenzene film surface.

Continued irradiation leads to a macroscopic mass transport, which results in a highly uniform sinusoidal grating.¹⁹ Recently, azo-containing polymers have also been utilized to construct well-ordered surface patterns *via* photo-responsive wrinkling.^{20–22}

These periodic patterns are promising templates for the formation of hierarchically ordered nanoparticle structures²³ with potential applications in sensing,^{24–26} light-harvesting,²⁷ plasmonic metasurfaces²⁸ and optical metamaterials.^{29,30} Conventional methods for creating well-defined particle arrays are based on soft templates using lithographic master structures³¹ or prepared *via* controlled wrinkling.^{32–36} Lithographic methods offer high structural versatility enabling sophisticated geometries, but they are comparatively complex and costly in terms of fabrication.³⁷ Templates prepared *via* controlled wrinkling are low-cost and easy to fabricate over large areas.³⁸ Utilizing substrates with a gradient in SiO_x film thickness and hence in wrinkle wavelength, particle alignment can be screened in one step.³⁹ Drawbacks of the wrinkling approach are the formation of defect structures like line-defects or cracks as a result of the relaxation process.⁴⁰ These defects disturb the alignment due to meniscus jumps of the particle solution and hence lead to an inhomogeneous particle distribution. Moreover, the wrinkling process does not provide the opportunity to control the wrinkle wavelength and the wrinkle depth independently from each other.

The use of replicated SRGs can overcome those limitations. It was already shown that a periodic pattern of SRGs can be transferred to other polymers like poly(dimethyl siloxane) (PDMS),⁴¹ photo polymers,⁴² and poly(3-hexylthiophene).⁴³ In addition, using a calcination process, SRGs can be used to build up a periodic array of metal oxide nanowires.^{44,45} Loebner *et al.* demonstrated that the depth of the sinusoidal wave pattern of SRGs has a guiding effect on the alignment of nanoparticles. This was shown for silica particles adsorbed at a low concentration on an azo polymer film. Exposure led to an increasing grating height that resulted in a guided particle motion.⁴⁶

Here, we present a procedure to first prepare defect-free confinement templates based on SRGs. In a second step, the SRGs are utilized for the alignment of close-packed nanoparticles prepared by spin-coating. By employing a graded approach with different sectors of increasing grating heights on one substrate, 1D, 2D, and 3D assemblies of polystyrene latex nanoparticles are prepared and compared under identical processing and aging conditions. This allows the investigation of different geometrical confinements in a single experiment.

The gratings are inscribed in an azobenzene-containing film of a molecular glass using a holographic setup. The formed SRGs can be easily replicated to PDMS, which can be again transferred to thermoplastic polymers like polycarbonate (PC) and polypropylene (PP). In particular, PP is more robust against polar organic solvents like acetone or ethanol and, hence, could extend the range of usable solvents for particle alignment.

4.4.4. Experimental

Materials

The spirobischroman-based 6,6',7,7'-tetraester with four azobenzene moieties per molecule was synthesized in our labs. The synthesis is described in the literature.⁴⁷ Poly(dimethyl siloxane) cast resin Sylgard 184® was purchased from Dow Corning. Raco-polypropylene RD208CF was used. Polycarbonate was extracted from a commercial DVD + R (Verbatim).

Particle synthesis

The synthesis of PS latex particles with grafted polyelectrolyte brushes is described in ref. 48. Briefly, PS core particles with a diameter of 198 nm (according to dynamic light scattering, dispersity: 1.00 according to analytical disk centrifugation) were prepared by emulsion polymerization. The monomer styrene (2.3 mol, corresponding to 20 wt% of the aqueous reaction mixture) was emulsified by sodium dodecyl sulfate (SDS, 8.3 mmol) and polymerized at 80 °C for 2 h using potassium persulfate (1.8 mmol) as initiator. By addition under starved conditions at 70 °C, the copolymerizable photoinitiator 2-[p-(2-hydroxy-2-methylpropiophenone)]-ethylene glycol-methacrylate (HMEM, 44.5 mmol) was anchored to the surface of the growing PS spheres (3 h). After purification of the cores by ultrafiltration, the water-soluble monomer sodium styrene sulfonate (265 mmol) was grafted from the surface of the particle (4.8 g PS in 2.4 l) by photopolymerization, carried out in a high-performance UV reactor (Laboclean LC Forschungsreaktor, a.c.k. aqua concept, Germany). The resulting core-shell particles have a hydrodynamic diameter of 213 nm.

Preparation of azobenzene films

Azobenzene films were prepared *via* spin-coating. A THF solution of spirobischroman-based 6,6',7,7'-tetraester with four azobenzene moieties per molecule (7 wt%) was filtrated with a PTFE syringe filter (0.2 mm) and spin-coated (CONVAC 1001, Germany) at 700 rpm for 60 s with a ramp of 10 s on cleaned glass slides (76 mm x 26 mm x 1 mm)/glass discs (diameter: 5 cm), which yields a film thickness of about 1 μm . Films were annealed at 80 °C under a nitrogen atmosphere for 1 h to remove residual solvent.

Holographic preparation of surface relief gratings

Films were exposed to holographic illumination with two coherent p-polarized laser beams ($\lambda = 489 \text{ nm}$) of equal intensity (1 W per cm^2 per beam). The angle between the beams was adjusted to 28.3°, which results in a periodicity of the surface relief grating of 1.0 μm .¹⁸

Replication of surface relief gratings to PDMS strips and discs

For substrates with strip geometry, a glass frame is built on top of the azobenzene films with inscribed surface relief gratings to obtain a mold (inlet dimension: 70 mm x 10 mm x 2 mm). 1.4 ml of Sylgard® 184 cast resin (siloxane/curing agent = 10:1 (w/w), mixed in a SpeedMixer™ DAC 150 SP (Hauschild, Germany) at 2000 rpm for 2min), was filled into the mold with a low-pressure syringe pump (cetoni neMESYS, Germany). The sample was cured at room temperature overnight, followed by a thermal curing step at 80 °C for 2 h.

For disc-like substrates, an azobenzene coated glass disc with a diameter of 5 cm (with 8 equidistantly inscribed SRGs on a concentric circle around the center of the sample) was placed in a circular mold and ca. 15 g of Sylgard 184 cast resin (siloxane/curing agent = 10:1 (w/w), mixed in a SpeedMixer™ DAC 150 SP (Hauschild, Germany) at 2000 rpm for 2 min) was added to obtain a thickness of about 3 mm. Analogous to the strip preparation, the sample was cured at room temperature overnight, followed by a thermal curing step at 80 °C for 2 h. After demolding and removal of the azo master, a circular PDMS template with a diameter of 3 cm was punched out.

Replication of surface relief gratings to other thermoplastic polymers

PDMS replicas were covered with polymer platelets (polycarbonate or polypropylene) and heated for 5 min at the embossing temperature (PC: 190 °C, PP: 210 °C). The gratings were then hot embossed at a load of 5 kN for 2 min. During embossing, the SRG was imprinted on the thermoplastic material and preserved after removal of the PDMS template.

Particle assembly

Immediately prior to spin coating, the PDMS replica comprising eight SRG spots of varying profile height was hydrophilized in a Flecto 10 plasma cleaner (Plasma Technology, Germany). The treatment in O₂ plasma (30 s, 0.2 mbar, 80 W) ensured good wettability of the particle solution on the surface. On the freshly plasma-treated sample, all spots were wetted with a continuous liquid film of 4 wt% aqueous particle solution located at the center of the substrate. Spin coating (SCE-150, KLM, Germany) was carried out at a spinning velocity of 33 rps for 120 s with an acceleration of 3.3 rps s⁻¹.

Atomic force microscopy

AFM height images ([Figure 4.4.2](#), [Figure 4.4.3](#) and [Figure 4.4.9A](#)) were recorded on a NanoScope Dimension IIIIm NanoScope V (Veeco Metrology group, USA) in tapping mode (OTESPAW probe from Bruker, 300 kHz, 42 N m⁻¹). AFM height images in [Figure 4.4.4](#), [Figure 4.4.9B](#) and [Figure 4.4.11](#) were measured with a Dimension FastScan (Bruker, USA) operated in PeakForce Tapping mode (FASTSCAN-C probe from Bruker, 300 kHz, 0.8 N m⁻¹).

Scanning electron microscopy

Samples were sputtered with a thin platinum layer with a thickness of 1.3 nm on a 208HR (Cressington Scientific Instruments, UK) before measurement. SEM images ([Figure 4.4.5](#)) were recorded on a FEI Quanta FEG 250 (Thermo Fisher Scientific, USA) in high vacuum using an Everhart-Thornley detector and a centric backscattering detector.

Replication of surface relief gratings

In the first step (Figure 4.4.1A), the azo master is prepared. A homogeneous film with a thickness of about 1 μm of a glass-forming azobenzene-containing small molecule was prepared by spin-coating and annealing. On this film, surface relief gratings with an exposure area of about 1 - 2 mm^2 were inscribed using a holographic technique.^{1,18} For comparability, all the gratings discussed in this paper were studied in the central region of the exposed area, where the grating height is maximum (cf. SI 4.4.10.1). In this area, the optical inscription process yielded gratings with a uniform grating period of about 1.0 μm (cf. SI 4.4.10.2). The grating height can be tuned by the exposure time; it refers to the maximum peak-to-valley distance. Gratings with heights up to 0.73 μm were inscribed (cf. SI 4.4.10.3).

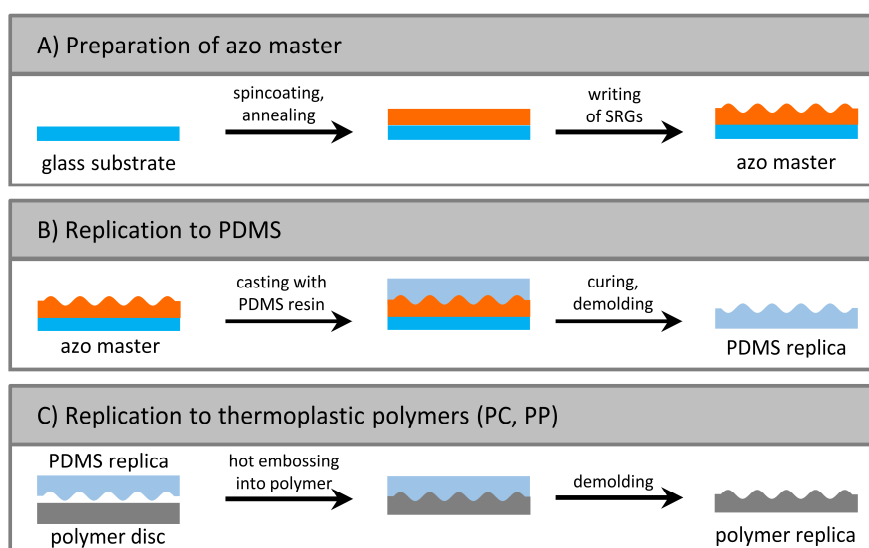


Figure 4.4.1: Scheme for the preparation of the azo master and replicas. An azobenzene film was spin coated on a glass substrate and annealed (A). After inscription of SRGs on this film, the azo master is obtained. The azo master is cast with PDMS resin (B). After curing and demolding, a PDMS replica is obtained. The gratings can be transferred to other polymers by hot embossing with the PDMS replica (C). After demolding, polymer replicas of the gratings are obtained.

It is possible to replicate the inscribed gratings with a poly(dimethyl siloxane) resin by casting the liquid reaction mixture on top of the azo master and subsequent curing (Figure 4.4.1B). The replicated PDMS gratings were precisely transferred from the azobenzene gratings without a significant loss in grating height and overall quality. Figure 4.4.2A depicts the AFM

height images of the azo master (exposure time: 400 s) and the corresponding PDMS replica. The loss in grating height during the transfer is negligible – the grating height on the replica is only about 1% smaller than on the azo master. This decrease is due to the slight shrinkage during curing. An exemplary large-area AFM height image of 90 μm x 90 μm of a PDMS replica is depicted in SI 4.4.10.4. No defects over the entire measurement range are visible. In comparison, templates prepared by controlled wrinkling with similar dimensions reveal severe defects like irregular cracks parallel to the stretching direction.

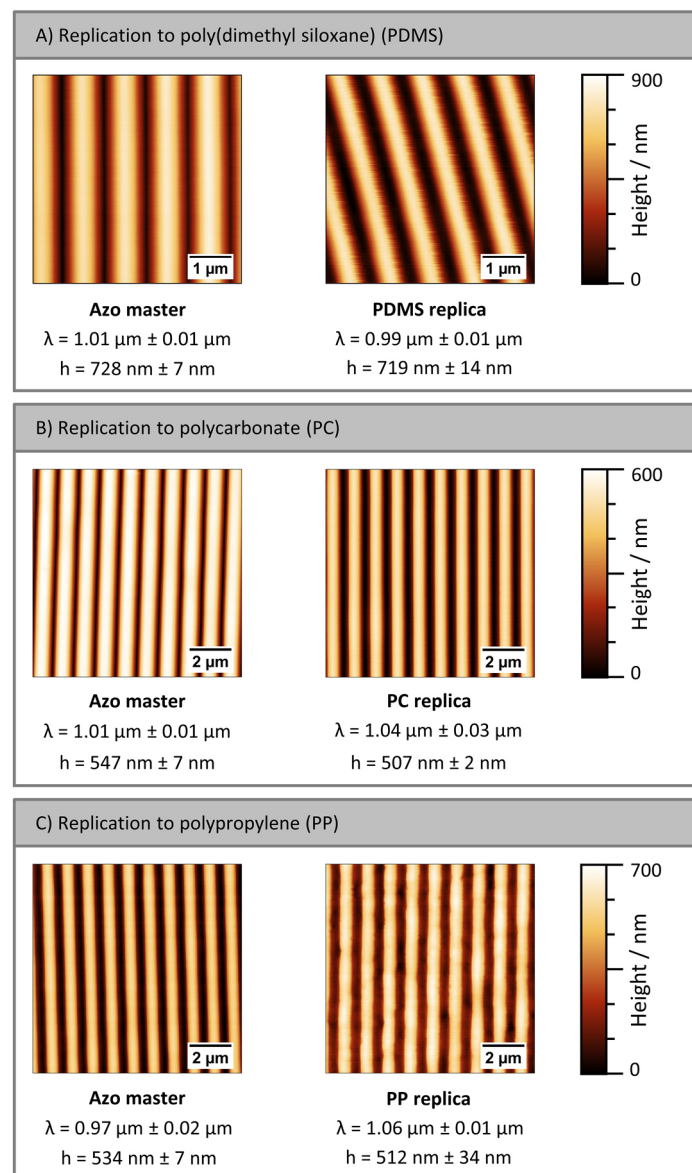


Figure 4.4.2: Comparison of AFM height images of the transfer of surface relief azo gratings to poly(dimethyl siloxane) (A) and to polycarbonate (B) and polypropylene (C). The comparisons reveal a well-defined and defect-free transfer with only marginal variations in grating period λ and grating height h .

To show the flexibility of grating pattern transfer in terms of processible material, the relief structure was additionally replicated into thermoplastic polymers by hot embossing (Figure 4.4.1C). We selected polycarbonate (PC) as an amorphous and polypropylene (PP) as a semi-crystalline polymer. The gratings were successfully transferred to both polymers, as shown in Figure 4.4.2B and Figure 4.4.2C. The PC and PP replicas exhibit well-defined and defect-free gratings with grating periods of about 1 μm and grating heights over 500 nm. As compared to the original azo master, the grating period is slightly increased, and the height slightly decreased, respectively, which can be attributed to a slight deformation of the PDMS stamp during hot embossing under the applied pressure. The resulting replicas give access to template materials of higher stiffness and less swelling, in particular in view of the alignment of nanoparticles from organic solvents.

Variation of grating height in PDMS replica

In the holographic writing of SRGs, both grating period and height can be tuned individually on one sample. This is not possible for strain-release wrinkling. To demonstrate the potential, we gradually increased inscription times at different positions of the azobenzene film. The inscription time was varied from 20 to 105 seconds yielding a linear increase of the grating height from 70 nm to 600 nm. The angle of the two interfering laser beams in the holographic setup was adjusted to 28.3° resulting in a grating period of 1.0 μm .¹⁸ This was kept constant for all inscribed gratings. The actual sample with three example images and the results of the variation of grating height with inscription time are shown in Figure 4.4.3.

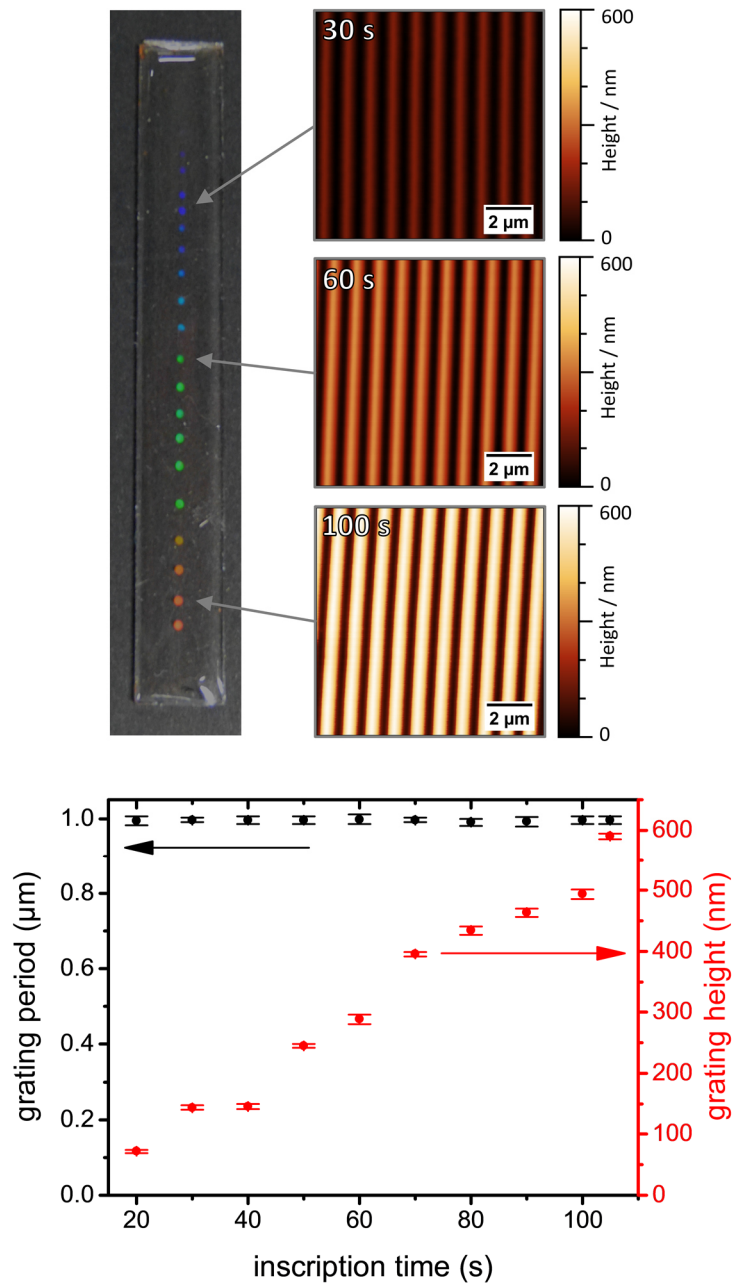


Figure 4.4.3: Photos of a PDMS strip with the size of 70 mm x 10 mm x 2 mm exhibiting different individual gratings with heights ranging from 70 nm to 600 nm. The strip was prepared from an azobenzene film and the SRGs were inscribed with different exposure times in order to obtain gratings with different heights. The periodicity and height of the gratings as a function of the inscription time are shown in the graph.

Particle alignment on PDMS replicas

A promising application of SRGs is their usage as topographical templates for colloidal self-assembly of nanoparticles. As compared to substrates obtained *via* strain-release wrinkling, the PDMS SRGs presented in this work represent high-quality substrates due to the absence of defects. This ensures a uniform spreading of the particle solution due to a continuous, smooth movement of the liquid meniscus in a solution-based assembly. Thus, regions of lower coverage caused by meniscus jumps can be avoided and a uniform and high-quality assembly can be obtained.

We used a circular PDMS template to study the particle alignment in a spin coating approach. This template was prepared from a circular azo master with several concentric inscribed SRGs with individual grating heights (cf. [SI 4.4.10.5](#)). The PDMS replica was treated with oxygen plasma prior to spin coating to improve the wettability with the nanoparticle solution. This process resulted in a relative loss in grating height of about 20% (cf. [SI 4.4.10.3](#)). The obtained template exhibits eight different SRGs with grating heights from 12 nm to 427 nm. This enables a fast and efficient screening of the alignment process on a single substrate in a one-step approach in a combinatorial manner.

For the alignment, we used spherical PS latex particles with a mean diameter of 186 ± 4 nm (cf. [SI 4.4.10.6](#)) in an aqueous suspension. The strongly charged PSS brushes grafted from the particle surface ensured good colloidal stability and repulsive particle–substrate interaction. In this way, the particles could easily be dragged by centripetal and capillary forces upon evaporation of the solvent to form colloidal crystals as defined by template geometry. [Figure 4.4.4](#) depicts the AFM height images of the assemblies of these nanoparticles. The formed structure depends on the period and height of the grating.

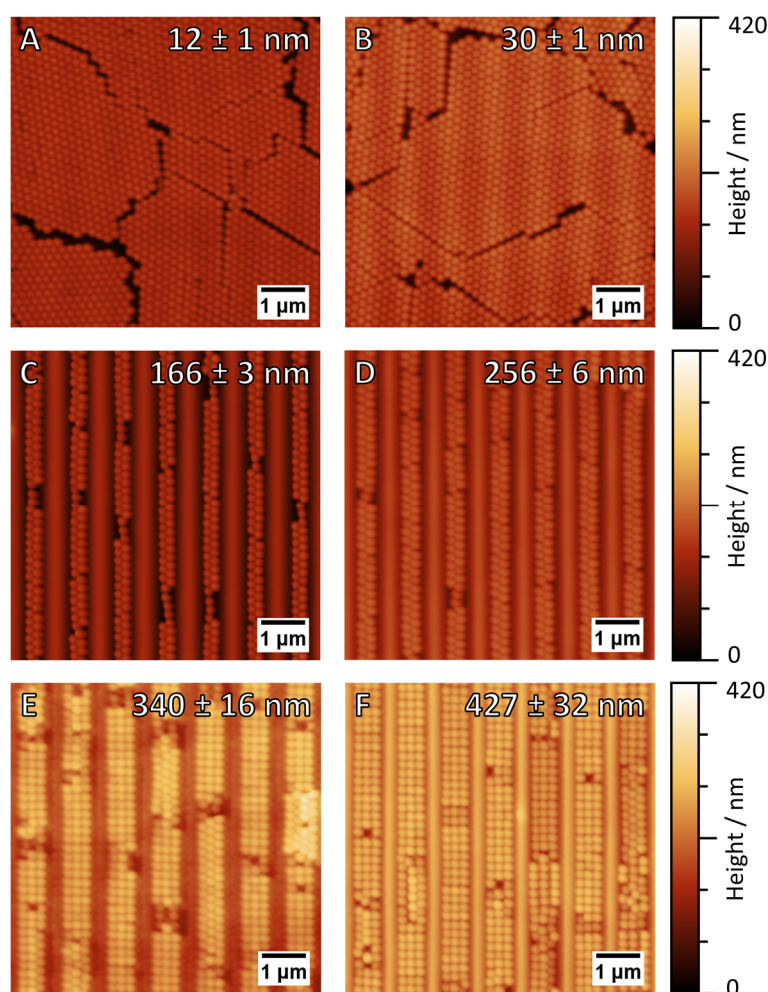


Figure 4.4.4: Alignment of polystyrene nanoparticles with a diameter of 186 ± 4 nm in replicated PDMS SRGs with different grating heights. The character of the formed particle lines changes with increasing grating height from a hexagonal monolayer (A and B) to a hexagonal double line (C and D) and finally to a 3D cubic assembly with six-fold strands in the filled grooves (E and F).

The ideal packing behavior of a non-confined particle assembly is a hexagonal monolayer. Gratings with a very small grating height of 30 nm and less (Figure 4.4.4A and Figure 4.4.4B) show a slightly corrugated film surface, but the closed hexagonal monolayer structure on top is still intact. With increasing grating heights of 166 nm (Figure 4.4.4C) and 256 nm (Figure 4.4.4D), a significant confinement occurs, which leads to an observable nanoparticle alignment. There are still 2D hexagonal double lines and sporadic 1D single lines observable. A further increase in grating height to 340 nm (Figure 4.4.4E) and 427 nm (Figure 4.4.4F) leads to 3D assemblies and a change in the packing behavior. The predominant packing behavior in each groove is now a cubic assembly consisting of six particle lines stacked in a layered fashion.

We further studied these assemblies at a transition area utilizing SEM images recorded with an Everhart-Thornley detector and additionally with a centric backscattering detector (Figure 4.4.5), to provide a deeper insight into the particle alignment. With the information obtained from both detectors, we could prove that the hierarchical 3D pattern consists of a single line at the bottom covered by a double line in the middle and a threefold particle line on top. We attribute the change from 2D hexagonal to 3D cubic packing as follows. The single line at the bottom of the grooves directs the second particle layer above in a cubic assembly. In the third layer, the cubic order is preserved. Thus, our approach allows determining the critical grating height for confinement into lines with different order and alignment patterns.

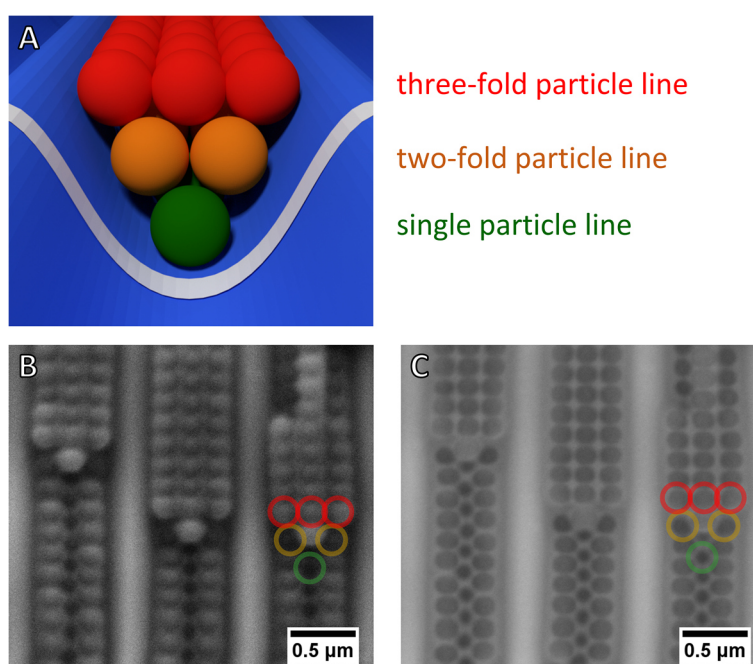


Figure 4.4.5: Schematic representation of a side-view of an assembly consisting of 6 lines of aligned nanoparticles (A). SEM images of aligned nanoparticles at a transition zone in a PDMS SRG with a grating height of 427 ± 32 nm, recorded with an Everhart-Thornley detector (B) and a centric backscattering detector (C) at the same position. Particles of each strand are exemplarily marked in color.

4.4.6. Conclusions

We have demonstrated the preparation of templates for particle alignment based on surface relief gratings that were written on azobenzene films. Due to the optical inscription process, the template materials reveal no significant defect structures. Besides PDMS, the grating can also be transferred to thermoplastic polymers like PC and PP, which probably allows for the alignment of nanoparticles dispersed in organic solvents. As compared to a controlled wrinkling approach, the grating height of the pattern can be tuned independently from the grating period. Tailoring of grating geometry defines the resulting morphology of hierarchical particle strands in terms of packing symmetry (hexagonal or cubic), width (2 - 3 particles) and dimensionality (2D single layer and 3D stacks). Furthermore, we can determine the critical grating height upon which particle confinement into lines becomes effective. Thus, these substrates are ideally suited for screening the template parameters for assembly of different particle systems. Beyond the “geometrical screening” application reported herein, gradient substrates offer unique potential for mechanical tuning of the particle assemblies and the optical effects connected to them. In previous work, we have already reported on pronounced optical effects upon stretching of single-line plasmonic particle assemblies.⁴⁹ For single lines, splitting into shorter chains occurs. Indeed, similar and even more complex scenarios are expected for multi-line structures reported herein and they could be screened efficiently, and more complex optical effects would become accessible. Thus, we envision applications in the field of strain sensing and (mechanically) tunable gratings up to metamaterials.

4.4.7. Conflicts of interest

There are no conflicts to declare.

4.4.8. Acknowledgements

Funding of this work was provided by the University of Bayreuth and the European Union’s Seventh Framework Program FP7/2007–2013 under Grant Agreement No. 318804 (SNM: Single Nanometer Manufacturing for beyond CMOS devices). AES and PTP thank the Elite

Network of Bavaria (ENB), Macromolecular Science for their individual support. We thank Christoph Hanske (Leibniz Institute for Polymer Research, Dresden) for providing the polystyrene nanoparticles as well as Andreas Frank and Martina Heider for their support with SEM measurements. Moreover, we thank the Keylabs “Small Scale Polymer Processing”, “Electron and Optical Microscopy” and “Surface and Interface Characterization” of the Bavarian Polymer Institute for their infrastructural support.

4.4.9. Notes and references

- [1] H. Audorff, K. Kreger, R. Walker, D. Haarer, L. Kador and H.-W. Schmidt, in *Complex Macromolecular Systems II*, ed. A. H. E. Müller and H.-W. Schmidt, Springer Berlin Heidelberg, Berlin, Heidelberg **2010**, pp. 59–121.
- [2] P. Rochon, E. Batalla and A. Natansohn, *Appl. Phys. Lett.* **1995**, *66*, 136–138, “Optically induced surface gratings on azoaromatic polymer films”.
- [3] D. Y. Kim, S. K. Tripathy, L. Li and J. Kumar, *Appl. Phys. Lett.* **1995**, *66*, 1166–1168, “Laser-induced holographic surface relief gratings on nonlinear optical polymer films”.
- [4] N. S. Yadavalli, S. Loebner, T. Papke, E. Sava, N. Hurduc and S. Santer, *Soft Matter* **2016**, *12*, 2593–2603, “A comparative study of photoinduced deformation in azobenzene containing polymer films”.
- [5] A. Priimagi and A. Shevchenko, *J. Polym. Sci. Part B: Polym. Phys.* **2014**, *52*, 163–182, “Azopolymer-based micro- and nanopatterning for photonic applications”.
- [6] S. Lee, H. S. Kang and J.-K. Park, *Adv. Mater.* **2012**, *24*, 2069–2103, “Directional photofluidization lithography: micro/nanostructural evolution by photofluidic motions of azobenzene materials”.
- [7] C. J. Barrett, J.-i. Mamiya, K. G. Yager and T. Ikeda, *Soft Matter* **2007**, *3*, 1249, “Photo-mechanical effects in azobenzene-containing soft materials”.

-
- [8] Y. Zhao and T. Ikeda,
John Wiley & Sons, Inc, Hoboken, NJ, USA **2009**,
"Smart Light-Responsive Materials".
- [9] K. G. Yager and C. J. Barrett,
J. Photochem. Photobiol., A **2006**, *182*, 250–261,
"Novel photo-switching using azobenzene functional materials".
- [10] A. Natansohn and P. Rochon,
Chem. Rev. **2002**, *102*, 4139–4176,
"Photoinduced Motions in Azo-Containing Polymers".
- [11] J. Konieczkowska, E. Schab-Balcerzak, M. Libera, I. Mihaila and I. Sava,
European Polymer Journal **2019**, *110*, 85–89,
"Surface relief gratings in azopolyimides induced by pulsed laser irradiation".
- [12] S. Moujdi, A. Rahmouni, T. Mahfoud, D. V. Nesterenko, M. Halim and Z. Sekkat,
Journal of Applied Physics **2018**, *124*, 213103,
"Surface relief gratings in azo-polymers revisited".
- [13] C. Probst, C. Meichner, H. Audorff, R. Walker, K. Kreger, L. Kador and H.-W. Schmidt,
J. Polym. Sci. Part B: Polym. Phys. **2016**, *54*, 2110–2117,
"Improving holographic writing performance of photo-orientable azobenzene polymers by molecular glasses".
- [14] R. H. Berg, S. Hvilsted and P. S. Ramanujam,
Nature **1996**, *383*, 505–508,
"Peptide oligomers for holographic data storage".
- [15] N. K. Viswanathan, D. Y. Kim, S. Bian, J. Williams, W. Liu, L. Li, L. Samuelson, J. Kumar and S. K. Tripathy,
J. Mater. Chem. **1999**, *9*, 1941–1955,
"Surface relief structures on azo polymer films".
- [16] K. Kreger, P. Wolfer, H. Audorff, L. Kador, N. Stingelin-Stutzmann, P. Smith and H.-W. Schmidt,
J. Am. Chem. Soc. **2010**, *132*, 509–516,
"Stable holographic gratings with small-molecular trisazobenzene derivatives".

- [17] H. J. Coufal, D. Psaltis and G. T. Sincerbox, eds., Springer, Berlin **2000**, vol. 76, *"Holographic data storage"*.
- [18] C. Meichner, A. E. Schedl, C. Neuber, K. Kreger, H.-W. Schmidt and L. Kador, *AIP Adv.* **2015**, 5, 87135, *"Refractive-index determination of solids from first- and second-order critical diffraction angles of periodic surface patterns"*.
- [19] H. Audorff, R. Walker, L. Kador and H.-W. Schmidt, *J. Phys. Chem. B* **2009**, 113, 3379–3384, *"Polarization dependence of the formation of surface relief gratings in azobenzene-containing molecular glasses"*.
- [20] H. Ji, Y. Zhao, C. Zong, J. Xie, X. Han, J. Wang, J. Zhao, S. Jiang, Y. Cao and C. Lu, *ACS Appl. Mater. Interfaces* **2016**, 8, 19127–19134, *"Simple and Versatile Strategy to Prevent Surface Wrinkling by Visible Light Irradiation"*.
- [21] C. Zong, Y. Zhao, H. Ji, X. Han, J. Xie, J. Wang, Y. Cao, S. Jiang and C. Lu, *Angew. Chem., Int. Ed. Engl.* **2016**, 55, 3931–3935, *"Tuning and Erasing Surface Wrinkles by Reversible Visible-Light-Induced Photoisomerization"*.
- [22] C. Zong, Y. Zhao, H. Ji, J. Xie, X. Han, J. Wang, Y. Cao, C. Lu, H. Li and S. Jiang, *Macromol. Rapid Commun.* **2016**, 37, 1288–1294, *"Patterning Surfaces on Azo-Based Multilayer Films via Surface Wrinkling Combined with Visible Light Irradiation"*.
- [23] A. M. Urbas, Z. Jacob, L. D. Negro, N. Engheta, A. D. Boardman, P. Egan, A. B. Khanikaev, V. Menon, M. Ferrera, N. Kinsey, C. DeVault, J. Kim, V. Shalaev, A. Boltasseva, J. Valentine, C. Pfeiffer, A. Grbic, E. Narimanov, L. Zhu, S. Fan, A. Alù, E. Poutrina, N. M. Litchinitser, M. A. Noginov, K. F. MacDonald, E. Plum, X. Liu, P. F. Nealey, C. R. Kagan, C. B. Murray, D. A. Pawlak, I. I. Smolyaninov, V. N. Smolyaninova and D. Chanda, *J. Opt.* **2016**, 18, 93005, *"Roadmap on optical metamaterials"*.
- [24] M. Tebbe, S. Lentz, L. Guerrini, A. Fery, R. A. Alvarez-Puebla and N. Pazos-Perez, *Nanoscale* **2016**, 8, 12702–12709, *"Fabrication and optical enhancing properties of discrete supercrystals"*.

-
- [25] M. Müller, M. Tebbe, D. V. Andreeva, M. Karg, R. A. Alvarez Puebla, N. Pazos-Pérez and A. Fery,
Langmuir **2012**, *28*, 9168–9173,
“Large-area organization of pNIPAM-coated nanostars as SERS platforms for polycyclic aromatic hydrocarbons sensing in gas phase”.
- [26] N. Pazos-Pérez, W. Ni, A. Schweikart, R. A. Alvarez-Puebla, A. Fery and L. M. Liz-Marzán,
Chem. Sci. **2010**, *1*, 174,
“Highly uniform SERS substrates formed by wrinkle-confined drying of gold colloids”.
- [27] M. Karg, T. A.F. König, M. Retsch, C. Stelling, P. M. Reichstein, T. Honold, M. Thelakkat and A. Fery,
Materials Today **2015**, *18*, 185–205,
“Colloidal self-assembly concepts for light management in photovoltaics”.
- [28] M. Mayer, M. J. Schnepf, T. A. F. König and A. Fery,
Adv. Opt. Mater. **2018**, *111*, 1800564,
“Colloidal Self-Assembly Concepts for Plasmonic Metasurfaces”.
- [29] M. Mayer, M. Tebbe, C. Kuttner, M. J. Schnepf, T. A. F. König and A. Fery,
Faraday Discuss. **2016**, *191*, 159–176,
“Template-assisted colloidal self-assembly of macroscopic magnetic metasurfaces”.
- [30] C. T. Riley, J. S. T. Smalley, J. R. J. Brodie, Y. Fainman, D. J. Sirbully and Z. Liu,
Proc. Natl. Acad. Sci. U. S. A. **2017**, *114*, 1264–1268,
“Near-perfect broadband absorption from hyperbolic metamaterial nanoparticles”.
- [31] A. P. Quist, E. Pavlovic and S. Oscarsson,
Anal. Bioanal. Chem. **2005**, *381*, 591–600,
“Recent advances in microcontact printing”.
- [32] C. Hanske, M. B. Müller, V. Bieber, M. Tebbe, S. Jessl, A. Wittemann and A. Fery,
Langmuir **2012**, *28*, 16745–16750,
“The role of substrate wettability in nanoparticle transfer from wrinkled elastomers: fundamentals and application toward hierarchical patterning”.
- [33] C. Hanske, M. Tebbe, C. Kuttner, V. Bieber, V. V. Tsukruk, M. Chanana, T. A. F. König and A. Fery,
Nano Lett. **2014**, *14*, 6863–6871,
“Strongly coupled plasmonic modes on macroscopic areas via template-assisted colloidal self-assembly”.

- [34] A. Schweikart and A. Fery,
Microchim. Acta **2009**, *165*, 249–263,
“Controlled wrinkling as a novel method for the fabrication of patterned surfaces”.
- [35] A. Schweikart, A. Fortini, A. Wittemann, M. Schmidt and A. Fery,
Soft Matter **2010**, *6*, 5860,
“Nanoparticle assembly by confinement in wrinkles”.
- [36] C. Lu, H. Möhwald and A. Fery,
Soft Matter **2007**, *3*, 1530,
“A lithography-free method for directed colloidal crystal assembly based on wrinkling”.
- [37] K. D. Sattler,
CRC Press, Boca Raton, Fla. **2011**, ed. by Klaus D. Sattler,
“Nanoelectronics and nanophotonics”.
- [38] A. Schweikart, N. Pazos-Pérez, R. A. Alvarez-Puebla and A. Fery,
Soft Matter **2011**, *7*, 4093,
“Controlling inter-nanoparticle coupling by wrinkle-assisted assembly”.
- [39] S. Hiltl, J. Oltmanns and A. Böker,
Nanoscale **2012**, *4*, 7338–7345,
“A one-step screening process for optimal alignment of (soft) colloidal particles”.
- [40] K. Efimenko, M. Rackaitis, E. Manias, A. Vaziri, L. Mahadevan and J. Genzer,
Nat. Mater. **2005**, *4*, 293–297,
“Nested self-similar wrinkling patterns in skins”.
- [41] S.-I. Na, S.-S. Kim, J. Jo, S.-H. Oh, J. Kim and D.-Y. Kim,
Adv. Funct. Mater. **2008**, *18*, 3956–3963,
“Efficient Polymer Solar Cells with Surface Relief Gratings Fabricated by Simple Soft Lithography”.
- [42] S. Lee, Y.-C. Jeong and J.-K. Park,
Opt. Express **2007**, *15*, 14550,
“Facile fabrication of close-packed microlens arrays using photoinduced surface relief structures as templates”.

-
- [43] B. Liu, M. Wang, Y. He and X. Wang,
Langmuir **2006**, *22*, 7405–7410,
“Duplication of photoinduced azo polymer surface-relief gratings through a soft lithographic approach”.
- [44] M. Kim, B. Kang, S. Yang, C. Drew, L. A. Samuelson and J. Kumar,
Adv. Mater. **2006**, *18*, 1622–1626,
“Facile Patterning of Periodic Arrays of Metal Oxides”.
- [45] S.-S. Kim, C. Chun, J.-C. Hong and D.-Y. Kim,
J. Mater. Chem. **2006**, *16*, 370–375,
“Well-ordered TiO₂ nanostructures fabricated using surface relief gratings on polymer films”.
- [46] S. Loebner, J. Jelken, N. S. Yadavalli, E. Sava, N. Hurduc and S. Santer,
Molecules (Basel, Switzerland) **2016**, *21*,
“Motion of Adsorbed Nano-Particles on Azobenzene Containing Polymer Films”.
- [47] H. Audorff, R. Walker, L. Kador and H.-W. Schmidt,
Chemistry **2011**, *17*, 12722–12728,
“Holographic investigations of azobenzene-containing low-molecular-weight compounds in pure materials and binary blends with polystyrene”.
- [48] M. Schrunner, B. Haupt and A. Wittemann,
Chem. Eng. J. **2008**, *144*, 138–145,
“A novel photoreactor for the production of electrosterically stabilised colloidal particles at larger scales”.
- [49] A. M. Steiner, M. Mayer, M. Seuss, S. Nikolov, K. D. Harris, A. Alexeev, C. Kuttner, T. A. F. König and A. Fery,
ACS Nano **2017**, *11*, 8871–8880,
“Macroscopic Strain-Induced Transition from Quasi-infinite Gold Nanoparticle Chains to Defined Plasmonic Oligomers”.

4.4.10. Supplementary Information

4.4.10.1. Schematic top view of the illuminated area

The holographic inscription process was carried out to generate SRGs with a spot diameter of 1 to 2 mm. While the grating periodicity (schematically indicated by vertical lines in [Figure 4.4.6](#)) remains constant over the whole spot size (cf. [4.4.10.2](#)), the grating height decreases from the center to the edges due to Gaussian beam profile (cf. [4.4.10.3](#)). An area with an approximately constant grating height exists around the center (blue circle) of the spot. For comparison, the typical size of an AFM image is shown in red.

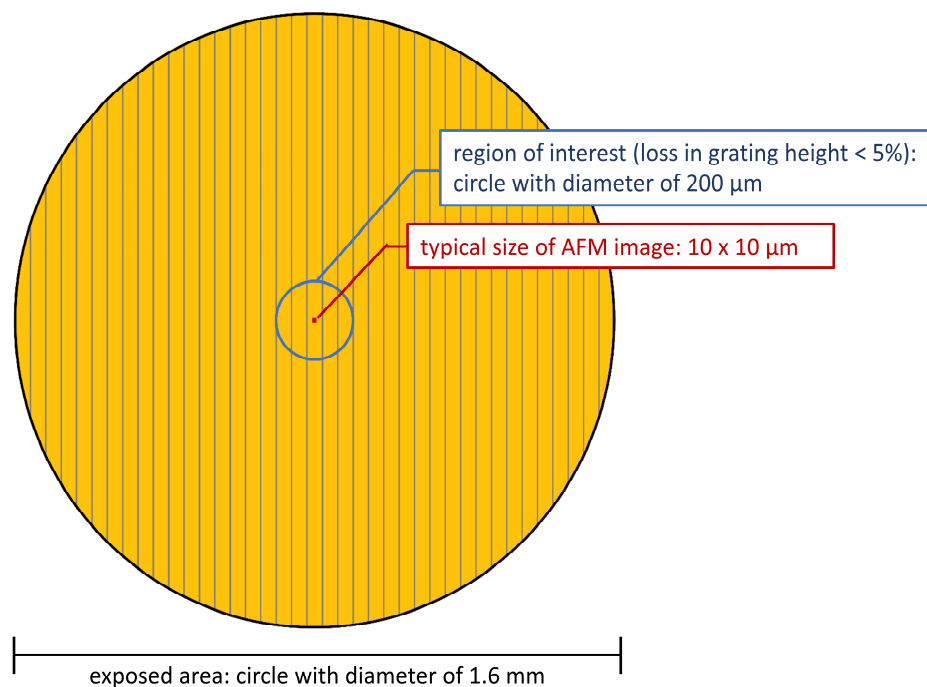


Figure 4.4.6: Scheme of the inscribed SRG spot with the indicated region of interest. The experiments were analyzed within this region.

4.4.10.2. Variation of grating period within the exposed area

We analyzed the variation of grating period and grating height along the entire exposed area of a PDMS replicated SRG. Over the entire area, the grating period remained constant. Treatment with oxygen plasma had no influence on this parameter.

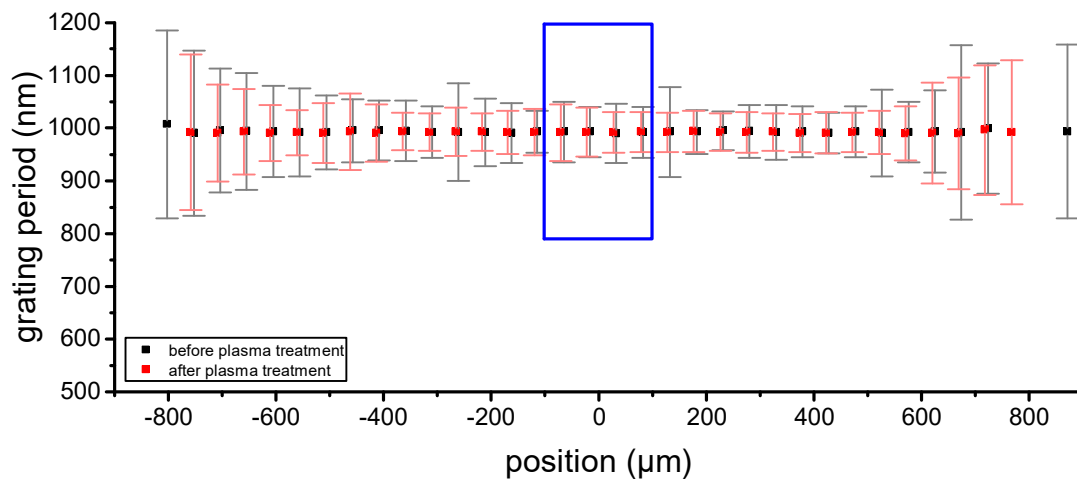


Figure 4.4.7: Variation of the grating period across the diameter of the exposed area of a PDMS replicated SRG before and after plasma treatment. The blue frame indicates the central region of interest for experiments.

4.4.10.3. Variation of grating height within the exposed area

The grating height has a maximum in the center of the PDMS SRG spot and decreases to the outside. It follows a Gaussian curve which can be attributed to the Gaussian beam intensity profile of the laser used to inscribe the gratings onto the azo film. Within a radius of about 100 μm around the central maximum, the grating height decreases by less than 5%. During surface activation by plasma etching, the overall grating height decreases by about 20%.

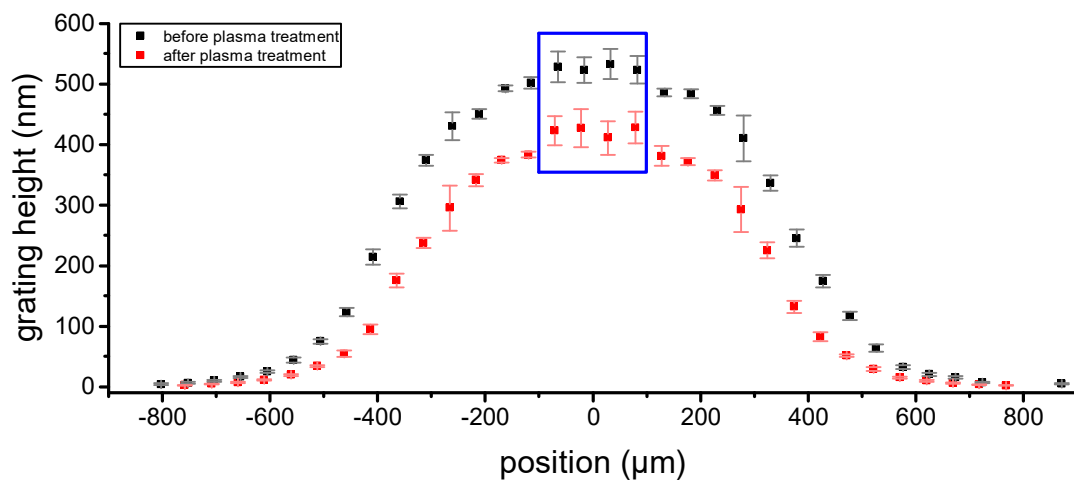


Figure 4.4.8: Variation of the grating height across the diameter of the exposed area of a PDMS replicated SRG before and after plasma treatment. The blue frame indicates the central region of interest in which the decrease of grating height is less than 5%.

4.4.10.4. Comparison of holographic writing and strain-release wrinkling

Due to the optical inscription process, surface relief gratings are defect-free over large areas. To demonstrate this, large-area AFM height images of $90 \times 90 \mu\text{m}$ were recorded. [Figure 4.4.9A](#) depicts a typical AFM height image of a PDMS SRG which was recorded in the central region of the exposed area. No defect structures are observable. In contrast, corrugated surfaces of similar dimensions fabricated *via* strain-release wrinkling show several defects ([Figure 4.4.9B](#)). In the stiff plasma-oxidized surface layer on a uni-axially pre-strained, compliant PDMS substrate, not only parallel periodic surface wrinkles formed upon release of the strain which are oriented perpendicular to the strain direction.¹⁻³ Due to lateral expansion, the brittle layer can form irregular cracks parallel to the stretching direction. Moreover, so-called y-branches can develop, if several regions of wrinkles merge together.⁴

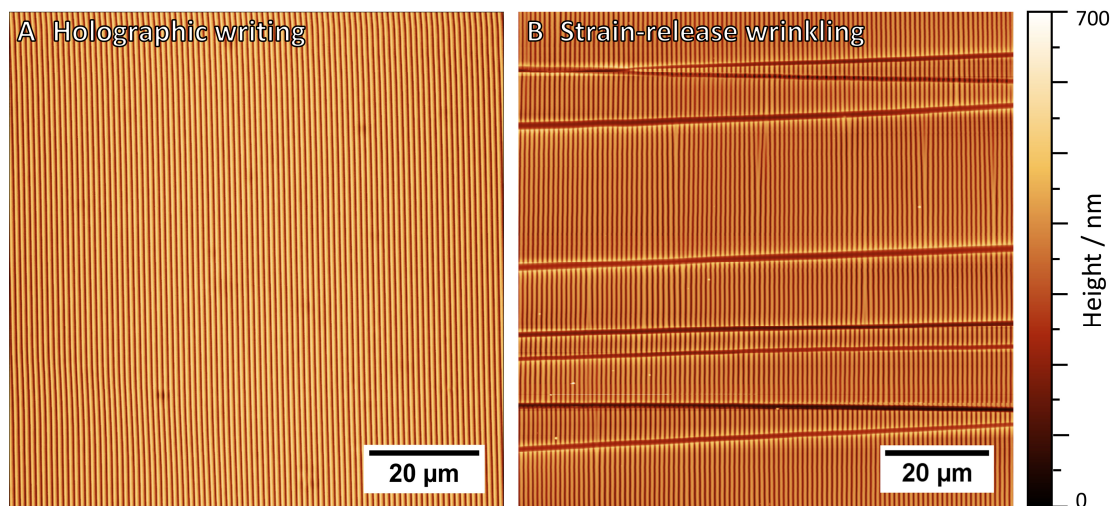


Figure 4.4.9: AFM height images of corrugated surfaces. Surface relief grating replicated with PDMS (A). Grating period is $1.0 \mu\text{m}$, grating height 580 nm . No significant defect structures are observable over large areas. Parallel surface wrinkles, grating period $892 \pm 67 \text{ nm}$ and grating height $261 \pm 22 \text{ nm}$, showing cracks and y-branches as defects (B).

References:

- [1] N. Bowden, S. Brittain, A. G. Evans, J. W. Hutchinson and G. M. Whitesides, *Nature* **1998**, 393, 146–149, *“Spontaneous formation of ordered structures in thin films of metals supported on an elastomeric polymer”*.
- [2] A. Schweikart, A. Fortini, A. Wittemann, M. Schmidt and A. Fery, *Soft Matter* **2010**, 6, 5860, *“Nanoparticle assembly by confinement in wrinkles: Experiment and simulations”*.
- [3] K. Efimenko, M. Rackaitis, E. Manias, A. Vaziri, L. Mahadevan and J. Genzer, *Nat. Mater.* **2005**, 4, 293–297, *“Nested self-similar wrinkling patterns in skins”*.
- [4] Z. Li, S. Zhang, P. Zhang, D. Yang, G. Jin and H. Ma, *Polym. Adv. Technol.* **2012**, 23, 1240–1245, *“Surface initiated polymerization from integrated poly(dimethylsiloxane) enables crack-free large area wrinkle formation”*.

4.4.10.5. Layout of the SRG substrate for particle alignment

We aligned the polystyrene nanoparticles on replicated PDMS SRGs *via* spin coating. To this end, we prepared a circular master sample with a diameter of 5 cm and inscribed 8 SRG spots with inscription times between 5 and 70 s (Figure 4.4.10). The SRGs are oriented towards the center.

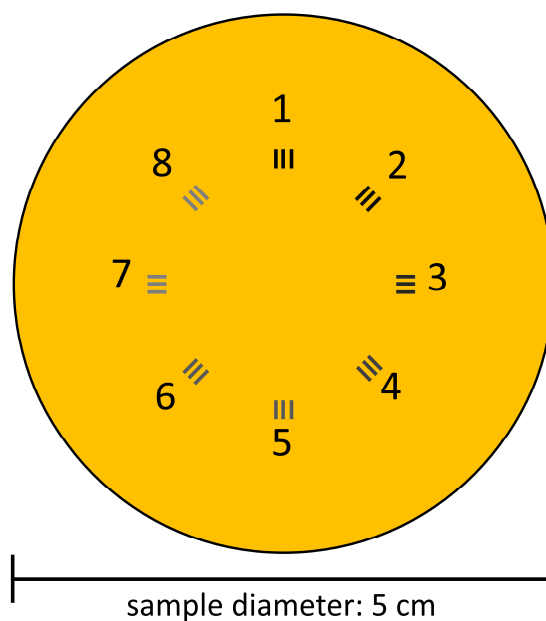


Figure 4.4.10: Circular master sample with 8 inscribed SRG spots for particle alignment *via* spin-coating.

4.4.10.6. Dimensions of particles used for the alignment investigations

Particle dimensions were measured *via* AFM analysis of dried PS latex particles on a silicon wafer. The evaluation of 136 individual particles reveals a mean diameter of 186 ± 4 nm (Figure 4.4.11).

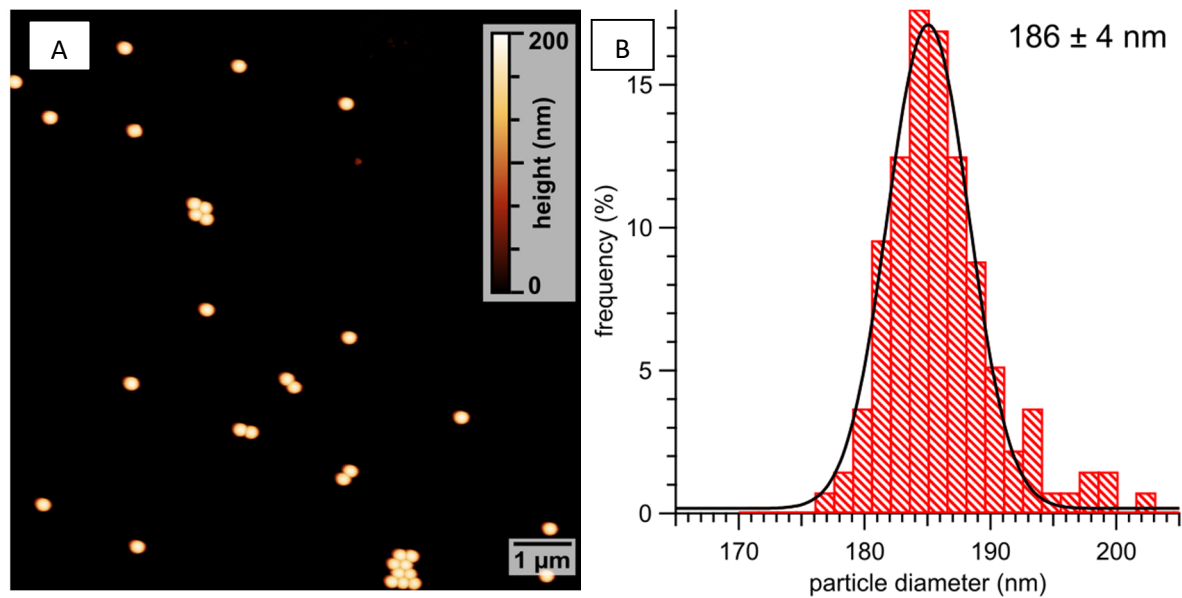


Figure 4.4.11: AFM analysis of particle dimensions. Representative AFM height image of PS latex particles dried on a silicon wafer (A). Diameter histogram of 136 particles evaluated (B).

4.5. Refractive-index determination of solids from first- and second-order critical diffraction angles of periodic surface patterns

*Christoph Meichner,^{*a} Andreas E. Schedl,^b Christian Neuber,^b Klaus Kreger,^b
Hans-Werner Schmidt^{*b} and Lothar Kador^{*a}*

a) Institute of Physics and Bayreuth Institute of Macromolecular Research,
University of Bayreuth, Universitätsstr. 30, 95447 Bayreuth, Germany

b) Macromolecular Chemistry I, Bayreuth Institute of Macromolecular Research and
Bayreuth Center for Colloids and Interfaces, Universitätsstr. 30, 95447 Bayreuth, Germany

The results of this chapter have been published as a full paper article in

AIP Advances **2015**, 5, 087135.

Published by the *American Institute of Physics*

under a Creative Commons Attribution 3.0 Unported License.

DOI: 10.1063/1.4928654

4.5.1. Abstract

We present two approaches for measuring the refractive index of transparent solids in the visible spectral range based on diffraction gratings. Both require a small spot with a periodic pattern on the surface of the solid, collimated monochromatic light, and a rotation stage. We demonstrate the methods on a polydimethylsiloxane film (*Sylgard*[®] 184) and compare our data to those obtained with a standard Abbe refractometer at several wavelengths between 489 and 688 nm. The results of our approaches show good agreement with the refractometer data. Possible error sources are analyzed and discussed in detail; they include mainly the linewidth of the laser and/or the angular resolution of the rotation stage. With narrow-band light sources, an angular accuracy of $\pm 0.025^\circ$ results in an error of the refractive index of typically $\pm 5 \cdot 10^{-4}$. Information on the sample thickness is not required.

4.5.2. Introduction

The precise knowledge of the refractive-index dispersion of solid materials is required for numerous applications such as thin-film coatings, fiber optics, optical elements, and many more.^{1,2} Hence, new methods for its determination are still being devised today,³ many of which are optimized for a particular type of application. In liquids, the refractive index can be measured precisely with common techniques⁴ which, however, become demanding when applied to solids. The Abbe refractometer, for example, often requires index-matching fluids of high refractive index to optically couple the solid sample to the prism. Immersion liquids tend to be chemically or physically aggressive and can dissolve the sample or even the surface of the prism. The dispersion of the prism must be known to high accuracy, and tedious calculations are necessary to correct the refractometer scale for different wavelengths. Spectral ellipsometry is an alternative method for investigating thin solid films. However, this technique is more elaborate and the accuracy of the results depends strongly on the model used to evaluate the experimental data. Exact information about the refractive index of the substrate and the thicknesses of all layers on the sample is necessary. Similar arguments apply to refractive indices derived from reflectance or transmittance spectra. Even though the method is simple and effective, the thickness of the sample must be known to the desired accuracy and needs to be constant across the entire illuminated area. Otherwise numerical

modeling is required or the spectroscopic technique becomes more complicated (e.g., involving angle-dependent measurements).⁵

Here we present two versions of a novel method which can be applied to transparent solids or solid films with a periodic pattern on a spot at or near their surface. In contrast to other methods, they allow the direct measurement of the index of refraction from the grating constant and/or the diffraction angles. Other, independently measured, quantities, e.g., the film thickness, are not required.

Periodic surface patterns can, for example, be embossed or imprinted with lithographic techniques, or generated holographically. In the latter case, all parameters can directly be obtained within the experimental setup. Holographic exposure of many azobenzene derivatives gives rise to photo-induced mass transport over macroscopic distances, which results in the formation of surface relief gratings (SRGs).^{6,7} However, the applicability of our method is not limited to photo-active systems because it only requires the periodic pattern. We demonstrate this for a transparent colorless polydimethylsiloxane (PDMS) working stamp. The surface pattern was generated by imprinting an SRG, which was holographically fabricated on an azobenzene glass.

4.5.3. Theory

Let us consider a transparent film with refractive index n_{mat} on a substrate and with an interface to air on its upper side. A periodic pattern with periodicity Λ shall be present on a small spot at the surface as sketched in [Figure 4.5.1](#). The cross-sectional shape of the structure is not important; it can vary over a wide range (sinusoidal, rectangular, etc.). A monochromatic plane light wave with wavelength λ (in air) incident at angle $\varphi_{l,\text{in}}$ is then diffracted into different orders l inside the material under angles $\varphi_{l,\text{out}}$. The angles are given by the grating equation

$$n_{\text{mat}} \sin \varphi_{l,\text{out}} = n_{\text{air}} \sin \varphi_{l,\text{in}} + l \frac{\lambda}{\Lambda} \quad (4.5.1)$$

which can be derived from simple geometrical considerations. A less heuristic approach presented by Petit⁸ shows that this equation is valid for any periodic structure (strictly speaking, of infinite lateral extension). In the limit of the Bragg regime,^{9–11} valid for thick

gratings, the diffraction shows angular selectivity, i.e., the intensity of orders other than $l = 0$ and $l = 1$ is zero. To avoid this situation, the grating amplitude must be sufficiently small, which is usually the case for periodic surface structures. The 0th order simply follows Snellius' law of refraction, so its angle $\varphi_{0,out}$ inside the material is smaller than the angle $\varphi_{0,in}$ in air. Higher orders, on the other hand, can propagate in the material at angles $\varphi_{l,out} > \varphi_{l,in}$ for suitable values of the ratio λ/Λ . In this case we can orient the sample in such a way that, e. g., the first order, which is usually most intense, has an angle of $\varphi_{1,out} = \pi/2$. Equation 4.5.1 then becomes

$$n_{mat} = \sin \varphi_{1,in}^{90^\circ} + \frac{\lambda}{\Lambda} \quad (4.5.2)$$

with n_{air} set to 1. This simple expression allows us to determine the refractive index n_{mat} of the material without knowledge of its thickness or of parameters of the substrate. Only the quantities λ , Λ , and $\varphi_{1,in}^{90^\circ}$ must be known to the desired accuracy.

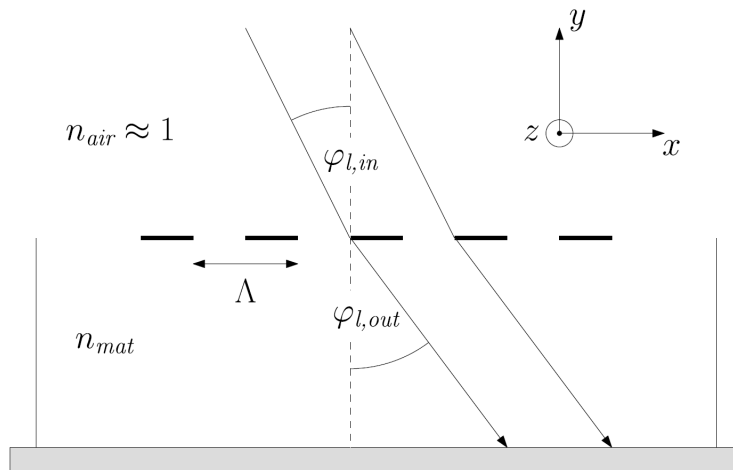


Figure 4.5.1: Sketch of a light beam incident onto a film carrying a periodic surface pattern. Only one diffraction order l is shown for clarity.

An alternative access to n_{mat} is obtained by writing down an expression analogous to Equation 4.5.2 for the second diffraction order and subtracting it from Equation 4.5.2,

$$\frac{\lambda}{\Lambda} = \sin \varphi_{1,in}^{90^\circ} - \sin \varphi_{2,in}^{90^\circ} \quad (4.5.3)$$

Inserting Equation 4.5.3 into Equation 4.5.2 finally yields

$$n_{\text{mat}} = 2 \sin \varphi_{1,\text{in}}^{90^\circ} - \sin \varphi_{2,\text{in}}^{90^\circ} \quad (4.5.4)$$

The refractive index n_{mat} can be calculated either from Equation 4.5.2 or Equation 4.5.4, depending on which experimental parameters are known to higher accuracy. Equation 4.5.2 requires the knowledge of the periodicity Λ , which can be obtained, e. g., from AFM or SEM investigations, and of the wavelength λ of the probing laser according to Equation 4.5.3. If the grating is inscribed holographically, its period can easily be calculated by $\Lambda = \lambda w [2 \sin(\phi/2)]^{-1}$.¹² In the case of Equation 4.5.4, the error margin depends solely on the accuracy of angle measurements.

The refractive index in Equation 4.5.2 is calculated from two terms, the sine term and the ratio λ/Λ . If λ/Λ is chosen too small (i.e., Λ too big), large values of n_{mat} cannot be measured, since the first term contributes a maximum value of 1. However, this constitutes no limitation to our approach. In a more general form, one can write the condition which an arbitrary diffraction order l has to fulfill in the form $l \lambda/\Lambda < n_{\text{mat}} < 1 + l \lambda/\Lambda$. If we assume, for example, that the refractive index is to be determined near a typical wavelength of 500 nm and Λ is chosen as 1000 nm, one can measure refractive indices within the range $n_{\text{mat}} < 1.5$ with an angular measurement of the first propagating order ($l = 1$). The second order ($l = 2$) allows determination of refractive indices between 1 and 2, and the third order ($l = 3$) between 1.5 and 2.5. Hence, there is always the possibility to measure any refractive index with an appropriate choice of the diffraction order. Similar arguments apply to the determination of the refractive index with Equation 4.5.4.

4.5.4. Experimental

We demonstrate our method on a cast film of PDMS. The periodic surface grating was prepared in a way similar to the procedure described in Ref. 13. First a thin film of a photo-addressable molecular glass, a spirobischroman-based 6,6',7,7' tetraester, containing four azobenzene moieties per molecule¹⁴ was prepared by spin-casting from a 7 wt% THF solution on a glass substrate. The substrate was spun at 700 rpm for 60 s, resulting in a film thickness of approximately 1 μm as determined by a step profiler. The film was annealed at 80 $^{\circ}\text{C}$ for 1 h under nitrogen atmosphere to remove residual solvent. Subsequently, it was exposed to holographic illumination with two coherent p-polarized laser beams ($\lambda_w = 489 \text{ nm}$, diameter ca. 2 mm) of equal intensity ($1\text{W}/\text{cm}^2$ per beam). The angle between the beams was adjusted to $\phi = 28.3^{\circ}$, resulting in a grating period Λ of $1000.6 \pm 1.7 \text{ nm}$. During 100 s of exposure, an SRG with a height of approximately 400 nm (minimum to maximum) is developed. SRGs were inscribed at different spots across the film surface to verify reproducibility.

In a second step 1 g of Sylgard[®] 184 cast resin (siloxane/curing agent = 10:1 (w/w)) was placed on top of the azobenzene film with the inscribed grating and pressed to a film with a second glass slide from above. Its thickness was adjusted with two spacers of Scotch tape on both sides of the substrate. In this way, the negative pattern of the SRG was imprinted on the PDMS film. Curing of the PDMS was performed at room temperature overnight, followed by a thermal curing step at 80 $^{\circ}\text{C}$ for 2 h. After curing, the two films on their substrates could easily be separated from each other. The resulting sample for the refractive-index measurements was a glass slide carrying a flat transparent PDMS coating of about 100 μm thickness with several negative type SRGs at different spots.

The PDMS sample was placed on a rotation stage and illuminated with collimated laser beams of 9 different wavelengths. A multi-color He-Ne laser provided lines at 593.932, 604.613, 611.802, and 632.816 nm, while different diode and diode-pumped solid-state lasers were used for the wavelengths 489.20, 532.06, 660.3, 671.8, and 688.4 nm. All lasers were s-polarized. The sample was rotated about the z axis as indicated in Figure 4.5.1 to measure the angles $\varphi_{i,\text{in}}^{90^{\circ}}$ to an accuracy of 0.025 $^{\circ}$. The diffracted orders passed PDMS film and glass substrate and were totally reflected at the back side of the substrate. The angle of incidence, for which a given diffraction order just does not reach the boundary between PDMS film and

substrate, is the angle $\varphi_{l,\text{in}}^{90^\circ}$. These angles could be determined for the first two diffraction orders ($l = 1$ and 2); for higher orders, Equation 4.5.1 had no solution.

The results of the refractive index are compared with data measured with an Abbe refractometer (Zeiss Abbe-Refraktometer Modell A). A PDMS strip of size $4 \times 1 \text{ cm}^2$ and thickness 2.5 mm was prepared to perfectly fit its prism size. Owing to the softness of the material and its adhesion to the prism, no immersion fluid was needed. For dispersion measurements, the internal scale of the refractometer had to be re-calculated for each wavelength at the neutral position of the compensator as described by the manufacturer. All experiments were conducted at room temperature.

4.5.5. Discussion

Figure 4.5.2 shows the wavelength-dependent refractive-index data of the PDMS elastomer as obtained by the different measurement procedures. The data of the Abbe refractometer are represented by open squares; their error bars result from the precision of its internal scale. With increasing wavelength, the refractive index decreases from 1.421 to 1.412, as is expected for a transparent, colorless material (normal dispersion). The refractive-index values measured with our approach are shown as open circles (calculated with Equation 4.5.2) and open triangles (Equation 4.5.4). All data points were obtained with light diffracted off the same imprinted surface pattern. They show a similar behavior, yet, with subtle deviations from the refractometer results. Most of them have systematically lower values. Whereas the deviation is roughly constant (ca. -0.002) when determined with Equation 4.5.4, the refractive index increases in the case of Equation 4.5.2 for wavelengths larger than 650 nm to a value slightly above the last refractometer point. No anomalous dispersion is observed here, because the sample is a transparent, colorless solid. This finding is confirmed by the dispersion data obtained with the Abbe refractometer.

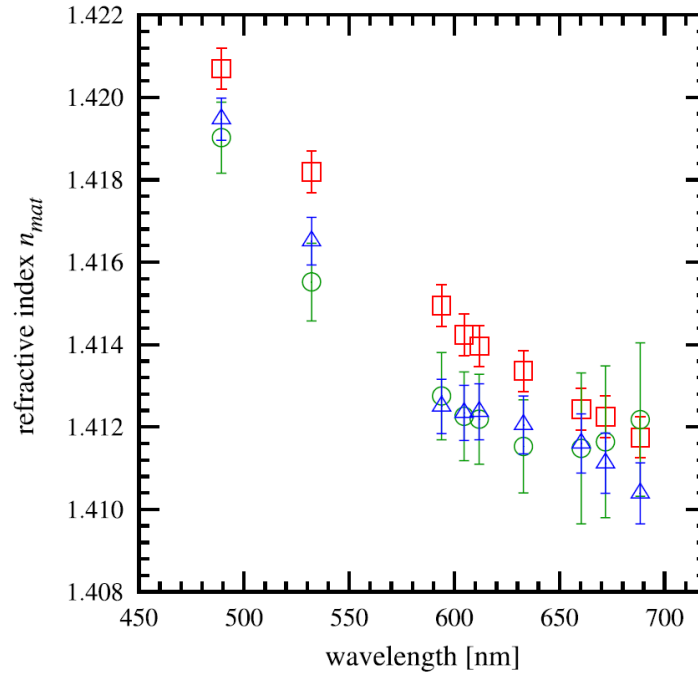


Figure 4.5.2: Wavelength-dependent refractive index of the Sylgard® 184 PDMS elastomer as obtained by different techniques. Open squares: Abbe refractometer data; open circles: As calculated from Equation 4.5.2; open triangles: As calculated from Equation 4.5.4.

The data calculated with Equation 4.5.2 and Equation 4.5.4 are affected by different experimental error sources. Equation 4.5.4 is sensitive only, but to a larger extent, to inaccurate determination of the angles of incidence, whereas Equation 4.5.2 suffers also from errors of the light wavelength λ and the grating periodicity Λ (as indicated by the larger error bars). Specifically, if Λ is not known exactly, an offset is caused in the whole data set. Hence, an inaccurate grating constant Λ cannot introduce errors only at longer wavelengths. Similarly, errors in the angle determination cannot be responsible for the increase of the refractive index, since the data calculated with Equation 4.5.4 would be affected as well. This indicates that the inserted wavelengths λ of the laser sources are responsible for the effect.

If three decimal digits of the refractive index are to be determined, the wavelength of the probing light must be known to an accuracy of about 1 nm. Also, its spectral width is important, since the angle $\varphi_{1,in}^{90^\circ}$ is determined by the experimental criterion that the first diffraction order does not propagate into the substrate. If the light source has a non-zero spectral width, Equation 4.5.1 implies that the shortest wavelength of its spectrum becomes evanescent for the largest angle $\varphi_{1,in}^{90^\circ}$. Hence, inserting the peak wavelength into Equation 4.5.2 gives rise to a systematic error if the spectral width is comparable to, or larger than, the error margin of 1 nm mentioned above. In our experiment, this is the case for the

diode lasers providing the long wavelengths 660.3, 671.8, and 688.4 nm. Their spectral width (FWHM; full width at half-maximum) was measured as 2.8 nm in a spectrometer, whereas all other laser sources have spectral widths below 0.1 nm.

A possibility to correct for this systematic error consists in replacing the peak wavelength λ of the laser in Equation 4.5.2 by a wavelength λ' close to the blue edge of its spectrum. Since the spectral profile of the diode lasers is Gaussian, it is reasonable to choose λ' as the wavelength at which the intensity has decreased to $1/e^2$ of its peak value. This leads to wavelengths λ' of 658.8, 669.9, and 686.9 nm, respectively, for the three diode lasers. Inserting them into Equation 4.5.2 (with all other data unchanged) yields the refractive indices shown in Figure 4.5.3. Now their values decrease monotonously as expected and are in good agreement with the data calculated with Equation 4.5.4. The error bars are quite large for the wavelengths above 650 nm, however.

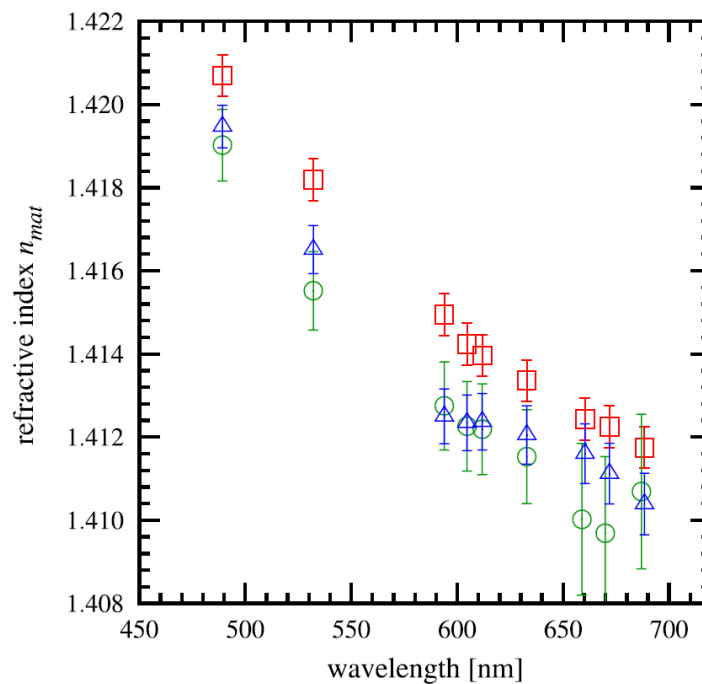


Figure 4.5.3: Same as Figure 4.5.2, but with the corrected wavelengths 658.8, 669.9 and 686.9 nm inserted into Equation 4.5.2 instead of the peak wavelengths 660.3, 671.8, and 688.4 nm, respectively.

The refractive indices calculated with both Equation 4.5.2 and Equation 4.5.4 are systematically smaller than those of the Abbe refractometer. The data obtained from Equation 4.5.2 become slightly larger when the grating period Λ determined from the parameters of the holographic inscription is replaced by $\Lambda = 999.7 \pm 1.0$ nm, the average of the Λ values calculated from Equation 4.5.3. This gives only rise to a minor change and affects only Equation 4.5.2, so the data are not shown.

To further investigate possible error sources, the influence of the laser polarization was checked. No difference of the refractive indices was found in measurements performed with s- and p-polarized light, so no anisotropy or birefringence was present in the PDMS sample. Furthermore, the measurements were repeated with gratings of different spots. All these experiments yielded identical data. Rotating the sample in the opposite direction and measuring $\varphi_{-1,\text{in}}^{90^\circ}$ and $\varphi_{-2,\text{in}}^{90^\circ}$ for the negative diffraction orders also resulted in the same refractive-index values. This demonstrates the robustness of our method with respect to slight variations of the surface quality of the sample.

We were not able to determine a clear origin of the offset between the refractometer data and those obtained with our method. Taking the error bars into account, the offset is almost negligible. The only quantity which enters in both Equation 4.5.2 and Equation 4.5.4 is the angle $\varphi_{1,\text{in}}^{90^\circ}$ of the first diffraction order. Hence, one possibility is that the offset of the data is due to a small systematic error in determining this angle. There is always some degree of ambiguity in the decision, at which position the intensity of a diffracted beam can be considered exactly zero, so the angles might be slightly larger than measured. In our experiments, the angles were determined by the criterion that the respective diffracted orders were just invisible to the human eye. If each angle $\varphi_{1,\text{in}}^{90^\circ}$ is increased by as little as 0.05° , our refractive indices coincide with the refractometer data within the error margins.

4.5.6. Conclusion

We have presented a method for measuring the refractive indices of solids, which is precise to about three decimal digits. Two different approaches of data evaluation were discussed which are sensitive to different experimental error sources. Our method is based on the diffraction of monochromatic laser light off a periodic surface pattern which must be present on a spot of the material. The profile of the grating (sinusoidal, rectangular, etc.) is not important, nor is the thickness of the material. Only the wavelengths and/or angles of incidence of the light must be known or measured precisely. Because periodic patterns can be obtained with various techniques (e.g., holographic inscription, embossing, imprinting, or others) the method offers a broad scope of applications.

4.5.7. Acknowledgments

This publication was funded by the University of Bayreuth in the funding program Open Access Publishing. The research leading to these results has received funding from the European Union's Seventh Framework Programme FP7/2007-2013 under Grant Agreement No. 318804 (SNM: Single Nanometer Manufacturing for beyond CMOS devices). We wish to thank W. Köhler for the loan of the Abbe refractometer and helpful instructions for its use.

4.5.8. References

- [1] H. A. Macleod,
Institute of Physics Publishing, 3rd edn. **2001**,
"Thin Film Optical Filters".

- [2] F. M. Mitschke,
Springer **2009**,
"Fiber Optics Physics and Technology".

- [3] R. J. Nussbaumer, M. Halter, T. Tervoot, W. R. Caseri and P. Smith, *J. Mater. Sci.* **2005**, *40*, 575–582, “A Simple Method for the Determination of Refractive Indices of (Rough) Transparent Solids”.
- [4] S. Singh, *Phys. Scripta* **2002**, *65*, 167–180, “Refractive Index Measurement and Its Applications”.
- [5] B. Šantić, *Thin Solid Films* **2010**, *518*, 3619–3624, “Measurement of the Refractive Index and Thickness of a Transparent Film From the Shift of the Interference Pattern Due to the Sample Rotation”.
- [6] H. Audorff, R. Walker, L. Kador and H.-W. Schmidt, *J. Phys. Chem. B* **2009**, *113*, 3379–3384, “Polarization Dependence of the Formation of Surface Relief Gratings in Azobenzene-Containing Molecular Glasses”.
- [7] H. Audorff, K. Kreger, R. Walker, D. Haarer, L. Kador and H.-W. Schmidt, *Adv. Polym. Sci.* **2010**, *228*, 59–121, “Holographic Gratings and Data Storage in Azobenzene-Containing Block Copolymers and Molecular Glasses”.
- [8] R. Petit, Springer **1980**, “Electromagnetic Theory of Gratings”.
- [9] M. G. Moharam, T. K. Gaylord and R. Magnusson, *Opt. Commun.* **1980**, *32*, 14–18, “Criteria for Bragg Regime Diffraction by Phase Gratings”.
- [10] H. Kogelnik, *Bell Syst. Tech. J.* **1969**, *48*, 2909–2947, “Coupled Wave Theory for Thick Hologram Gratings”.
- [11] R. Magnusson and T. Gaylord, *J. Opt. Soc. Am.* **1977**, *67*, 1165–1170, “Analysis of Multiwave Diffraction of Thick Gratings”.

- [12] R. Magnusson and T. Gaylord,
J. Opt. Soc. Am. **1978**, *68*, 806–809,
“Diffraction Efficiencies of Thin Phase Gratings with Arbitrary Grating Shape”.
- [13] R. Walker, H. Audorff, L. Kador and H.-W. Schmidt,
Adv. Funct. Mater. **2009**, *19*, 2630–2638,
“Synthesis and Structure-Property Relations of a Series of Photochromic Molecular Glasses for Controlled and Efficient Formation of Surface Relief Nanostructures”.
- [14] H. Audorff, R. Walker, L. Kador and H.-W. Schmidt,
Chem. Eur. J. **2011**, *17*, 12722–12728,
“Holographic Investigations of Azobenzene-Containing Low-Molecular-Weight Compounds in Pure Materials and Binary Blends with Polystyrene”.

4.6. Gradient photonic materials based on one-dimensional polymer photonic crystals

*Andreas E. Schedl,^a Irene Howell,^b James J. Watkins^{*b} and Hans-Werner Schmidt^{*a}*

a) Department of Macromolecular Chemistry I and Bavarian Polymer Institute, University of Bayreuth, 95440 Bayreuth, Germany

b) Center for Hierarchical Manufacturing, Department of Polymer Science and Engineering, University of Massachusetts Amherst, 120 Governors Drive, Amherst, Massachusetts 01003, USA

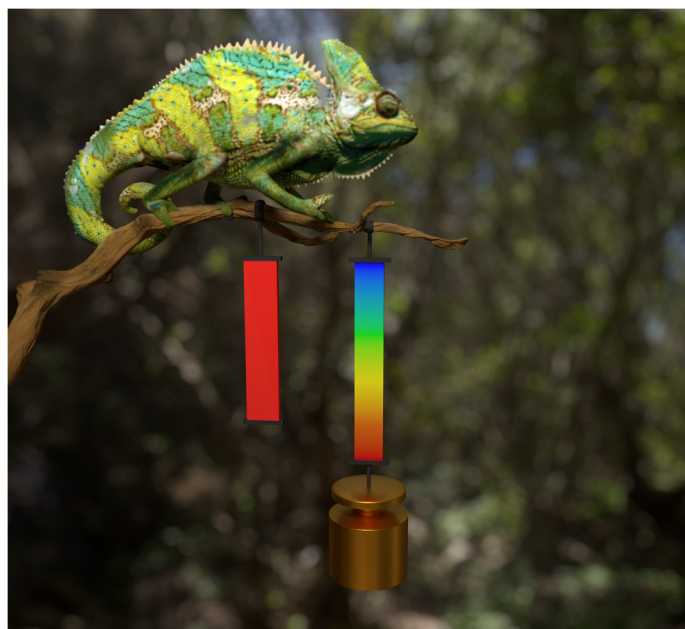
The results of this chapter have been published as a communication article in

Macromolecular Rapid Communications **2020**, *41*, 2000069.

Published by *WILEY-VCH Verlag GmbH & Co. KGaA*

under a Creative Commons Attribution 4.0 International License.

DOI: 10.1002/marc.202000069



Gradient photonic materials consisting of a 1D polymer photonic crystal attached to an elastomer with a defined gradient in stiffness are able to change their color upon strain. Tuning the stiffness and the architecture of the gradient elastomer allows the formation of tailored reflectance patterns.

4.6.1. Front cover

Volume 41 • Number 8 • April 20, 2020

www.mrc-journal.de



Macromolecular Rapid Communications



8/2020

WILEY-VCH

4.6.2. Abstract

In nature, animals such as chameleons are well-known for the complex color patterns of their skin and the ability to adapt and change the color by manipulating sophisticated photonic crystal systems. Artificial gradient photonic materials are inspired by these color patterns. A concept for the preparation of such materials and their function as tunable mechanochromic materials is presented in this work. The system consists of a 1D polymer photonic crystal on a centimeter scale on top of an elastic poly(dimethylsiloxane) substrate with a gradient in stiffness. In the unstrained state, this system reveals a uniform red reflectance over the entire sample. Upon deformation, a gradient in local strain of the substrate is formed and transferred to the photonic crystal. Depending on the magnitude of this local strain, the thickness of the photonic crystal decreases continuously, resulting in a position-dependent blue shift of the reflectance peak and hence the color in a rainbow-like fashion. Using more sophisticated hard-soft-hard-soft-hard gradient elastomers enables the realization of stripe-like reflectance patterns. Thus, this approach allows for the tunable formation of reflectance gradients and complex reflectance patterns. Envisioned applications are in the field of mechanochromic sensors, telemedicine, smart materials, and metamaterials.

4.6.3. Main text

Living organisms with an amazing variety of colors are found in nature. The various coloration effects may arise due to pigments, bioluminescence, or periodic structure.¹ The colors arising due to periodic structure, structural color, exhibit a large variety of color tones and can change color if subjected to external stimuli.² In nature, the reflecting colors of butterfly³ or beetle wings,⁴ peacock feathers,⁵ tropical fish scales,⁶ and the chameleon skin demonstrate nonresponsive and responsive optical phenomena based on structural color.⁷ Motivations for such color changes include camouflage, warning, exhibition, and communication.⁸

Fulfilling certain requirements, photonic crystals will give rise to structural color.⁹ The principle of photonic crystals was explained by John and Yablonovitch in the late 1980s.^{10,11} It is based on the periodic arrangement (1D, 2D, or 3D) of regularly shaped, mostly transparent materials with different dielectric constants.¹² One of the major characteristics of a photonic crystal is

the photonic band gap, which forbids light within a certain wavelength range from propagating within the periodic arrangement.¹³ If the photonic band gap is in the visible region, structural color due to Bragg diffraction of the decoupled light is observed. Applications for photonic crystals are found in the fields of sensors,¹⁴⁻¹⁷ light-emitting diodes,¹⁸⁻²⁰ photovoltaics,²¹ and lasers.²²

Responsive photonic crystals can undergo a color change if subjected to external stimuli.²³ A well-known example from nature is the remarkable color shift of chameleon skin that is based on a lattice of guanine nanocrystals embedded in dermal iridophores.⁷ Deformation of the skin rapidly alters the spacing of the nanocrystals within the lattice that in turn causes a reversible color change.

A 1D photonic crystal (1DPC) — often also called a Bragg mirror — is the simplest geometry of a photonic crystal and possesses a periodicity in one direction.¹² It consists of alternating layers of high and low refractive index layers, resulting in an enhanced reflection due to constructive interference. Optical properties of 1DPCs depend on the refractive index contrast, the number and thickness of layers, and the angle of incident light. The thickness, and therefore the reflectance of certain wavelengths, can be tuned via the strain.²⁴ Most publications on responsive photonic crystals are limited to systems that reveal only a discrete color change in response to an external stimulus.^{25,26}

In this work, we demonstrate the preparation and function of a gradient photonic material that reveals a gradient color change upon application of an external stimulus. The composite material consists of a polymer-based 1DPC that is attached on top of an elastomer with a longitudinal stiffness gradient ([Figure 4.6.1](#)). The 1DPC has been designed to reveal a uniform reflectance in the red region of the visible spectrum in the unstrained state. Application of a strain leads to a gradient color shift in the reflectance along the sample. This effect is caused by the stiffness gradient of the substrate that transfers a gradient in local strain to the 1DPC upon deformation. The magnitude of this local strain influences the local thickness of the refractive index layers and hence the magnitude of the local color shift. In this manner, a position-dependent gradient in reflectance with a strain-tunable wavelength range is formed. A strain of 25% yields a rainbow-like gradient in reflectance from red to blue.

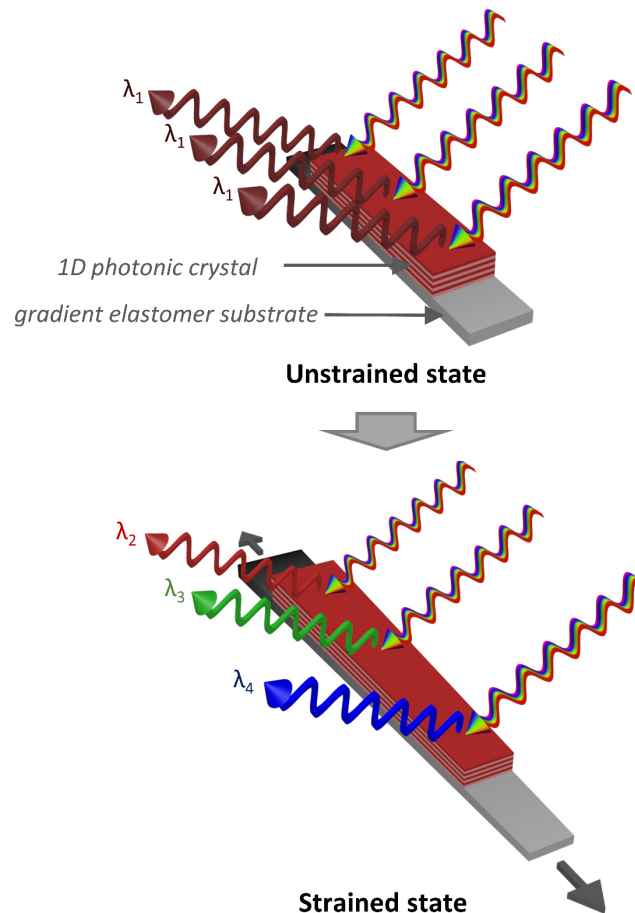


Figure 4.6.1: Gradient photonic material with a 1DPC on top of a longitudinal gradient elastomer substrate. The unstrained sample (top) reveals a uniform reflectance at one wavelength over the entire sample surface during illumination with visible light. Application of a strain (bottom) leads to a position-dependent gradient in reflectance along the sample.

To fabricate a gradient photonic material, a strain-tunable 1DPC was prepared in a first step from a photo-curable sliding elastomer resin in a manner similar to that of Howell et al. (cf. SI 4.6.7.1 for experimental details).²⁴ The crosslinks in such an elastomer consist of functionalized, figure-of-eight shaped cyclodextrin rings that are freely movable along polyethylene glycol chains.²⁷ This allows a very homogeneous stress distribution within the elastomer upon loading, since the cross-links can act like pulleys. Additionally, this elastomer system has the potential to be highly filled with nanoparticles, by that different refractive indices can be realized. The 1DPC film was prepared via sequential spincoating and UV-curing of alternating high and low refractive index layers on top of a polyvinylalcohol-coated silicon wafer (Figure 4.6.2). Polyvinylalcohol was used as a sacrificial layer for the later film transfer. The low refractive index layer consists exclusively of the UV-cured slide-ring elastomer. The

high refractive index layer is composed of the slide-ring elastomer that is additionally highly filled with functionalized and well-dispersed zirconium oxide nanocrystals with an average diameter of 6 nm. ZrO_2 is well-known to increase the refractive index of composite materials^{28,29} and was dispersed very well in this resin at a percentage of 70 wt%.

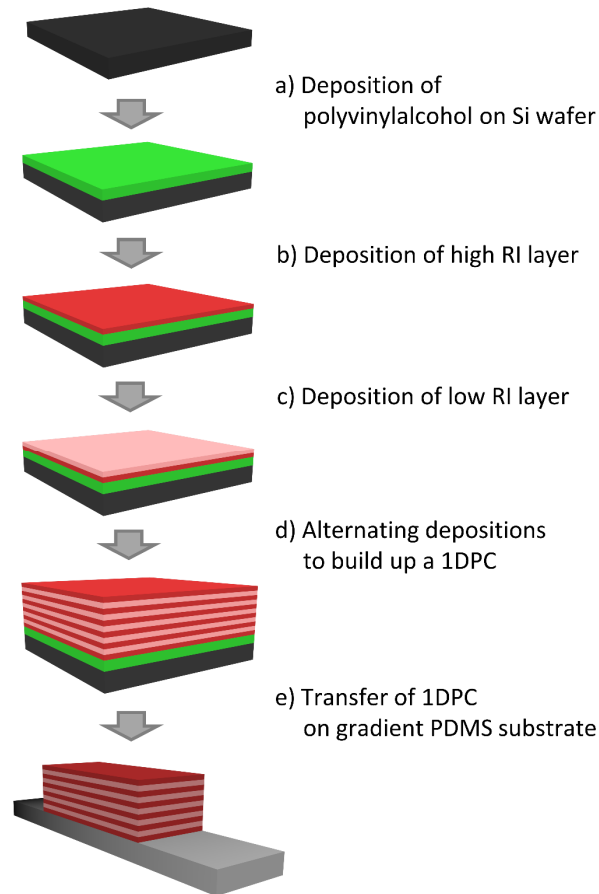


Figure 4.6.2: Preparation steps to a gradient photonic material: A) Polyvinyl alcohol is spin coated on top of a silicon wafer. B) A high refractive index layer is spin coated and UV-cured. C) Subsequently, a low refractive index layer is deposited on top and UV-cured. D) The 1DPC is built up by repeating these two steps multiple times. e) Finally, the 1DPC is floated and placed on top of a plasma-activated PDMS substrate with a gradient in stiffness to yield a gradient photonic material.

Utilizing this procedure, reversible strain-tunable 1DPCs with defined layer structures can be prepared. An analysis of the cross section of that 1DPC system as well as a cycling analysis at a strain of 10% was reported previously.²⁴ Ellipsometric measurements revealed thicknesses of 110 nm for the high refractive index layer and 125 nm for the low refractive index layer.

Refractive indices at 750 nm were determined as $n_{\text{low}} = 1.50$ and $n_{\text{high}} = 1.66$ that gives a difference in refractive index of 0.16.

The substrate for the gradient photonic material was prepared utilizing a high-precision syringe pump setup (cf. SI 4.6.7.2 for a detailed description of the elastomer preparation and characterization). This setup allows the preparation of longitudinal polymer gradient materials.³⁰⁻³⁴ In this study, a poly(dimethylsiloxane) (PDMS) substrate with a gradient in stiffness was prepared from a “hard” and a “soft” silicone resin that differ in the concentration of curing agent. The siloxane/curing agent ratio was 10:1 for the “hard” resin and 25:1 for the “soft” resin. The two silicone resins were mixed with the syringe pump setup and extruded with a flow profile into a moving mold. After cross-linking via thermal curing, substrates with a longitudinal hard-soft gradient in Young’s modulus from 0.6 to 1.3 MPa were obtained. The surface of the PDMS elastomer substrate was then activated via O_2 plasma. This step is necessary to ensure an optimal adhesion of the 1DPC on the substrate.

The 1DPC was then transferred to the gradient PDMS substrate (cf. SI 4.6.7.3 for a detailed experimental description). For that, both components were immersed in water. After dissolving the sacrificial PVOH layer, the 1DPC floated on the water surface and was transferred to the gradient PDMS substrate. After draining the water and drying, a gradient photonic material was obtained.

In an unstrained state, the entire surface of the 1DPC appears red (Figure 4.6.3). Reflectance was measured at five different positions (cf. SI 4.6.7.4 for experimental description) with distances of 1 cm in the unstrained state. The maximum reflectance peak occurs at 616 ± 5 nm and does not vary significantly over the entire sample surface. Upon stretching to 25%, the intrinsic stiffness gradient causes a gradient in local strain (cf. S2, Supporting Information). This local strain is transferred to the 1DPC, resulting in a rainbowlike gradient color shift of the reflected wavelength. The maximum reflectance peak here is shifted down to 524 ± 5 nm that indicates a color shift of 92 nm compared to the initial reflectance in the unstrained state.

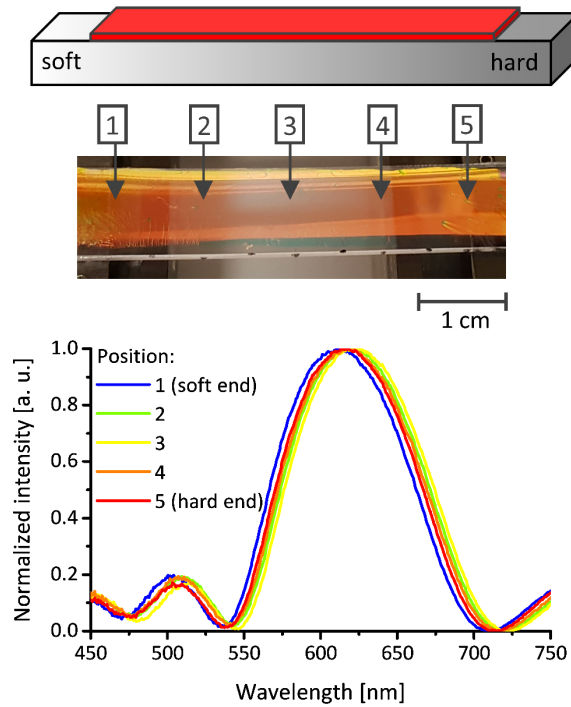
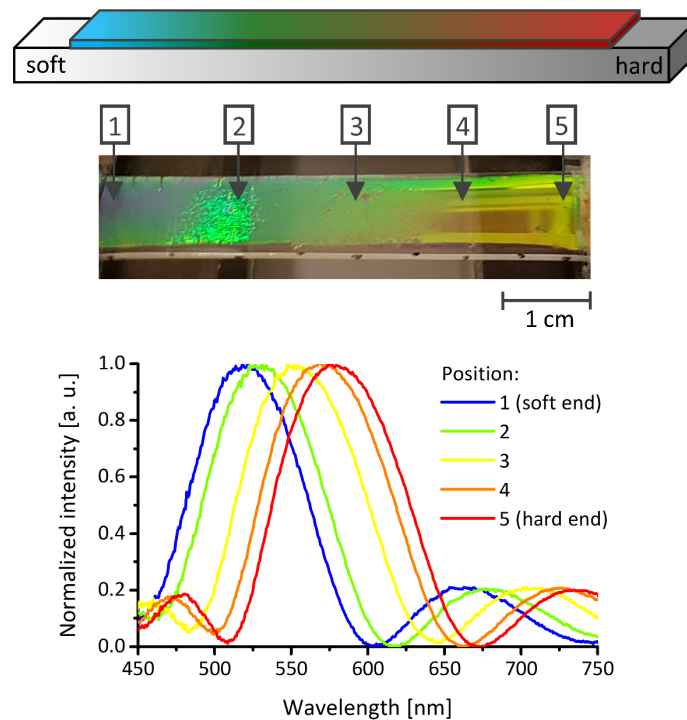
A: 0% strain**B: 25% strain**

Figure 4.6.3: Influence of strain on the reflectance of a 1DPC on PDMS with a hard-soft gradient. A) The unstrained sample (0% strain) reveals a uniform reflectance over the entire surface. B) Upon application of a strain (25%), a gradient in reflectance with smaller wavelengths is obtained. Reflectance spectra were normalized to the maximum peak height for better visualization of the color shift effect.

To demonstrate the versatility of our approach, even more complex gradient structures can be realized beside the hard-soft gradient. [Figure 4.6.4](#) depicts a 1DPC attached to a hard-soft-hard-soft-hard gradient PDMS elastomer. The stiffness is also controlled via the siloxane/curing agent ratio of the resins and is 50:1 in the soft parts and 5:1 in the hard parts. The Young's modulus ranges from 0.038 ± 0.004 MPa in the soft part and 2.3 ± 0.1 MPa in the hard part. Reflectance was measured at nine different positions with distances of 0.5 cm in the unstrained state. The maximum of the reflectance peak in the unstrained state occurs at 612 ± 6 nm and is comparable to the hard-soft gradient sample. Straining to 25% leads to a stripe-like appearance. The initial red appearance is shifted towards smaller wavelengths whereby the softer regions reveal a larger color shift than the harder regions.

We have demonstrated a facile preparation of gradient photonic materials consisting of a 1D polymer photonic crystal on a centimeter scale on top of an elastic PDMS substrate with a gradient in stiffness. In the unstrained state, this system reveals a uniform red reflectance over the entire sample. Upon deformation, a gradient in local strain of the substrate is formed and transferred to the photonic crystal. Depending on the magnitude of this local strain, the thickness of the photonic crystal decreases continuously, resulting in a position-dependent blue shift of the reflectance peak and hence the color in a rainbow-like fashion. Using more sophisticated hard-soft-hard-soft-hard gradient elastomers enables the realization of stripe-like reflectance patterns. We envision applications in the field of mechanochromic sensors, telemedicine, smart materials, and metamaterials.

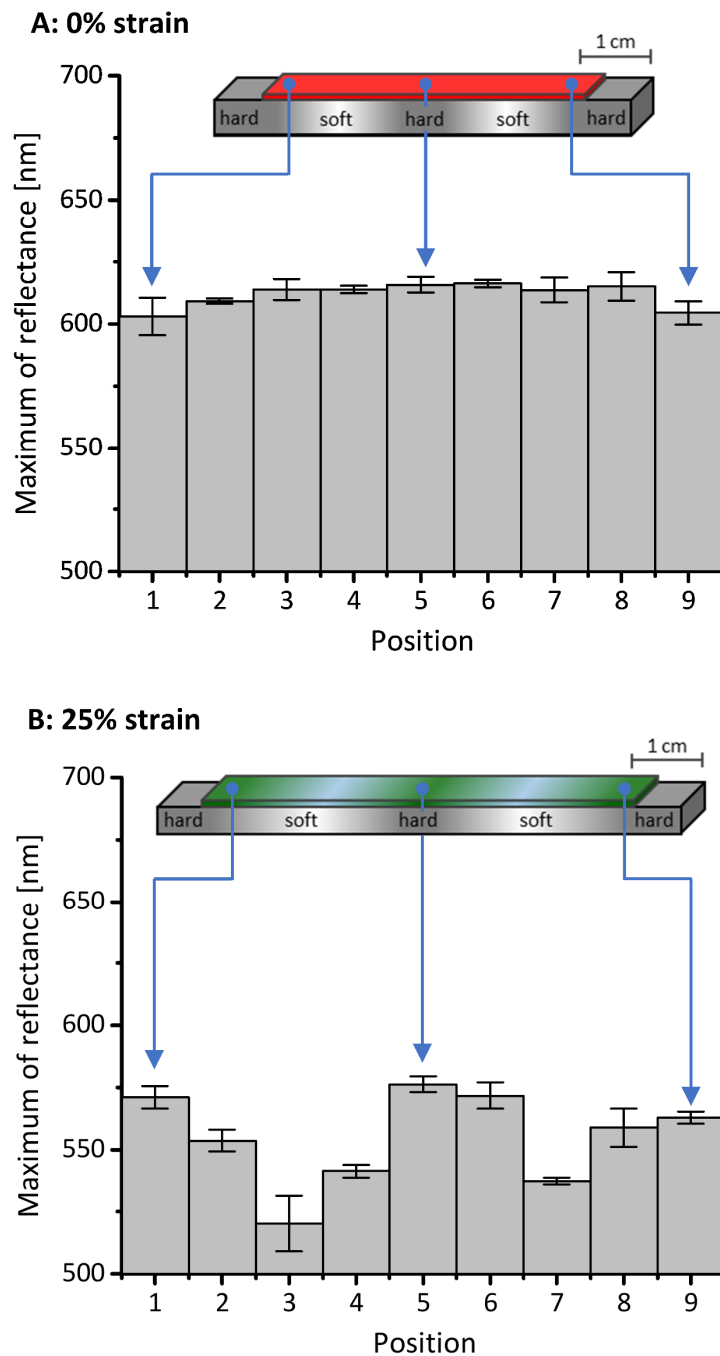


Figure 4.6.4: Influence of strain on the reflectance of a 1DPC on PDMS with a hard-soft-hard-soft-hard gradient. A) The unstrained sample reveals a uniform red reflectance over the entire surface with only slight deviations to the edges. B) Upon application of a strain (25%), the 1DPC reveals a gradient reflectance pattern with smaller wavelengths.

4.6.4. Acknowledgements

Funding of this work was provided by the University of Bayreuth, and the Elite Network of Bavaria (ENB), Macromolecular Science, is gratefully acknowledged. This work was further supported by the NSF Center for Hierarchical Manufacturing at the University of Massachusetts, Amherst (CMMI-1025020) and the Army Research Lab (W911NF-15-2-0026).

4.6.5. Conflict of interest

The authors declare no conflict of interest.

4.6.6. References

- [1] C. L. Booth,
Biol. J. Linn. Soc. **1990**, *40*, 125–163,
“Evolutionary significance of ontogenetic colour change in animals”.
- [2] G. Isapour and M. Lattuada,
Adv. Mater. **2018**, *30*, e1707069,
“Bioinspired Stimuli-Responsive Color-Changing Systems”.
- [3] L. P. Biro, Z. Balint, K. Kertesz, Z. Vertesy, G. I. Mark, Z. E. Horvath, J. Balazs, D. Mehn, I. Kiricsi, V. Lousse and J.-P. Vigneron,
Phys. Rev. E: Stat., Nonlinear, Soft Matter Phys. **2003**, *67*, 21907,
“Role of photonic-crystal-type structures in the thermal regulation of a Lycaenid butterfly sister species pair”.
- [4] J. W. Galusha, L. R. Richey, J. S. Gardner, J. N. Cha and M. H. Bartl,
Phys. Rev. E: Stat., Nonlinear, Soft Matter Phys. **2008**, *77*, 50904,
“Discovery of a diamond-based photonic crystal structure in beetle scales”.
- [5] J. Zi, X. Yu, Y. Li, X. Hu, C. Xu, X. Wang, X. Liu and R. Fu,
Proc. Natl. Acad. Sci. U. S. A. **2003**, *100*, 12576–12578,
“Coloration strategies in peacock feathers”.

- [6] Y. Yue, T. Kurokawa, M. A. Haque, T. Nakajima, T. Nonoyama, X. Li, I. Kajiwara and J. P. Gong,
Nat. Commun. **2014**, *5*, 4659,
"Mechano-actuated ultrafast full-colour switching in layered photonic hydrogels".
- [7] J. Teyssier, S. V. Saenko, D. van der Marel and M. C. Milinkovitch,
Nat. Commun. **2015**, *6*, 6368,
"Photonic crystals cause active colour change in chameleons".
- [8] H. Fudouzi,
Sci. Technol. Adv. Mater. **2011**, *12*, 64704,
"Tunable structural color in organisms and photonic materials for design of bioinspired materials".
- [9] J. Sun, B. Bhushan and J. Tong,
RSC Adv. **2013**, *3*, 14862,
"Structural coloration in nature".
- [10] E. Yablonovitch,
Phys. Rev. Lett. **1987**, *58*, 2059–2062,
"Inhibited spontaneous emission in solid-state physics and electronics".
- [11] S. John,
Phys. Rev. Lett. **1987**, *58*, 2486–2489,
"Strong localization of photons in certain disordered dielectric superlattices".
- [12] C. Fenzl, T. Hirsch and O. S. Wolfbeis,
Angew. Chem., Int. Ed. Engl. **2014**, *53*, 3318–3335,
"Photonic crystals for chemical sensing and biosensing".
- [13] Z. Lin, Y. Yang and A. Zhang,
Springer International Publishing, Cham **2017**,
"Polymer-Engineered Nanostructures for Advanced Energy Applications".
- [14] S. A. Asher, V. L. Alexeev, A. V. Goponenko, A. C. Sharma, I. K. Lednev, C. S. Wilcox and D. N. Finegold,
J. Am. Chem. Soc. **2003**, *125*, 3322–3329,
"Photonic crystal carbohydrate sensors: low ionic strength sugar sensing".
- [15] D. K. C. Wu, B. T. Kuhlmeier and B. J. Eggleton,
Opt. Lett. **2009**, *34*, 322–324,
"Ultrasensitive photonic crystal fiber refractive index sensor".

-
- [16] K. Lee and S. A. Asher,
J. Am. Chem. Soc. **2000**, *122*, 9534–9537,
"Photonic Crystal Chemical Sensors: pH and Ionic Strength".
- [17] E. Chow, A. Grot, L. W. Mirkarimi, M. Sigalas and G. Girolami,
Opt. Lett. **2004**, *29*, 1093,
"Ultracompact biochemical sensor built with two-dimensional photonic crystal microcavity".
- [18] T. N. Oder, K. H. Kim, J. Y. Lin and H. X. Jiang,
Appl. Phys. Lett. **2004**, *84*, 466–468,
"III-nitride blue and ultraviolet photonic crystal light emitting diodes".
- [19] K. McGroddy, A. David, E. Matioli, M. Iza, S. Nakamura, S. DenBaars, J. S. Speck, C. Weisbuch and E. L. Hu,
Appl. Phys. Lett. **2008**, *93*, 103502,
"Directional emission control and increased light extraction in GaN photonic crystal light emitting diodes".
- [20] J. J. Wierer, A. David and M. M. Megens,
Nat. Photonics **2009**, *3*, 163–169,
"III-nitride photonic-crystal light-emitting diodes with high extraction efficiency".
- [21] A. Chutinan, N. P. Kherani and S. Zukotynski,
Opt. Express **2009**, *17*, 8871,
"High-efficiency photonic crystal solar cell architecture".
- [22] H.-G. Park, S.-H. Kim, S.-H. Kwon, Y.-G. Ju, J.-K. Yang, J.-H. Baek, S.-B. Kim and Y.-H. Lee,
Science **2004**, *305*, 1444–1447,
"Electrically driven single-cell photonic crystal laser".
- [23] J. Ge and Y. Yin,
Angew. Chem., Int. Ed. Engl. **2011**, *50*, 1492–1522,
"Responsive photonic crystals".
- [24] I. R. Howell, C. Li, N. S. Colella, K. Ito and J. J. Watkins,
ACS Appl. Mater. Interfaces **2015**, *7*, 3641–3646,
"Strain-tunable one dimensional photonic crystals based on zirconium dioxide/slide-ring elastomer nanocomposites for mechanochromic sensing".

- [25] L. M. Fortes, M. C. Gonçalves and R. M. Almeida, *Opt. Mater.* **2011**, *33*, 408–412, “Flexible photonic crystals for strain sensing”.
- [26] G. H. Lee, T. M. Choi, B. Kim, S. H. Han, J. M. Lee and S.-H. Kim, *ACS Nano* **2017**, *11*, 11350–11357, “Chameleon-Inspired Mechanochromic Photonic Films Composed of Non-Close-Packed Colloidal Arrays”.
- [27] K. Ito, *Curr. Opin. Solid State Mater. Sci.* **2010**, *14*, 28–34, “Slide-ring materials using topological supramolecular architecture”.
- [28] P. Kim, C. Li, R. E. Riman and J. Watkins, *ACS Appl. Mater. Interfaces* **2018**, *10*, 9038–9047, “Refractive Index Tuning of Hybrid Materials for Highly Transmissive Luminescent Lanthanide Particle-Polymer Composites”.
- [29] D.-P. Song, C. Li, W. Li and J. J. Watkins, *ACS Nano* **2016**, *10*, 1216–1223, “Block Copolymer Nanocomposites with High Refractive Index Contrast for One-Step Photonics”.
- [30] K. U. Claussen, T. Scheibel, H.-W. Schmidt and R. Giesa, *Macromol. Mater. Eng.* **2012**, *297*, 938–957, “Polymer Gradient Materials”.
- [31] K. U. Claussen, M. Tebbe, R. Giesa, A. Schweikart, A. Fery and H.-W. Schmidt, *RSC Adv.* **2012**, *2*, 10185, “Towards tailored topography: facile preparation of surface-wrinkled gradient poly(dimethyl siloxane) with continuously changing wavelength”.
- [32] K. U. Claussen, E. S. Lintz, R. Giesa, H.-W. Schmidt and T. Scheibel, *Macromol. Biosci.* **2013**, *13*, 1396–1403, “Protein gradient films of fibroin and gelatine”.
- [33] K. U. Claussen, R. Giesa, T. Scheibel and H.-W. Schmidt, *Macromol. Rapid Commun.* **2012**, *33*, 206–211, “Learning from nature: synthesis and characterization of longitudinal polymer gradient materials inspired by mussel byssus threads”.

- [34] K. U. Claussen, R. Giesa and H.-W. Schmidt,
Polymer **2014**, *55*, 29–38,
"Longitudinal polymer gradient materials based on crosslinked polymers".

4.6.7. Supporting Information

4.6.7.1. Preparation and characterization of the one-dimensional polymer photonic crystal

1DPCs were prepared via alternating stacking of high and low refractive index layers using an approach similar to that reported by Howell et al.¹ A silicon wafer (5 cm x 5 cm) was hydrophilized via UV/ozone (UVO cleaner 342, Jelight Company, USA) for 7 min. A sacrificial layer of polyvinyl alcohol (Mowiol 4-88, Sigma Aldrich, 10 wt% in water, filtered with a Nylon syringe filter 0.45 µm) was spin coated on the silicon wafer (3000 rpm, 60 s, acceleration: 1500) and baked at 80 °C for 1 min to remove residual water. Then, 6 high refractive index layers and 5 low refractive index layers were deposited alternately, whereat the high refractive index layer was the first and the last deposited layer.

The solution for the *high refractive* index layer was prepared from toluene solutions of the slide-ring elastomer SA2400C (Soft Materials Inc., 5 wt%), photoinitiator (10 wt%) and zirconium oxide nanocrystals (5 wt%). The as-prepared solution contained 3 wt% of the photoinitiator Irgacure 819 (BASF) with regard to the SA2400C content and 70 wt% of ZrO₂ nanocrystals (PCNI-50-TOL, Pixelligent) with regard to solids. Spin coating of this solution (1700 rpm, 15 s, acceleration: 1500) on top of the PVOH layer, followed by UV-curing at 254 nm for 5 min gave a high refractive index layer film with a thickness of about 100 nm.

The solution for the *low refractive* index layer was prepared from toluene solutions of SA2400C (4 wt%) and the photoinitiator Irgacure 819 (10 wt%). The as-prepared solution contained 3 wt% of the photoinitiator with regard to SA2400C content). Spin coating of this solution on top of the high refractive index layer (2700 rpm, 15 s, acceleration: 2700), followed by UV-curing at 254 nm for 5 min gave a low refractive index layer film with a thickness of about 100 nm.

¹ I. R. Howell, C. Li, N. S. Colella, K. Ito, J. J. Watkins, *ACS Appl. Mater. Interfaces* **2015**, *7*, 3641, "Strain-tunable one dimensional photonic crystals based on zirconium dioxide/slide-ring elastomer nanocomposites for mechanochromic sensing".

4.6.7.2. Preparation and characterization of gradient elastomers

1. Preparation of gradient elastomers via syringe pump setup

Hard-soft (*hs*) and hard-soft-hard-soft-hard (*hshsh*) gradient materials were prepared from a “hard” and a “soft” silicone resin component. These components were prepared from the elastomer resin Sylgard 184 (Dow Corning) and consist of a mixture of siloxane and curing agent with defined mixing ratio (Table 4.6.1). Mixing of each component was done using a SpeedMixer™ DAC 150 SP (Hauschild, Germany) with a rotational speed of 2000 rpm for 2 min.

Table 4.6.1: Ratio of siloxane : curing agents used for preparation of hard and soft components for the *hs* gradient and the *hshsh* gradient.

Gradient	Hard component	Soft component
	siloxane : curing agent	siloxane : curing agent
<i>hs</i> gradient	10:1	25:1
<i>hshsh</i> gradient	5:1	50:1

The *hs* gradient material was prepared with a high-precision syringe pump system (Cetoni neMESYS). Glass syringes with the two components were mounted on the pump and connected via PVC tubing to a custom-made mixing head with an attached disposable static mixer (Sulzer Quadro 5.3/16 PP). Mixing of both components was controlled via a flow profile (Figure 4.6.5). The so-prepared compositional gradient was extruded into a Teflon mold (dimension: 60 mm x 10 mm x 2 mm) which was attached to a linear motion slide. The samples were cured at room temperature overnight and then post-cured at 80 °C for two hours.

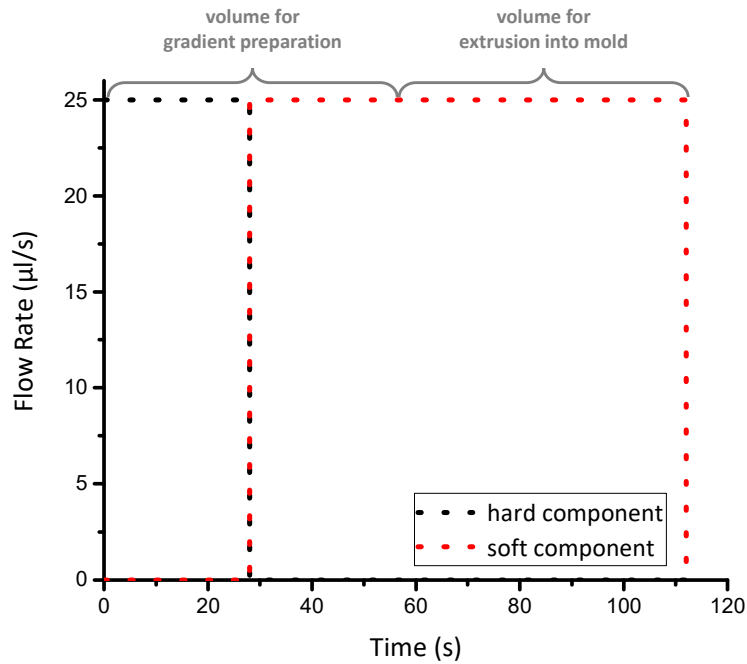


Figure 4.6.5: Flow profile which was used for processing the hard-soft gradient on a syringe pump setup. First, only “hard” component is filled into the static mixer, then the “soft” component is given into it. After thorough mixing in the static mixer, more “soft” component is used to extrude the pre-mixed gradient into a mold on a linear motion slide.

The *hshsh* gradient material consists of an oscillating gradient profile with very steep gradients between hard and soft areas. Since such steep gradients cannot be prepared with the mixing unit of the syringe pump setup, this material was prepared with a manual casting technique from a “hard” and a “soft” component (Table 4.6.1) in a Teflon mold (dimension: 60 mm x 10 mm x 2 mm) with polystyrene spacers (Figure 4.6.6). These spacers reduce the initial diffusion of hard and soft components.

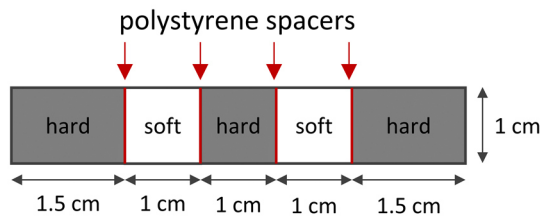


Figure 4.6.6: Design of the mold (top view) used for the hard-soft-hard-soft-hard gradient.

The “hard” and “soft” component were filled alternately in the separated zones. After an initial curing at room temperature for 30 min, the spacers were removed to allow a diffusion of the now more viscous components. The sample was cured at room temperature overnight and post-cured at 80 °C for two hours.

2. Optimization of the flow profile for the hard-soft gradient

The hard-soft gradient elastomer was prepared from two viscous silicone resin components. The optimization of the corresponding flow profile was done with the help of a sensitive fluorescence dye (Fluorescence red, CAS-Nr. 123174-58-3, Kremer Pigments, Germany) which was added in small amounts of only 0.02 wt% to the “soft” component. By that, the gradient can be visualized by measuring the UV-absorption position-dependently with a FLASHScan 530 (Analytik Jena AG, Germany). [Figure 4.6.7](#) depicts the position-dependent UV-absorption of a dyed hard-soft gradient sample after curing. The measurements were done on a 384-well microplate with a distance between each measuring spot of 4.7 mm. UV-Vis spectra were recorded between 375 and 900 nm and set to zero at 650 nm for comparison. The reported values for the absorption maxima at 560 nm were determined from 4 equally prepared samples (each sample was measured twice) and averaged.

After optimizing the flow profile with the fluorescent dye, an undyed gradient sample was prepared accordingly with that flow profile. This gradient sample was then used for the preparation of the gradient photonic material. From both ends of the 6 cm long sample, a length of 1 cm each is necessary for clamping. This allows a preparation and characterization of the photonic gradient over an effective length of 4 cm.

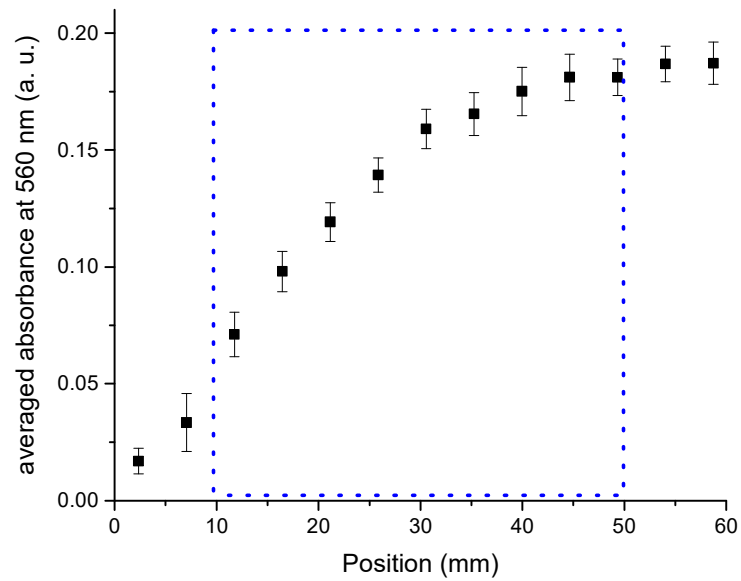


Figure 4.6.7: Visualization of the gradient via dyed reference samples. A fluorescent dye was added to the soft component. Position-dependent UV-Vis spectroscopy detects the dye absorption and indicates a continuous gradient from the hard to the soft end. The reported values are based on 8 measurements on 4 equally prepared gradient samples. The blue rectangle indicates the area which is used for the preparation and characterization of the gradient photonic material.

3. Mechanical characterization of gradient elastomers

The Young's Modulus was measured with an Instron 5565 universal testing machine (Instron, USA) coupled with a video extensometer. Sample thickness was determined at 5 positions using a caliper and averaged. 5 black adhesive dots (diameter: 3 mm) were attached to the surface of longitudinal PDMS samples (6 cm x 2 cm x 0.2 cm) in distances of 10 mm, resulting in 6 segments. The two outer segments were used for clamping. Testing was done at a test speed of 2 mm/min up to a strain of 3%. The extension of each of the 4 interior segments was recorded with the video extensometer between two dots. The Young's Modulus was determined from the initial slope of the stress-strain curve.

The hard-soft gradient material reveals a gradient in stiffness with a steadily increasing Young's modulus from 0.6 to 1.3 MPa (Figure 4.6.8).

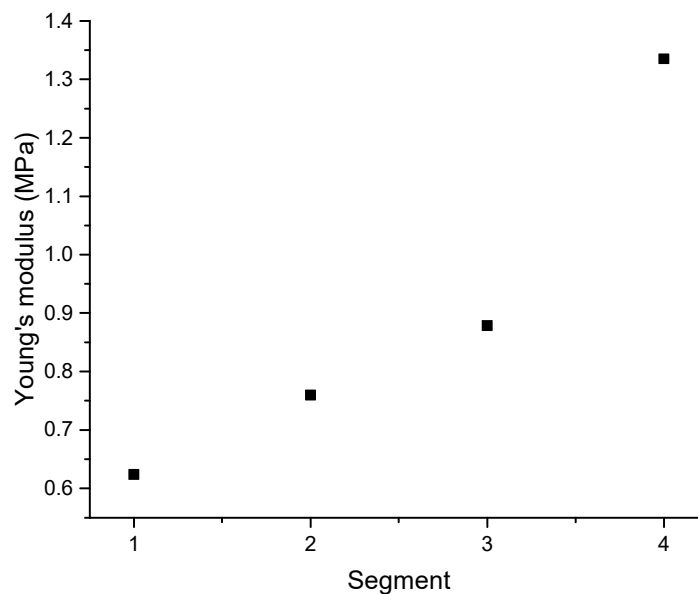


Figure 4.6.8: Variation of the Young's modulus within a hard-soft gradient material.

Figure 4.6.9 depicts the local strain within a hard-soft gradient photonic material upon application of an overall strain of 25%. The stiffness gradient within the substrate causes a linear gradient of local strain from 41.1% at the soft end down to 7.0% at the hard end.

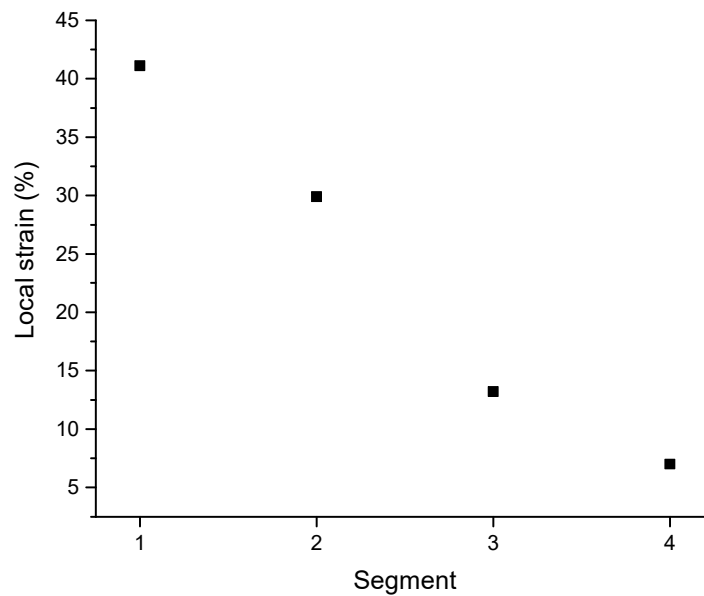


Figure 4.6.9: Variation of the local strain within a hard-soft gradient material upon application of an overall strain of 25%.

The hard-soft-hard-soft-hard gradient material reveals several steep stiffness gradients which could not be characterized utilizing the video extensometer. The Young's modulus was therefore determined from discrete samples with uniform composition. This gave a Young's modulus of 0.038 ± 0.004 MPa for the soft part and 2.3 ± 0.1 MPa for the hard part.

4.6.7.3. Transfer of the photonic crystal on top of the gradient elastomer

1DPCs were built up on a gradient PDMS elastomer via film transfer. PDMS is treated with O₂ plasma (PDC-32G, Harrick Plasma) for 5 min at high intensity to hydrophilize the surface. The hydrophilized PDMS elastomer and the silicon wafer with the 1DPC were fixed in a Petri dish and immersed in water to dissolve the PVOH sacrificial layer and float the 1DPC on the water surface. The 1DPC film was then transferred to the PDMS surface, the floating medium was drained, and the sample was dried under nitrogen flow to remove residual water from the interface between the 1DPC and PDMS.

4.6.7.4. Reflectance measurements on gradient photonic materials

Reflectance spectra on gradient photonic materials were measured with a Filmetrics F40-UV. A custom-made stage was used to strain the sample to defined values. Strain values were determined via a caliper. After recording a baseline using a silicon wafer, reflectance measurements were conducted at defined strains and defined positions of the sample. For each strain and position, at least three measurements were conducted.

5. Extended summary

This thesis focuses on the preparation, characterization and application of *gradient topographies and gradient functional materials*. For that, polydimethylsiloxane elastomers are surface-modified in different manners by three methods *controlled wrinkling*, formation of *surface relief gratings*, and preparation of *responsive photonic crystals*.

The motivation for the work arises from nature. In nature, well-defined hierarchical structures and gradients to create functional materials with advanced surface topography and tailored mechanical properties can be found. Examples in nature for tailored surface topographies are colorful butterfly wings and shark skin with improved hydrodynamics. Examples for responsive functional surfaces are the impressive skin color variations of chameleons and the brilliant appearance of tropical fish, both based on photonic crystals. Often, nature must connect materials with an extreme difference within their properties, e. g. stiffness. However, sharp transitions are often vulnerable for failure. Nature utilizes a strategy to bypass the fracture susceptibility by employing a gradient to mediate between the materials to be connected. An example for improved mechanical properties can be found in the sea mussel which uses a byssus to connect the soft interior of the mussel to the surface of a hard rock. Each byssus thread possesses a gradient in composition which in turn causes a gradient in stiffness. This stiffness gradient provides an improved connection and shock absorption within the rough environment of the sea. The natural concepts of these functional materials and surfaces can be transferred to technical systems. This is subject of this thesis.

In this context, the introduction of this thesis gives a brief overview about tailored materials and surfaces in nature and their corresponding functionalities. Furthermore, methods to artificially prepare surface topographies and functionalities are presented with respect to the state of the art. The first method is controlled wrinkling which is a comparatively simple technique to form surface patterns. The principle is based on a hard surface film which is attached to a soft elastomer substrate. Compression of such a composite material leads to the formation of wrinkled patterns. Hereby, the wavelength can be tuned *via* the Young's moduli and Poisson ratios of film and substrate, respectively, as well as the thickness of the hard film. The second method is the optical inscription of surface relief gratings in azobenzene films utilizing a holographic technique. This technique allows the inscription of gratings with a

sinusoidal wave pattern. Compared to patterns obtained by controlled wrinkling, these patterns are highly defect-free. The third approach utilizes photonic crystals. These materials reveal a photonic band gap and decouple a certain wavelength upon illumination with visible light.

This cumulative thesis consists of five topics which result in five publications. An overview of the thesis as well as a summary of the major achievements is presented in a synopsis.

The *first* and the *second topic* focus on the formation of gradient surfaces *via* controlled wrinkling. In the *first topic*, the formation of such gradient surfaces is based on a continuous gradient in the Young's modulus of the polydimethylsiloxane elastomer substrate. Embedding of such a stiffness gradient material in a matrix allows the systematic formation and investigation of hierarchical line-defects at the interface. The investigations on these line-defects as well as the developed prevention strategy contribute essentially to the fundamental understanding of controlled wrinkling.

The *second topic* covers the formation of gradient surfaces *via* controlled wrinkling by variation of the thickness of the hard film. For that, thin metal films with a gradient in film thickness were deposited on polydimethylsiloxane substrates using a combinatorial vapor deposition technique. Gold, chromium, and indium were investigated with respect to wrinkling behavior and surface morphology. An important achievement was the introduction of intermediate bonding layers to solve the issue of adhesion between the metal film and the polydimethylsiloxane substrate. The formed wavelength of the obtained gradient wrinkles can be explained well with theoretical considerations. The technique is a powerful approach to efficiently screen metal wrinkles with respect to their wavelengths on one substrate.

The *third* and the *fourth topic* cover the preparation of functional materials with sinusoidal surfaces *via* surface relief gratings. These gratings were inscribed optically in azobenzene films with a holographic technique. The *third topic* demonstrates the non-destructive grating transfer to polydimethylsiloxane and two thermoplastic polymers. Replicas with surface relief gratings with varying grating height were used as confinement templates for the guided self-assembly of nanoparticles. It is possible to align 1D, 2D and 3D hierarchical structures of polystyrene latex nanoparticles in dependency of the grating height. This represents a very elegant and efficient technique to screen assemblies of colloidal nanoobjects in one single experiment.

The *fourth topic* presents a novel technique to determine the refractive-index from transparent solids based on surface relief gratings. The principle is based on the angle-dependent investigation of the first and second order diffraction of monochromatic light on these gratings. Refractive-index determination is demonstrated for polydimethylsiloxane replicas of surface relief gratings. Results are compared to values obtained by an Abbe refractometer for various laser wavelengths. The developed technique is a powerful alternative to refractive-index determination *via* an Abbe refractometer or spectral ellipsometry.

The *fifth topic* focuses on the preparation of gradient photonic materials inspired by the chameleon skin. These materials consist of a strain-tunable one-dimensional photonic crystal which is attached on top of a polydimethylsiloxane elastomer substrate with a gradient in stiffness. The photonic band gap of photonic crystal causes the reflection of a certain wavelength. Unstrained samples reveal a uniform reflectance over the entire surface of the photonic crystal. Upon strain, a blueshift with a gradient in reflectance occurs. The reflectance pattern can be controlled by tailoring the architecture of the polydimethylsiloxane substrate. A rainbow-like reflectance pattern is formed by utilizing a hard-soft gradient substrate. The principle is also transferable to more complex substrate architectures as shown for a hard-soft-hard-soft-hard gradient revealing a stripe-like reflectance pattern. The presented gradient photonic materials are models for the development of nature-inspired mechanochromic sensors.

The *gradient topographies and functional gradient materials* presented in this thesis offer high potential for use in various applications. Envisioned fields are surface structuring, metamaterials, optics, electro-optics, metrology and sensors.

6. Danksagung

An dieser Stelle möchte ich mich bei allen Menschen bedanken, die direkt oder indirekt zum Gelingen dieser Arbeit beigetragen haben.

Mein besonderer Dank gilt meinem Doktorvater Prof. Dr. Hans-Werner Schmidt für das interessante interdisziplinäre Thema, die vielen gewinnbringenden Diskussionen sowie das tolle Vertrauensverhältnis. Die gewährte wissenschaftliche Freiheit bei der Ausgestaltung, die zahlreichen Möglichkeiten zur Präsentation meiner Ergebnisse im wissenschaftlichen Umfeld sowie die erstklassige Ausstattung des Arbeitsplatzes habe ich sehr zu schätzen gewusst!

Ein weiteres großes Dankeschön geht an Dr. Christian Neuber, der mir bei wissenschaftlichen Fragestellungen zur Seite stand und stets eine Lösung für die unmöglichsten Probleme hatte.

Herzlichen Dank an Dr. Reiner Giesa für die vielen hilfreichen Diskussionen und die Unterstützung bei technischen Fragestellungen aller Art!

Meinem Vorgänger Dr. Kai-Uwe Claußen danke ich herzlich für die Einarbeitung in die Thematik der Gradientenmaterialien. Von ihm habe ich nicht nur wissenschaftlich sehr viel gelernt, er ist für mich auch ein persönliches Vorbild geworden.

Herzlichen Dank an die Kooperationspartner vom Leibniz Institut für Polymerforschung in Dresden (Prof. Dr. Andreas Fery, Dr. Bernhard Glatz und Patrick Probst) und vom Bayreuther Institut für Makromolekülforschung (Prof. Dr. Lothar Kador, Dr. Christoph Meichner, Samuel Grimm, Stefan Hartung) für die sehr gute Zusammenarbeit.

Während meiner Auslandsaufenthalte durfte ich an der University of Massachusetts in Amherst (USA) arbeiten. Ein herzliches Dankeschön hierfür geht an Prof. Dr. James Watkins und Dr. Irene Howell für die sehr gute Zusammenarbeit. Danke auch an Dr. Jacobo Morere Rodriguez, Dr. Stephen Strassburg, Jo-Ann Bourguignon und Mary Ann Mish für die organisatorische Unterstützung während dieser Aufenthalte.

Für die Zusammenarbeit mit dem Lehrstuhl Biomaterialien danke ich Prof. Dr. Thomas Scheibel und Christian Haynl. Es war für mich stets ein Genuss, mit euch über den Tellerrand der Polymerchemie zu schauen!

Viele Praktikanten haben bei mir im Labor mitgearbeitet. Danke an Olga Isakin, Anna Lechner, Vanessa Leffler, Moritz Salzmann, Max Schnepf, Tobias Schwob, Thomas Tran und Kasper van der Zwan!

Ebenso herzlichen Dank an meine Hiwis in der „AG Schedl“ Felix Bretschneider, Julian Hungenberg, Leonie Kanzler, Dennis Schröder und Melina Weber! Es hat mir äußerst viel Spaß gemacht, mit euch zu arbeiten!

Ein großes Dankeschön geht an meine Bürokollegen Andreas Frank, Eva Fürsattel, Simon Gumbel, Dr. Tristan Kolb, Markus Stihl und Lisa Weber für die exzellente Arbeitsatmosphäre!

Herzlichen Dank an Petra Weiß und Christina Wunderlich für die herausragende Unterstützung bei organisatorischen Angelegenheiten jeglicher Art!

Mit seiner umfangreichen Expertise hat mir Dr. Klaus Kreger vor allem in den Publikationsprozessen sehr geholfen. Vielen Dank hierfür!

Herzlichen Dank an Martina Heider für die REM-Aufnahmen und an Markus Hund für die technische Unterstützung bei AFM-Messungen.

Doris Hanft danke ich für die Synthese des verwendeten Azobenzolmoleküls.

Abschließend ein großes Dankeschön an alle Mitarbeiter des Lehrstuhls Makromolekulare Chemie I für das fantastische Arbeitsklima. Ich bin jeden Tag sehr gerne hierhergekommen!

Nicht alle verwendeten Gerätschaften gab es fertig zu kaufen. Herzlichen Dank an die Belegschaft der GEO-Werkstatt für die schnelle und unkomplizierte Anfertigung diverser Gerätschaften.

Danke an das Elitenetzwerk Bayern und die University of Bayreuth Graduate School für die Unterstützung meiner Auslandsaufenthalte, die bestens organisierten Softskill-Seminare sowie die erstklassigen Lehrveranstaltungen! Besonderer Dank geht an Christina Wunderlich und Dr. Daniel Wagner für die stets einwandfreie Organisation im Elitestudienprogramm „Macromolecular Science“!

Eine Doktorarbeit kann nicht ohne Geldgeber angefertigt werden. Herzlichen Dank an den Freistaat Bayern und die Europäische Union für die finanzielle Förderung!

Ich danke dem Alumniverein der Chemie CSG e.V. und dem JCF Bayreuth für die Förderung des guten Miteinanders unter Bayreuther Chemikern! Es war mir eine Ehre, in beiden Vereinen Verantwortung übernehmen zu dürfen und dabei das wissenschaftliche Angebot sowie das Campusleben an der Universität Bayreuth aktiv mitzugestalten.

Herzlichen Dank an Alex, Cathy, Chris, Christoph, Eddie, Felix, Francesco, Hasi, Heike, Hubi, Ibo, Jannik, Jessi, Julia, Lena, Markus, Matthias, Sabrina und Tanja. Die zahlreichen hochinterdisziplinären Diskussionen beim Mittagessen oder bei unseren gelegentlichen Koch- und Spieleabenden werde ich nicht vergessen!

Danke an Alexander, Julian, Simon und Stefan aus der AG Köhler. Ihr habt mir bei unserem Schafkopfstammtisch nicht nur einen tiefen Einblick in die Irrungen und Wirrungen der Physik gegeben, sondern mir auch den „Sie“ – den Traum jedes Schafkopfspielers – erfüllt!

Ebenso vielen Dank an Andi, Anna, Attila, Benny, Channy, Claudia, Diana, Dobbie, Elias, Isabella, Jonas, Mischa, Stefan, Thomas und Zeißi! Unser regelmäßiger Sonntagsbrunch und unsere Wanderungen waren eine sehr angenehme Abwechslung zum Laboralltag!

Abschließend möchte ich meiner Familie für die Unterstützung in jeder Lebenslage und das stets offene Ohr danken.

(Eidesstattliche) Versicherungen und Erklärungen

(§ 9 Satz 2 Nr. 3 PromO BayNAT)

Hiermit versichere ich eidesstattlich, dass ich die Arbeit selbstständig verfasst und keine anderen als die von mir angegebenen Quellen und Hilfsmittel benutzt habe (vgl. Art. 64 Abs. 1 Satz 6 BayHSchG).

(§ 9 Satz 2 Nr. 3 PromO BayNAT)

Hiermit erkläre ich, dass ich die Dissertation nicht bereits zur Erlangung eines akademischen Grades eingereicht habe und dass ich nicht bereits diese oder eine gleichartige Doktorprüfung endgültig nicht bestanden habe.

(§ 9 Satz 2 Nr. 4 PromO BayNAT)

Hiermit erkläre ich, dass ich Hilfe von gewerblichen Promotionsberatern bzw. -vermittlern oder ähnlichen Dienstleistern weder bisher in Anspruch genommen habe noch künftig in Anspruch nehmen werde.

(§ 9 Satz 2 Nr. 7 PromO BayNAT)

Hiermit erkläre ich mein Einverständnis, dass die elektronische Fassung meiner Dissertation unter Wahrung meiner Urheberrechte und des Datenschutzes einer gesonderten Überprüfung unterzogen werden kann.

(§ 9 Satz 2 Nr. 8 PromO BayNAT)

Hiermit erkläre ich mein Einverständnis, dass bei Verdacht wissenschaftlichen Fehlverhaltens Ermittlungen durch universitätsinterne Organe der wissenschaftlichen Selbstkontrolle stattfinden können.

Bayreuth, den 02. Oktober 2019

Andreas Schedl